Micromechanics of ultra-high molecular weight polyethylene fibre composites

Burigede Liu
Queens' College

Submitted for the degree of Doctor of Philosophy
at the University of Cambridge

November 2018

Micromechanics of ultra-high molecular weight polyethylene fibre composites

Burigede Liu

Ultra-high molecular weight polyethylene (UHMWPE) fibre composites are considered to be state-of-the-art materials for penetration and ballistic impact protection applications. The composites are made of strong UHMWPE fibres with a soft compliant matrix. The extreme anisotropy caused by the mismatch between the stiffness and strength of the fibres and the matrix resulted in unique deformation and failure mechanisms which cannot be found in conventional engineering materials. Therefore, the thesis contributes towards understanding the governing mechanisms of UHMWPE composites that resulted in their high penetration and impact resistance, as well as characterizing their mechanical response under dynamic loading.

In the first part of the thesis, we focus on the quasi-static penetration response of UHMWPE composites by sharp-tipped punches. It is shown that the punch penetrates the composites without fibre fracture but by the formation of mode-I cracks along the fibre directions. The results indicate that the high penetration resistance of the composites by sharp-tipped punches is attributed to the high toughnesses of the composites. In the second part of the thesis, failure mechanism maps are developed to illustrate the mechanisms by which failure can initiate in UHMWPE composite beams impacted by blunt projectiles. We reveal that beams with low shear strengths fail by the indirect tension mode at high impact velocities while beams with high shear strengths fail by the bending mode at significantly lower impact velocities. The study thus provides a mechanistic understanding of the experimental observations that high ballistic performance composites require low matrix shear strength. Finally, in the third part of the thesis we investigate the dynamic in-plane compressive response of the composites. It is revealed that compressive deformation of the composites occurs by ply level kink band formation. Additionally, the study shows that the composites become strongly strain rate dependent at strain rates above $100\ \mathrm{s}^{-1}$ and the observed strain rate dependency is mainly attributed to that of the matrix.

The findings presented throughout this thesis reveal the key mechanisms and material parameters of the UHMWPE composites which governs their impact and penetration resistance, hence open new avenues and additional routes towards the design of composite materials with ultimate performance.

Preface

This thesis is submitted for the degree of Doctor of Philosophy, at the University of Cambridge. The research herein was conducted at the Department of Engineering in Cambridge University between October 2014 and November 2018 and under the supervision of Prof. Vikram S. Deshpande. The research work was sponsored by Defence Advanced Research Projects Agency (DARPA) and Cambridge Commonwealth Trusts (CCT).

The work is original and my own, except where specified or referenced as work of others in the text. This document in whole or part, has not been submitted for any other degree, diploma or qualification.

This thesis contains approximately 50000 words, 63 figures and 1 table, in accordance with specifications laid down by the Board of Graduate Studies.

Burigede Liu

Cambridge, UK

November 2018

Abstract

Ultra-high molecular weight polyethylene (UHMWPE) fibre composites are considered to be state-of-the-art materials for penetration and ballistic impact protection applications. The composites are made of strong UHMWPE fibres with a soft compliant matrix. The extreme anisotropy caused by the mismatch between the stiffness and strength of the fibres and the matrix resulted in unique deformation and failure mechanisms which cannot be found in conventional engineering materials. Therefore, the thesis contributes towards understanding the governing mechanisms that resulted in their high penetration and impact resistance, as well as characterizing their mechanical response under dynamic loading. A comprehensive review of the existing literature for the mechanical properties as well as indentation and impact mechanisms of the UHMWPE fibres and composites are presented in Chapter 2.

In the first part of the thesis (Chapter 3), we focus on the penetration response of unidirectional (UD) and $[0°/90°]$ cross-ply UHMWPE composites by sharp-tipped cylindrical punches. Experimental observations using combined optical microscopy and X-ray tomography revealed that in both cases the composites fail by the formation of mode-I cracks along the fibre directions, following by the wedging open of the crack to accommodate the advancing punch. For the cross-ply composites, delamination between adjacent $0°$ and $90°$ layers also occurs to compensate the incompatible deformation between adjacent plies containing orthogonal mode-I cracks. Micromechanical models are developed to model the steady-state penetration pressure for both composites. A pressure-dependent crystal plasticity framework is developed to accurately model the material anisotropy as well as the large shear strains and fibre rotations occurred during the penetration. The effect of intra and inter-ply fracture are characterized by mode-I and delamination toughness respectively. These models successfully predict the experimental observations and design maps revealing possible ways to increase the penetration resistance were constructed based on the theoretical study.

We then present in Chapter 4 a numerical study on the mechanisms by which failure is initiated in cross-ply UHMWPE composite beams impacted by cylindrical projectiles. The crystal plasticity framework developed in Chapter 3 is used to model each ply and failure mechanism maps are constructed for a range of impact velocities, beam shear strengths and ply tensile strengths. We identify two dominant failure modes from the study. The mode I failure is the failure of plies immediately under the projectile via an indirect tension mechanism. The mode

II failure is due to the fibre straining at the rear of the impacted beam resulting from beam bending and ply stretching. For beams with low shear strengths, mode-I indirect tension failure is the dominant failure mode while for beams with high shear strengths, failure is governed by the mode-II failure. It is found that low shear strengths help to relax tensile stresses within the beam, and results in the need for higher impact velocity to initiate failure. Thus the numerical calculations provide a mechanistic understanding of the experimental observations that composites with low shear strengths possess a higher ballistic performance.

In Chapter 5, we investigate the dynamic in-plane compressive response of cross-ply UHMWPE composites in the range $0.01\ s^{-1}$ to $4000\ s^{-1}$. The strain rate sensitivity is mild for strain rates less than about $100\ s^{-1}$ but a steep increase is observed at higher rates. We show that the governing deformation mechanism over the whole range of strain rates investigated is kinking (micro-buckling) of the plies. In order to gain a mechanistic understanding of the measured strain rate sensitivity, we employed finite element calculations of the compression experiments with each ply explicitly modelled using the crystal plasticity model developed in chapter 3. In the calculations, two limits are considered with perfectly-bonded plies and completely un-bonded plies. The calculations with perfectly-bonded plies agree well with the measurements confirming that ply delamination plays a small role in setting the compressive strength at least at moderate strain levels. Additionally, the calculations reveal that misalignment of the specimen between the compression platens has a strong influence on the compressive response. Importantly, it is revealed that the strong rate sensitivity observed for strain rates above 100 is mainly associated with rate sensitivity of the matrix rather than the inertial stabilization effect.

Finally in Chapter 6, the overarching conclusion drawn from these studies are discussed along with suggestions for future work.

Acknowledgements

It has been an honour and a privilege to study in Cambridge during my PhD and being supervised by Prof. Vikram Deshpande. I owe deep gratitude to Prof. Deshpande for all the guidance and helps through the years. His knowledge and insights in mechanics as well as the enthusiasm in research have always inspired me through my graduate study. I would like to thank him for his patience, kindness and encouragement which have made my time as a PhD student fruitful and productive.

I am also grateful to Prof. Norman Fleck for being my advisor. Many of our studies are inspired by his phenomenal work and theory, and I owe him my thanks for making me being cautious about my assumptions and arguments when doing research. I would also like to thank Prof. Haydn Wadley for his insightful suggestions and inspiring discussions on our study. I must thank Dr. Ulrich Heisserer for many detailed discussions on our research, inviting me to visit the great DSM company which manufactures the materials we examined, as well as supplying these materials to us.

As a PhD student, I benefited a lot from the wisdom from the postdocs in the Oatley lab. I would like to especially thank Dr. Karthikeyan Kandan for his help on our experimental studies. His great knowledge on experiments and exceptional experimental skills never ceases to amaze me. I acknowledge Drs. Sohrab Kazemahvazi, William Ronan and Andrea Vigliotti for teaching me the details of numerical modelling and programming. I am grateful to Dr Siamak Soleymanishishvan for countless enjoyable discussions and lessons on the theory of solid mechanics. I must also thank Drs Lucas Meza, Harika Tankasala, Mark O'masta, Arun Raina, Emilio Paneda, Wei Tan, Ying Zhao, Lili Zhang and Tiantian Li for many inspiring discussions on different aspects of my research.

The PhD students in the Oatley lab have always been the source of happiness and joy. I shared a lot of good times and memories with Satyajit, Bosco, Varun and Chen. I am grateful to Hamsini, Joe, Angkur, Alberto and Verner for all the good food in Pembroke and Queens' Colleges as well as the interesting anecdotes, jokes and funny stories. I also thank Adam and Frederick for many enjoyable discussions on our work and life as PhD students.

Finally, I am deeply gratitude to my family for their unconditional love and support, without whom this thesis would not have been possible.

It has truly been an unforgettable journey during the past four years in Cambridge as a PhD. To each and every one of you, thank you.

Contents

List of figures

List of Tables

CHAPTER ONE

1 Introduction

Ultra-high molecular weight polyethylene (UHMWPE) fibre composites are made of strong UHMWPE fibres with a compliant polyurethane matrix. The UHMWPE fibres and composites are increasingly used in a wide range of engineering applications including fish ropes, cutting resistant gloves, golf clubs and radomes (Marissen, 2011). In the form of cross-ply composites with a $[0°/90°]$ stacking sequence, they possess exceptional impact and penetration resistance (Van Der Werff and Heisserer, 2016) and are hence considered to be state-of-the-art materials for ballistic protection applications.

Driven by the interests on their high ballistic performance, a large volume of research has investigated the dynamic impact (Attwood et al., 2016) and static indentation mechanism (O'Masta et al., 2016) of the composites using blunt (spherical or flat-bottomed) projectiles. When impacted by such projectiles, the composites fail by the so-called indirect tension mechanism (Attwood et al., 2014), where the compressive stress imposed normal to the plies induces tensile in-plane ply straining due to the anisotropic expansion of the alternating plies. However, few studies have focused on the penetration mechanisms of the composites by sharp-tipped projectiles.

A common way to understand the ballistic performance of fibre composites is provided by Cunniff (1999). He used dimensional analysis to suggest that the ballistic limit velocity is governed by a material-dependent property which is related to the specific stiffness and energy absorption of the composites. While the Cuniff theory is shown to be invaluable to predict the ballistic limit of single fibres, it is less successful when used to gauge the ballistic performance of fibre composite structures. The primary limitation of the Cunniff model is that it suggests the ballistic limit velocity is independent of the composite shear strength. However, a range of experimental findings (De Ruijter et al., 2010; Karthikeyan et al., 2013; Yu et al., 2017) on composite materials suggests that the shear strength plays a critical role and the ballistic limit velocity tends to increase for composites with lower shear strength. A mechanistic understanding of this shear strength dependency is missing in the literature.

The UHMWPE composites are primarily used under dynamic loading and subjected to complex multi-axial stress fields, hence it is important to understand the dynamic properties of the composites in all loading directions. A large number of studies have investigated tensile properties of the composites (Govaert and Peijs, 1995; Kromm et al., 2003; Russell et al., 2013) while a few studies focused on their out-of-plane compression responses (Shaker et al., 2017). Surprisingly very few studies have focused on their in-plane compressive response with one exception from Attwood et al. (2015) who reported the static in-plane compression of the composites. On the contrary, the dynamic in-plane compressive response of the composites remains largely unexplored.

1.1 Objectives

This thesis aims to explore the micromechanics of the UHMWPE composites by considering the following objectives:

(i) To develop an understanding of the deformation and failure mechanisms of both unidirectional (UD) and cross-ply composites penetrated by a sharp-tipped punch, and to contrast them with those of blunt punches.

(ii) To investigate the interplay between ply shear strength, tensile fibre strength, beam thickness and impact velocity on the mechanisms by which failure is initiated in composite beams impacted by blunt projectiles.

(iii) To understand the dynamic in-plane compressive response of the UHMWPE composites and explore the strain rate sensitivity of these materials.

1.2 Outline

The thesis comprises of three studies and is constructed as follows. Chapter 2 reviews the existing literature on the mechanical response as well as the ballistic impact mechanism of UHMWPE fibres and composites.

Chapter 3 investigates the deep penetration mechanisms of the UHMWPE fibre composites by sharp-tipped punches. The associated failure mechanisms are revealed and the effect of punch diameter as well as ply thickness are investigated.

Chapter 4 studies the impact mechanisms of UHMWPE composite beams by blunt projectiles and develops failure mechanism maps to reveal the interplay between ply shear strength, tensile ply strength and impact velocity on the failure initiation in the composite beams.

Chapter 5 explores the high strain rate compressive response of the UHMWPE composite and investigates the material strain rate sensitivity as well as the relative influence of inertia and matrix rate effects.

Finally, in chapter 6 the overall conclusions of the thesis are presented with recommendations for future work.

1.3 Published work

The thesis was based upon journal articles written over the course of my study. Chapter 3 was based on an article published in *Journal of the Mechanics and Physics of Solids.* A paper based on Chapter 4 was submitted to *International Journal of Solids and Structures.* A paper based on Chapter 5 was submitted to *International Journal of plasticity.*

References

Attwood, J.P., Fleck, N.A., Wadley, H.N.G., Deshpande, V.S., 2015. The compressive response of ultra-high molecular weight polyethylene fibres and composites. Int. J. Solids Struct. 71, 141–155. https://doi.org/10.1016/j.ijsolstr.2015.06.015

Attwood, J.P., Khaderi, S.N., Karthikeyan, K., Fleck, N.A., O′Masta, M.R., Wadley, H.N.G., Deshpande, V.S., 2014. The out-of-plane compressive response of Dyneema composites. J. Mech. Phys. Solids 70, 200–226. https://doi.org/10.1016/j.jmps.2014.05.017

Attwood, J.P., Russell, B.P., Wadley, H.N.G., Deshpande, V.S., 2016. Mechanisms of the penetration of ultra-high molecular weight polyethylene composite beams. Int. J. Impact Eng. 93, 153–165. https://doi.org/10.1016/j.ijimpeng.2016.02.010

Cunniff, P.M., 1999. Dimensionless Parameters for Optimization of Textile-Based Body Armor Systems. 18th Int. Symp. Ballist. 1303–1310.

De Ruijter, C., Van Der Zwaag, S., Stolze, R., Dingemans, T.J., 2010. Liquid crystalline matrix polymers for aramid ballistic composites. Polym. Compos. 31, 612–619. https://doi.org/10.1002/pc.20835

Govaert, L.E., Peijs, T., 1995. Tensile strength and work of fracture of oriented polyethylene fibre. Polymer (Guildf). 36, 4425–4431. https://doi.org/10.1016/0032-3861(95)96848-3

Karthikeyan, K., Russell, B.P., Fleck, N.A., Wadley, H.N.G., Deshpande, V.S., 2013. The effect of shear strength on the ballistic response of laminated composite plates. Eur. J. Mech. - A/Solids 42, 35–53. https://doi.org/10.1016/j.euromechsol.2013.04.002

Kromm, F.X., Lorriot, T., Coutand, B., Harry, R., Quenisset, J.M., 2003. Tensile and creep properties of ultra high molecular weight PE fibres. Polym. Test. 22, 463–470. https://doi.org/10.1016/S0142-9418(02)00127-7

Marissen, R., 2011. Design with Ultra Strong Polyethylene Fibers. Mater. Sci. Appl. 02, 319–330. https://doi.org/10.4236/msa.2011.25042

O'Masta, M.R., Crayton, D.H., Deshpande, V.S., Wadley, H.N.G., 2016. Indentation of polyethylene laminates by a flat-bottomed cylindrical punch. Compos. Part A Appl. Sci. Manuf. 80, 138–147. https://doi.org/10.1016/j.compositesa.2015.10.015

Russell, B.P., Karthikeyan, K., Deshpande, V.S., Fleck, N.A., 2013. The high strain rate response of Ultra High Molecular-weight Polyethylene: From fibre to laminate. Int. J. Impact Eng. 60, 1–9. https://doi.org/10.1016/j.ijimpeng.2013.03.010

Shaker, K., Jabbar, A., Karahan, M., Karahan, N., Nawab, Y., 2017. Study of dynamic compressive behaviour of aramid and ultrahigh molecular weight polyethylene composites using Split Hopkinson Pressure Bar. J. Compos. Mater. 51, 81–94. https://doi.org/10.1177/0021998316635241

Van Der Werff, H., Heisserer, U., 2016. High-performance ballistic fibers: Ultra-high molecular weight polyethylene (UHMWPE), in: Advanced Fibrous Composite Materials for Ballistic Protection. https://doi.org/10.1016/B978-1-78242-461-1.00003-0

Yu, B., Karthikeyan, K., Deshpande, V.S., Fleck, N.A., 2017. Perforation resistance of CFRP beams to quasi-static and ballistic loading: The role of matrix strength. Int. J. Impact Eng. 108, 389–401. https://doi.org/10.1016/j.ijimpeng.2017.04.002

Chapter Two

2. Literature review

Ultra-high molecular weight polyethylene fibre composites are considered to be state-of-the-art materials for ballistic and impact protection applications. Over the past two decades, intensive research has been conducted on ultra-high molecular weight polyethylene (UHMWPE) fibres and composites. The following literature survey begins with a brief introduction on the UHMWPE fibres and UHMWPE composites, followed by a review of the characterization of their mechanical properties in tension, shear and compression. We then discuss the studies on the indentation and impact response of the UHMWPE composites as well as the associated modelling frameworks, and contrast them with other conventional composite materials such as carbon fibre reinforced plastics as well as aramid woven fabrics.

2.1 UHMWPE fibres and their applications

UHMWPE in the bulk form is a linear homopolymer first synthesized by Karl Ziegler in 1953, at the Max Planck Institute in northern Germany (Kelly, 2002). The polymer possesses a repeat unit $[C_2H_4]_\eta$ as seen in Fig. 2.1a, where η denotes the degree of polymerization. According to ASTM standards (ASTM, 2018), the term "ultra-high" indicates that this class of polyethylene possesses a degree of polymerization $\eta \approx 110{,}000$, which is $10-100$ times higher than the standard high density polyethylene. The material is a semi-crystalline polymer which consists of a crystalline phase and an amorphous phase (Lin and Argon, 1994). The extremely long polymer chains of the molecule result in exceptional friction and wear resistance. Additionally, the bulk UHMWPE is biologically inert, hence it is widely used in arthroplasty for total joint replacement today (Kurtz, 2004).

In 1979, Smith et al. (1979) reported a solution spinning/drawing process to produce UHMWPE fibres, as depicted in Fig. 2.1b. The high molecular weight polyethylene is first dissolved in a volatile solvent under nitrogen. The polymer solution is then drawn through a fine spinneret and the liquid filament is then quenched in a cooling bath of inert gas or insoluble

liquid to form a gel fibre. The gel fibre is subsequently drawn at high strain rate of the order 1 s^{-1} through an air oven to remove the solvent and yield the highly oriented UHMWPE fibres (Smith and Lemstra, 1980; Russell et al. 2013).

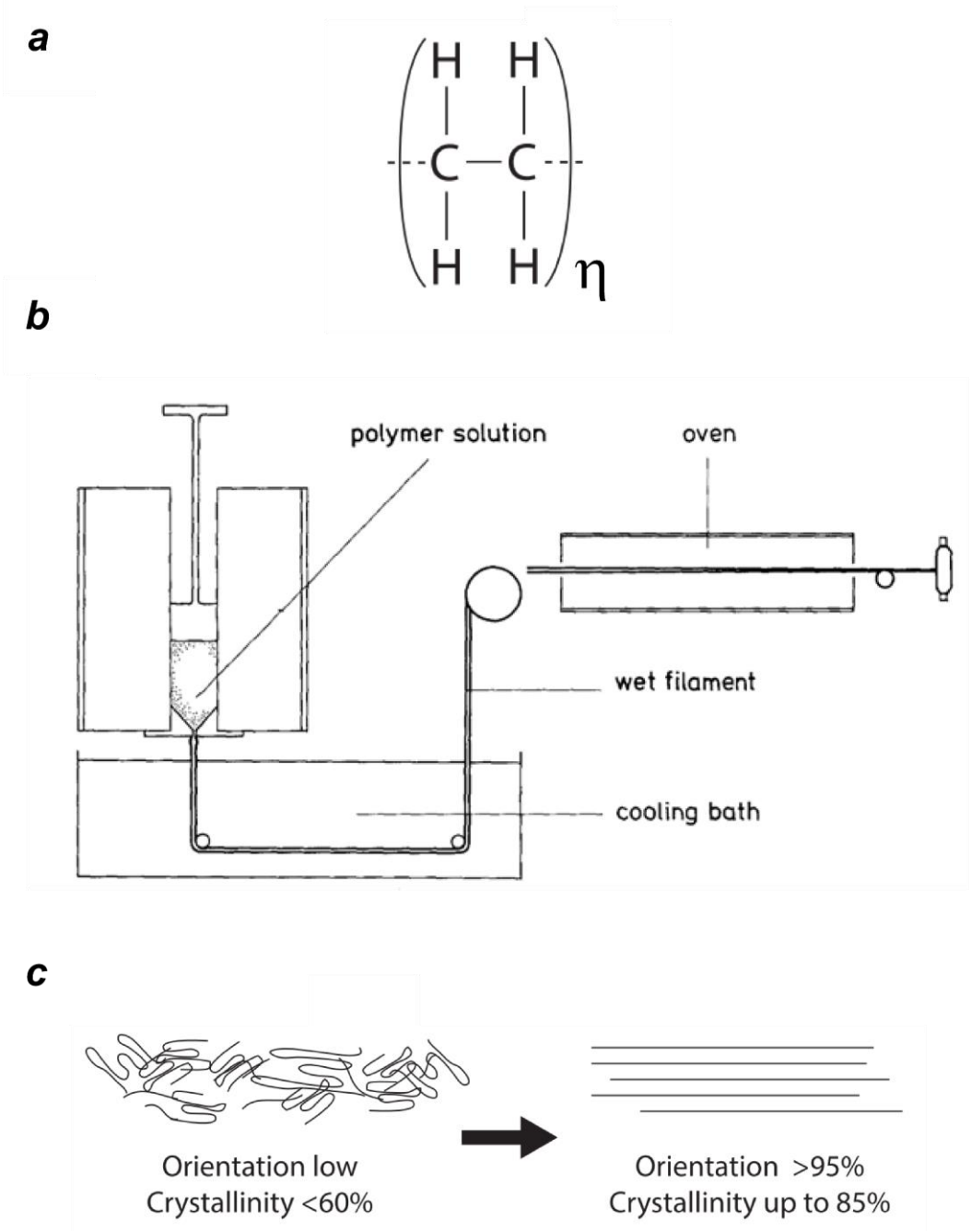

Figure 2.1: (a) Chemical structure of polyethylene. (b) Sketch of the solution spinning/drawing process in manufacturing the UHMWPE fibres. (c) Schematic illustration showing the improvement of molecular orientation and crystallinity of the UHMWPE fibres through the solution spinning/drawing process. Source: Smith and Lemstra (1980), Nguyen (2015).

The drawing process results in UHMWPE fibres with highly aligned molecular chains which significantly improve the mechanical properties of the material along the fibre direction. Compared to the bulk UHMWPE which possesses a typical tensile strength of 20−40 MPa (Greer et al., 2004), the fibres produced using the drawing process have a typical tensile strength of 3 GPa with a molecular orientation greater than 95% and crystallinity of up to 85% (Van, Dingenen, 2001), as depicted in Fig. 2.1c. Fig. 2.2 shows the material property chart of specific strength versus specific modulus for common fibres. It is clearly seen that the UHMWPE fibres are among the best when gauged by specific stiffness and strength.

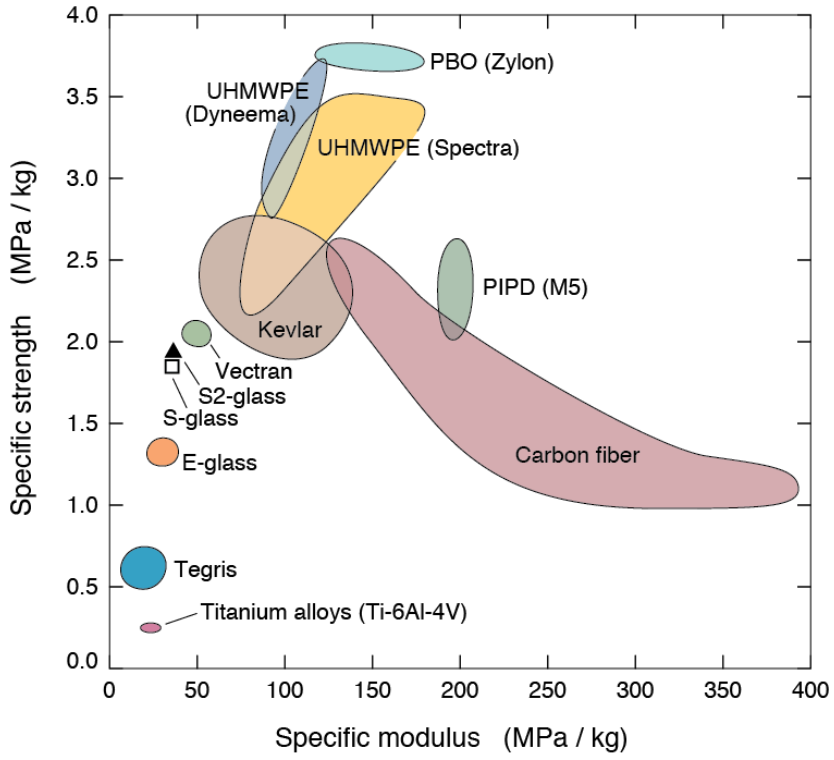

Figure 2.2: Material property chart for specific strength versus specific modulus for common fibres. Source: O'Masta et al. (2014).

UHMWPE fibres were later commercialized by DSM (DSM, Het Overloon 1, 6411 TE Heerlen, The Netherlands) under the trade name Dyneema® in Europe, and Honeywell (Honeywell Advanced Fibers and Composites, Morris Township, N.J., USA) under the trade name Spectra® in the US. A combination of low density and high strength make the fibres appealing for multiple industries. Ropes, lines and slings made of UHMWPE fibres possess a density of about 970 kg m^{-3} and are capable of floating in water. The ultra-strong fibres make it possible to use thinner yarns which can reduce drag and consequentially lead to less fuel consumption. Therefore they are ideal for heavy-lifting and off-shore applications. In the meanwhile, the

fibres are also difficult to cut and resistant to wear, thus they are widely used to make cutting-resistant gloves and denim (DSM.com).

In addition to their superior mechanical properties, UHMWPE fibres possess good multifunctional properties. They are attractive materials for the apparel industry as the high thermo-conductivity yielded from the highly aligned fibres (Shen et al., 2010) allows heat from the body to be efficiently transferred to the environment (Marissen, 2011). The fibres are shown to be transparent to a wide range of radio wave frequencies hence they are also ideal for radomes (Kozakoff et al., 2017).

2.2 UHMWPE fibre composites and their manufacturing process

Although the UHMWPE fibres and composites have an incredibly wide range of applications, in the current study we shall focus on their use for the ballistic protection applications. In these cases, $10-20$ μm diameter UHMWPE fibres are combined with polyurethane matrices to form unidirectional plies with ply thicknesses ranging from 20 μm to 100 μm and fibre volume fractions of 80 - 85% with the unidirectional plies typically combined to form a $[0^o/90^o]$ cross-ply composite. The composites have been proved to possess exceptional ballistic and impact resistance (Van Der Werff and Heisserer, 2016). They are widely used in personal and vehicle armours as well as bullet-proof helmets (Jacobs and Van Dingenen, 2001). According to Russell et al. (2013) and Attwood et al. (2014), the cross-ply UHMWPE fibre composites are manufactured in the following steps (see Fig. 2.3):

(i) A gel-spinning/hot drawing process (Smith et al., 1979; Smith and Lemstra, 1980) is used to produce highly orientated and highly crystalline fibres of diameter 17 μm.

(ii) Fibres are coated in a resin solution and are then formed into a $[0^o/90^o/0^o/90^o]$ stack. A drying process removes the matrix solvent from the stack, and several stacks are placed on top of each other in order to form the desired laminate.

(iii) The laminate is hot pressed at a temperature below that where the molecular crystallinity is lost. Bonding of the layers is achieved through use of a sufficiently high temperature to induce partial melting of the matrix material. The fibre diameter is unchanged by the hot-pressing operation, although some fibres may change their cross-sectional shape.

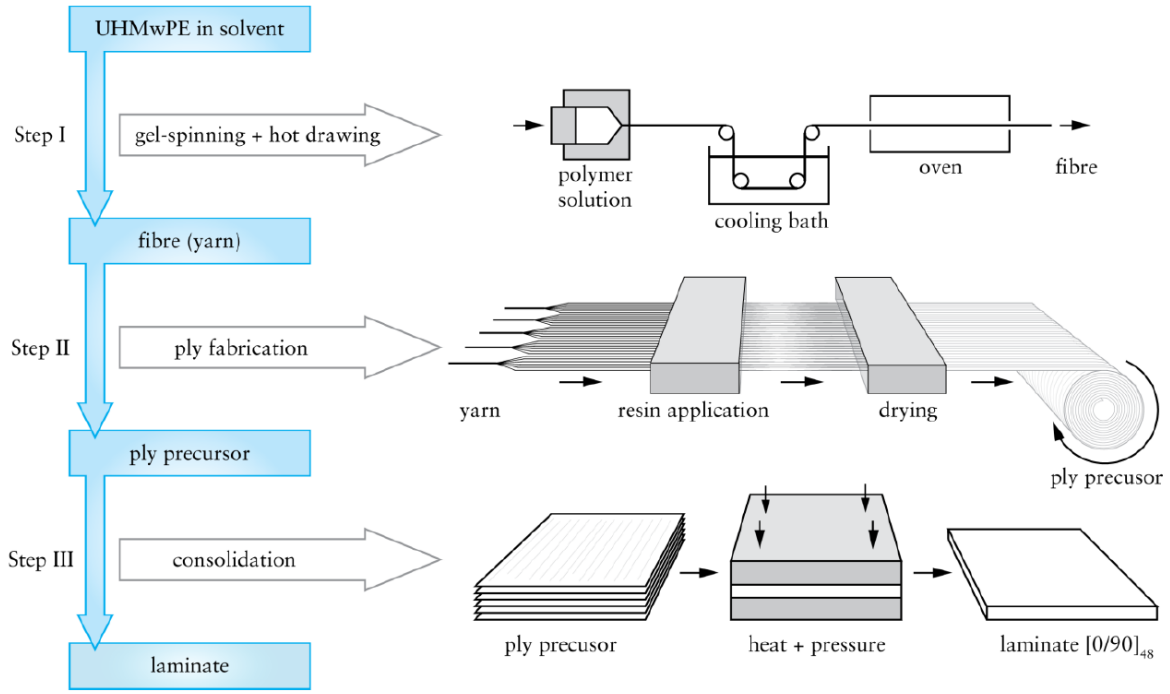

Figure 2.3: Sketch of the manufacturing steps in making the UHMWPE composites. Source: Russell et al. (2013).

2.3 Mechanical characterization of the UHMWPE composites

In order to understand the ballistic and impact mechanisms of the UHMWPE composites which involves complex multi-axial stress fields, it is crucial to first investigate the materials' response to basic loadings. In this section, we review the existing literature on the static and dynamic response of both UHMWPE fibres and UHMWPE fibre composites, in terms of three most basic modes of deformation: tension, shear and compression.

2.3.1 Tension

As one of the most basic modes of deformation, the tensile response of the UHMWPE composite has been widely studied in the literature. A series of early works (Capaccio et al., 1976; Capaccio and Ward, 1973; Gibson et al., 1974) focused on the static response of the melt-spun/drawn polyethylene fibres. They revealed that the tensile response of the fibres is elastic with Young's moduli increasing with the drawn ratio. With a drawn ratio of about 30, the moduli can reach 70 GPa which is comparable to the theoretical attainable unidirectional modulus of fully aligned polyethylene chains which is on the order of 220 GPa (Frank, 1970). In addition, it is found that the material tends to creep over a long period of time at a given stress, and both reversible viscoelastic creep and irreversible plastic flow can be observed

during the experiments (Wilding and Ward, 1978). Later work by Govaert and Lemstra (1992) shown that the gel-spun/drawn UHMWPE fibres possess similar tensile and creep behaviour and revealed that the irreversible plastic flow is related to the translational movement of the molecular chains within the crystal region of the fibre, while the reversible part of the creep deformation is related to the imperfect extension of the molecular chains. Berger et al. (2003) investigated the tensile creep deformation of the UHMWPE fibers under using Raman microscopy, they found that the stress distribution within the fibres during the tensile test is not uniform, and the peak stresses located in a small fraction of the fibre. They thus concluded that the discrepancy between the theoretically feasible and practically achievable strength and modulus is caused by the defects in the non-perfect structure of the manufactured UHMWPE fibres. In order to improve the creep properties, Jacobs et al. (2000) proposed a chemical cross-linking method and reported that the creep rate of the fibres can be significantly reduced at an expense of slightly decreased fibre stiffness and strength.

The effect of strain rate on the tensile response of the UHMWPE fibres is also extensively studied in the literature. At strain rates below $0.1\ s^{-1}$, the creep effect described above becomes significant, with a drop in both stiffness and strength of the fibre observed from the experiments (Koh et al., 2010; Kromm et al., 2003; Peijs et al., 1994). By contrast, the fibres are found to be almost insensitive to the strain rate in the range $0.1\ s^{-1}$ to $1000\ s^{-1}$ (Huang et al., 2004; Koh et al., 2010; Russell et al., 2013). Although the measured tensile strength of the fibres (on the order of 2.5 GPa at high strain rates) is consistent in the literature, the actual value of the tensile stiffness of the fibre is subjected to some debate. Huang et al. (2004) used a tensile Hopkinson pressure bar method and measured the dynamic stress strain relationship of the fibres under impact loading and reported a fibre stiffness of about 80 GPa. Using a similar method, Koh et al. (2010) reported a fibre stiffness of about 60 GPa. In a comprehensive study, Russell et al. (2013) pointed out that the inconsistent and often un-repeatable stiffness measurement from the literature is resulted from the fact that the strain measured from a tensile Hopkinson bar test is often inferred from the displacement of the grip, and the slip between the grip and the fibre leads to an over-estimation of the actual strain. They proposed a modified experimental apparatus as sketched in Fig. 2.4a, where the fibres are wrapped around a semi-circular anvil and adhered to it in order to ensure the correct measurement of the axial strain. It is shown that the stiffness of the UHMWPE fibre is on the order of 130 GPa at strain rates

higher than $0.1\ s^{-1}$. The measured stress strain relationship from Russel et al. (Russell et al., 2013) is presented in Fig. 2.4b at selected strain rates.

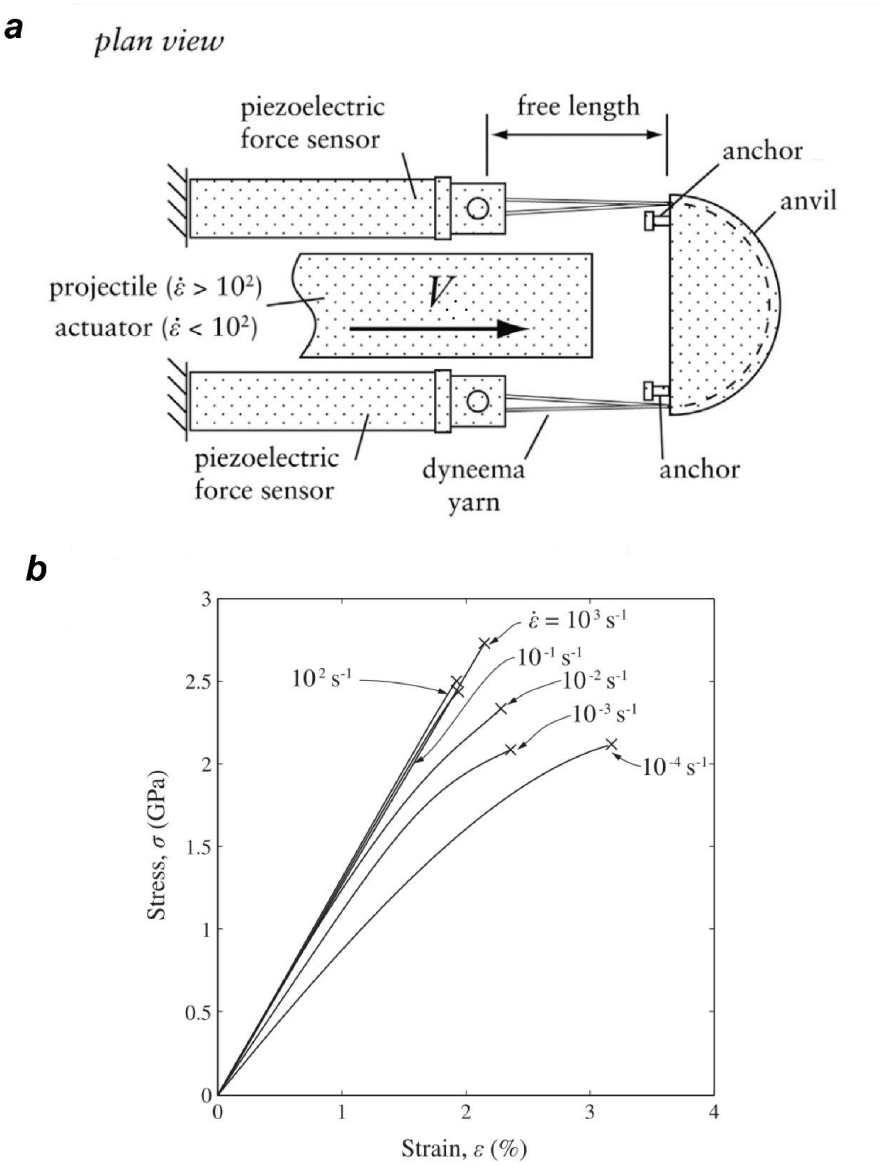

Figure 2.4: (a) The experimental set-up used to measure the dynamic tensile stress strain response of the UHMWPE fibres. (b) The stress and strain relationship of the UHMWPE fibres at selected strain rates. Source: Russell et al. (2013).

Several studies have considered the in-plane tensile response of the UHMWPE composite, in the form of cross-ply [0°/90°] structure. Similar to the fibre case, the exact value of the stiffness as well as the tensile strength of the UHMWPE composite is not consistently reported in the literature. Early studies (Chocron et al., 2014; Koh et al., 2008) using standard Instron and tensile Hopkinson bar tests reported a stiffness of about 5 GPa and a strength of 500 MPa

at quasi-static strain rate, with a strong rate sensitivity on both stiffness and strength of the composites. In addition, the measured stiffness and strength is one order of magnitude smaller than the measured fibre properties. The reason of this discrepancy is due to the fact that it is hard to introduce tensile load to the specimen because of the soft matrix which comprises the composite.

To address this problem, Russell et al. (2013) designed a dog-bone specimen (Fig. 2.5a) to introduce high axial stresses into the gauge section to avoid pull-out of the fibres from the gripped region by shear, and consequently measured a stiffness and strength which is comparable to the fibre stiffness when converted to the fibre stress according to the rule of mixture, as shown in Fig. 2.5b. Using a similar design, Lässig et al. (2016) measured the same tensile strength but a slightly lower failure strain compared to that reported to Russell et al. (2013).

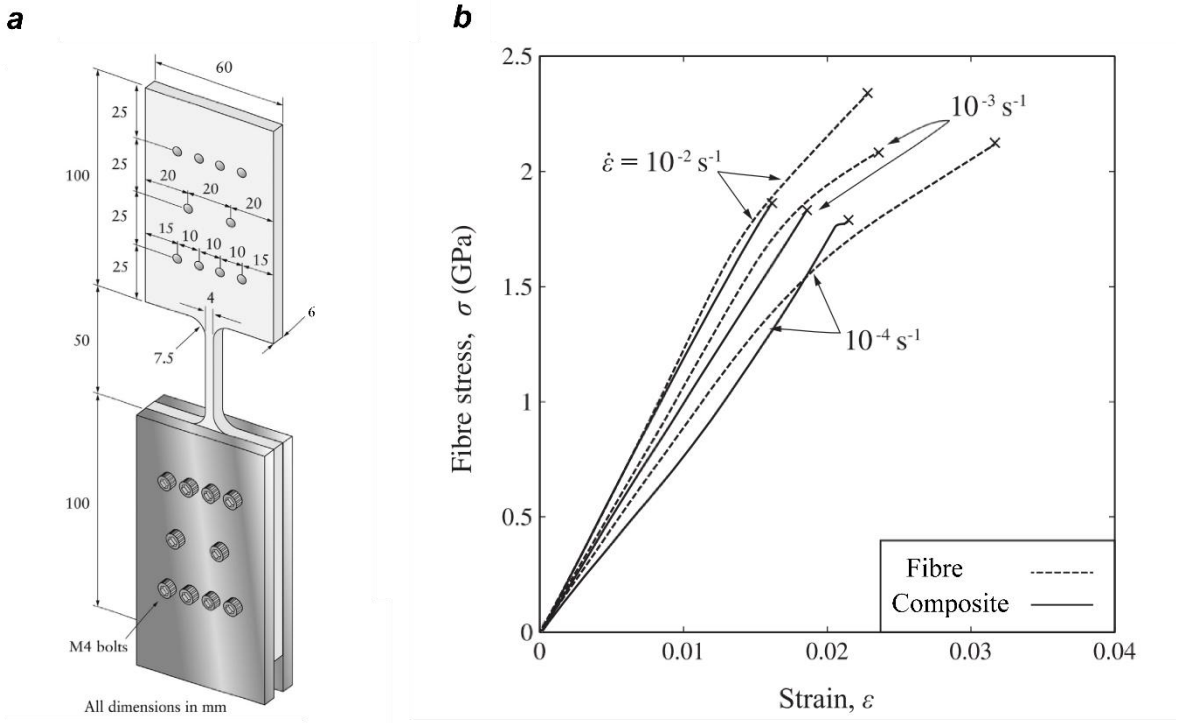

Figure 2.5: (a) The dog-bone specimen used to measure the tensile response for the UHMWPE composite. (b) Comparison of the tensile fibre stress versus axial strain for the UHMWPE fibre and composite. Source: Russell et al. (2013).

A detailed experimental and numerical study by Hazzard et al. (2015) revealed that the through-thickness strain distribution at the centre of the specimen as sketched in Fig. 2.5a is still not

uniform, and a small portion of fibre being pulled out is observable after the test. Furthermore, the experimental set up developed in the literature (Hazzard et al., 2015; Lässig et al., 2016; Russell et al., 2013) is only capable of measuring the low strain rate response up to 10^{-2} s^{-1}, and a dynamic experiment which is capable of accurately measuring the tensile stress strain response of the UHMWPE composite still remains elusive. However, considering the fact that the volume fraction of fibre is about 83% in the composite, it is reasonable to expect that the strain rate sensitivity of the composites should be similar to that of the fibres, such that the tensile response is relatively insensitive to the strain rate in the range 10^{-1} s^{-1} to 10^{3} s^{-1}.

2.3.2 Shear

In contrast to the well-recorded studies on the tensile response of the UHMWPE fibre, few studies directly investigated the shear response of the material. One exception is Hine and Ward (1996), who measured the elastic shear modulus of the fibre using an ultrasonic immersion method Dyer et al. (1992), and reported a shear modulus of 1.36 GPa. Additionally, the theoretical study by Dong et al. (2018) developed a combined continuum−molecular dynamics model and predicted a shear modulus of the fibre in the order of 0.5 to 1 GPa with a shear yield strength of 0.1 to 0.5 GPa depending on the elastic properties of the amorphous phase of the fibres.

For the UHMWPE composites, Liu et al. (2014) conducted a double-notched shear test to measure the interlaminar shear properties for cross-ply UHMWPE composite using the set-up sketched in Fig. 2.6a. A three-hole arrangement was employed to introduce localized shear deformation on the two planes marked by the dotted lines, with the shear traction derived from the load measured from the end of the specimen. The measured shear traction versus displacement relation reported in Liu et al. (2014) is presented in Fig. 2.6b and it is seen that the interlaminar shear strength of the composite is about on the order of 2 MPa which is governed by the matrix property. Similar responses are also reported by Attwood et al. (2014) suggesting that the composite possesses a shear strength of a few MPa. However, the experimental set up by Liu et al. (2014) is not capable of measuring the shear strain and subsequently the shear strain rate due to the non-uniform distribution of the shear deformation within the specimen.

An alternative way to indirectly measure the shear response of the UHMWPE composite is to measure the tensile response of a specimen $\pm 45°$ lay up using the apparatus sketched in Fig. 2.5a, as the deformation is mainly achieved by scissoring of the fibres and shearing of the matrix (Hazzard et al., 2015; Russell et al., 2013). It is hard to derive the actual shear stiffness and strength from this type of experiment as the shear deformation is accompanied with the orientation-hardening due to the rotation of the fibres. However, the test is capable of indicating the relative shear response of the composite and is employed by Hazzard et al. (2015) to study the effect of the consolidation pressure (see Fig. 2.3) on the shear response of the composite. It is revealed that the shear strength of the composite increase with the consolidation pressure while the shear stiffness remains approximately the same.

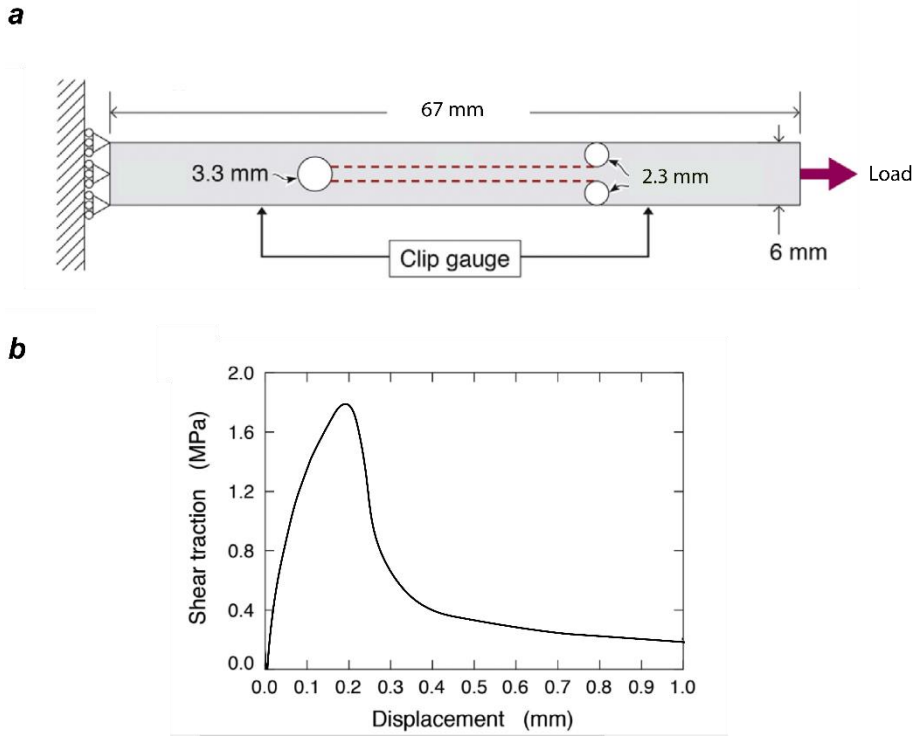

Figure 2.6: (a) Sketch of the double-notched shear test used to measure the interlaminar shear response of the UHMWPE composite. (b) The measured shear traction versus displacement relation. Source: Liu et al. (2014).

2.3.3 In-plane compression

The UHMWPE composites are rarely used as a structural component due to their low shear strength as discussed in Section 2.3.2, and hence few studies focused on their in-plane compressive response. One exception is Attwood et al. (2015) who investigated the

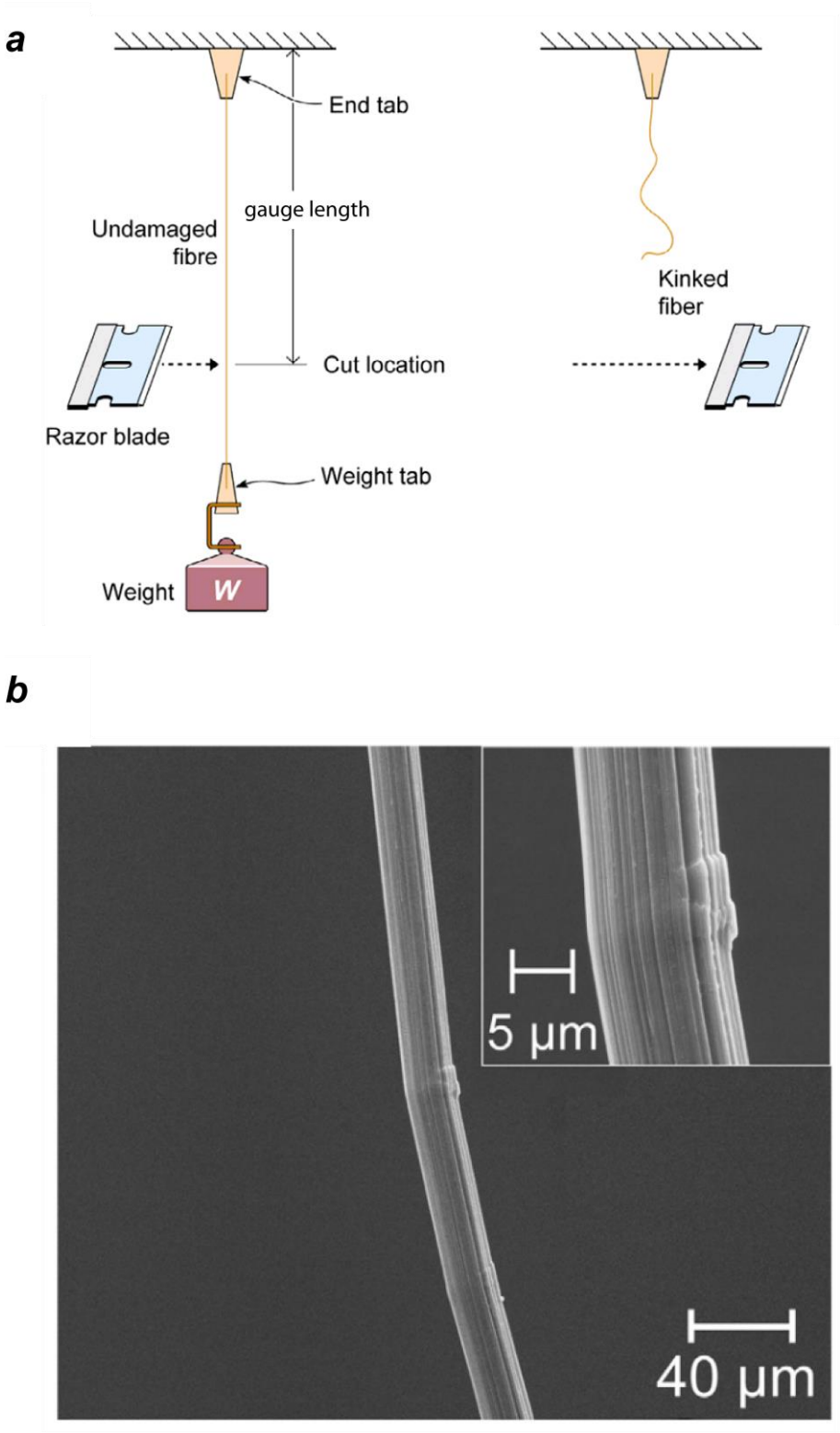

Figure 2.7: (a) Sketch of the experimental setup for the recoil test used to measure the compressive strength of the UHMWPE fibre. (b) Post recoil test SEM micrographs showing the kink developed in the fibre. Source: Attwood et al. (2015).

compressive response of both UHMWPE fibres as well as UHMWPE fibre composites. They employed a recoil test based on the experimental procedure developed by Allen (1987) to measure the compressive strength of the fibre, as sketched in Fig. 2.7a. A single fibre was suddenly cut, thus resulting in a zero-stress wave front to travel upstream along the fibre direction. Upon reflection at the rigid support, a compressive stress wave was generated and subsequently resulted in the kinking compressive failure (Fleck, 1997) of the fibres. A post recoil test scanning electron microscopy (SEM) image is shown in Fig. 2.7b and a single kink of a few μm wide is clearly visible. The compressive strength of UHMPW fibres measured from the recoil test is on the order of 300 MPa and is one order of magnitude lower than the tensile strength which is on the order of 2.5 GPa (Russell et al., 2013).

Attwood et al. (2015) also investigated the in-plane compressive response of UHMWPE composites under quasi-static loading. They found that the compressive response comprised of an initial linear elastic phase followed by subsequent softening. It was shown that the peak compressive strain is governed by the inter-laminar shear strength and ply waviness of the composites, and hence the composites fail by plastic micro-buckling (Fleck, 1997) which is a common failure mechanism for conventional composite materials such as carbon fibre reinforced plastics (CFRP). The main difference is that the UHMPWE composites fail by the micro-buckling on the ply level rather than the fibre level. The peak compressive strength is observed to be on the order of a few MPa. They demonstrated that, with continued compression, a kink band of width approximately 1 mm at an inclined angle of about 30° is formed. The kink band rotates with increasing level of applied strains until the ply rotates to a lock up angle of approximately 60°, after which the compression occurs with broadening of the kink and the kink fixed at a constant rotation angle. Furthermore, they employed the classical kinking theory by Budiansky and Fleck (1993) for CFRP composites and demonstrated that the theory suffices to predict the compressive strength of the UHMWPE composites.

2.3.4 Out-of-plane compression

There are growing interests in the past few years on the out-of-plane compressive responses of the UHMWPE fibres and composites, as the compressive loading is common in ballistic and impact applications. For the UHMWPE fibres, both static (Golovin and Phoenix, 2016; McDaniel et al., 2017) and dynamic (Sockalingam et al., 2018) stress-strain relations have been investigated in the literature. An early study by Hine and Ward (1996) using the ultrasonic

velocity method reported a transverse compressive stiffness on the order of 5 GPa. McDaniel et al. (2017) investigated the quasi-static compressive response of a single fibre on a custom-built compression apparatus fit to an Instron MicroTester. They observed that the stress-strain relation is non-linear with an initial elastic regime followed by a plastic hardening regime as the strain increases. The elastic modulus is estimated to be about 2 GPa with a yield strength in the order of 20 MPa. Additionally, it is observed that the plastic Poisson's ratio is greater than 0.5 and fibre reorientation as well as initiation and growth of nanoscale voids is shown to become significant with increasing plastic strain. Sockalingam et al. (2018) measured the dynamic compressive response of the fibres with a Kolsky bar using the method developed by Casem et al. (2012) of strain rate in the range $10^4\ \mathrm{s}^{-1}$ to $10^5\ \mathrm{s}^{-1}$. Similar non-linear inelastic stress strain relations are observed as the quasi-static case and the compressive stress is seen to increase with increasing strain rate.

The out-of-plane compressive response of the UHMWPE composites is investigated by Attwood et al. (2014) for both unidirectional (UD) and cross-ply $[0°/90°]$ composites. Similar to the fibre case, the response of a UD composite is elasto-plastic comprising a linear elastic phase followed by a plastic hardening phase, as shown in Fig. 2.8a. The compressive stress increases mildly to a strain of approximately 0.4 after which it rises sharply, and the response is shown to be independent of the size of the specimen. No catastrophic failure can be observed even at large strain and the composite deforms with shear band formation and significant lateral expansion.

By contrast, the compressive response for cross-ply composite is rather different from the UD composite (Attwood et al., 2014). It is found that the compressive response is dependent on the size of the specimen. With a specimen size smaller than $4\ \mathrm{mm}$, the stress strain response is similar to the UD case with a linear elastic phase followed by a plastic hardening phase, as seen in Fig. 2.8b. For specimens with size greater than 4mm, the response becomes approximately linear elastic as evidenced from the unloading curve shown in Fig. 2.8c. It is also reported that the compressive strength is dependent on the thickness of each individual ply with the strength increasing with decreasing ply thickness. Furthermore, catastrophic failure is observed at the peak stress accompanied by significant acoustic emission resulting from fibre tensile fracture. The alternative 0° and 90° plies are seen to be extruded out of the free surfaces of the specimen

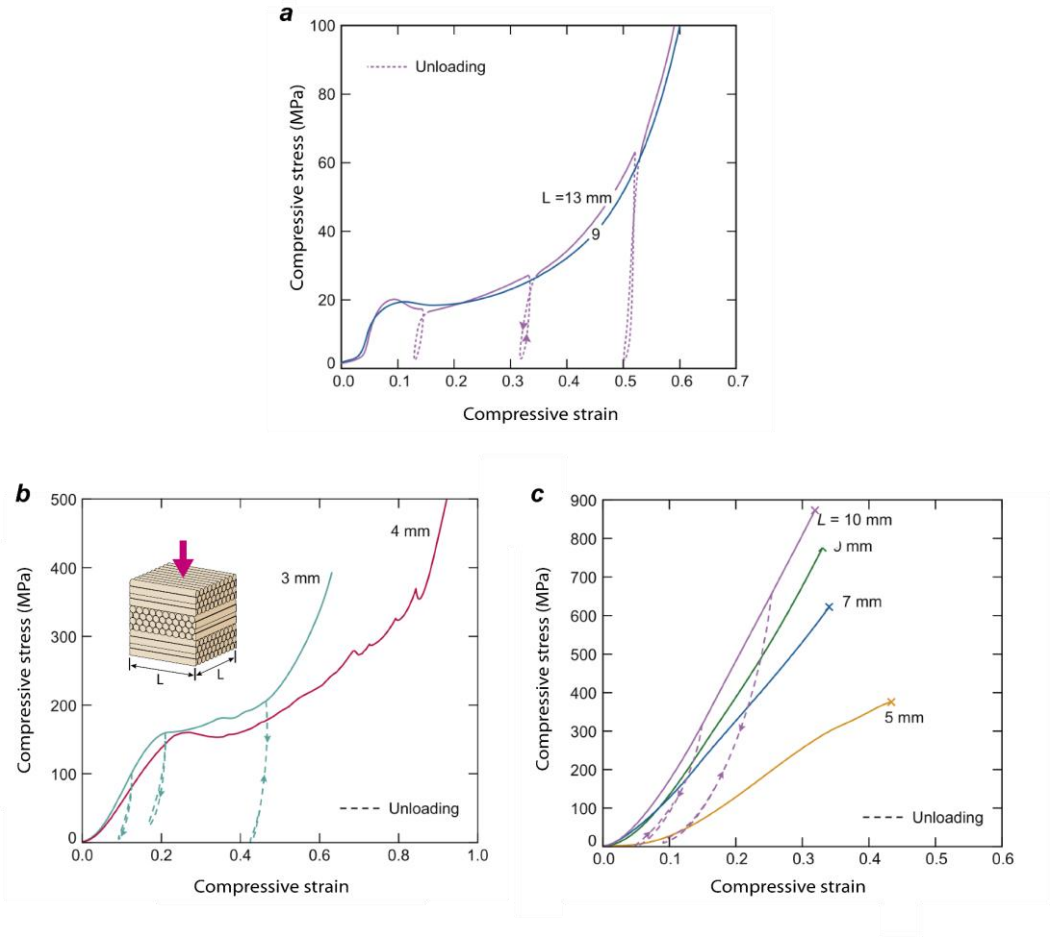

Figure 2.8: Out-of-plane compressive response of (a) unidirectional composites and (b) cross-ply composites with specimen size smaller than 4mm. (c) cross-ply composites with specimen size greater than 4mm. Source: Attwood et al. (2014).

perpendicular to their fibre direction, as shown in Fig. 2.9a. Attwood et al. (2014) demonstrated that the observed deformation and failure mechanism can be explained by the indirect tension theory which is first hypothesised by Woodward et al. (1994). Upon compression, the plastic Poisson expansion caused the individual 0° and 90° plies to expand in the direction perpendicular to their reinforced direction, while the Poisson expansion parallel to the fibre direction is small due to the high fibre stiffness. This anisotropic Poisson expansion resulted in the 0° ply to be loaded in tension which is generated by the adjacent 90° ply above and below it, as sketched in Fig. 2.9b. This tensile stress is transferred between the plies via a shear lag mechanism, and tensile ply failure occurs when the stress within the ply exceeds the ply strength. The predictions from the indirect tension model agree well with the experimental observations, and the model is capable of explaining both specimen size and ply thickness dependency of the composite's transverse compressive strength.

The Experimental study by O'Masta et al. (2015b) investigated the defects within the cross-ply UHMWPE composites as well as their influence on the out-of-plane compressive strength. They identified two types of defects within the composite: (i) tunnel cracks that resulted from anisotropic thermal contraction of the plies after the manufacturing and (ii) void-like defects resulting from missing groups of fibres. Both defects extended many centimetres in a ply's fibre direction. It is revealed that the type one defects have minimal effects on the compressive strength as they health upon out-of-plane compression. On the contrary, the type two defects significantly degrade the composite's strength which is predicted by the indirect tension model such that the missing fibres reduced the tensile load carrying capacity of the composites.

The dynamic compressive response of the cross-ply UHMWPE composites was investigated by Walley et al. (2009) using drop-weight tests and subsequently Shaker et al. (2017) and Zhu et al. (2017) using split Hopkinson pressure bar tests. It is seen that the compressive strength increases with increasing imposed strain rate. Furthermore, the failure process is again highly energetic with a massive amount of heat generated during the compression that can cause smoke as well as fibre carbonization within the composites.

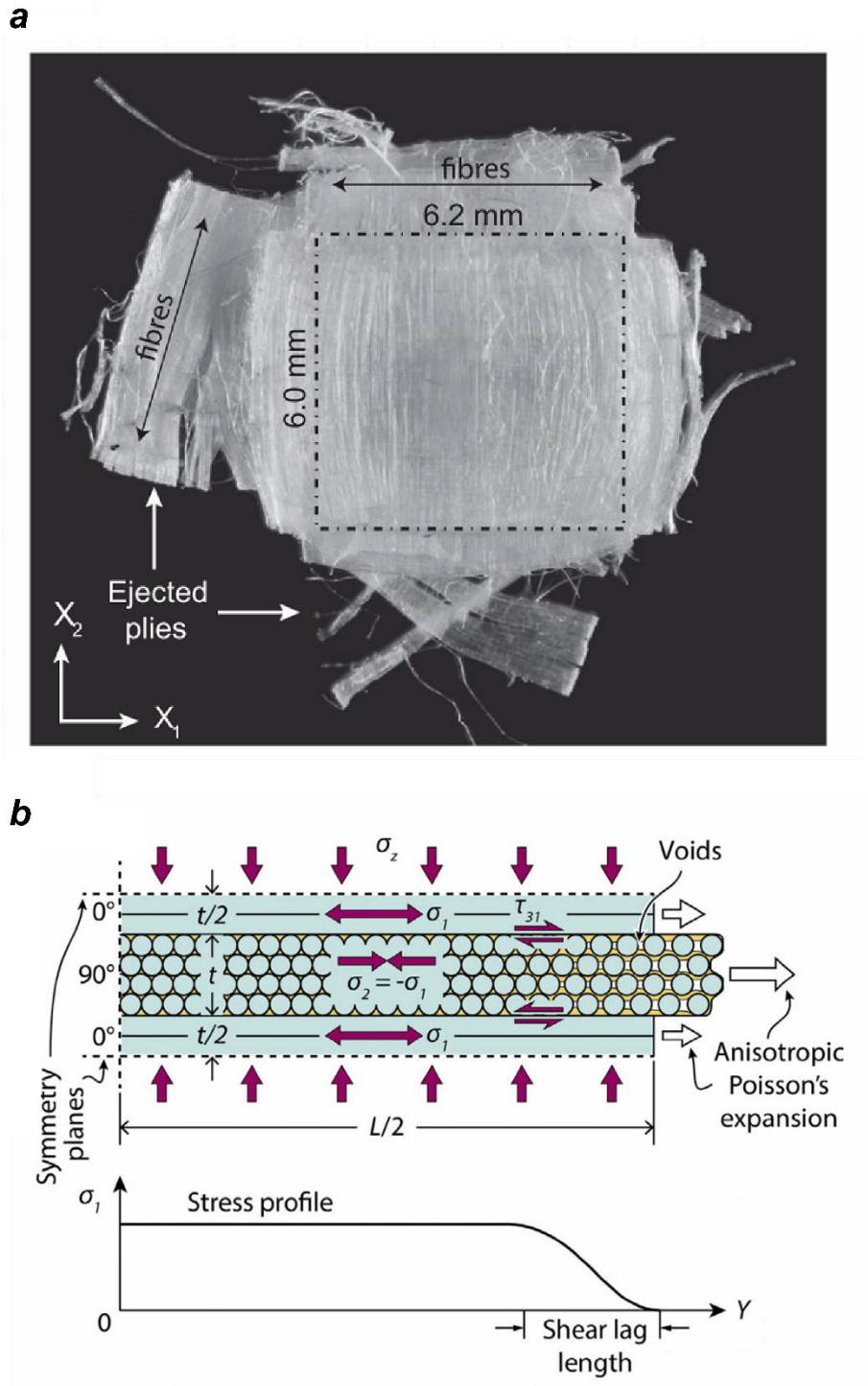

Figure 2.9: (a) A top view image of a cross-ply composite compressed to failure where the compressive load is applied along the $-X_3$ direction. Source: Attwood et al. (2014). (b) Schematic illustration of a cross-ply composite subjected to out-of-plane compressive loading. The out-of-plane compressive load is converted to the in-plane tensile load via the shear lag mechanism at the edge of the sample. Source: O'Masta et al. (2016).

2.3.5 Indentation

The actual deformation and failure of the UHMWPE composites during a ballistic impact process are complicated and often hard to investigate due to their transient dynamic nature. As an initial step to understand the impact mechanisms, quasi-static indentation tests provide valuable insights into the deformation and failure mechanisms during the impact process. The indentation response of cross-ply UHMWPE composites is investigated in the literature for both plate structures (O'Masta et al., 2016) and beam structures (Attwood et al., 2016) using flat-bottomed punches. It is shown that the typical indentation response resulted in a 'saw-tooth' load versus displacement profile with increasing indentation depth as presented in Fig. 2.10a. The deformation and failure immediately underneath the indenter is shown in Fig. 2.10b at four different indentation depth (Attwood et al., 2016), and a progressive failure mode is clearly observed from the images. Optical micrographs (O'Masta et al., 2016) obtained after the indentation test (Fig. 2.10c) suggest that the sudden load drop observed in the Fig. 2.10a is caused by the tensile failure of the fibres immediately underneath the punch, and the damage mode is similar to that observed in the ballistic impact experiments (O'Masta et al., 2014a, 2015a). Additionally, the peak indentation pressure observed from the experiment is on the order of 2 GPa which is identical to the intrinsic compressive strength of the composite. These observations indicate that the failure caused by the indentation of a flat-bottomed punch is the indirect tension mechanism (Fig. 2.10d) rather than the shear-plug mechanism which is common in conventional composites with a stiffer matrix such as carbon or glass-fibre reinforced composites (Cantwell and Morton, 1990; Culnane et al., 1991; Gama and Gillespie, 2008). In fact, Attwood et al. (2016) developed an analytical model to predict the peak indentation stress associated with the shear plug failure based on the classical results of the pressure distribution on the indented surface given by Johnson (2003). They argued that if the composites were to fail by shear then the peak indentation pressure should scale with the inverse square root of the indenter's width. However, their experiments (Attwood et al., 2016) shown that the peak pressure is independent to the indenter's width and thus failure is not governed by the high stress concentration at the edges of the projectile. Therefore, penetration and failure of the UHMWPE composite by blunt projectiles are achieved by tensile fibre (and equivalently ply) failure via the indirect tension mechanism.

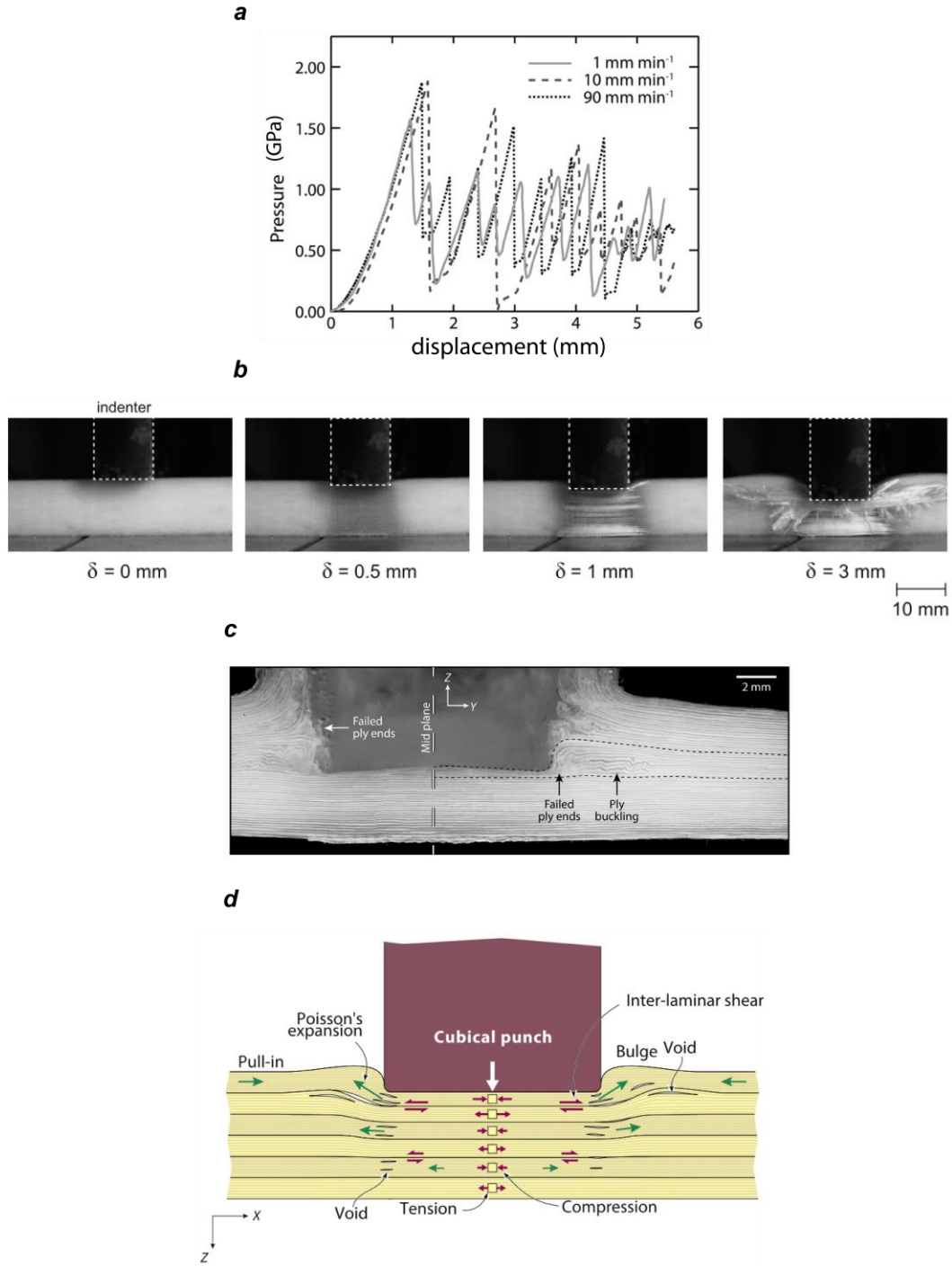

Figure 2.10: (a) Typical indentation pressure versus displacement relation at selected punch displacement rate showing the 'saw-tooth' profiles for the indentation of cross-ply UHMWPE composites. (b) Montage of images showing the deformation and failure of the composites immediately under the indenter. Images are shown for four different values of indentation depth δ. (c) Optical micrographs showing the indirect tension failure of UHMWPE composites after indentation. (d) Schematic illustration of the indirect tension mechanism developed immediately underneath the punch by the indentation of a cross ply UHMWPE composite. Source: Attwood et al. (2016), O'Masta et al. (2016).

2.4 Ballistic impact response of UHMWPE composites

2.4.1 Ballistic impact of single fibre

The study of impact mechanisms of single fibres/yarns can be traced back to the well-known study by Von Karman and Duwez (1950), where the stress wave caused by the longitudinal impact at the end of a cylindrical bar was theoretically analysed. Following Von Karman and Duwez (1950), Smith et al. (1958) investigated the transverse impact at the centre of an infinitely long single fibre/yarn and revealed the underlying mechanisms that govern the deformation of the material. It is shown that upon impact, two stress waves which travel at different velocities emanate from the centre of the fibre and propagate symmetrically along the longitudinal direction. The first stress wave is an elastic tensile stress wave which is associated with longitudinal stretching of the fibres, while the second stress wave is associated with transverse deflection of the fibre and can be visualised by a traveling "shear hinge" at a much lower velocity. Further, it is revealed that the impact resulted in a 'V' shaped profile which evolves in a self-similar manner.

The theory by Smith et al. (1958) on the deformation of a single fibre/yarn under impact has been experimentally validated by numerous studies for different types of fibres including UHMWPE fibres, see for example (Bazhenov et al., 2001; Carr, 1999; Chocron et al., 2011). In general, it is found that the analytical prediction on the transverse wave speed as well in the fibre agrees well with experimental observations (Chocron et al., 2011). However, the theory tends to overpredict the critical velocity at which the fibre ruptures, and this was investigated by Bazhenov et al. (2001) for the impact of aramid fibres using spherical projectiles. They argued that the combined effect of nonlinear stress-strain response of the fibres as well as the detailed projectile geometry caused the observed discrepancy. Using finite element simulations, Walker and Chocron (2011) reported the deformation of single fibre impacted by flat-bottomed projectiles. They show that the critical velocity is at least 11% lower than the classical predictions if the effect of strain waves launched from the edges of the projectile is accounted for. Furthermore, they have shown that a 40% reduction on the critical velocity can be explained if the yarn were to 'bounce off' the projectile during the impact process, such that the particle velocity is doubled in the elastic case. Such 'bounce off' mechanism was captured in their study using the numerical simulations as well as experimentally observed by Field and Sun (1990) for the impact of spherical projectiles on a rubber band. Song et al. (2011) used a

split Hopkinson bar test with high speed photography to reveal the transient deformation of single Kevlar fibres. However, the 'bounce off' mechanism as proposed by Walker and Chocron (2011) was not observed. In a comprehensive study, Phoenix et al. (2017) took account for the local stress wave propagation immediately under the projectile and shown that the mismatch between the classical theory and the experimental observations on the critical velocity can be explained by considering the tensile wave collision mechanism within the fibre. Overall, the extensive studies on the impact of single fibre/yarn reveal that the critical velocity associated with fibre rupture is dependent on the complex stress distribution immediately underneath the projectile.

In an effort to specify the governing mechanical and geometrical properties that affect the ballistic performance of the fibres, Cunniff (1999) used dimensional analysis supported by a wealth of experimental data to show that the ballistic limit velocity, labelled V_{50}, is governed by a function of the form

$$\Phi\left(\frac{V_{50}}{c^*}, \frac{\bar{\rho}_d}{\bar{\rho}_p}\right) = 0\,, \tag{2.1}$$

where $\bar{\rho}_d$ and $\bar{\rho}_p$ are the areal densities of fibres and projectile respectively while the material-dependent velocity c^* is given in terms of the fibre density ρ_f as

$$c^* = \left[\frac{\sigma_f \varepsilon_f}{2\rho_f}\sqrt{\frac{Y_f}{\rho_f}}\right]^{1/3}. \tag{2.2}$$

Here, σ_f and ε_f fibre tensile strength and failure strain, respectively while $Y_f \equiv \sigma_f/\varepsilon_f$ is Young's modulus of the fibres. This analysis suggests that the V_{50} scales with a material dependent velocity c^* and confirms that a high specific strength and stiffness enhances ballistic performance. More importantly, c^* is a metric that aids to vector the development of ballistic fibres as fibres with a higher c^* are predicted to have a higher ballistic performance. A mechanistic explanation for the existence of the material parameter c^* was provided by Phoenix and Porwal (2003) by assuming that the impacted fibres deform in a string-like stretching mode, and they subsequently derived a mathematical expression of the function Φ which is proven to be basically material-independent. A material property map with axes of specific energy absorption $(\sigma_f\ \varepsilon_f)/\rho_f$ and longitudinal wave speed $\sqrt{(Y_f/\rho_f\ )}$ is shown in Fig. 2.11 with contours of constant Cunniff velocity c* included. It is clearly seen that the

UHMWPE fibres (Dyneema® SK76) possess one of the highest c* values among the range of the materials investigated here.

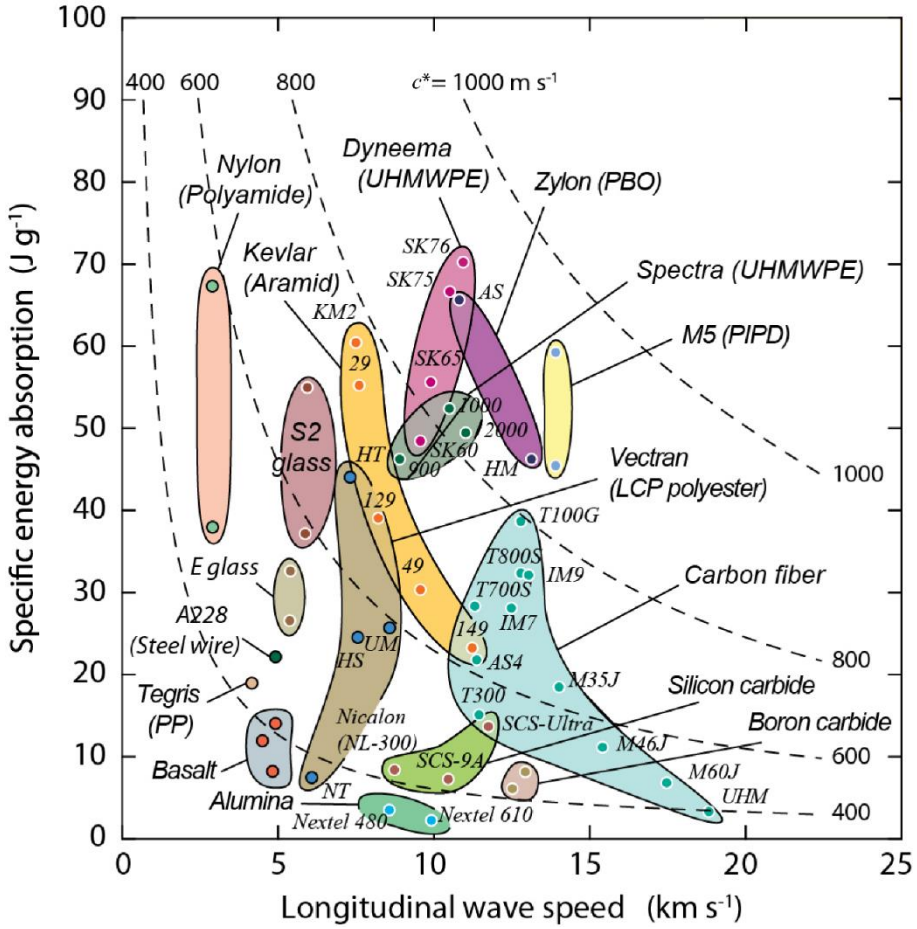

Figure 2.11: Material property chart comparing the specific energy absorption $(\sigma_f\ \varepsilon_f)/\rho_f$ and longitudinal wave speed $\sqrt{(Y_f/\rho_f\ )}$ for different fibres. Contours of the Cunniff velocity, c*, are also plotted. Source: O'Masta et al. (2014).

2.4.2 Ballistic impact of UHMWPE fibre composites

The ballistic impact of UHMWPE composites is drawing considerable interest in recent years. Chocron et al. (2013) investigated the ballistic impact mechanisms of cross-ply UHMWPE composites with different thicknesses ranging from 0.12 mm (4 alternating UD plies) to 23 mm (147 plies) using fragment simulating projectiles (FSP), and compared the results with the classical impact theory for single fibres (Smith et al., 1958). They revealed that upon impact, the composites deflect in a self-similar manner which resulted in a 'V' shaped profile as observed in the fibre case (see Section 2.4.1). Furthermore, the elastic tensile wave velocity as well as the transverse shear hinge velocity measured from the impact of composites agrees well

with those predicted using the classical fibre impact theory. In addition, they reported that a brief flash lasting in the order of microseconds can be observed immediately after the impact and argued that this might be due to the autoignition of the material.

On the other hand, the failure mechanism of the composites is much more complicated compared to that of single fibres. Numerous studies have investigated the ballistic impact mechanism of UHMWPE composites using a blunt (spherical or flat-bottomed) projectile. An early study by Lee et al. (1994) investigated the failure mode of laminated as well as woven Spectra® fibre composites impacted by FSP. They observed sequential delaminations between the adjacent layers, shear failure of the fibres near the edge of the projectile resulting in the formation of a cut-out plug (shear plug) as well as tensile failure of the fibres after the tests. The shear plug failure mechanism has also been observed by Flanagan et al. (1999) for woven fabrics made of Spectra® fibres. However, this shear plug failure mode has not been observed in a series of recent experiments (Attwood et al., 2016; Karthikeyan et al., 2013a, 2013b; O'Masta et al., 2014) on cross-ply Dyneema® fibre composites. Rather, the failure is dominated by the indirect tension mechanism (Attwood et al., 2016) as explained in section 2.3.5. Furthermore, experiments (Karthikeyan et al., 2013b) have shown that the failure of the UHMWPE composites impacted by blunt projectiles is progressive, with the fibre immediately underneath the projectile fail first and the number of failed plies increasing with increasing velocity. Fractographic studies by Greenhalgh et al. (2013) investigated the penetration of thick UHMWPE composites (in the sense that the projectile diameter is much smaller than the thickness of the composites). They reported that a major delamination crack can be identified after the test, and this delamination crack divides the composite into two regions. The portion of the composites within the regime which is close to the projectile is subjected to fibre fracture with mild delamination and little deflection, while in the region away from the projectile large deflection of the composite can be observed accompanied with severe delamination between the adjacent plies.

The effect of ply lay up on the ballistic performance of UHMWPE composites using blunt projectiles is investigated by Karthikeyan et al. (2016) and Hazzard et al. (2017). It is shown that the ballistic limit velocity is highest for composites with a cross-ply $[0°/90°]$ structure, but composites with a quasi-isotropic/helicoidal lay up possess the minimum back face deflection. In an effort to identify the effect of the manufacturing process on the impact resistance, Lässig et al. (2018) employed ballistic tests with varying consolidation pressure (see

Section 2.2) and found that the ballistic limit velocity increases with increasing manufacturing pressure.

2.5 Modelling frameworks for UHMWPE composites

A number of studies have investigated the ways to model the UHMWPE composites. The existing models can be divided into two categories. The first group of studies (Grujicic et al., 2008; Hazzard et al., 2018; Iannucci and Pope, 2011) developed homogenised models at continuum scale using effective properties of the cross-ply composite. Early study by Grujicic et al. (2008) proposed a multi-scale material model for cross-ply UHMWPE composites. They attempted to use fundamental material properties of the fibres and matrix within a homogenisation framework, where the global deformation gradient was passed to a so-called "unit cell" which composed of explicitly modelled fibres and matrix to calculate the stiffness of a global material point. They subsequently compared the numerical prediction to the experimental measurements for composite plates penetrated by a sharp-tipped projectile. The model is capable of qualitatively rather than quantitatively predicting the deformation and fracture of the composites during the penetration process. Iannucci and Pope (2011) modelled the cross-ply composites as a homogenized medium with a non-linear shear stress versus strain relationship fitted to measured data and validated their model by comparing with the experimental measurement for the impact of composite plates using spherical projectiles. Similar approaches are developed by Nguyen et al. (2016) and Lässig et al. (2015). Although these models give results that are in qualitative agreement with measurements, they do not predict the observed progressive failure mode of penetration with sufficient accuracy as discussed in Section 2.4.2. Hazzard et al. (2018) proposed a homogenised sub-laminate approach for the UHMWPE composites with cohesive contact between the sub-laminate layers. The model is capable of predicting a number of important characteristics observed during the experiments such as the ballistic limit velocity and back face deflections. However, it requires an excessive amount of curve fitting and the result is mesh-size dependent.

The second group of models comprises of homogenised models for individual UD composite layers. Nazarian and Zok (2014) developed a binary model where fibres are included as so-called rebars within an isotropic matrix. They subsequently compare the model's prediction with experimental measurements for the quasi-static tensile response of the UHMWPE

composites with [$\pm 45°$] stacking sequence as well as the dynamic impact of the composites using a flat-bottomed punch. This model is capable of accurately capturing the large fibre rotations during the deformation process and hence agrees well with the experimental observations. However, it is hard to incorporate the pressure sensitivity of yield that is known to be significant for UHMWPE composites (Attwood et al., 2014; Chocron et al., 2014). Attwood et al. (2014) proposed an anisotropic plasticity model for UD UHMWPE composites. They assume that the composite is linear elastic in fibre direction but follows a Tresca yield criterion in all other directions. They subsequently introduced the pressure dependent yield criteria and inferred the pressure sensitivity coefficient by comparing the experiments with numerical predictions. However, this model does not accurately account for the evolution of fibre orientations in a finite deformation and hence only works for situations where the fibre rotation is small.

2.6 Other composites

As discussed in the previous sections, the penetration and impact mechanisms of UHMWPE composites are complicated and accompanied by several different failure modes which are not all well understood. Therefore it is often necessary to consider other composite materials when exploring the current understanding of the impact and penetration mechanisms. There exists a vast library of literature on the subject of conventional fibre composites such as carbon and aramid fibre reinforced plastics. In this section we shall restrict ourselves to the studies on the indentation, impact and the associated modelling frameworks of these composites and contrast them with those of the UHMWPE composites.

2.6.1 Carbon fibre composites

Carbon fibre reinforced plastics (CFRP), in the form of laminated composites are used in numerous light-weight engineering applications for their excellent structural load carrying capacities. However, one major restriction on the usage of the CFRP composites is their low damage tolerance and the catastrophic failure under impact loading so that they are rarely used in ballistic protection applications. As a result, numerous studies have investigated the indentation as well as impact mechanism of these composites.

The quasi-static indentation response of laminated cross-ply CFRP composites was investigated by Jorgensen et al. (1998) using a spherical indenter. The measured load versus indenter displacement is shown in Fig. 2.12. Through thickness cracks caused by the transverse shear failure of the plies are shown to initiate on the front face of the composites immediately under the indenter and propagate downwards layer by layer to the rear face of the composites.

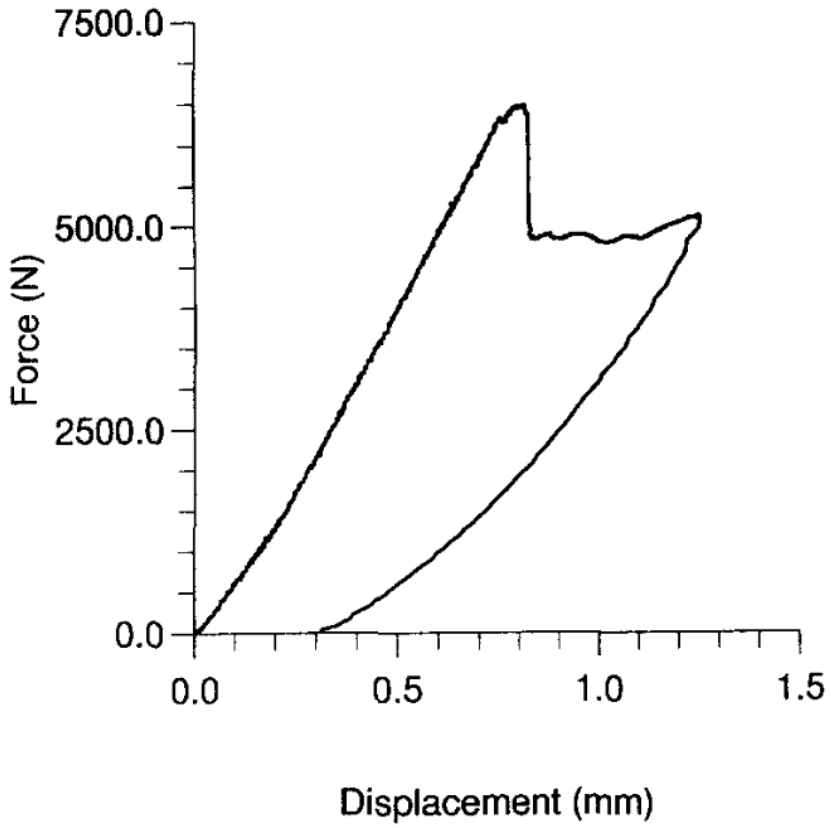

Fig. 2.12. Typical force versus indenter displacement plot for the indentation of cross-ply CFRP composites. Source: Jorgensen et al. (1998)

The propagation of the through-thickness cracks is accompanied by the delamination between the adjacent 0° and 90° plies. The load is seen to increase monotonically until a major through thickness crack splits the rear face of the composites which caused the sudden load drop. Symons (2000) investigated the low and high velocity impact of CFRP composites with spherical projectiles. Similar fracture modes can be observed as in the static case, and the through thickness cracks as well as the delamination cracks are clearly visible after the test (see Fig. 2.13). They reported that compared to the low speed impact, high speed impact damage is more localised and resulted in shear out failure of the laminate as depicted in Fig. 2.13. As the CFRP composites are mainly used for structural applications, they are typically under certain

stress-state rather than completely unloaded when subjected to impact load. Therefore, a number of studies (Butcher, 1979; Butcher and Fernback, 1981; Heimbs et al., 2009) have investigated the effect of preload on the impact response of CFRP composites. It is found that the existence of the pre-stress affected both fracture behavior and fracture modes. For example, Heimbs et al. (2009) reported that the total absorbed energy is higher for composites under compressive preload. They observed that the deflection of preloaded composites is higher than the unloaded specimens after experiments, which resulted in a higher extent of material damage.

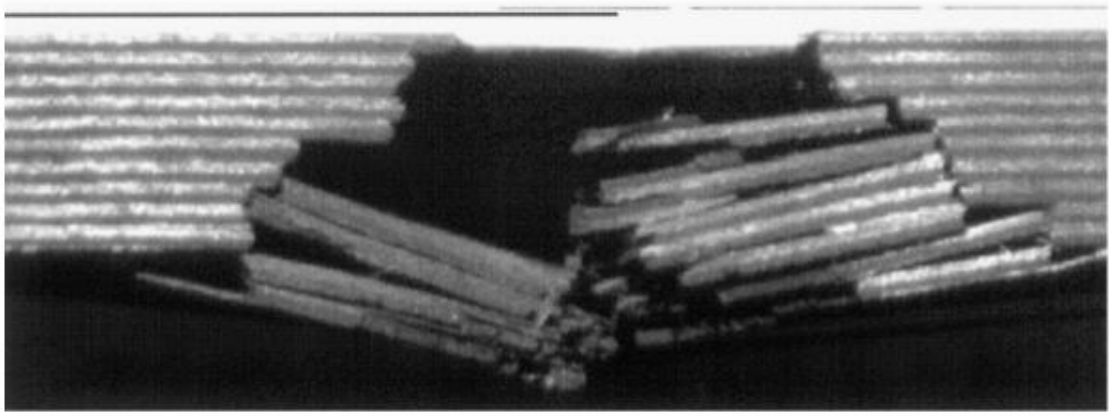

Fig. 2.13. Optical micrographs showing the fracture of cross-ply CFRP composites impacted by a spherical projectile at 143 m s^{-1}. Source: Symons (2000).

Various models have been presented in the literature to study the damage and fracture of CFRP composites under impact loading. Most of the models are based on the continuum damage mechanics (CDM) framework proposed by Kachanov (2013) and further developed by Lemaitre and Chaboche (1994). These models typically introduce damage variables to measure the local damage in a representative volume element of the composite material. For uni-directional loading, the definition of a damage variable allows the effective stress over the section of the RVE to be defined. The damage variable is assumed to be zero for undamaged material while complete fracture is accomplished when the variable reaches one, and the material is assumed to lose all load-carrying capacities. The constitutive relationship for the damaged material is then derived from the principle of strain equivalence as stated by Lemaitre and Chaboche (1994). In the case of multi-axial loading, several damage variables are defined with each of them relating to a form of intralaminar damage, thus allowing a complete description of damage in all possible directions. Donadon et al. (2008) developed a three-dimensional CDM based failure model to model the impact of CFRP composites. Their model

is capable of quantitatively capturing the impact force-time history and qualitatively capturing the fracture mode. A similar approach has been proposed by Faggiani and Falzon (2010) to model the impact of CFRP composites supported by stiffening panels. More recent studies (Hongkarnjanakul et al., 2013; Tan et al., 2015) have also incorporated the cohesive surface model (Xu and Needleman, 1994) to describe the delamination between the adjacent 0°/90° plies. In general, CDM based models are shown to be able to accurately reproduce many important macroscopic characteristics of the impact experiments such as the force histories and deflection of the composites. However, these phenomenological approaches are typically mesh-size dependent and require a large amount of curve-fitting to specify the constitutive relationship.

2.6.2 Aramid woven fabrics

Unlike CFRP fibre composites which are mainly used for structural applications, Aramid fibres are widely used in ballistic protection applications due to their high impact resistance, hence they are often compared with the UHMWPE composites. A vast amount of literature has focused on the woven fabric cloths made of Aramid fibres. Therefore in this section, we discuss the existing literature on the ballistic impact mechanisms of these woven fabrics.

A number of studies have investigated the impact of mechanisms of fabrics and a comprehensive review on this subject can be found in Cheeseman and Bogetti (2003). In general, it has been shown that the impact of fabrics is similar to that of single fibres (Smith et al. 1958), see Fig. 2.14. When a projectile impacts the fabric, a transverse deflection of the yarns which are in direct contact with the projectile is produced, and subsequently generates a longitudinal strain wave that propagates along the axis of the yarns. These yarns are defined as principal yarns. The orthogonal yarns which intersect the principal yarns are then pulled out from the fabric plane and deflect in a similar manner as the principle yarns. Analogously, the yarns which intersect the orthogonal yarns then start to deform by the same mechanisms. And hence the interaction between yarns which is essentially governed by the friction between them provides the driving force of the transverse deflection. During the impact process, the major part of the kinematic energy of the projectile is shown to be absorbed by the straining of the principle yarns while a small amount of the energy is transferred to the orthogonal yarns (Roylance, 1980), as depicted in Fig. 2.14c. The projectile then penetrates the fabrics when the maximum tensile stress reaches the strength of the yarns which resulted in fibre fracture.

The material-dependent velocity (Cunniff, 1999) given in Eqn. (2.2) is shown to be able to gauge the ballistic performance of the woven fabrics. However, the ballistic performance of these materials is also affected by the so-called cover factor which is the density of the weave determined from the width and pitch of the warp and weft yarns. According to Chitrangad (1993), the proper value of the cover factor should be between 0.6 to 0.95. Loosely woven fabrics with too small cover factors are susceptible to having the projectile wedge through (Tabiei and Nilakantan, 2008) the yarn mesh.

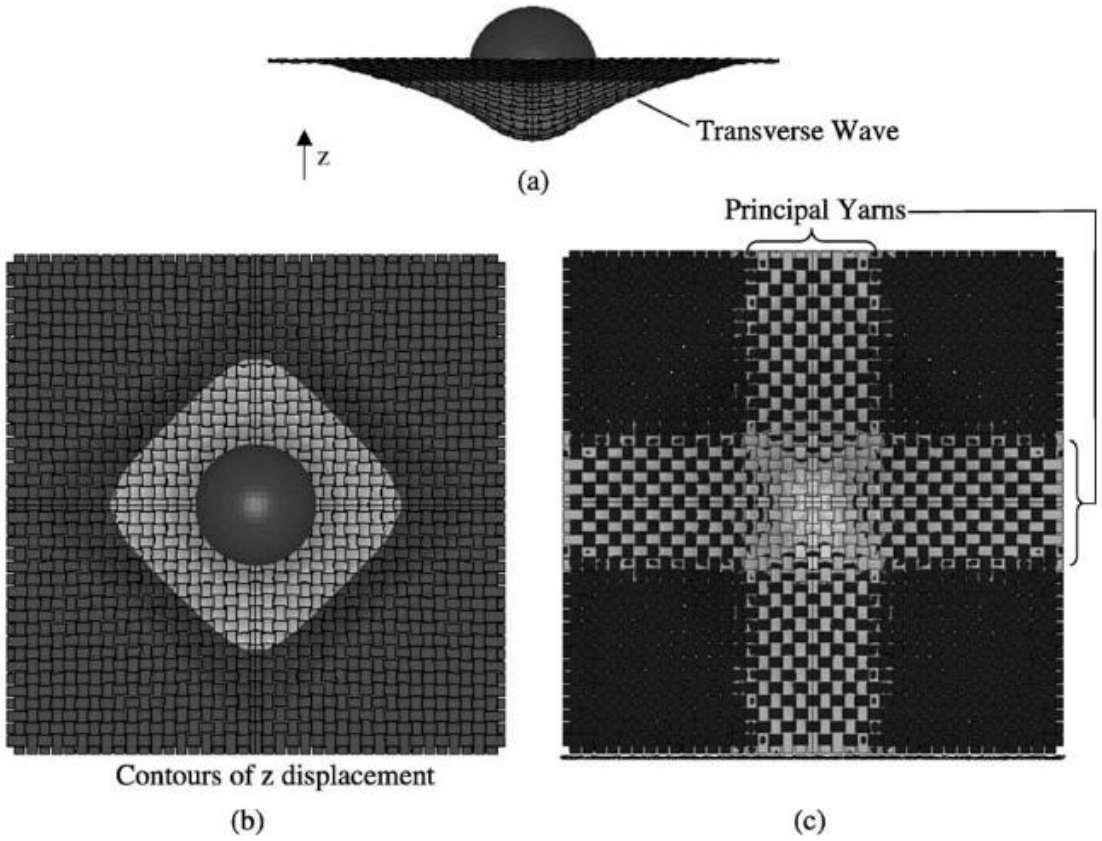

Figure 2.14: Deformation of a single ply of woven fabric impacted by spherical projectiles. (a) side view, (b) top view of *z* displacement contours and (c) bottom view showing principle yarns under high stress. Source: Cheeseman and Bogetti (2003).

In addition to the cover factor, the shape of the projectile is also shown to have a strong effect on the ballistic performance of fabrics. An experimental study by Lim et al. (2002) reveals that the ballistic limit velocity for woven aramid fabrics is higher when impacted by blunt projectiles compared to sharp-tipped projectiles. Tan et al. (2003) demonstrated that the amount of pull-out of the fibres after the test is largest for hemispherical projectiles and lowest for

conical and ogival projectiles while flat-bottomed projectiles tend to shear through the yarn thickness.

2.7 Effect of matrix properties on the ballistic performance of composite materials

As reviewed in the previous section, the material-dependent velocity proposed by Cunniff in (2.2) can be used to gauge the ballistic performance of both UHMWPE composites as well as aramid woven fabrics. The Cunniff model as rationalised by Phoenix and Porwal (2003) is based on the impact of single fibre/yarns and hence ignores the shear property of the composites that is usually governed by the matrix.

Several studies have studied the effect of matrix properties on the ballistic limit velocity of UHMWPE composites (Karthikeyan et al., 2013b), carbon fibre composites (Yu et al., 2018) as well as aramid composites (De Ruijter et al., 2010). For UHMWPE composites, Karthikeyan et al. (2013b) investigated the ballistic limit velocity of cross-ply composites comprised of SK76 Dyneema® fibres with two different matrices with shear strength of about 2 MPa (designated HB26) and 0.2 MPa (designated HB50) respectively, and reported that the HB50 composites possess a higher ballistic limit velocity. Yu et al. (2018) studied the effect of matrix shear strength on both damage initiation velocity and ballistic limit velocity of CFRP composites with shear strengths range from 0.1 MPa to 100 MPa, and the results are shown in Fig. 2.15. It is seen that both failure initiation velocity as well as the ballistic limit velocity remains approximately the same for matrix shear strength from 0.1 to 20 MPa but decrease sharply when the shear strength is greater than 20 MPa. This is also accompanied by a change of fracture mode. Composites are seen to fail by the shear plug mechanism detailed in Section 2.6.1 with high shear strengths but fail by the indirect tension mode in Section detailed in 2.3.4 with low shear strengths.

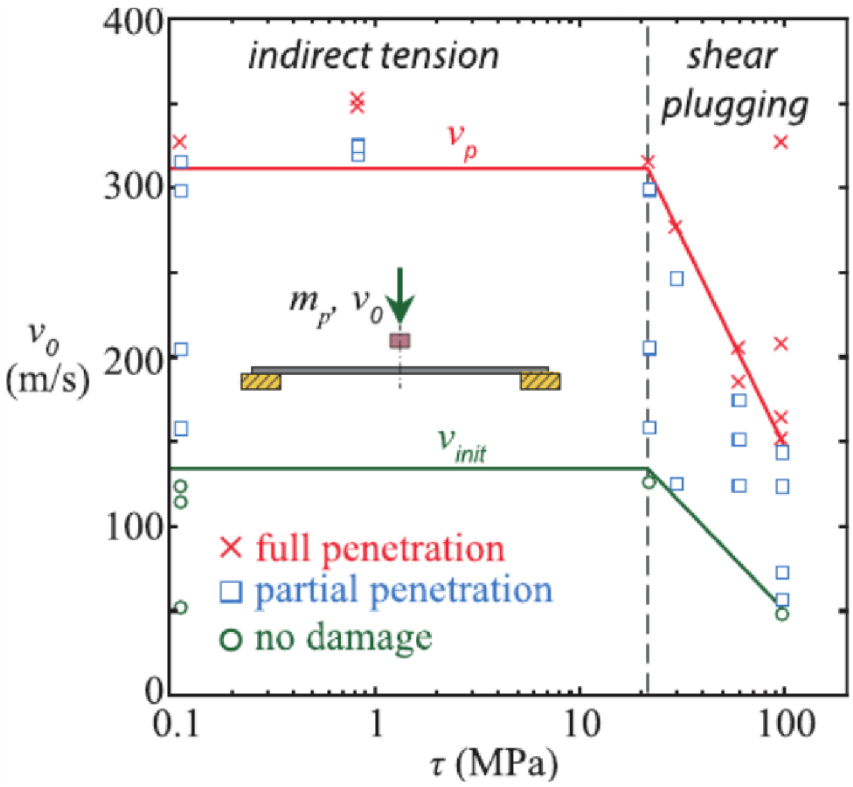

Figure 2.15: Failure initiation velocity v_{init} and ballistic limit velocity v_p plotted as functions of matrix shear strength τ. Source: Yu et al. (2018).

Similar effects are observed in aramid fibre composites. De Ruijter et al. (2010) tested a series of composites made of thermotropic liquid crystalline polyesters and polyester-amides. They observed that the ballistic limit velocity increases with matrix stiffness increasing from 0 to 0.01 GPa, followed by a regime where the ballistic limit velocity remains constant with increasing matrix stiffness from 0.01 to 1 GPa. Further increase in the resin stiffness greater than 1 GPa resulted in a sharp decrease in the ballistic limit velocity similar to that observed in Fig. 2.15 for CFRP composites.

In general, the literature suggests that the ballistic limit velocity is dependent on the matrix properties, and this dependency is observed in different types of composites with various fibres. However, a mechanistic understanding of phenomena is missing in the literature.

2.8 Concluding remarks

In this Chapter we have reviewed the existing literature on the mechanical response of UHMPWE fibres composites as well as their indentation and impact mechanisms. The literature has shown that the UHMWPE composites fail by the indirect tension mechanism when subjected to indentation and impact loading by a flat-bottomed punch. However, an understanding on the penetration mechanism of the composites by a sharp-tipped punch is missing in the literature, although the studies on other composites such as aramid woven fabrics have shown that the projectile shape also governs the penetration response.

Experimental studies reveal that the ballistic performance of UHMWPE composites is dependent on their shear strength, and high ballistic performance composites typically require low shear strength. However, a mechanistic understanding of this shear strength dependency of the ballistic performance is missing in the literature.

In order to fully understand the impact mechanism of UHMWPE composites, it is crucial to first understand their mechanical responses under simple loading scheme. It is found that the quasi-static response of the UHMWPE fibre composites under tension, shear and compression are well studied in the literature. However, few studies have investigated their dynamic responses under such cases. Therefore, an understanding of the high strain rate response of the UHMWPE composites would bring valuable insights to their deformation and failure mechanisms under impact loading.

References

Allen, S.R., 1987. Tensile recoil measurement of compressive strength for polymeric high performance fibres. J. Mater. Sci. https://doi.org/10.1007/BF01103520

ASTM, 2018. ASTM D4020-18 Standard Specification for Ultra-High-Molecular-Weight Polyethylene Molding and Extrusion Materials. ASTM B. Stand. https://doi.org/10.1520/D4020-11.2

Attwood, J.P., Fleck, N.A., Wadley, H.N.G., Deshpande, V.S., 2015. The compressive response of ultra-high molecular weight polyethylene fibres and composites. Int. J. Solids Struct. 71, 141–155. https://doi.org/10.1016/j.ijsolstr.2015.06.015

Attwood, J.P., Khaderi, S.N., Karthikeyan, K., Fleck, N.A., O′Masta, M.R., Wadley, H.N.G., Deshpande, V.S., 2014. The out-of-plane compressive response of Dyneema composites. J. Mech. Phys. Solids 70, 200–226. https://doi.org/10.1016/j.jmps.2014.05.017

Attwood, J.P., Russell, B.P., Wadley, H.N.G., Deshpande, V.S., 2016. Mechanisms of the penetration of ultra-high molecular weight polyethylene composite beams. Int. J. Impact Eng. 93, 153–165. https://doi.org/10.1016/j.ijimpeng.2016.02.010

Bazhenov, S.L., Dukhovskii, I.A., Kovalev, P.I., Rozhkov, A.N., 2001. The fracture of SVM aramide fibers upon a high-velocity transverse impact. Polym. Sci. A, Chem. Phys. 43, 61–71.

Berger, L., Kausch, H.H., Plummer, C.J.G., 2003. Structure and deformation mechanisms in UHMWPE-fibres. Polymer (Guildf). 44, 5877–5884. https://doi.org/10.1016/S0032-3861(03)00536-6

Budiansky, B., Fleck, N.A., 1993. Compressive failure of fibre composites. J. Mech. Phys. Solids 41, 183–211. https://doi.org/10.1016/0022-5096(93)90068-Q

Butcher, B.R., 1979. The impact resistance of unidirectional CFRP under tensile stress. Fibre Sci. Technol. 12, 295–326. https://doi.org/10.1016/0015-0568(79)90038-1

Butcher, B.R., Fernback, P.J., 1981. Impact resistance of unidirectional CFRP under tensile stress: Further experimental variables. Fibre Sci. Technol. 14, 41–58. https://doi.org/10.1016/0015-0568(81)90047-6

Cantwell, W.J., Morton, J., 1990. Impact perforation of carbon fibre reinforced plastic. Compos. Sci. Technol. 38, 119–141. https://doi.org/10.1016/0266-3538(90)90002-M

Capaccio, G., Crompton, T. a., Ward, I.M., 1976. The drawing behavior of linear polyethylene. I. Rate of drawing as a function of polymer molecular weight and initial thermal treatment. J. Polym. Sci. Polym. Phys. Ed. https://doi.org/10.1002/pol.1976.180140910

Capaccio, G., Ward, I.M., 1973. Properties of Ultra-High Modulus Linear Polyethylenes. Nat. Phys. Sci.

Carr, D.J., 1999. Failure mechanisms of yarns subjected to ballistic impact. J. Mater. Sci. Lett. https://doi.org/10.1023/A:1006655301587

Casem, D.T., Grunschel, S.E., Schuster, B.E., 2012. Normal and Transverse Displacement Interferometers Applied to Small Diameter Kolsky Bars. Exp. Mech. 52, 173–184. https://doi.org/10.1007/s11340-011-9524-x

Cheeseman, B.A., Bogetti, T.A., 2003. Ballistic impact into fabric and compliant composite laminates. Compos. Struct. 61, 161–173. https://doi.org/10.1016/S0263-8223(03)00029-1

Chitrangad, 1993. Hybrid ballistic fabric. 5,187,003.

Chocron, S., King, N., Bigger, R., Walker, J.D., Heisserer, U., van der Werff, H., 2013. Impacts and Waves in Dyneema ® HB80 Strips and Laminates. J. Appl. Mech. 80, 031806. https://doi.org/10.1115/1.4023349

Chocron, S., Kirchdoerfer, T., King, N., Freitas, C.J., 2011. Modeling of Fabric Impact With High Speed Imaging and Nickel-Chromium Wires Validation. J. Appl. Mech. 78, 051007. https://doi.org/10.1115/1.4004280

Chocron, S., Nicholls, A.E., Brill, A., Malka, A., Namir, T., Havazelet, D., Werff, H. van der, Heisserer, U., Walker, J.D., 2014. Modeling unidirectional composites by bundling fibers into strips with experimental determination of shear and compression properties at high pressures. Compos. Sci. Technol. 101, 32–40. https://doi.org/10.1016/j.compscitech.2014.06.016

Culnane, A.H., Woodward, R.L., Egglestone, G.T., 1991. Failure examination of composite materials using standard metallographic techniques. J. Mater. Sci. Lett. 10, 333–334. https://doi.org/10.1007/BF00719700

Cunniff, P.M., 1999. Dimensionless Parameters for Optimization of Textile-Based Body Armor Systems. 18th Int. Symp. Ballist. 1303–1310.

De Ruijter, C., Van Der Zwaag, S., Stolze, R., Dingemans, T.J., 2010. Liquid crystalline matrix polymers for aramid ballistic composites. Polym. Compos. 31, 612–619. https://doi.org/10.1002/pc.20835

Donadon, M. V., Iannucci, L., Falzon, B.G., Hodgkinson, J.M., de Almeida, S.F.M., 2008. A progressive failure model for composite laminates subjected to low velocity impact damage. Comput. Struct. https://doi.org/10.1016/j.compstruc.2007.11.004

Dong, H., Wang, Z., O'Connor, T.C., Azoug, A., Robbins, M.O., Nguyen, T.D., 2018. Micromechanical models for the stiffness and strength of UHMWPE macrofibrils. J. Mech. Phys. Solids 116, 70–98. https://doi.org/10.1016/j.jmps.2018.03.015

DSM.com, n.d. Applications [WWW Document]. URL https://www.dsm.com/products/dyneema/en_GB/applications.html

Dyer, S., Lord, D., Hutchinson, I.J., Ward, I.M., Duckett, R.A., 1992. Elastic anisotropy in unidirectional.

Faggiani, A., Falzon, B.G., 2010. Predicting low-velocity impact damage on a stiffened composite panel. Compos. Part A Appl. Sci. Manuf. 41, 737–749. https://doi.org/10.1016/j.compositesa.2010.02.005

Field, J.E., Sun, Q., 1990. A high speed photographic study of impact on fibres and woven fabrics. High-Speed Photogr. Photonics 1358, 703–712. https://doi.org/10.1117/12.23993

Flanagan, M.P., Zikry, M.A., Wall, J.W., El-Shiekh, A., 1999. Experimental investigation of high velocity impact and penetration failure modes in textile composites. J. Compos. Mater. https://doi.org/10.1177/002199839903301202

Fleck, N.A., 1997. Compressive Failure of Fiber Composites. Adv. Appl. Mech. https://doi.org/10.1016/S0065-2156(08)70385-5

Frank, F.C., 1970. The Strength and Stiffness of Polymers. Proc. R. Soc. A Math. Phys. Eng. Sci. 319, 127–136. https://doi.org/10.1098/rspa.1970.0170

Gama, B.A., Gillespie, J.W., 2008. Punch shear based penetration model of ballistic impact of thick-section composites. Compos. Struct. 86, 356–369. https://doi.org/10.1016/j.compstruct.2007.11.001

Gibson, A.G., Ward, I.M., Cole, B.N., Parsons, B., 1974. Hydrostatic extrusion of solid polyethylene. Polym. Eng. Sci. 14, 641–645. https://doi.org/10.1002/pen.760140909

Golovin, K., Phoenix, S.L., 2016. Effects of extreme transverse deformation on the strength of UHMWPE single filaments for ballistic applications. J. Mater. Sci. 51, 8075–8086. https://doi.org/10.1007/s10853-016-0077-3

Govaert, L.E., Lemstra, P.J., 1992. Deformation behavior of oriented UHMW-PE fibers. Colloid Polym. Sci. 270, 455–464. https://doi.org/10.1007/BF00665989

Greenhalgh, E.S., Bloodworth, V.M., Iannucci, L., Pope, D., 2013. Fractographic observations on Dyneema?? composites under ballistic impact. Compos. Part A Appl. Sci. Manuf. 44, 51–62. https://doi.org/10.1016/j.compositesa.2012.08.012

Greer, K.W., King, R.S., Chan, F.W., 2004. The Effects of Raw Material, Irradiation Dose, and Irradiation Source on Crosslinking of UHMWPE. J. ASTM Int. 1, 1–11. https://doi.org/10.1520/STP11932S

Grujicic, M., Arakere, G., He, T., Bell, W.C., Cheeseman, B.A., Yen, C.F., Scott, B., 2008. A ballistic material model for cross-plied unidirectional ultra-high molecular-weight polyethylene fiber-reinforced armor-grade composites. Mater. Sci. Eng. A 498, 231–241. https://doi.org/10.1016/j.msea.2008.07.056

Hazzard, M.K., Curtis, P.T., Iannucci, L., Hallett, S., Trask, R., 2015. An Investigation of the in-plane performance of ultra-high molecular weight polyethylene fibre composites. Int. Conf. Compos. Mater. 19–24.

Hazzard, M.K., Hallett, S., Curtis, P.T., Iannucci, L., Trask, R.S., 2017. Effect of fibre orientation on the low velocity impact response of thin Dyneema®composite laminates. Int. J. Impact Eng. 100, 35–45. https://doi.org/10.1016/j.ijimpeng.2016.10.007

Hazzard, M.K., Trask, R.S., Heisserer, U., Van Der Kamp, M., Hallett, S.R., 2018. Finite element modelling of Dyneema® composites: From quasi-static rates to ballistic impact. Compos. Part A Appl. Sci. Manuf. 115, 31–45. https://doi.org/10.1016/j.compositesa.2018.09.005

Heimbs, S., Heller, S., Middendorf, P., Hähnel, F., Weiße, J., 2009. Low velocity impact on CFRP plates with compressive preload: Test and modelling. Int. J. Impact Eng. 36, 1182–1193. https://doi.org/10.1016/j.ijimpeng.2009.04.006

Hine, P.J., Ward, I.M., 1996. Measuring the elastic properties of high-modulus fibres. J. Mater. Sci. 31, 371–379.

Hongkarnjanakul, N., Bouvet, C., Rivallant, S., 2013. Validation of low velocity impact modelling on different stacking sequences of CFRP laminates and influence of fibre failure. Compos. Struct. 106, 549–559. https://doi.org/10.1016/j.compstruct.2013.07.008

Huang, W., Wang, Y., Xia, Y., 2004. Statistical dynamic tensile strength of UHMWPE-fibers. Polymer (Guildf). 45, 3729–3734. https://doi.org/10.1016/j.polymer.2004.03.062

Iannucci, L., Pope, D., 2011. High velocity impact and armour design. Express Polym. Lett. 5, 262–272. https://doi.org/10.3144/expresspolymlett.2011.26

Jacobs, M., Heijnen, N., Bastiaansen, C., Lemstra, P., 2000. A novel, efficient route for the crosslinking and creep improvement of high modulus and high strength polyethylene fibres. Macromol. Mater. Eng. 283, 120–125. https://doi.org/10.1002/1439-2054(20001101)283:1<120::AID-MAME120>3.0.CO;2-N

Jacobs, M.J.N., Van Dingenen, J.L.J., 2001. Ballistic protection mechanisms in personal armour. J. Mater. Sci. 36, 3137–3142. https://doi.org/10.1023/A:1017922000090

Johnson, K.L., 2003. Contact Mechanics. J. Tribol. https://doi.org/10.1115/1.3261297

Jorgensen, O., Giannakopoulos, A.E., Suresh, S., 1998. Spherical indentation of composite laminates with controlled gradients in elastic anisotropy. Int. J. Solids Struct. 35, 5097–5113. https://doi.org/10.1016/S0020-7683(97)00209-6

Kachanov, L., 2013. Introduction to continuum damage mechanics. Springer Science & Business Media.

Karthikeyan, K., Kazemahvazi, S., Russell, B.P., 2016. Optimal fibre architecture of soft-matrix ballistic laminates. Int. J. Impact Eng. 88, 227–237. https://doi.org/10.1016/j.ijimpeng.2015.10.012

Karthikeyan, K., Russell, B.P., Fleck, N.A., O'Masta, M., Wadley, H.N.G., Deshpande, V.S., 2013a. The soft impact response of composite laminate beams. Int. J. Impact Eng. 60, 24–36. https://doi.org/10.1016/j.ijimpeng.2013.04.002

Karthikeyan, K., Russell, B.P., Fleck, N.A., Wadley, H.N.G., Deshpande, V.S., 2013b. The effect of shear strength on the ballistic response of laminated composite plates. Eur. J. Mech. - A/Solids 42, 35–53. https://doi.org/10.1016/j.euromechsol.2013.04.002

Kelly, J.M., 2002. Ultra-High Molecular Weight Polyethylene*. J. Macromol. Sci. Part C Polym. Rev. 42, 355–371. https://doi.org/10.1081/MC-120006452

Koh, A.C.P., Shim, V.P.W., Tan, V.B.C., 2010. Dynamic behaviour of UHMWPE yarns and addressing impedance mismatch effects of specimen clamps. Int. J. Impact Eng. 37, 324–332. https://doi.org/10.1016/j.ijimpeng.2009.10.008

Koh, C.P., Shim, V.P.W., Tan, V.B.C., Tan, B.L., 2008. Response of a high-strength flexible laminate to dynamic tension. Int. J. Impact Eng. 35, 559–568. https://doi.org/10.1016/j.ijimpeng.2007.04.010

Kozakoff, D.J., Corallo, C., Petra, D., Roovers, W., 2017. 5G Cellular Electromagnetic Window Considerations. Www.Dsm.Com 1–6.

Kromm, F.X., Lorriot, T., Coutand, B., Harry, R., Quenisset, J.M., 2003. Tensile and creep properties of ultra high molecular weight PE fibres. Polym. Test. 22, 463–470. https://doi.org/10.1016/S0142-9418(02)00127-7

Kurtz, S.M., 2004. The UHMWPE Handbook: Ultra-High Molecular Weight Polyethylene in Total Joint Replacement, The UHMWPE Handbook: Ultra-High Molecular Weight Polyethylene in Total Joint Replacement. https://doi.org/10.1016/B978-0-12-429851-4.X5000-1

Lässig, T., Nguyen, L., May, M., Riedel, W., Heisserer, U., Van Der Werff, H., Hiermaier, S., 2015. A non-linear orthotropic hydrocode model for ultra-high molecular weight polyethylene in impact simulations. Int. J. Impact Eng. 75, 110–122. https://doi.org/10.1016/j.ijimpeng.2014.07.004

Lässig, T.R., May, M., Heisserer, U., Riedel, W., Bagusat, F., van der Werff, H., Hiermaier, S.J., 2018. Effect of consolidation pressure on the impact behavior of UHMWPE composites. Compos. Part B Eng. 147, 47–55. https://doi.org/10.1016/j.compositesb.2018.04.030

Lässig, T.R., Nolte, F., Riedel, W., May, M., 2016. An assessment of experimental techniques for measuring the mode I fracture toughness of uhmw-pe composites. Proc. 17th Eur. Conf. Compos. Mater. ECCM17 26–30.

Lee, B.L., Song, J.W., Ward, J.E., 1994. Failure of Spectra® Polyethylene Fiber-Reinforced Composites under Ballistic Impact Loading. J. Compos. Mater. 28, 1202–1226. https://doi.org/10.1177/002199839402801302

Leigh Phoenix, S., Porwal, P.K., 2003. A new membrane model for the ballistic impact response and V50 performance of multi-ply fibrous systems. Int. J. Solids Struct. 40, 6723–6765. https://doi.org/10.1016/S0020-7683(03)00329-9

Lemaitre, J., Chaboche, J.L., 1994. Mechanics of solid materials. Cambridge university press.

Lim, C.T., Tan, V.B.C., Cheong, C.H., 2002. Perforation of high-strength double-ply fabric system by varying shaped projectiles. Int. J. Impact Eng. https://doi.org/10.1016/S0734-743X(02)00004-0

Lin, L., Argon, A.S., 1994. Structure and plastic deformation of polyethylene. J. Mater. Sci. 29, 294–323. https://doi.org/10.1007/BF01162485

Liu, G., Thouless, M.D., Deshpande, V.S., Fleck, N.A., 2014. Collapse of a composite beam made from ultra high molecular-weight polyethylene fibres. J. Mech. Phys. Solids 63, 320–335. https://doi.org/10.1016/j.jmps.2013.08.021

Marissen, R., 2011. Design with Ultra Strong Polyethylene Fibers. Mater. Sci. Appl. 02, 319–330. https://doi.org/10.4236/msa.2011.25042

McDaniel, P.B., Sockalingam, S., Deitzel, J.M., Jr., J.W.G., JPepe, S., Settembre, C., Nusco, E., Auricchio, A., Naldini, L., Ballabio, A., Cosma, M.P., 2017. The effect of fiber meso/nanostructure on the transverse compressionresponse of ballistic fibers. Compos. Part A Appl. Sci. Manuf. 94, 133–145. https://doi.org/10.1016/j.compositesa.2016.12.003

Nazarian, O., Zok, F.W., 2014. Constitutive model for the shear response of Dyneema® fiber composites. Compos. Part A Appl. Sci. Manuf. 66, 73–81. https://doi.org/10.1016/j.compositesa.2014.06.012

Nguyen, L.H., Lässig, T.R., Ryan, S., Riedel, W., Mouritz, A.P., Orifici, A.C., 2016. A methodology for hydrocode analysis of ultra-high molecular weight polyethylene composite under ballistic

impact. Compos. Part A Appl. Sci. Manuf. 84, 224–235. https://doi.org/10.1016/j.compositesa.2016.01.014

O'Masta, M.R., Crayton, D.H., Deshpande, V.S., Wadley, H.N.G., 2016. Indentation of polyethylene laminates by a flat-bottomed cylindrical punch. Compos. Part A Appl. Sci. Manuf. 80, 138–147. https://doi.org/10.1016/j.compositesa.2015.10.015

O'Masta, M.R., Crayton, D.H., Deshpande, V.S., Wadley, H.N.G., 2015a. Mechanisms of penetration in polyethylene reinforced cross-ply laminates. Int. J. Impact Eng. 86, 249–264. https://doi.org/10.1016/j.ijimpeng.2015.08.012

O'Masta, M.R., Deshpande, V.S., Wadley, H.N.G., 2015b. Defect controlled transverse compressive strength of polyethylene fiber laminates. Int. J. Solids Struct. 52, 130–149. https://doi.org/10.1016/j.ijsolstr.2014.09.023

O'Masta, M.R., Deshpande, V.S., Wadley, H.N.G., 2014. Mechanisms of projectile penetration in Dyneema® encapsulated aluminum structures. Int. J. Impact Eng. 74, 16–35. https://doi.org/10.1016/j.ijimpeng.2014.02.002

Peijs, T., Smets, E.A.M., Govaert, L.E., 1994. Strain rate and temperature effects on energy absorption of polyethylene fibres and composites. Appl. Compos. Mater. 1, 35–54. https://doi.org/10.1007/BF00567210

Phoenix, S., Heisserer, U., van der Werff, H., van der Jagt-Deutekom, M., 2017. Modeling and Experiments on Ballistic Impact into UHMWPE Yarns Using Flat and Saddle-Nosed Projectiles. Fibers 5, 8. https://doi.org/10.3390/fib5010008

Phoenix, S.L., Porwal, P.K., 2003. A new membrane model for the ballistic impact response and V50 performance of multi-ply fibrous systems. Int. J. Solids Struct. 40, 6723–6765. https://doi.org/10.1016/S0020-7683(03)00329-9

Roylance, D., 1980. Stress Wave Propagation in Fibres: Effect of Crossovers. Fibre Sci. Technol. 13, 385–395. https://doi.org/10.1016/0015-0568(80)90011-1

Russell, B.P., Karthikeyan, K., Deshpande, V.S., Fleck, N.A., 2013. The high strain rate response of Ultra High Molecular-weight Polyethylene: From fibre to laminate. Int. J. Impact Eng. 60, 1–9. https://doi.org/10.1016/j.ijimpeng.2013.03.010

Shaker, K., Jabbar, A., Karahan, M., Karahan, N., Nawab, Y., 2017. Study of dynamic compressive behaviour of aramid and ultrahigh molecular weight polyethylene composites using Split Hopkinson Pressure Bar. J. Compos. Mater. 51, 81–94. https://doi.org/10.1177/0021998316635241

Shen, S., Henry, A., Tong, J., Zheng, R., Chen, G., 2010. Polyethylene nanofibres with very high thermal conductivities. Nat. Nanotechnol. 5, 251–255. https://doi.org/10.1038/nnano.2010.27

Smith, J.C., Mccrackin, F.L., Schiefer, H.F., 1958. Stress-Strain Relationships in Yarns Subjected to Rapid Impact Loading:Part V: Wave Propagation in Long Textile Yarns Impacted Transversely. Text. Res. J. https://doi.org/10.1177/004051755802800402

Smith, P., Lemstra, P.J., 1980. Ultra-high strength polyethylene filaments by solution spinning/drawing. J Mater Sci 15, 505–514. https://doi.org/10.1016/0032-3861(80)90205-0

Smith, P., Lemstra, P.J., Kalb, B., Pennings, A.J., 1979. Ultrahigh-strength polyethylene filaments by solution spinning and hot drawing. Polym. Bull. 1, 733–736. https://doi.org/10.1007/BF00256272

Sockalingam, S., Casem, D.T., Weerasooriya, T., Jr, J.W.G., 2018. High strain rate transverse compression response of ballistic single fibers. Dyn. Behav. Mater. 1, 51–55. https://doi.org/10.1007/978-3-319-62956-8

Song, B., Park, H., Lu, W.-Y., Chen, W., 2011. Transverse Impact Response of a Linear Elastic Ballistic Fiber Yarn. J. Appl. Mech. https://doi.org/10.1115/1.4004310

Symons, D.D., 2000. Characterisation of indentation damage in 0/90 lay-up T300/914 CFRP. Compos. Sci. Technol. 60, 391–401. https://doi.org/10.1016/S0266-3538(99)00139-6

Tabiei, A., Nilakantan, G., 2008. Ballistic Impact of Dry Woven Fabric Composites: A Review. Appl. Mech. Rev. https://doi.org/10.1115/1.2821711

Tan, V.B.C., Lim, C.T., Cheong, C.H., 2003. Perforation of high-strength fabric by projectiles of different geometry. Int. J. Impact Eng. https://doi.org/10.1016/S0734-743X(02)00055-6

Tan, W., Falzon, B.G., Chiu, L.N.S., Price, M., 2015. Predicting low velocity impact damage and Compression-After-Impact (CAI) behaviour of composite laminates. Compos. Part A Appl. Sci. Manuf. 71, 212–226. https://doi.org/10.1016/j.compositesa.2015.01.025

Van Der Werff, H., Heisserer, U., 2016. High-performance ballistic fibers: Ultra-high molecular weight polyethylene (UHMWPE), in: Advanced Fibrous Composite Materials for Ballistic Protection. https://doi.org/10.1016/B978-1-78242-461-1.00003-0

von Karman, T., Duwez, P., 1950. The Propagation of Plastic Deformation in Solids.pdf 987–994.

Walker, J.D., Chocron, S., 2011. Why Impacted Yarns Break at Lower Speed Than Classical Theory Predicts. J. Appl. Mech. 78, 051021. https://doi.org/10.1115/1.4004328

Walley, S.M., Chapman, D.J., Williamson, D.M., Morley, M.J., Fairhead, T.W., Proud, W.G., 2009. High rate mechanical properties of Dyneema in compression. DYMAT 2009 - 9th Int. Conf. Mech. Phys. Behav. Mater. under Dyn. Load. 2, 1133–1138. https://doi.org/10.1051/dymat/2009158

Wilding, M.A., Ward, I.M., 1978. Tensile creep and recovery in ultra-high modulus linear polyethylenes. Polymer (Guildf). 19, 969–976. https://doi.org/10.1016/0032-3861(78)90208-2

Woodward, R.L., Egglestone, G.T., Baxter, B.J., Challis, K., 1994. Resistance to penetration and compression of fibre-reinforced composite materials. Compos. Eng. 4, 329–341. https://doi.org/10.1016/0961-9526(94)90083-3

Xu, X.P., Needleman, A., 1994. Numerical simulations of fast crack growth in brittle solids. J. Mech. Phys. Solids. https://doi.org/10.1016/0022-5096(94)90003-5

Yu, B., Khaderi, S.N., Deshpande, V.S., Fleck, N.A., 2018. The effect of matrix shear strength on the out-of-plane compressive strength of CFRP cross-ply laminates. Int. J. Solids Struct. 139–140, 79–95. https://doi.org/10.1016/j.ijsolstr.2018.01.023

Zhu, L., Li, Y., Zhu, X., Zhu, Z., 2017. Compressive Mechanics and Failure Mechanism for Uhmwpe Fiber Reinforced Composite Laminates Under Hygrothermal Environment 20–25.

CHAPTER THREE

3. Deep penetration of ultra-high molecular weight polyethylene composites by a sharp-tipped punch

Synopsis

The penetration of unidirectional (UD) and $[0^o/90^o]$ cross-ply ultra-high molecular weight polyethylene fibre composites by sharp-tipped cylindrical punches has been investigated. While the measured penetration pressure for both composite types increased with decreasing punch diameter, the pressure was significantly higher for the cross-ply composites and increased with decreasing ply thickness. A combination of optical microscopy and X-ray tomography revealed that in both composites, the sharp-tipped punch penetrated without fibre fracture by the formation of mode-I cracks along the fibre directions, followed by the wedging open of the crack by the advancing punch. In the cross-ply composites, delamination between adjacent 0^o and 90^o plies also occurred to accommodate the incompatible deformation between plies containing orthogonal mode-I cracks. Micromechanical models for the steady-state penetration pressure were developed for both composites. To account for material anisotropy as well as the large shear strains and fibre rotations, the deformation of the composites was modelled via a pressure-dependent crystal plasticity framework. Intra and inter-ply fracture were accounted for via mode-I and delamination toughnesses respectively. These models account for the competition between deformation and fracture of the plies and accurately predict the measured steady-state penetration pressures over the wide range of punch diameters and ply thicknesses investigated here. Design maps for the penetration resistance of cross-ply composites were constructed using these models and subsequently used to infer composite designs that maximise the penetration resistance for a user prescribed value of fibre strength.

3.1. Introduction

There is considerable interest in the use of ultra-high molecular weight polyethylene (UHMWPE) fibre composites in ballistic protection applications. This interest has primarily been driven by the high strength and stiffness to weight ratios of the polyethylene fibres (Van Dingenen, 1989; Russell et al., 2013). As detailed in Chapter 2, the studies on the ballistic impact of UHMWPE composites to-date have been largely restricted to the out-of-plane (transverse) loading of the composites by blunt projectiles/indenters. Early theoretical investigations by Phoenix and Porwall (2003) of the transverse impact of UHMWPE composite plates suggested that the failure of these composites occurs in a membrane stretching mode with the Cunniff (1999) dimensional analysis providing a reasonable estimate of the material properties that set the ballistic limit. For this membrane stretching approximation, the composite plate either completely fails or suffers no fracture. However, a series of more recent experimental studies using flat-bottomed (O'Masta et al., 2016; Attwood et al., 2016;) and spherical (O'Masta et al. 2015; Heisserer et al., 2013; Karthikeyan and Russel, 2014) projectiles revealed that penetration occurs in a progressive manner in which fibre failure is occurring by the indirect tension mechanism introduced by Attwood et al. (2014). These studies indicate the penetration response is sensitive to the shear strength of the composite with the penetration mode eventually transitioning to a shear-off mode with increasing shear strength (Cheeseman and Bogetti, 2003; Attwood et al., 2016). In parallel with these experimental investigations of the penetration mechanisms, significant efforts have sought to model the observed responses. Iannucci and Pope (2011) modelled the cross-ply composites as a homogenized medium with a non-linear shear stress versus strain relationship fitted to measured data. By contrast, Grujicic et al. (2008) proposed a multi-scale material model for a cross-ply UHMWPE composite. They attempted to use fundamental material properties of the fibres and the matrix within a homogenisation framework. While both models give results that are in qualitative agreement with measurements, they do not predict the observed progressive mode of penetration with sufficient accuracy.

While the investigations of the penetration resistance of UHMWPE composites described above have largely been restricted to blunt projectiles, the effect of the projectile tip shape on the penetration resistance of traditional carbon and glass fibre composites has received extensive attention. Experimental investigations have ranged from low-velocity drop weight tests (Mitrevski et al., 2005) to high-velocity gas gun tests (Mines et al., 1999; Onyechi et al.,

2014) with flat, conical and hemispherical tipped projectiles. While pervasive damage in these brittle composites made the effect of the projectile tip shape on the penetration mode difficult to quantify, clear differences in the energy absorption and ballistic limit were observed. Modelling efforts for these materials have been predominantly based on continuum damage formulations with both analytical (Wen, 2000) and numerical (Kim and Goo, 1997) approaches. A related class of investigations is the stab/puncture resistance of composites performed with the aim of developing composites for application in stab-resistant or knife-resistant vests; readers are referred to Bilisik (2017) for a recent review. These studies are restricted to the quasi-static penetration by sharp-tipped punches of composites that include woven aramid fabrics (Mayo et al., 2009; Decker et al., 2007), Dyneema® (Li et al., 2016) and non-woven mats (Bao et al., 2016). These investigations illustrate the importance of matrix properties in setting the penetration resistance, but a quantitative understanding of the effect of material properties upon penetration by sharp penetrators is missing. This in large part is due to the absence of a modelling framework.

In this study, we report a combined experimental and theoretical investigation of the penetration resistance of unidirectional and cross-ply UHMWPE fibre composites by cylindrical punches with a conical tip. The aim is to develop an understanding of the penetration modes, and to contrast them with those of blunt punches. The outline of the study is as follows. We first report the experimental investigation of the penetration resistance of unidirectional and cross-ply composites along with optical microscopy and X-ray imaging to elucidate the penetration modes. Second, this understanding is used to develop a penetration model for these composites that includes the anisotropic plastic deformation of the composite and the appropriate fracture modes. Finally, the models are used to construct penetration mechanism maps which aid the design of optimal composite microstructures.

3.2. Experimental protocol

The aim of the experimental study was to investigate the resistance of both unidirectional (UD) and cross-ply UHMWPE composites against penetration by a cylindrical punch of radius a and a conical tip characterised by half angle α; see Fig. 3.1a.

3.2.1 Composite manufacture and configurations

Four grades of UHMWPE composites supplied by DSM under the tradename Dyneema® comprising SK76 UHMWPE fibres in a polyurethane matrix were employed in this investigation. The manufacturing steps for the cross-ply composites with a $[0^o/90^o]$ stacking sequence of the plies were detailed in Russell et al. (2013) and Attwood et al. (2014), and here we summarise these steps in order to clarify the differences in the process used to manufacture the UD composites.

(i) A gel-spinning/hot drawing process (Smith et al., 1979; Smith and Lemstra, 1980) is used to produce highly orientated and highly crystalline fibres of diameter 17 μm.

(ii) Fibres are coated in a resin solution and are then formed into a $[0^o/90^o/0^o/90^o]$ stack. A drying process removes the matrix solvent from the stack, and several stacks are placed on top of each other in order to form the desired laminate.

(iii) The laminate is hot-pressed with bonding of the layers achieved through partial melting of the matrix material. The fibre diameter is unchanged by the hot-pressing operation, although some fibres may change their cross-sectional shape.

DSM supplied all the cross-ply composites used in this study in plates of dimensions $400\ \text{mm} \times 400\ \text{mm}$ and 50 mm thick (i.e. the plies were stacked to give a 50 mm thick composite). Three grades of cross-ply composites were employed with ply thicknesses $t = 30\ \mu\text{m}, 60\ \mu\text{m}$ and $120\ \mu\text{m}$. The commercial designations of these composites are HB80, HB26 and HB25 respectively but throughout this study we refer to them by their ply thicknesses. With X_1 and X_2 denoting directions of a Cartesian co-ordinate system aligned with the orthogonal fibres of the cross-ply (Fig. 3.1b), dark field optical images of an $X_1 - X_3$ plane through the three grades of the cross-ply composites are included in Fig. 3.2. The ply architecture and the closely packed fibres are clearly visible in these images.

An analogous hot-pressing process was used to manufacture the UD composites. Matrix-impregnated UD plies were laid-up into a plate of size $100\ \text{mm} \times 100\ \text{mm}$ and 50 mm thick. These plies were then pressed together at a temperature of $127\ ^o\text{C}$ and a consolidation pressure of 21 MPa for 20 minutes to produce a UD laminate. Again, we define a Cartesian co-ordinate system with X_1 aligned with the fibre direction and X_3 aligned with the transverse direction along which the composite was consolidated in the manufacturing process. All of the composite grades contained a fibre volume fraction $v_f \approx 83\%$. The quasi-static tensile, shear and out-of-

plane compression responses of the four grades of UHMWPE composites used in this study were reported by Attwood et al. (2014), and we shall use those property measurements to inform the material models in Section 3.4.2.

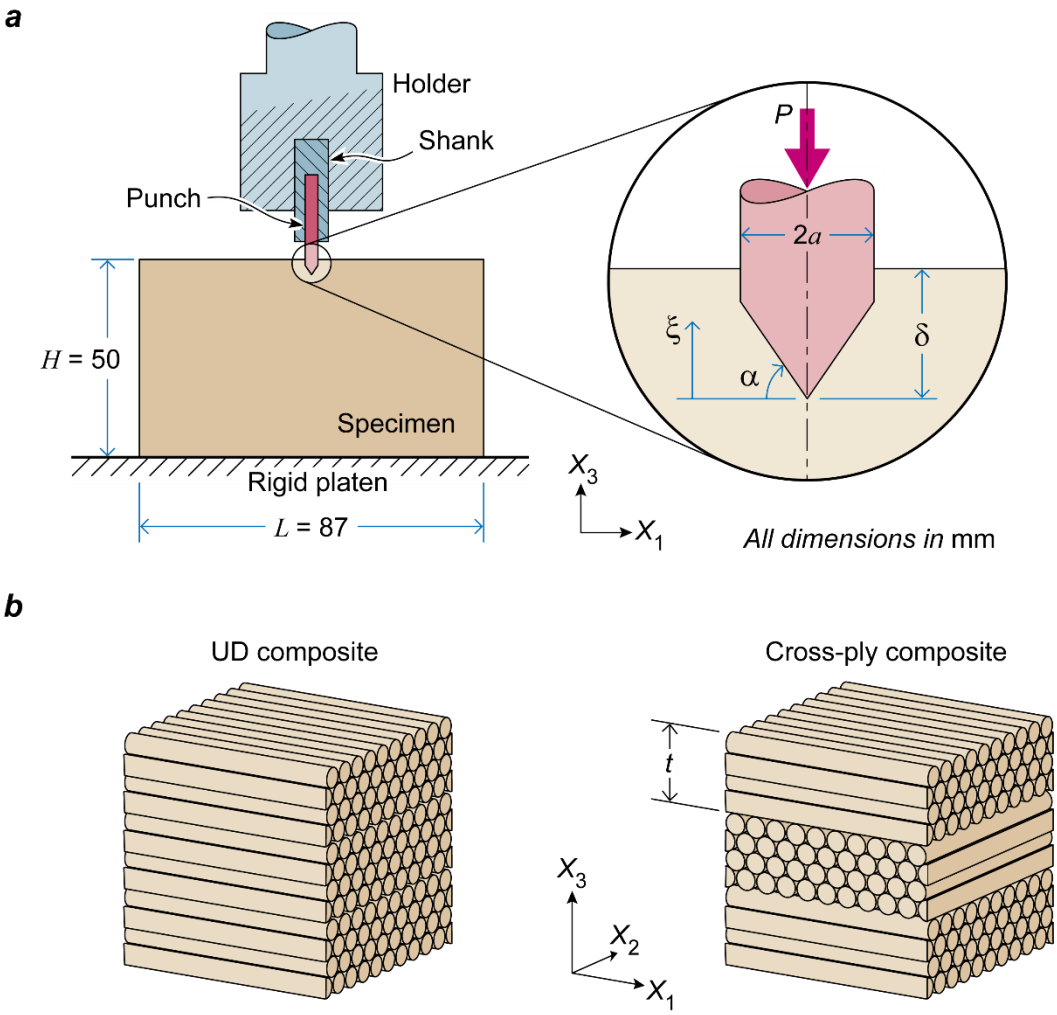

Figure 3.1: (a) Schematic of the penetration of UHMWPE composites by a sharp-tipped cylindrical punch. The inset shows details of the conical tip of the punch. (b) Sketches of the UD and cross-ply composites with the definition of the global Cartesian co-ordinate system X_i.

3.2.2 Measurements and imaging

All measurements reported in the main body of this paper were conducted on cuboidal blocks of the UHMWPE composite of lateral dimension $L \times L = 87\ \text{mm} \times 87\ \text{mm}$ and thickness $H = 50\ \text{mm}$ (Fig. 3.1a). These blocks were cut from the as-manufactured plates using a medium-fine blade band-saw and were sufficiently large that the measured penetration response was reasonably insensitive to further increases in the specimen size.

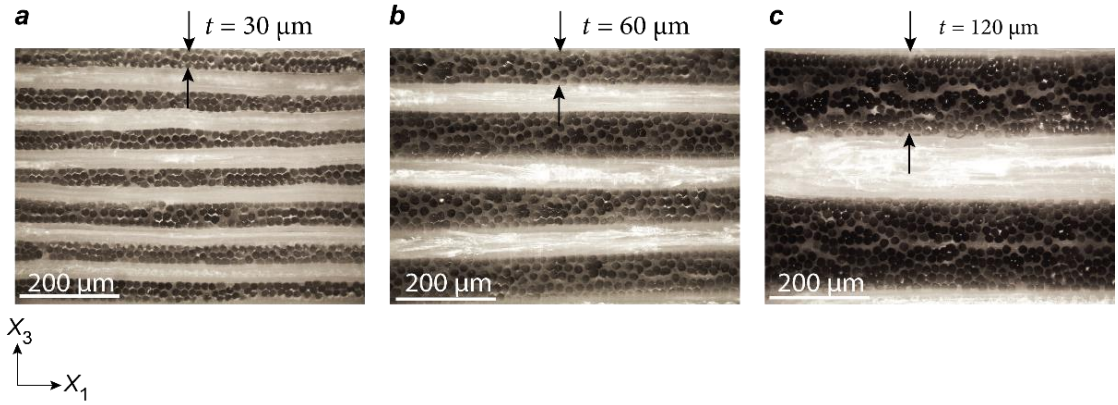

Figure 3.2: Dark field optical micrographs of an $X_1 - X_3$ plane through the three grades of the cross-ply Dyneema® composites with ply thicknesses (a) $t = 30$ μm, (b) $t = 60$ μm and (c) $t = 120$ μm.

Penetration experiments were conducted as shown in Fig. 3.1a with both the UD and cross-ply composites penetrated in the X_3 −direction by a cylindrical punch with a conical tip. The composite blocks were placed on a rigid backing and the penetration experiments were conducted in a screw-driven test machine with a holder as sketched in Fig. 3.1a to grip the punch. The penetration δ was defined as the depth of the tip below the surface of the composite block (Fig. 3.1a) and measured using a laser extensometer. The punch was displaced at a rate of $\dot{\delta} = 0.5$ mm min^{-1} and the applied load P was measured via the load cell of the test machine. The measurements are presented in terms of the applied nominal pressure $p \equiv P/(\pi a^2)$ and the normalized penetration $\bar{\delta} \equiv \delta/d$, where $d = 17$ μm is the fibre diameter and a relevant length scale for both the UD and cross-ply composites. Measurements are reported for punches with diameters in the range $0.25 \text{ mm} \leq 2a \leq 4$ mm with cone tip half angles $\alpha = 30^o$, 45^o and 60^o. The punches for the UD composites were made from hardened silver steel (800 Vickers). However, the high pressure required to penetrate the cross-ply composites resulted in elastic buckling of the silver steel punches inside the cross-ply composites. Thus, Tungsten-Carbide/Cobalt (WC 94 Co 6 wt%) rods with a modulus twice that of the silver steel punches were used for the penetration of the cross-ply composites. Nevertheless, buckling of the penetrator restricted the experiments on cross-ply composites to punches with diameters $2a \geq 2$ mm. At-least 3 repeat tests were performed in each case to check the reproducibility of the measurements.

Both the UD and cross-ply composites penetration experiments were interrupted at regular intervals to conduct the optical and X-ray observations of the penetration modes. However, the protocol varied between the UD and cross-ply composites. The penetration mode of the UD composite involved splitting and separation of the fibres with no fibre breakage and only a small elastic deformation of the fibres. This implied that removal of the punch from the specimen resulted in negligible spring back and left the intact penetration cavity. This cavity was then filled with a solder powder (Sn 60, Pb 38, Ag 2wt%) with an average particle size of 30 μm[1]. X-ray computed tomography (XCT) enabled three-dimensional (3D) reconstruction of the cavity around the punch. In addition, we also conducted optical imaging of interior $X_1 - X_2$ planes of the UD composites in order to visualise the fibre deformations around the indenter. This optical imaging involved peeling-off layers to expose the specimen interior and hence was a destructive process. Fibre layers of the specimen, with the penetration cavity filled with the solder powder, were peeled-off until a layer at a depth of approximately $26a$ below the specimen surface was exposed. Then, another 1 mm or so of the specimen was abraded using a fine-grit (P800-P4000) in order to obtain a clean and smooth surface for imaging. The imaged area of this exposed specimen surface was then divided into a grid comprising approximately 200 squares. Each of these squares was imaged separately and the entire imaged area was then reconstructed by stitching together these sub-images. This procedure enabled us to obtain a relatively high resolution over a large area.

The cross-ply composites were penetrated by Tungsten-Carbide/Cobalt rods at significantly higher pressures. Elastic deformations of the fibres in these specimens meant that the inserted punches were tightly gripped within the specimen and their removal resulted in not only extensive damage of the specimen but also collapse of the penetration cavity. Thus, optical imaging of the specimen interior by peeling-off plies was not feasible. Moreover, since Tungsten-Carbide/Cobalt is nearly X-ray opaque, the shadow cast by the rod inhibited a 3D reconstruction of the specimen deformation around the punch. Instead, we used plain radiographs taken by imaging the specimen along the X_3 −direction so as to infer some aspects of the penetration mode. Additional details of the X-ray imaging and analysis method are provided in Appendix A.

[1] The solder powder enhanced the X-ray contrast and improved the X-ray imaging of the penetrated UHMWPE composite specimen.

3.3. Experiment measurements and observations

We proceed to detail the measurements of the penetration response. The objectives are to characterize the effect of the punch radius a and ply-thickness t on the $p - \bar{\delta}$ response as well as to elucidate the penetration modes.

3.3.1 Unidirectional composites

The measured p versus $\bar{\delta}$ responses for UD composites penetrated by punches of diameters in the range $0.25\ \text{mm} \leq 2a \leq 2\ \text{mm}$ and a tip angle $\alpha = 45^{\text{o}}$ are included in Fig. 3.3a. In each case two measured responses are included to illustrate the repeatability of the measurements. Two regimes are observed for all indenter diameters: *regime I* where the pressure p increases with penetration $\bar{\delta}$; and *regime II* where p remains approximately constant and we denote this steady-state pressure by p_{ss}. The effect of the tip angle α is illustrated in Fig. 3.3b for the $2a = 2\ \text{mm}$ punch. During the initial stage of penetration, decreasing α reduced the penetration pressure. However, the steady-state pressure p_{ss} was unaffected by α.

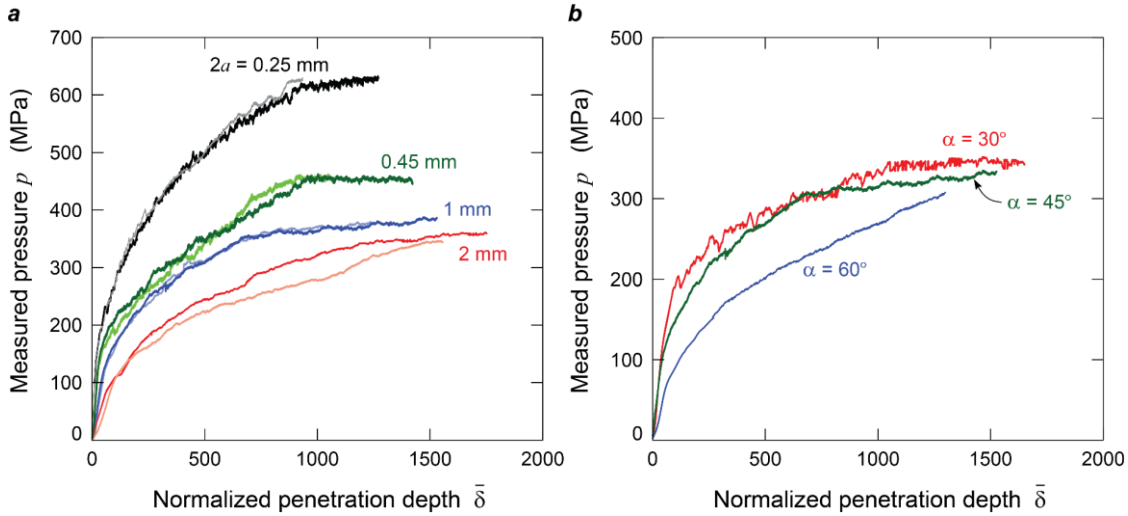

Figure 3.3: The measured pressure p versus normalized penetration $\bar{\delta}$ responses for UD composites penetrated by (a) punches with diameters in the range $0.25\ \text{mm} \leq 2a \leq 2\ \text{mm}$ with tip angle $\alpha = 45^{\text{o}}$ and (b) a $2a = 2\ \text{mm}$ diameter punch and three cone angles α. In (a) two repeat measurements are included for each punch diameter.

The data in Fig. 3.3a indicates that the steady-state penetration pressure p_{ss} increased with decreasing punch diameter. Such a penetration/indentation size effect is well-established for metals and related to micron-sized dislocation structures therefore only observed for punch/indenter diameters on the micron length scale. In the UD composite investigated here, the size effect is observed for millimetre size punch diameters even though the only relevant

microstructural length scale is related to the 17 μm diameter UHMWPE fibres. To investigate the source of this penetration size effect and understand the mode of penetration we include in Fig. 3.4 XCT images of a diametrical $X_1 - X_3$ plane through the $2a = 2$ mm punch ($\alpha = 45^o$) at three selected penetration depths into the specimen. The outline of the punch has been highlighted to clearly contrast the punch and the surrounding cavity within the UD composite. Cross-sectional images on $X_1 - X_2$ planes at the marked heights are also included in each case to show the formation of a cavity in the form of a crack around the cylindrical punch. The length 2ℓ of this crack increases from the tip of the punch such that $\cot^{-1}(\xi/\ell) > \alpha$, where ξ is the distance measured upstream from the tip of the punch as shown in Fig. 3.1a: the crack length reaches a steady state value of $2\ell_{ss} = 9.50$ mm for $\xi > 3.2$ mm. We note that near the surface of the specimen there is a considerable pile-up of material. This pile-up is due to the formation of the cavity whose finite volume results in material being pushed up near the surface of the specimen. However, deep within the specimen, the increasing constraint results in negligible deformation in the X_3 −direction with the formation of the cavity accommodated by in-plane deformation of the specimen.

In order to better understand the crack formation mechanism, Fig. 3.5 shows an optical micrograph of the $X_1 - X_2$ plane at a depth 26 mm below the surface of the specimen penetrated by the $2a = 2$ mm punch ($\alpha = 45^o$). This optical micrograph confirms that the crack seen in the XCT images of Fig. 3.4 is a mode-I crack along the fibre direction and a result of a splitting mode due to the wedging action of the penetrator, i.e. the penetrator induces tensile stresses Σ_{22} that open a crack via matrix cracking with no associated fibre fracture. The material remains in contact with the surface of the cylindrical punch over a region defined by an included angle $2\beta = 68^o$ (Fig. 3.5), with the remaining cavity surface being traction-free. Thus, the wedging pressure generated over the region where the punch is in contact with the cavity provides the driving force for the extension of the crack. We emphasize here that friction between the cylindrical surface of the punch and the UHMWPE composite does not contribute significantly to the observed size effect. A simple work balance suggests that the penetration pressure with friction present is given by

$$p_{ss} = p_{ss}^0 + \frac{4\tau_f \beta \delta}{\pi a}, \qquad (3.1)$$

where τ_f is the frictional stress between the UHMWPE composite and the punch while p_{ss}^0 is the intrinsic steady-state penetration pressure. The frictional contribution (3.1) increases with increasing penetration depth and decreasing punch diameter. The data in Fig. 3.3 clearly shows

that a steady-state is attained such that $p_{ss} \approx p_{ss}^{0}$ suggesting that $\tau_f \ll p_{ss}$. In fact, the measurements of the force to extract the punch from the specimen suggest that $\tau_f < 2$ MPa confirming that friction between the punch and the composite plays a negligible role in these measurements. Moreover, the specimens employed in this study were sufficiently large so that no pull-in was observed at the specimen edges with the specimen size playing no role in the observed penetrator size effects. In fact, the analysis in Section 3.4 will show that the penetrator was accommodated within the specimen by elastic extension of the fibres with the observed penetration size effect for millimetre-sized diameter punches associated with the mode-I splitting toughness of the UD composite.

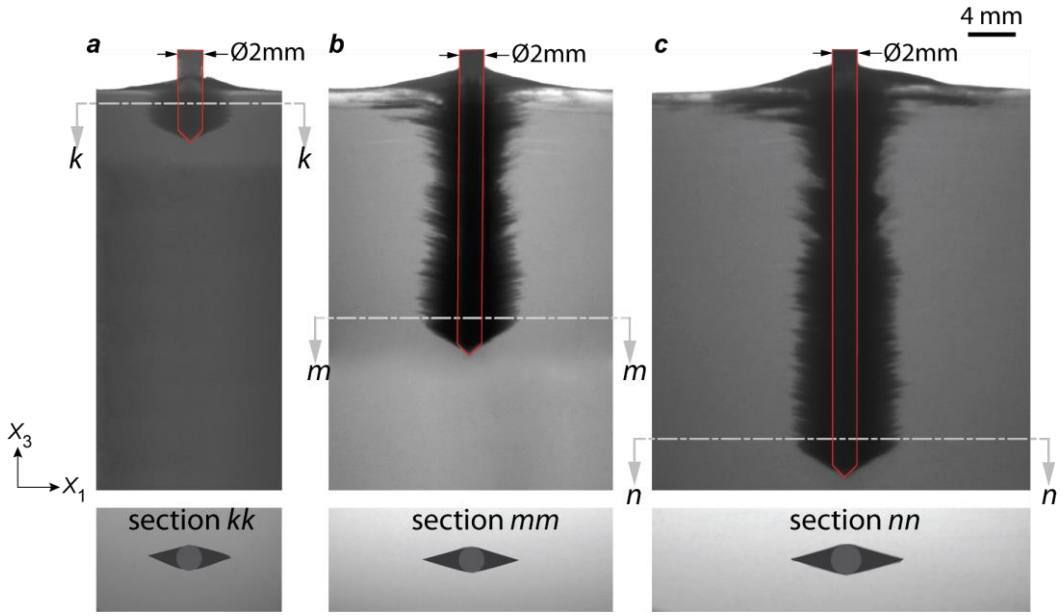

Figure 3.4: X-ray computed tomographic images of the UD composite penetrated by a $2a = 2$ mm diameter punch with cone angle $\alpha = 45^{o}$. The images show a diametrical section through the punch for penetrations (a) $\delta = 5$ mm, (b) $\delta = 19$ mm and (c) $\delta = 27$ mm. In each case cross-sectional images of the $X_1 - X_2$ plane at the marked heights are also included and the indenter is outlined in red for clarity.

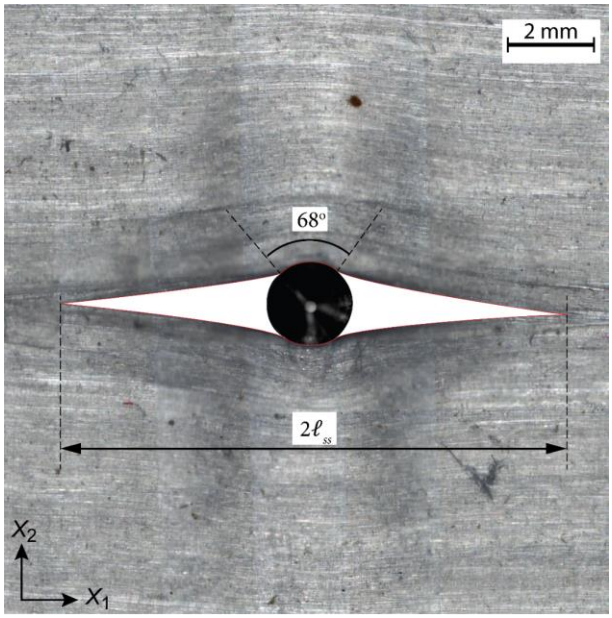

Figure 3.5: An optical micrograph of the $X_1 - X_2$ plane at a depth 26 mm below the surface of the UD specimen penetrated by a $2a = 2$ mm punch with cone angle $\alpha = 45^{\circ}$. The mode-I crack length $2\ell_{ss} = 11.75$ mm and the angle through which the composite conforms over the punch are labelled.

Experiments using different punch diameters indicated very similar deformation/fracture mechanisms to those observed above, and their micrographs are excluded for the sake of brevity. The key observations of the observed size effects are summarised Fig. 3.6a where the measured steady-state penetration pressure p_{ss} and the associated normalized crack length ℓ_{ss}/a are plotted as a function of the punch diameter $2a$. While the penetration pressure p_{ss} increased with decreasing a, the opposite trend was observed for ℓ_{ss}/a. Three repeat tests were conducted in each case and the error bars indicate the variation over these three measurements while the data points represent the mean measurement.

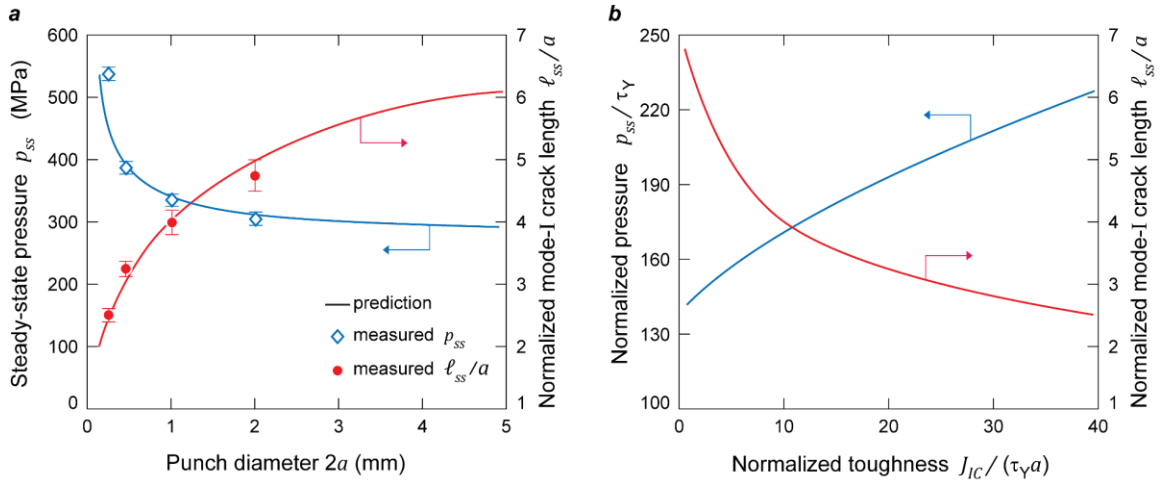

Figure 3.6: (a) Measurements and corresponding predictions of the steady-state penetration pressure p_{ss} and normalized mode-I crack length ℓ_{ss}/a as a function of the punch diameter $2a$ for the UD composite. The error bars indicate the variability between the 3 repeat measurements. (b) Predictions of the normalized penetration pressure p_{ss}/τ_Y and ℓ_{ss}/a as a function of the normalized toughness $J_{IC}/(\tau_Y a)$ for the UD composite.

3.3.2 Cross-ply composites

The measured p versus $\bar{\delta}$ response of the $t = 60$ μm cross-ply composite is included in Fig. 3.7a for $\alpha = 45^o$ punches of size in the range $2\text{ mm} \leq 2a \leq 4\text{ mm}$. The responses are qualitatively similar to that of the UD composites except that the penetration pressures are significantly larger. A penetration size effect is again observed although weaker compared to the UD case. We emphasize that experiments on the cross-ply composites could only be performed for relatively large punch diameters with $2a \geq 2$ mm, and it will be shown in Section 3.5 that this weak size effect is related to the large punch diameters. The ply thickness t, is an additional microstructural length scale in cross-ply composites. The effect of t on the $p - \bar{\delta}$ response is illustrated in Fig. 3.7b where measurements are included for cross-ply composites with $t = 30$ μm, 60 μm and 120 μm penetrated by the $2a = 2$ mm ($\alpha = 45^o$) punch. A very strong size effect is now observed with the penetration pressure higher for composites with thinner plies over nearly the entire range of penetration depths.

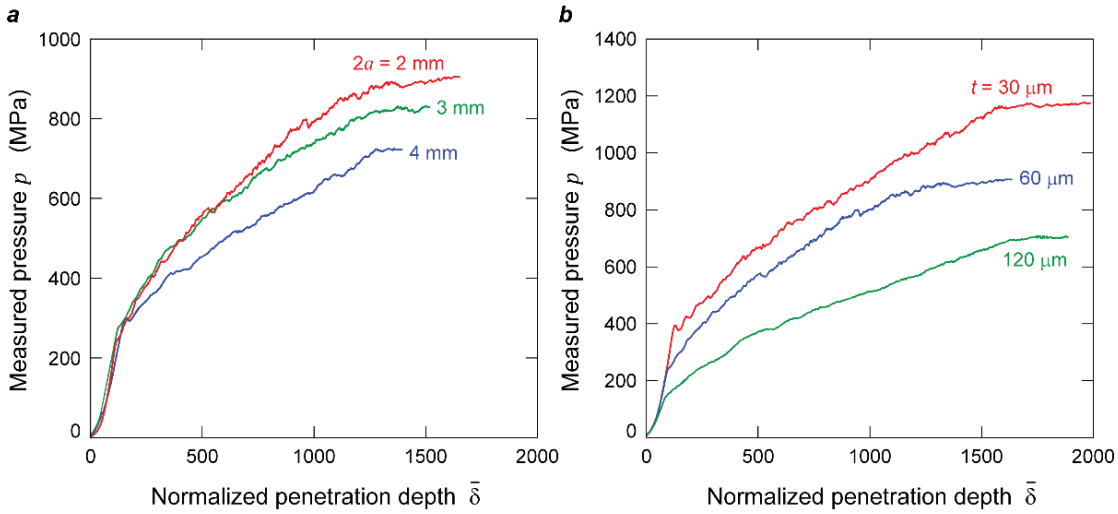

Figure 3.7: The measured pressure p versus normalized penetration $\bar{\delta}$ responses for (a) the $t = 60$ μm cross-ply composite penetrated by punches with diameters in the range $2\text{ mm} \leq 2a \leq 4\text{ mm}$ and (b) cross-ply composites with ply thicknesses $t = 30\ \mu\text{m}, 60\ \mu\text{m}$ and $120\ \mu\text{m}$ penetrated by the $2a = 2$ mm punch. In all cases the cone angle of the punch tip was $\alpha = 45^{\text{o}}$.

XCT imaging of the cross-ply composites penetrated by the Tungsten-Carbide/Cobalt penetrators was not feasible as discussed earlier. Thus, visualisation of the deformation/fracture modes are restricted to plain radiographs such as the one shown in Fig. 3.8 for the $t = 60$ μm cross-ply composite penetrated by the $2a = 3$ mm ($\alpha = 45^{\text{o}}$) punch. In this image we observe a central circular dark zone with an outer concentric circular partially illuminated region. These are the umbra and penumbra shadows of the penetrator that is opaque to the X-rays. In addition, two orthogonal cracks are seen to emanate from the central zone each akin to the single crack seen for the UD composite. We argue that these cracks are mode-I cracks similar to the UD composite but now in the alternating $[0^{\text{o}}/90^{\text{o}}]$ plies. A quantitative interpretation of this image to extract the crack length is complex and readers are referred to Appendix A for details. The analysis indicates that the central dark zone is an enlarged image of the circular cross-section of the punch and obscures some part of the orthogonal mode-I cracks. This gives an optical illusion that the cavity formed around the punch conforms over nearly the entire cylindrical surface of the punch. Note that the scale on Fig. 3.8 is for the image on the detector plane and cannot be directly used to infer ℓ_{ss}: rather a more involved analysis as detailed in Appendix A needs to be conducted from which we infer that the mode-I crack length $2\ell_{ss} = 14$ mm.

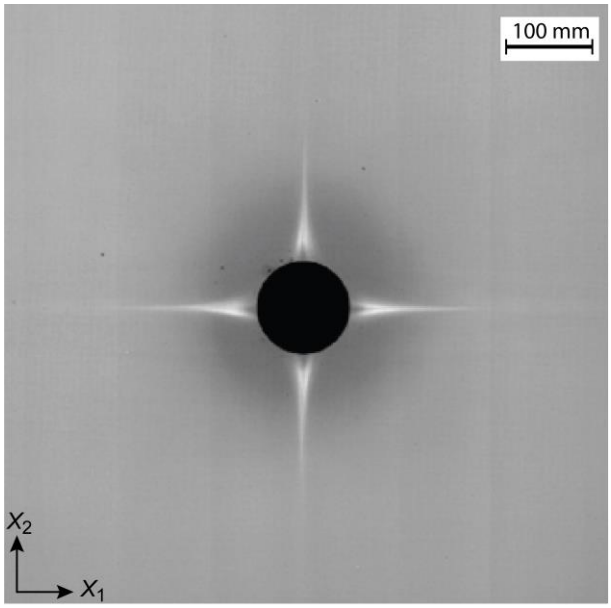

Figure 3.8: A plain radiograph of an $X_1 - X_2$ plane of the $t = 60$ μm cross-ply composite penetrated by the $2a = 3$ mm punch. The scale bar represents the size of the image on the detector plane; see Appendix A for further details.

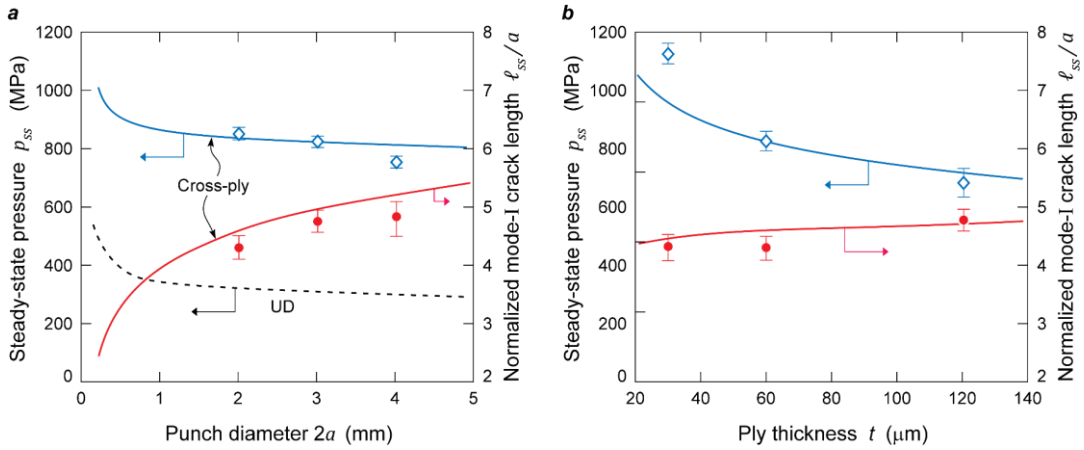

Figure 3.9: Measurements and corresponding predictions of the steady-state penetration pressure p_{ss} and normalized mode-I crack length ℓ_{ss}/a as a function of (a) the punch diameter $2a$ for the $t = 60$ μm cross-ply composite and (b) the ply thickness t for penetration by the $2a = 2$ mm punch. In all cases the cone angle $\alpha = 45^{\circ}$ and the error bars indicate the variability between the 3 repeated measurements.

Measurements of the steady-state pressure p_{ss} and associated normalized crack lengths ℓ_{ss}/a (estimated using the procedure described in Appendix A) are summarised in Fig. 3.9a as a function of $2a$ for the $t = 60$ μm cross-ply composite penetrated by $\alpha = 45^{\circ}$ punches. The results are qualitatively similar to the UD composite with p_{ss} increasing with decreasing $2a$

while ℓ_{ss}/a displays the opposite trend. The corresponding p_{ss} and ℓ_{ss}/a measurements for cross-ply composites penetrated by the $2a = 2$ mm punch ($\alpha = 45^{o}$) are included in Fig. 3.9b as a function of the ply thickness t. The trends are similar to the dependence on the punch diameter with p_{ss} increasing with decreasing t while ℓ_{ss}/a displays the opposite trend although the dependence of the mode-I crack length on the ply thickness is relatively mild.

3.4. Analysis of the steady-state penetration of the unidirectional composite

Our aim here is to develop an understanding of the key physical phenomena that govern the penetration response including the observed size effect of the diameter of the punch. With this in mind, we develop a semi-analytical model for the steady-state penetration motivated by the experimental observations reported above. In order to motivate this analysis, we summarise the observed deformation and fracture modes for the penetration of UD and cross-ply composites by a sharp-tipped punch in Figs. 3.10a and 3.10b, respectively. The UD composites form a single mode-I crack with the punch wedging open a crack along the fibres, i.e. mode-I splitting by matrix cracking with no fibre fracture. The cross-ply composites also deform in a similar mode with orthogonal mode-I splitting cracks forming in the alternating $[0^{o}/90^{o}]$ plies. These cracks however cause a mismatch in deformation due to crack opening in the X_2 and X_1 directions in the 0^{o} and 90^{o} plies, respectively. The high modulus of the fibres prevents large localised fibre extensions and thus these deformations cannot be accommodated by ply deformations. Rather we anticipate delamination to occur between each pair of adjacent 0^{o} and 90^{o} plies to accommodate this incompatible deformation. We note that the inability to acquire XCT images for the cross-ply composites meant this delamination could not be directly visualised. Moreover, deep within the specimen the delamination occurs via mixed mode-II/III fracture with no separation between the plies in the $X_3 -$ direction. Thus, these delamination cracks are unlikely to be visualised via X-ray tomography. In Fig. 3.10b, we depict this delamination to be a circular zone of radius b_{ss}. We emphasize that in both UD and cross-ply composites no fibre fracture was observed for penetration by a sharp-tipped punch.

By contrast, the penetration of the composites by a blunt punch occurs by radically different mechanisms as shown in Figs. 3.10c and 3.10d for UD and cross-ply composites, respectively; see Attwood et al. (2016) and O'Masta et al. (2016) for further details. Briefly, the UD

composites deform in a plastic indentation mode involving matrix shear with minimal fibre deformation.

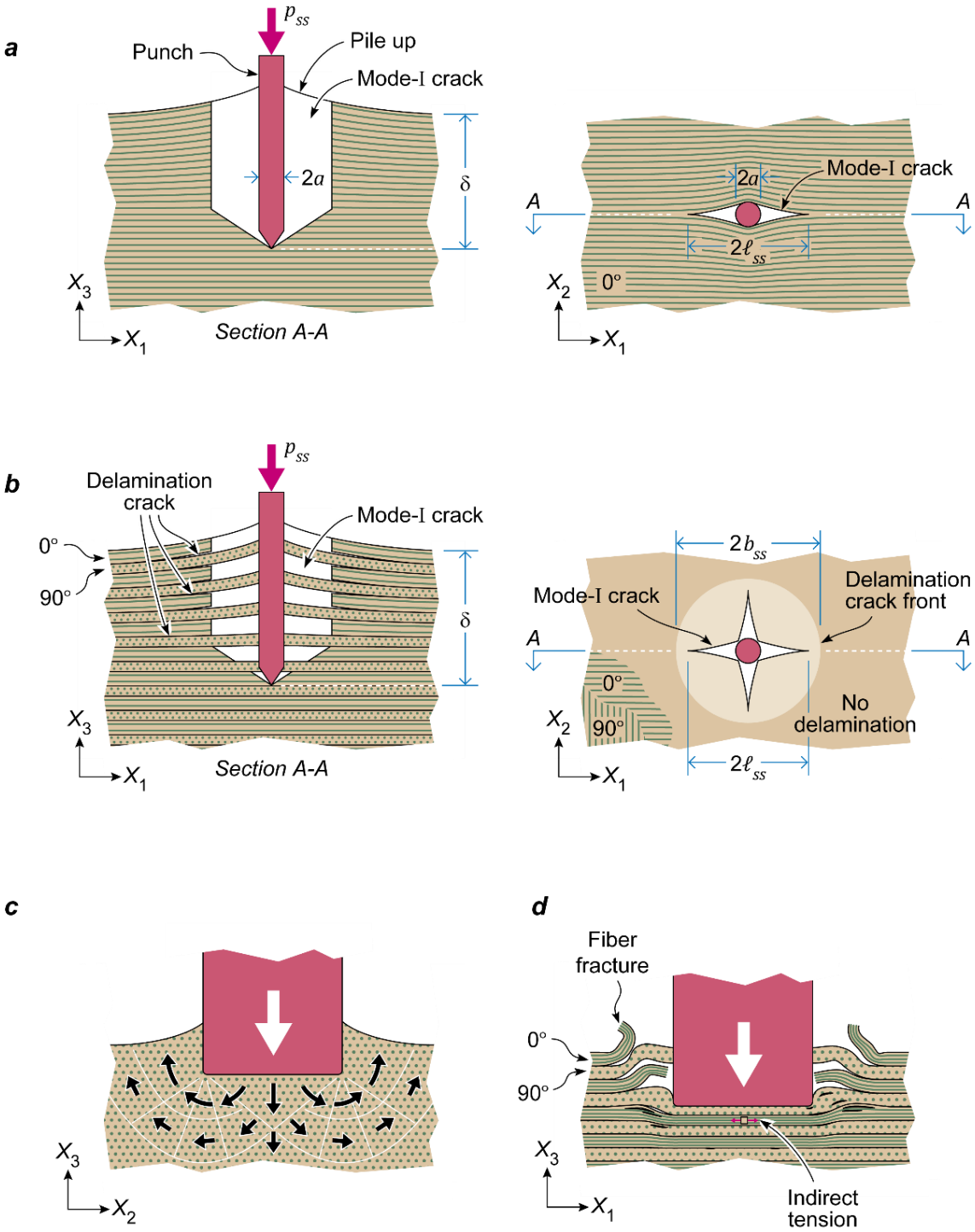

Figure 3.10: Sketches of the penetration modes of the (a) UD and (b) cross-ply composites by a sharp-tipped punch. The mode-I cracks along the fibres and the delamination zones in the cross-ply composite are labelled. Sketches of the deformation/failure modes for indentation of (c) UD and (d) cross-ply composites by a blunt punch.

On the other hand, the compressive indentation stresses induced in the cross-ply composite by a blunt punch generate a state of indirect tension (Attwood et al., 2014), i.e., tensile stresses are generated in the fibre directions in the alternating $[0^o/90^o]$ plies. Continued penetration of the cross-ply composite then occurs by fibre fracture and the elastic recoil (and thus removal) of the failed plies; readers are referred to Attwood et al. (2016) and O'Masta et al. (2016) for further details. This blunt punch penetration mode results in a penetration resistance that is independent of both the punch size and ply thickness (Attwood et al., 2016).

Using the above insight into the deformation and fracture processes for penetration by a sharp-tipped punch, we proceed in this section to develop a semi-analytical model for the steady-state penetration of UD composites and extend it to cross-ply composites in Section 3.5.

3.4.1 Penetration analysis

Consider a rigid cylindrical punch of radius a with a conical tip pushed into a semi-infinite block of the UD composite, as shown in Fig. 3.1a. In line with the measurements and discussion in Section 3.3 we shall neglect the role of friction between the punch and the composite and thus model the punch as frictionless. The composite splits open creating a mode-I crack along the fibres at the tip of the punch. A detailed solution for the deformation and fracture at the punch tip requires a full 3D calculation of considerable complexity. Here, in keeping with our aim of understanding the key physical phenomena, we propose a simplified analysis for the steady-state penetration pressure p_{ss} of the fibre composite. The analysis is motivated by the model of Shergold and Fleck (2004) for the penetration of soft elastomers. The steady-state advance of the punch by an increment $d\delta$ involves the transformation of a slice of thickness $d\delta$ of the material from its undeformed upstream state to a cracked downstream state with a plane strain crack of length $2\ell_{ss}$ that is opened by the wedging action of the punch of radius a (Fig. 3.10a). The energy required to transform a slab of thickness $d\delta$ from its upstream to downstream state is provided by the work done in advancing the punch and an energy balance dictates

$$p_{ss}(\pi a^2)d\delta = 2d\delta \int_0^{\ell} J_I d\ell + U_D d\delta. \qquad (3.2)$$

Here J_I is the mode-I inter-fibre splitting toughness while U_D is the energy required to open the crack of length 2ℓ to accommodate a cylinder of radius a (Fig. 3.10a) in a unit thickness slab of the composite. At steady-state penetration, the crack just arrests upon reaching a length $2\ell_{ss}$

and is thus at a state of incipient advance. Recalling the energy release rate definition of the deformation J integral (Anderson, 2005) it follows that

$$J_I = -\frac{1}{2}\frac{\partial U_D}{\partial \ell}. \tag{3.3}$$

For a given UHMWPE composite with a shear strength τ_Y, it is convenient to express U_D as

$$U_D \equiv \tau_Y a^2 \mathcal{F}\left(\frac{\ell}{a}, \mathcal{M}\right), \tag{3.4}$$

where the non-dimensional function $\mathcal{F}(\ell/a, \mathcal{M})$ needs to be numerically evaluated for the given composite material properties represented here by $\mathcal{M}$. Assuming that the mode-I toughness is independent of crack advance (i.e. no R-curve effect) and denoting this constant toughness as J_{IC}, the steady-state penetration pressure follows from (3.2) as

$$p_{ss} = \frac{2}{\pi}\left(\frac{J_{IC}}{a}\right)\left(\frac{\ell_{ss}}{a}\right) + \frac{\tau_Y}{\pi}\mathcal{F}\left(\frac{\ell_{ss}}{a}, \mathcal{M}\right), \tag{3.5}$$

with (3.3) specifying that the steady-state crack length ℓ_{ss} satisfies the relation

$$J_{IC} = -\frac{\tau_Y a}{2}\frac{\partial \mathcal{F}}{\partial(\ell/a)}\bigg|_{\ell=\ell_{ss}}. \tag{3.6}$$

It now remains to specify the procedure for the calculation of U_D (or equivalently $\mathcal{F}$). We do this in two steps: first we detail a constitutive model for unidirectional UHMWPE composites and then discuss the numerical procedure to evaluate U_D using this constitutive model.

3.4.2 Constitutive model for the UD composite

The deformation of the UHMWPE composite around the punch involves large shear strains and fibre rotations; see Fig. 3.5. The deformation of the SK76 UHMWPE fibres is purely elastic and thus shearing of the matrix is restricted along planes dictated by the fibre directions. For example, consider the deformation of the UD composite by simple shear via the application of a shear strain γ_{13} as shown in Fig. 3.11a. The composite deforms primarily by the relative displacement of the fibres in the X_1 −direction by the shear straining of the intermediate matrix. As a consequence, while the material is subjected to a rotation $\gamma_{13}/2$ the fibres undergo no rotation. This is akin to crystals that deform by shearing along slip planes due to the motion of dislocations and thus we proceed to develop a constitutive model for unidirectional UHMWPE composites motivated by crystal plasticity (Asaro, 1983; Hill and Rice, 1972). This crystal plasticity formulation for UD composites is expected to accurately account for the large plastic shear strains and associated fibre rotations in these composites. Other equivalent approaches such as the rebar approach proposed by Nazarian and Zok (2014) are also feasible although the

crystal plasticity approach is ideally suited to model the pressure dependency of plastic flow in UHMWPE composites as discussed subsequently.

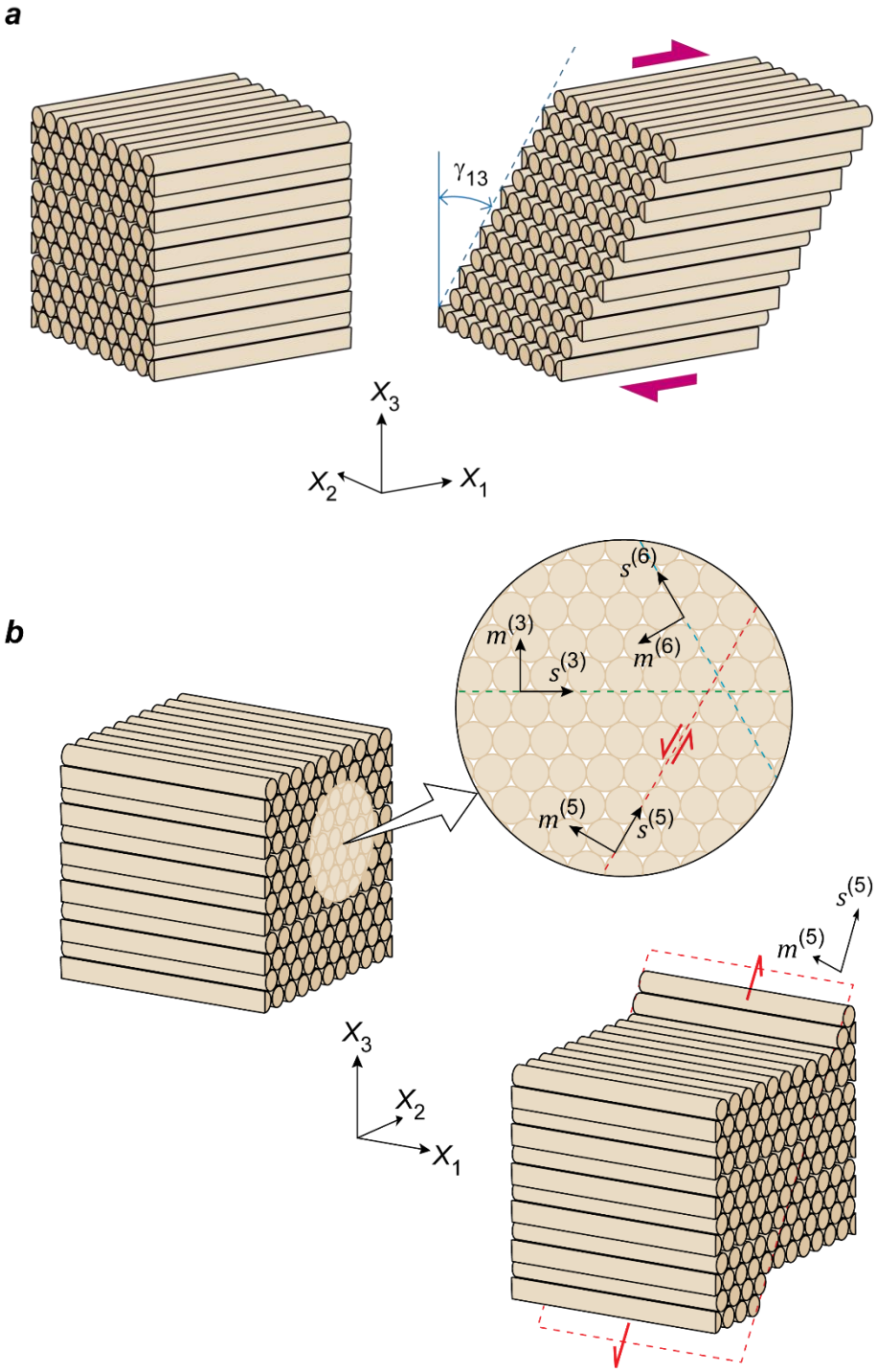

Figure 3.11: (a) The UD composite subjected to a simple shear γ_{13} resulting in no rotation of the fibres. (b) A sketch of the UD composite showing some selected slip systems with their associated directions $(s_i^{(\kappa)}, m_i^{(\kappa)})$ labelled.

3.4.2.1Kinematics

Following the usual notions in crystal plasticity, we define a lattice labelled by the fibre direction. The material is presumed to flow through the lattice due to shearing of the matrix and then the lattice with the embedded material undergoes elastic deformations and rigid body rotations. Using Cartesian tensor notation, the material deformation gradient F_{ij} is written as a multiplicative decomposition of the elastic and plastic deformations characterised by F_{ij}^{*} and F_{ij}^{p}, respectively such that

$$F_{ij} = F_{ik}^{*} F_{kj}^{p}. \tag{3.7}$$

Thus, there exists an intermediate configuration arising from the pure plastic deformation F_{ij}^{p} of the material. The deformations embodied in F_{ij}^{p} are described in terms of shearing along crystallographic slip systems set by the fibre direction. A particular slip system (κ) is specified by vectors $(s_i^{(\kappa)}, m_i^{(\kappa)})$ where $s_i^{(\kappa)}$ specifies the slip direction and $m_i^{(\kappa)}$ is the slip plane normal in the undeformed configuration. These vectors convect with the lattice so that in the deformed lattice they become

$$s_i^{*(\kappa)} = F_{ij}^{*} s_j^{(\kappa)} \qquad \text{and} \qquad m_i^{*(\kappa)} = m_j^{(\kappa)} \left(F_{ji}^{*}\right)^{-1}. \tag{3.8}$$

With the fibres aligned with the X_1 −direction in the undeformed configuration, the $N = 6$ slip systems in the UD composite are listed in Table 3.1 and selected systems are illustrated in Fig. 3.11b. The slip systems $\kappa = 1$ to 4 involve shearing in the X_i directions while the $\kappa = 5$ and 6 systems involve shearing on planes oriented at $\pm 45^{\circ}$ with respect to X_2 direction with no shear component along the X_1 (fibre) direction. These slip systems accommodate all possible modes of deformation that do not involve fibre deformation. The plastic component of the deformation gradient associated with shearing on the slip systems then follows as

$$\dot{F}_{ik}^{p} \left(F_{kj}^{p}\right)^{-1} = \sum_{\beta=1}^{N} \dot{\gamma}^{(\kappa)} s_i^{(\kappa)} m_j^{(\kappa)}, \tag{3.9}$$

where $\dot{\gamma}^{(\kappa)}$ is the shear rate on slip system (κ).

Table 3.1: The six slip systems in the UD composites as specified by $(s_i^{(\kappa)}, m_i^{(\kappa)})$. The unit vectors are denoted as (a, b, c) where a, b, c are components in the X_1, X_2 and X_3 −directions, respectively.

Slip direction		Slip plane normal	
$s^{(1)}$	$(1,0,0)$	$m^{(1)}$	$(0,1,0)$
$s^{(2)}$	$(1,0,0)$	$m^{(2)}$	$(0,0,1)$
$s^{(3)}$	$(0,1,0)$	$m^{(3)}$	$(0,0,1)$
$s^{(4)}$	$(0,0,1)$	$m^{(4)}$	$(0,1,0)$
$s^{(5)}$	$(0,1/\sqrt{2},1/\sqrt{2})$	$m^{(5)}$	$(0,-1/\sqrt{2},1/\sqrt{2})$
$s^{(6)}$	$(0,-1/\sqrt{2},1/\sqrt{2})$	$m^{(6)}$	$(0,-1/\sqrt{2},-1/\sqrt{2})$

3.4.2.2Elastic-plastic relations

The experiments of Attwood et al. (2014) suggested that the deformation of UHMWPE composites is adequately characterised by an anisotropic elastic and pressure dependent plastic relation. Here we propose elastic-plastic constitutive relations within the crystal plasticity context motivated by the experimental findings of Attwood et al. (2014).

Let σ_{ij} denote the Cauchy stress and we introduce a material stress measure Σ_{ij} for the intermediate configuration such that

$$\Sigma_{ij} = \det\left(F_{ij}^*\right)(F_{ik}^*)^{-1}\sigma_{kl}\left(F_{jl}^*\right)^{-1}. \tag{3.10}$$

This stress measure Σ_{ij} is work conjugate to an elastic Green-Lagrange strain defined as

$$E_{ij}^* = \frac{1}{2}\left(F_{ki}^* F_{kj}^* - \delta_{ij}\right), \tag{3.11}$$

where δ_{ij} is the Kronecker delta. Following Attwood et al. (2014) we specify a linear elastic constitutive relation of the form $E_{ij}^* = C_{ijkl}\Sigma_{kl}$ in terms of the compliance tensor C_{ijkl}. Further, the UD composite is assumed to be transversely isotropic with the X_1 fibre direction normal to the plane of isotropy. The elastic law is then written in the form

$$\begin{pmatrix} E_{11}^* \\ E_{22}^* \\ E_{33}^* \\ E_{23}^* \\ E_{13}^* \\ E_{12}^* \end{pmatrix} = \begin{pmatrix} \frac{1}{E_f} & -\frac{\upsilon_{12}}{E_f} & -\frac{\upsilon_{12}}{E_f} & 0 & 0 & 0 \\ -\frac{\upsilon_{12}}{E_f} & \frac{1}{E_m} & -\frac{\upsilon_{23}}{E_m} & 0 & 0 & 0 \\ -\frac{\upsilon_{12}}{E_f} & -\frac{\upsilon_{23}}{E_m} & \frac{1}{E_m} & 0 & 0 & 0 \\ 0 & 0 & 0 & \frac{1+\upsilon_{23}}{E_m} & 0 & 0 \\ 0 & 0 & 0 & 0 & \frac{1}{2G_{12}} & 0 \\ 0 & 0 & 0 & 0 & 0 & \frac{1}{2G_{12}} \end{pmatrix} \begin{pmatrix} \Sigma_{11} \\ \Sigma_{22} \\ \Sigma_{33} \\ \Sigma_{23} \\ \Sigma_{13} \\ \Sigma_{12} \end{pmatrix}. \quad (3.12)$$

Here E_f and E_m are the Young's moduli in the fibre and transverse directions, respectively, while υ_{12} and υ_{23} are the Poisson's ratios in the $X_1 - X_2$ and $X_2 - X_3$ planes, respectively. The shear modulus in the $X_1 - X_2$ plane is denoted as G_{12}.

It now remains to specify the constitutive relations for the plastic slip rate $\dot{\gamma}^{(\kappa)}$. Significant numerical difficulties are associated with determining the active slip systems and the amount of slip on each of these systems if a rate independent model is employed for $\dot{\gamma}^{(\kappa)}$. Thus, Asaro and Needleman (1985) proposed a simple rate dependent crystal plasticity formulation that provides a good approximation to the rate independent limit and we employ their methodology here. Plastic deformation due to shearing on each slip system (κ) depends on the resolved shear stress

$$\tau^{(\kappa)} = s_i^{*(\kappa)} \sigma_{ij} m_j^{*(\kappa)}. \quad (3.13)$$

However, unlike metallic crystals, plastic flow in the UHMWPE composites is pressure dependent as shown by the experiments of Attwood et al. (2014) and Chocron et al. (2014). Attwood et al. (2014) demonstrated that this pressure dependency is adequately characterised by a friction coefficient and based on these findings we define an effective resolved shear stress as

$$\hat{\tau}^{(\kappa)} = \begin{cases} \max\left[\left(\left|\tau^{(\kappa)}\right| - \mu p\right), 0\right] & p \geq 0 \\ \left|\tau^{(\kappa)}\right| & p < 0. \end{cases} \quad (3.14)$$

The pressure dependency is primarily associated with deformations of the matrix and hence the pressure p is a measure of the pressure absent the fibre stresses. This pressure is thus defined in terms of the material stresses in the intermediate configuration as

$$p \equiv -\frac{1}{2}(\Sigma_{22} + \Sigma_{33}), \quad (3.15)$$

and the non-negative friction parameter μ quantifies the pressure sensitivity of the composite. Then following Asaro and Needleman (1985), the shear rate $\dot{\gamma}^{(\kappa)}$ is specified by a rate dependent law as

$$\dot{\gamma}^{(\kappa)} = \dot{\gamma}_0 \left(\frac{\hat{\tau}^{(\kappa)}}{\tau_Y} \right)^{1/m} \operatorname{sgn}\left[\tau^{(\kappa)}\right], \tag{3.16}$$

where τ_Y is the shear strength with the pressure $\not{p} = 0$, $\dot{\gamma}_0$ is a reference strain rate and m is a rate sensitivity exponent such that the rate independent limit is retrieved for $m \to 0$. The deformation energy rate per unit volume of the undeformed composite can then be calculated as $\dot{\mathcal{E}} = \mathrm{S}_{ij}\dot{E}_{ij}$ where the total Green-Lagrange strain is defined as

$$E_{ij} = \frac{1}{2}\left(F_{ki}F_{kj} - \delta_{ij}\right), \tag{3.17}$$

and its work-conjugate 2nd Piola-Kirchhoff stress is given by

$$\mathrm{S}_{ij} = \det\left(F_{ij}^{*}\right)\left(F_{ik}\right)^{-1}\sigma_{kl}\left(F_{jl}\right)^{-1}. \tag{3.18}$$

This completes the specification of the crystal plasticity constitutive description of the UD composite.

3.4.2.3 Material properties

Unless otherwise specified, all calculations used parameters for the Dyneema® composites described in Section 3.2.1 These material parameters are based on measurements reported in Russell et al. (2013) and Attwood et al. (2014). The moduli of the composite in the fibre and transverse directions are $E_f = 80$ GPa and $E_m = 10$ GPa, respectively while the Poisson's ratios are $\upsilon_{12} = 0$ and $\upsilon_{23} = 0.5$ with $G_{12} = 3$ GPa. The shear strength of the composites with a polyurethane matrix is $\tau_Y = 2$ MPa while the pressure sensitivity co-efficient is $\mu = 0.05$. The rate sensitivity parameters are chosen to approximately recover the rate independent limit and thus we take $\dot{\gamma}_0 = 0.1\ \mathrm{s}^{-1}$ and $m = 0.1$. There are no reported measurements of the toughness J_{IC} of UHMWPE composites and this parameter shall be selected in order to obtain agreement with the penetration measurements reported here. In addition, parametric studies for the dependence of the predictions on J_{IC} are also reported.

3.4.3 Finite element calculation of the deformation energy

We wish to calculate the energy U_D required to open a crack of length 2ℓ to accommodate a cylinder of radius a (Fig. 3.10a) in a unit thickness slab of the composite. This is required to calculate the steady-state penetration pressure p_{ss} and, as discussed in Section 3.4.1, this

occurs with negligible deformation in the X_3 −direction. Thus, it suffices to consider the plane strain problem sketched in Fig. 3.12a with deformation of the slab constrained to occur in the $X_1 - X_2$ plane and the crack lying along the X_1 −direction. Using symmetry considerations, we only model one quadrant of the slab with the centre of the punch located at the midpoint of the crack. For the elastic-plastic composite constitutive model described above, the deformation energy U_D is in general dependent on the deformation path pursued to insert the cylindrical punch within the crack. The penetration of the conical tipped punch occurs by the opening and growth of the crack driven by the expansion of a cylindrical insert from an initial radius $r = 0$ at the conical tip to the radius $r = a$ of the punch. Here we try to emulate this deformation path as closely as possible by calculating U_D with loading specified by the expansion of a cylinder located at the centre of the crack[2].

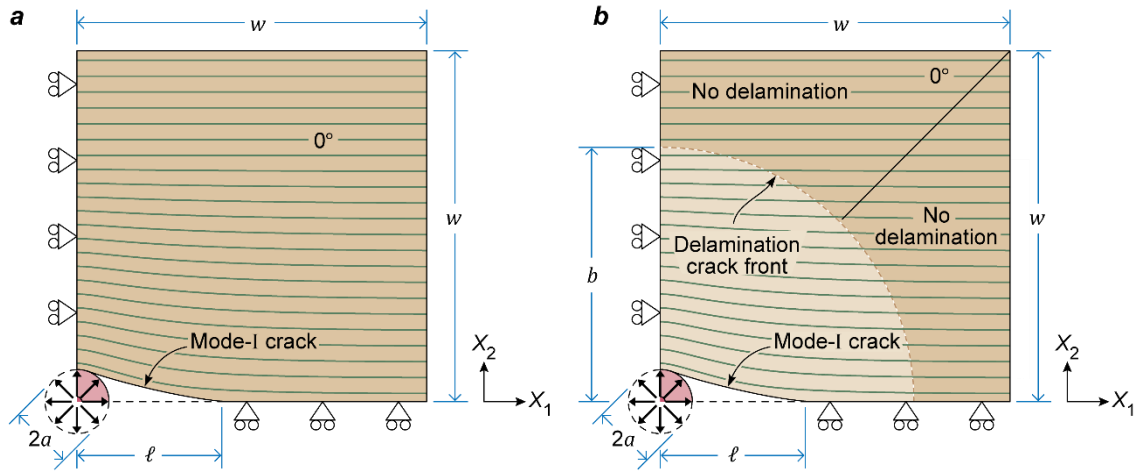

Figure 3.12: Sketches of the plane strain boundary value problems used to evaluate the energies (a) U_D for the UD composite and (b) V_D for the cross-ply composite, for inserting a circular punch of diameter $2a$ into the composites. The global co-ordinate system and the fibre direction are indicated in each case.

The one quadrant of the plane strain slab of dimensions $w \times w$ (unit thickness in the X_3 −direction) along with the imposed symmetry boundary conditions is sketched in Fig. 3.12a. A crack of length 2ℓ spans $-\ell \leq X_1 \leq \ell$ and lies along $X_2 = 0$ and all calculations reported here used a slab of size $w = 20\ell$ (numerical experimentation confirmed that increasing the size of the block had a negligible effect on U_D). Loading was specified by expanding a circular

[2] Other loading paths such as indentation of a cylindrical punch of radius a to a depth a (Shergold and Fleck, 2004) were also investigated. These numerical results suggest that U_D is relatively insensitive (to within 2%) to the loading path.

body centred at $(X_1, X_2) = (0,0)$ from an initial radius $r = 0^+$ to $r = a$ at a strain rate $\dot{r}/r = \dot{\gamma}_0$ with frictionless hard contact specified between the surface of the circular body and the crack flanks. The circular body is rigid in the sense that the loading imposed by the composite induces no deformation of the body. All calculations were performed using the commercial finite element (FE) package ABAQUS with the crystal plasticity constitutive model implemented as a user defined material model. The slab was meshed using 6-noded plane strain elements (CPE6 in the ABAQUS notation) and U_D calculated as

$$U_D = \int_0^T \int_A \dot{\mathcal{E}}\, dA\; dt'. \tag{3.19}$$

Here A denotes the undeformed domain of the composite with the circular body expanding from its initial radius $r = 0^+$ at time $t' = 0$ to $r = a$ at $t' = T$. FE calculations were performed to determine U_D in the range $2 \leq \ell/a \leq 6.2$ and the non-dimensional function $\mathcal{F}$ estimated via the definition (3.4). (FE predictions of $\mathcal{F}$ as a function of ℓ/a are included in Appendix B.) For a given toughness J_{IC}, the steady-state crack length ℓ_{ss} was then estimated via (3.6) which involved the numerical differentiation of $\mathcal{F}$ with respect to ℓ/a and the steady-state penetration pressure then follows from (3.5). We emphasize that consistent with the experiments, the expansion of the cylindrical insert for all values of ℓ/a investigated here was accommodated by elastic deformations and plastic shearing with negligible pull-in of the composite along the $X_1 = w$ plane.

3.4.4 Comparison of measurements and predictions

Predictions of the steady-state penetration pressure p_{ss} and the corresponding normalized crack lengths ℓ_{ss}/a are included in Fig. 3.6a along with the measurements for the choice of toughness $J_{IC} = 10$ kJ m^{-2}. Excellent agreement is observed for both p_{ss} and ℓ_{ss}/a over the range of punch diameters investigated here. In order to understand the dependence of these results on the choice of toughness we include in Fig. 3.6b predictions of the non-dimensional steady-state penetration pressure p_{ss}/τ_Y and crack length ℓ_{ss}/a as function of the non-dimensional toughness $J_{IC}/(\tau_Y a)$. With increasing toughness (or equivalently decreasing punch diameter a), the penetration pressure p_{ss} increases. This is a result of a reduction in the relative cracking of the composite (i.e. decreasing ℓ_{ss}/a) and the consequent increase in the deformation that the composite needs to undergo to allow the punch to penetrate. The penetration size effect is thus a result of this competition between deformation and cracking of the composite with the relevant material length scale characterised by J_{IC}/τ_Y: for the choice of

$J_{IC} = 10$ kJ m^{-2} and $\tau_Y = 2$ MPa, $J_{IC}/\tau_Y \approx 5$ mm and thus size effects are observed for millimetre size punch diameters.

One of the important outcomes of this analysis is that it provides an estimate of the mode-I inter-fibre splitting toughness J_{IC} of the UHMWPE composites. No independent measurement of this toughness has been reported in the literature to-date, presumably because the design of traditional fracture specimens such as compact tension or bend specimens has proved elusive. To understand this recall that the plane strain plastic zone size at fracture scales as

$$r_p = \frac{1}{3\pi}\left(\frac{J_{Ic}}{\tau_Y}\right)\left(\frac{E_f}{\tau_Y}\right), \tag{3.20}$$

with $r_p \approx 21$ m for the material parameter values used here with $J_{IC} = 10$ kJ m^{-2}. Thus, a traditional fracture test such as a compact tension test (which involves applying a load remote from the crack tip) will result in plastic collapse of the specimen with no associated asymptotic *J*-field around the crack tip for any reasonable test specimen size. The penetration tests reported here, which involve wedging open of the crack, circumvent this issue by directly applying an opening displacement near the crack tip. This permits the generation of a *J*-field in a relatively small specimen. In fact, such wedging/cutting tests represent the only practical option for measuring the fracture toughness of soft materials (e.g. butter) and UHMWPE composites fall into this class of materials due to their extreme anisotropy with a very low shear strength. Nevertheless, the mode-I delamination toughness of cross-ply composites with the crack propagating at the interface between the 0^o and 90^o plies has been reported (Lässig et al., 2016) to be ~400 J m^{-2}. The intra-ply mode-I toughness inferred here is about 25 times higher at $J_{IC} = 10$ kJ m^{-2}. To rationalise this, recall that Liu et al. (2014) and Attwood et al. (2015) observed that deformation of cross-ply UHMWPE composites occurs primarily by inter-laminar shear rather than shearing within the plies. This suggests that intra-ply bonding of the matrix and the fibres is stronger than bonding between orthogonal plies. We thus argue that the higher intra-ply mode-I toughness is related to the stronger matrix/fibre bonding within plies compared to bonding between plies.

3.5. Extension to the steady-state penetration of cross-ply composites

We now proceed to extend the analysis of Section 3.4 to the steady-state penetration of the cross-ply composites with a ply thickness t. The X-ray image (Fig. 3.8) shows that penetration

involves the formation of mode-I cracks along the fibre directions in the alternating $[0^o/90^o]$ plies. The high stiffness of the plies in the fibre direction relative to their transverse stiffness implies that the deformations from the opening of inter-fibre cracks within the plies cannot be accommodated via compatible deformations. Rather the crack opening deformations are accommodated by inducing shear delaminations between the plies. Deep within the specimen these delaminations do not result in opening in the X_3 −direction and thus the delaminations cannot be observed in X-ray images. Here we propose a model by assuming that delaminations form between every ply and these delamination zones are circles of radius b centred on the axis of the punch; see Fig. 3.10b.

Consider the steady-state penetration of a cross-ply composite. The advance of the punch by the ply thickness t results in the transformation of a single ply from its undeformed upstream state to its downstream state. In this downstream state the ply has a mode-I crack of length 2ℓ that accommodates the punch of radius a and is delaminated from its adjacent ply over a circular zone of radius b. A work balance then dictates

$$p_{ss}(\pi a^2)t = 2t\int_0^{\ell} J_I d\ell + 2\pi\int_0^{b} J_d b\, db + V_D, \tag{3.20}$$

where V_D is the energy required to open the crack of length 2ℓ to accommodate a cylinder of radius a in a 0^o ply of thickness t that has delaminated from its adjacent 90^o ply over a circular region of radius b (Fig. 3.10b). Recalling that at steady-state the cracks are in a state of incipient crack advance, the mode-I and delamination toughnesses are related to V_D via the usual energy release rate definitions as

$$J_I = -\frac{1}{2t}\frac{\partial V_D}{\partial \ell}, \tag{3.21}$$

and

$$J_d = -\frac{1}{2\pi b}\frac{\partial V_D}{\partial b}, \tag{3.22}$$

respectively. Here we emphasize that J_d is a combined mode-II/III delamination toughness with no mode-I delamination component. Following Section 3.4.1 we express V_D as

$$V_D \equiv \tau_Y a^2 t\mathcal{G}\left(\frac{\ell}{a}, \frac{b}{a}, \mathcal{M}\right), \tag{3.23}$$

and again, assuming that the toughnesses are independent of crack advance (i.e. no R-curve effect) it follows that

$$p_{ss} = \frac{2}{\pi}\left(\frac{J_{IC}}{a}\right)\left(\frac{\ell_{ss}}{a}\right) + \left(\frac{J_{dC}}{t}\right)\left(\frac{b}{a}\right)^2 + \frac{\tau_Y}{\pi}\mathcal{G}\left(\frac{\ell_{ss}}{a}, \frac{b_{ss}}{a}, \mathcal{M}\right). \quad (3.24)$$

Here J_{IC} and J_{dC} are the intra-ply mode-I and delamination toughnesses, respectively and the crack lengths ℓ_{ss} and b_{ss} during steady-state penetration satisfy the relations

$$J_{IC} = -\frac{\tau_Y a}{2}\frac{\partial \mathcal{G}}{\partial(\ell/a)}\Big|_{\ell=\ell_{ss}}, \quad (3.25)$$

and

$$J_{dC} = -\frac{\tau_Y a\, t}{2\pi b}\frac{\partial \mathcal{G}}{\partial(b/a)}\Big|_{b=b_{ss}}, \quad (3.26)$$

respectively.

3.5.1 Finite element calculation of the deformation energy

The energy V_D (or equivalently $\mathcal{G}$) was calculated via FE calculations in a manner analogous to that described for the UD composite in Section 3.4.3. The main difference lies in simulating the bonded and delaminated parts of the plies of the cross-ply composite. This is accomplished by modelling a single ply of thickness t with appropriately imposed boundary conditions and constraints. Here we explain these constraints by considering a single 0^o ply although a completely equivalent analysis is possible for a 90^o ply.

We wish to calculate V_D for penetration by a punch of radius a with a mode-I crack of length 2ℓ and a circular delaminated zone of radius b centred at the axis of the punch. Using symmetry considerations, we model a quarter segment of a single 0^o ply of thickness t as shown in Fig. 3.12b such that the mode-I crack lies along $X_2 = 0$ over the region $-\ell \le X_1 \le \ell$. The delaminated zone is a circle of radius $b \ge \ell$ centred at $(X_1, X_2) = (0,0)$ with deformation of the ply restricted to the $X_1 - X_2$ plane, i.e. plane strain condition is imposed. Loading is specified by the expansion of a circular body centred at $(0,0)$ as explained in Section 3.4.3 and here we focus on explaining the application of constraints to simulate the delaminated and bonded portions of the ply.

In the delaminated region $\sqrt{X_1^2 + X_2^2} < b$, there is no deformation constraint imposed by the adjacent 90^o ply and hence no further constraints are specified on the material point displacement (u_1, u_2) in this region. In the bonded region, $\sqrt{X_1^2 + X_2^2} \ge b$, the adjacent 90^o plies impose constraints on the deformation of the 0^o ply. To understand these constraints,

recall that the 90^o and 0^o plies are identical except rotated 90^o with respect to each other about the X_3-axis. Thus, in the bonded zone $\sqrt{X_1^2+X_2^2} \geq b$, the displacements in the region (X_1, X_2) with $X_1 \leq X_2$ are related to the displacements in the region (X_1, X_2) with $X_1 > X_2$ as

$$u_1(X_1, X_2) = u_2(X_2, X_1),$$
$$u_2(X_1, X_2) = u_1(X_2, X_1). \qquad (3.27)$$

The energy V_D (or equivalently the non-dimensional function $\mathcal{G}$) was evaluated via FE calculations using the material properties detailed in Section 3.4.2 and the constraints on deformation described above. Calculations were performed for crack lengths ranging $2 \leq \ell/a \leq 5.4$ and $12 \leq b/a \leq 29$. (FE predictions of $\mathcal{G}(\ell/a, b/a, \mathcal{M})$ are included in Appendix B.) The steady-state crack length ℓ_{ss} and b_{ss} then follow from Eqs. (3.25) and (3.26) with appropriate choices of the toughnesses J_{IC} and J_{dC}.

3.5.2 Comparison of measurements and predictions

Predictions of the steady-state pressure p_{ss} and associated normalized mode-I crack lengths ℓ_{ss}/a are included in Fig. 3.9a as a function of the punch diameter $2a$ for the cross-ply composite with ply thickness $t = 60$ μm. The mode-I intra-ply toughness is taken to be equal to that estimated from the UD penetration measurements and predictions (i.e. $J_{IC} = 10$ kJ m^{-2}) while the delamination toughness was set to $J_{dC} = 25$ J m^{-2} so as to obtain the high level of agreement between predictions and measurements seen in Fig. 3.9a. The high penetration pressure p_{ss} of the cross-ply composites relative to the UD composites (the predictions of p_{ss} for the UD composites from Fig. 3.6a are included in Fig. 3.9a) is due to a combination of the constrained deformation of the plies in the non-delaminated region and the additional dissipation resulting from the delamination of the plies around the penetrator. Moreover, over the range of punch diameters investigated in the experimental study, the size effect on the steady-state penetration pressure is relatively small. However, the predictions in Fig. 3.9a indicate that similar to the UD composites, p_{ss} rises sharply for $2a < 1$ mm. The corresponding predictions for cross-ply composites penetrated by a punch of diameter $2a = 2$ mm are included in Fig. 3.9b as a function of the ply thickness t: the good agreement with the measurements confirms the fidelity of the model and that the J_{IC} and J_{dC} values inferred here give good predictions over a range of composite types (UD and cross-ply), punch diameters and ply thicknesses of the cross-ply composites.

Measurements of the size b_{ss} of the delamination zone are not available as discussed above. Thus, while comparisons between observations and predictions of b_{ss} are not possible it is instructive to discuss predictions of the size of delamination zone. Predictions of b_{ss}/a as well as ℓ_{ss}/a are included in Fig. 3.13 as a function of the normalized delamination toughness $J_{dC}/(\tau_Y t)$ for selected values of the normalized mode-I toughness $J_{IC}/(\tau_Y a)$. These results are restricted to a toughness ratio $J_{IC}/J_{dC} = 400$ corresponding to $J_{IC} = 10\ \mathrm{kJ\ m^{-2}}$ and $J_{dC} = 25\ \mathrm{J\ m^{-2}}$. While both b_{ss}/a and ℓ_{ss}/a decrease with increasing J_{dC} (or equivalently decreasing ply thickness t), there are three crucial differences: (i) the delamination zone as parameterised by b_{ss}/a extends out much further than the mode-I cracks, i.e. $b_{ss}/a \gg \ell_{ss}/a$; (ii) the size of the delaminated zone b_{ss}/a depends strongly on $J_{dC}/(\tau_Y t)$ while the mode-I crack lengths display only a mild dependence on $J_{dC}/(\tau_Y t)$ and (iii) ℓ_{ss}/a is sensitive to the punch diameter as parameterised by $J_{IC}/(\tau_Y a)$ while this parameter has no influence on b_{ss}/a (at-least to within the numerical accuracy of the calculations). Thus, we argue that the delamination zone sizes are mainly set by the delamination toughness and the ply thickness.

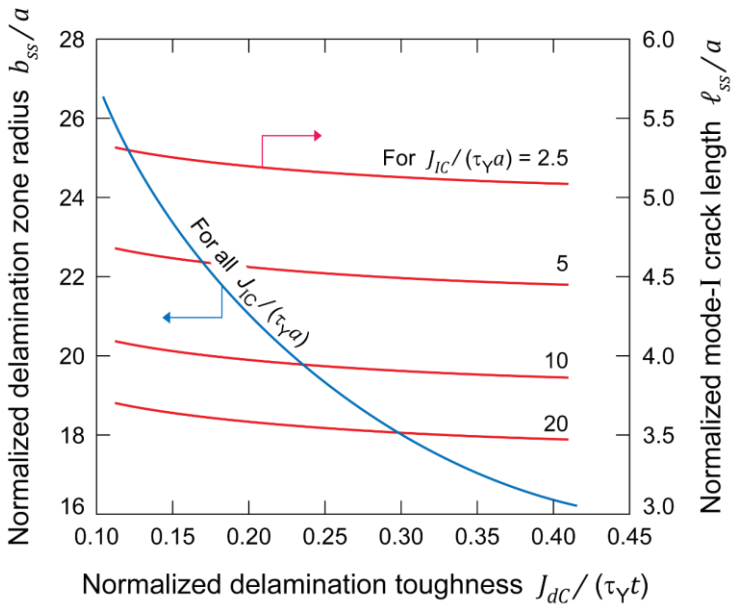

Figure 3.13: Predictions of the normalized delamination zone size b_{ss}/a and the corresponding normalized mode-I crack lengths ℓ_{ss}/a as a function of the normalized delamination toughness $J_{dC}/(\tau_Y t)$ for cross-ply composites with a toughness ratio $J_{IC}/J_{dC} = 400$. Results are shown for selected values of the mode-I toughness $J_{IC}/(\tau_Y a)$.

The relatively large delamination zone size of $b_{ss}/a \approx 21$ for the $t = 60$ μm cross-ply composite implies that specimens of size $L > 42$ mm are required to ensure that the delamination zone does not extend to the edge of a specimen penetrated centrally by a $2a = 2$ mm punch. In fact, penetration experiments conducted on $L = 40$ mm specimens of the $t = 60$ μm cross-ply composite displayed delaminations extending to the edge of the specimen. This indirectly confirmed both the existence of the delamination zones as well as the quantitative fidelity of the predictions.

Similar to the measurement of J_{IC} inferred from the penetration experiments on the UD composites, the penetration measurements on the cross-ply composites provide an estimate of the combined mode-II/III delamination toughness J_{dC} . Again, there are no reported independent measurements of this toughness. The predictions and measurements reported here suggest that $J_{dC} \ll J_{IC}$. Thus, consistent with the observations made in Section 3.4.4 on the inferior inter-laminar properties of UHMWPE composites we surmise that this difference in the magnitude of the two toughnesses is related to the poor inter-ply bonding between the matrix and the fibres.

3.6. Design maps for penetration resistance

The high penetration resistance of the cross-ply UHMWPE composites makes them attractive candidates for use in systems such as vests for protection against knife attacks. With the development of new higher strength UHMWPE fibres as well as methods to manufacture composites with specified ply thicknesses, an immediate question that arises is: what is the optimal combination of material and microstructural parameters to maximise penetration resistance? With this in mind we will develop a design methodology to optimise the ply thickness for a given tensile strength Σ_f of the ply in the fibre direction and a delamination toughness J_{dC}. Unless otherwise specified, the design maps in this section use all materials properties fixed at the values specified in Section 3.4.2 with $J_{IC} = 10$ kJ m^{-2} and $J_{dC} = 25$ J m^{-2}.

3.6.1 Deformation mechanism map

The UHMWPE composite conforms around the penetrating cylindrical punch as seen in Fig. 3.5. This deformation is expected to generate the highest fibre stresses at or near the contact between the composite and the cylindrical surface of the punch. In all the measurements

reported here, these fibre stresses were insufficient to result in fibre fracture although it is conceivable that penetration of a composite with a sufficiently high toughness and/or sufficiently thin plies will result in fibre fracture. Here we develop a deformation mechanism map to investigate the range of material parameters where fibre fracture will be triggered by penetration.

In order to evaluate the occurrence of fibre fracture we define a co-rotational stress in the intermediate configuration

$$\hat{\sigma}_{ij} = R^*_{mi}\sigma_{mn}R^*_{nj}, \tag{3.28}$$

such that $\hat{\sigma}_{11}$ gives the true ply stress in the local fibre direction in a 0^o ply with R^*_{ij} denoting the proper orthogonal rotation tensor of F^*_{ij}. FE predictions of $\hat{\sigma}_{11}$ in a 0^o ply within a cross-ply composite penetrated by a $2a = 2$ mm punch are shown in Fig. 3.14a for normalized mode-I crack length $\ell/a = 4$ and delamination zone radius $b/a = 21$. Recall that the model is only applicable for steady-state penetration and hence these predictions only pertain to 0^o plies which are both far downstream from the punch tip and deep within the specimen. The maximum value of $\hat{\sigma}_{11}$, labelled $\hat{\sigma}_{\max}$ occurs at the contact between the composite and the punch along the $X_1 = 0$ symmetry line. Fibre fracture will occur if $\hat{\sigma}_{\max}$ exceeds a material critical value Σ_f ($\Sigma_f = \mathscr{v}_f\sigma_f$ for UHMWPE composites comprising a volume fraction $\mathscr{v}_f$ of fibres with a tensile strength σ_f) and thus we proceed to investigate the dependence of $\hat{\sigma}_{\max}$ on ply thickness t and delamination toughness J_{dC} for a cross-ply composite penetrated by a punch of diameter $2a = 2$ mm. All other material parameters are held fixed at their reference values.

A deformation mechanism map with axes J_{dC} and ply thickness t is plotted in Fig. 3.14b for penetration by the $2a = 2$ mm punch. Contours of both the maximum ply stress $\hat{\sigma}_{\max}$ and the steady-state penetration pressure p_{ss} are included in the map. These contours are approximately parallel to each other indicating that both these metrics have a similar dependence on (J_{dC}, t) with $\hat{\sigma}_{\max}$ as well as p_{ss} increasing with increasing J_{dC} and decreasing t. The contour $\hat{\sigma}_{\max} = \Sigma_f$ demarcates the regime where fibre fracture is expected to occur for the choice $\Sigma_f = 2.5$ GPa (This choice is based on the strength $\sigma_f = 3$ GPa of the SK76 UHMWPE fibres and a fibre volume fraction $\mathscr{v}_f = 83\%$ in the composites investigated here.) The composites investigated here have a delamination toughness $J_{dC} = 25$ J m^{-2} and the map

in Fig. 3.14b suggests that fibre fracture in this class of composites will occur for composites with ply thickness $t < 25$ μm.

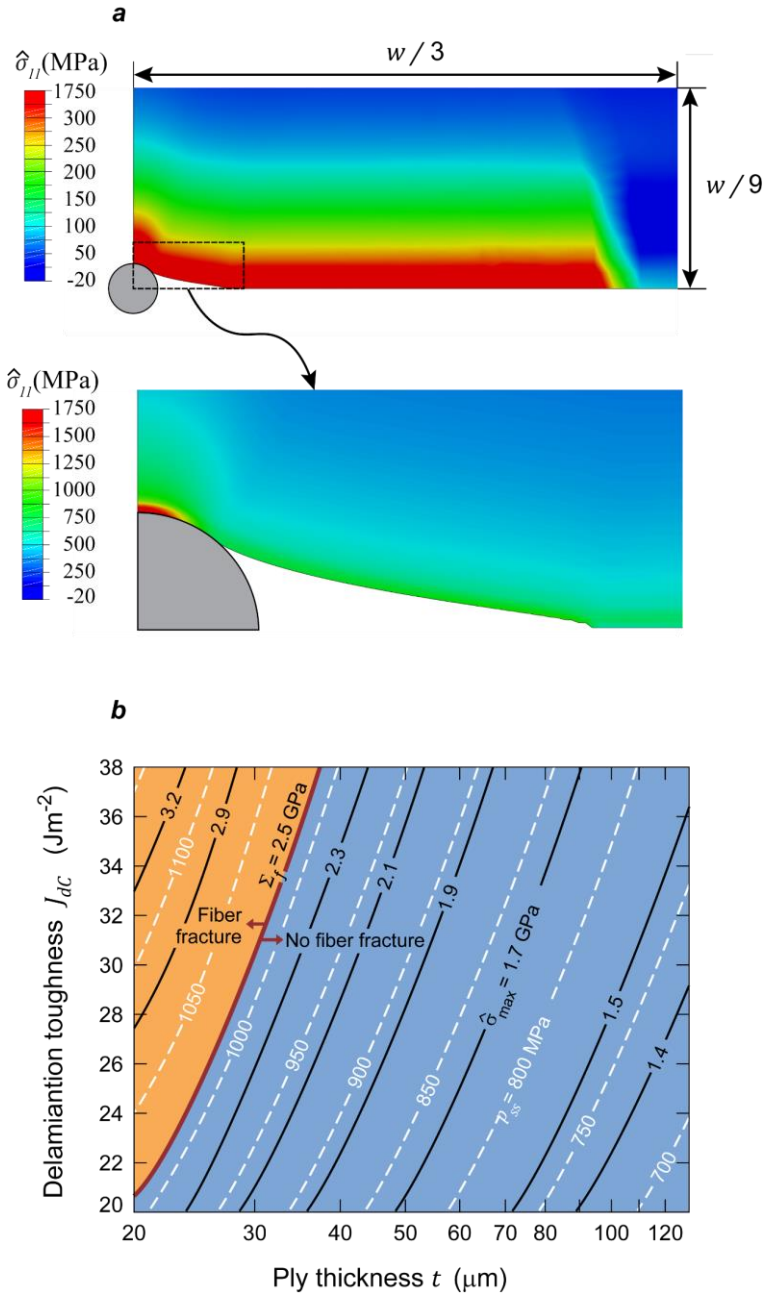

Figure 3.14: (a) FE predictions of the corotational stress $\hat{\sigma}_{11}$ around the punch in a 0^o ply within a $t = 60$ μm cross-ply composite penetrated by a $2a = 2$ mm punch, with normalized mode-I crack length $\ell/a = 4$ and delamination zone radius $b/a = 21$. Note that the magnified view is shown with a different stress scale to illustrate the highly stressed regions more clearly. (b) A deformation mechanism map with axes of the delamination toughness J_{dC} and ply thickness t for penetration by a $2a = 2$ mm punch. Contours of the steady-state penetration pressure p_{ss}

and maximum ply stress $\hat{\sigma}_{\max}$ are included with the boundary demarcating the region of fibre fracture marked for the choice of ply strength $\Sigma_f = 2.5$ GPa.

3.6.2 Optimal designs

Suppose we wish to maximise the penetration resistance of the cross-ply composite as parameterised by p_{ss} for a given ply strength Σ_f. Since the contours of p_{ss} and $\hat{\sigma}_{\max}$ are parallel to each other in Fig. 3.14b, this optimisation reduces to determining the combination of J_{dC} and t such that the maximum ply stress $\hat{\sigma}_{\max} = \Sigma_f$. Moreover, this also implies that the maximum penetration pressure $p_{ss}^{\max}$ is a unique function of Σ_f. This dependence of $p_{ss}^{\max}$ on Σ_f for the $2a = 2$ mm diameter punch is plotted in Fig. 3.15a from the design map in Fig. 3.14b, i.e. material properties listed in Section 3.4.2 with $J_{IC} = 10$ kJ m^{-2}. We observe that increasing the ply strength from $\Sigma_f = 2.5$ GPa to 3 GPa increases $p_{ss}^{\max}$ from approximately 1 GPa to about 1.1 GPa.

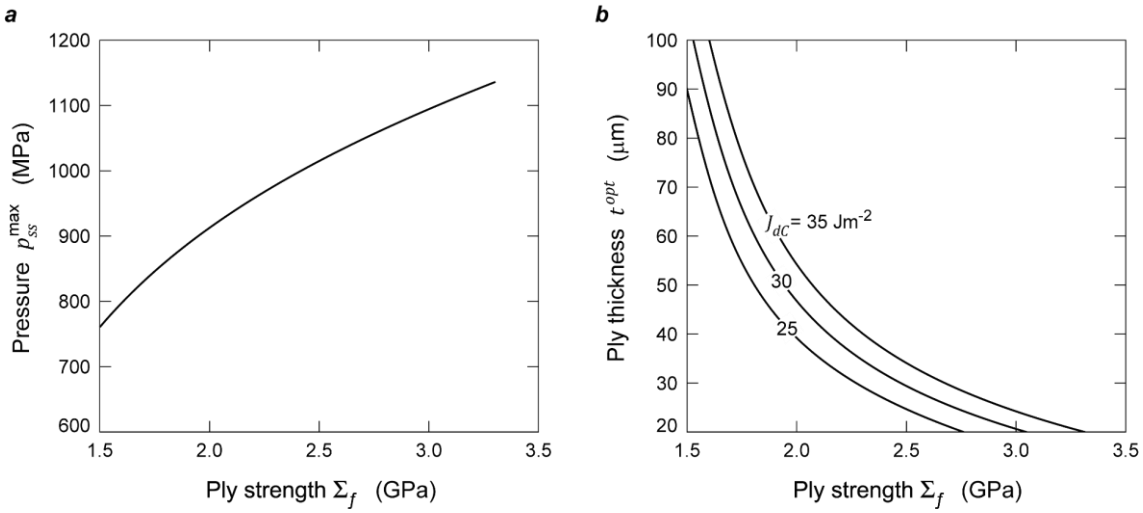

Figure 3.15: Predictions of (a) the maximum steady-state penetration pressure $p_{ss}^{\max}$ as a function of the ply strength Σ_f of the cross-ply composite. (b) The corresponding optimal ply thickness t^{opt} as a function of Σ_f for three selected values of the delamination toughness J_{dC}.

Optimal designs as characterised by $(J_{dC}^{\text{opt}}, t^{\text{opt}})$ for a given Σ_f (all have an equal penetration resistance $p_{ss}^{\max}$ as plotted in Fig. 3.15a) can immediately be obtained by following the contour $\hat{\sigma}_{\max} = \Sigma_f$ in Fig. 3.14a. However, it is typically difficult to alter the ply strength (set mainly by the fibre strength) and the delamination toughness but relatively straightforward to change the ply thickness. Thus, a practical optimisation problem is to determine the optimal ply thickness t^{opt} for a given combination of J_{dC} and Σ_f. Predictions of this optimal ply thickness

are included in Fig. 3.15b as a function of Σ_f for three selected values of J_{dC}. With increasing ply strength Σ_f, the ply thickness t^{opt} required to attain the maximum penetration pressure $p_{ss}^{\max}$ decreases. In fact, for $\Sigma_f > 2.75$ GPa, the optimum ply thickness drops below 20 μm for $J_{dC} = 25\ \mathrm{J\ m^{-2}}$. Composites with such thin plies are not only challenging to manufacture but also impractical as they have a thickness on the order of the fibre diameter. The results in Fig. 3.15 suggest that t^{opt} increases with increasing J_{dC} for a given ply strength, i.e. increasing the delamination toughness will permit optimal performance for composites with practical ply thicknesses.

3.7. Concluding remarks

The penetration of fibre reinforced ultra-high molecular weight polyethylene (UHMWPE) composites by sharp-tipped cylindrical punches was investigated through both measurements and associated micro-mechanical models. The main findings can be summarised as follows:

(i) Penetration occurred with no fibre fracture and the penetration pressure increased with decreasing punch diameter for both UD and cross-ply composites. This size dependence was observed for punch diameters on the millimetre length scale and thus much stronger than the micron scale size dependence of the indentation/penetration response of metals.

(ii) The penetration pressure also increased with decreasing ply thickness of the cross-ply composites. In both UD and cross-ply composites, the sharp-tipped punch penetrates by the formation of mode-I cracks along the fibre directions, followed by the wedging open of the crack by the advancing punch. These mode-I cracks form in orthogonal directions in the adjacent 0^{o} and 90^{o} plies in the cross-ply composite. The ensuing incompatible deformation between these adjacent plies induces delamination around the penetrator.

(iii) A combination of the dissipation due to delamination and the constraint imposed on the deformation of each ply by the alternating 0^{o} and 90^{o} plies results in a penetration pressure on the order of 1 GPa for the cross-ply composites and is approximately 3 times larger than that of a UD composite penetrated by a punch of equal diameter.

(iv) The micro-mechanical models suggest that the competition between the deformation of the composite by wedging open of the crack and the extension of

the mode-I and delamination cracks results in the observed size dependence of the penetration pressure.

(v) The models were used to develop design maps for the penetration resistance of cross-ply composites and to infer composite designs that maximise the penetration resistance for a given fibre strength. In particular, these calculations suggest that increasing the delamination toughness permits optimum performance for composites with thicker plies that are more practical from a manufacturing perspective.

The penetration measurements and models reported here have provided estimates of the mode-I inter-fibre splitting toughness J_{IC} and the combined mode-II/III delamination toughness J_{dC}. The large mode-I fracture toughness and the low shear strength of UHMWPE composites make the design of traditional fracture toughness tests (e.g. compact tension) very difficult and hence to-date no measurements of these toughnesses have been reported in the literature. In fact, our estimates suggest that $J_{IC}/J_{dC} = 400$ with $J_{IC} = 10\ \mathrm{kJ\ m^{-2}}$. Most UHMWPE composite penetration experiments involve blunt penetrators with continued penetration occurring via fibre fracture. The high penetration resistance in such circumstances is attributed to the high fibre strength. By contrast, penetration by sharp-tipped punches involves no fibre fracture, and we argue that the high penetration resistance in such cases is to a large extent due to the high toughnesses of these composites.

Appendix A: Protocol for estimating crack lengths in the cross-ply specimens from plain radiographs

X-ray tomographic imaging of the cross-ply composites was not feasible as the X-ray opaque Tungsten-Carbide/Cobalt punches cast a large shadow. We thus inferred the sizes of the mode-I intra-ply cracks in the cross-ply composites from plain radiographs. In plain radiographs, geometric magnification results from the fact that the detector is further away from the source than the object and here we explain the methodology used to determine the *radiographic magnification factor* and hence extract the mode-I crack lengths from plain radiographs such as the image shown in Fig. 3.8.

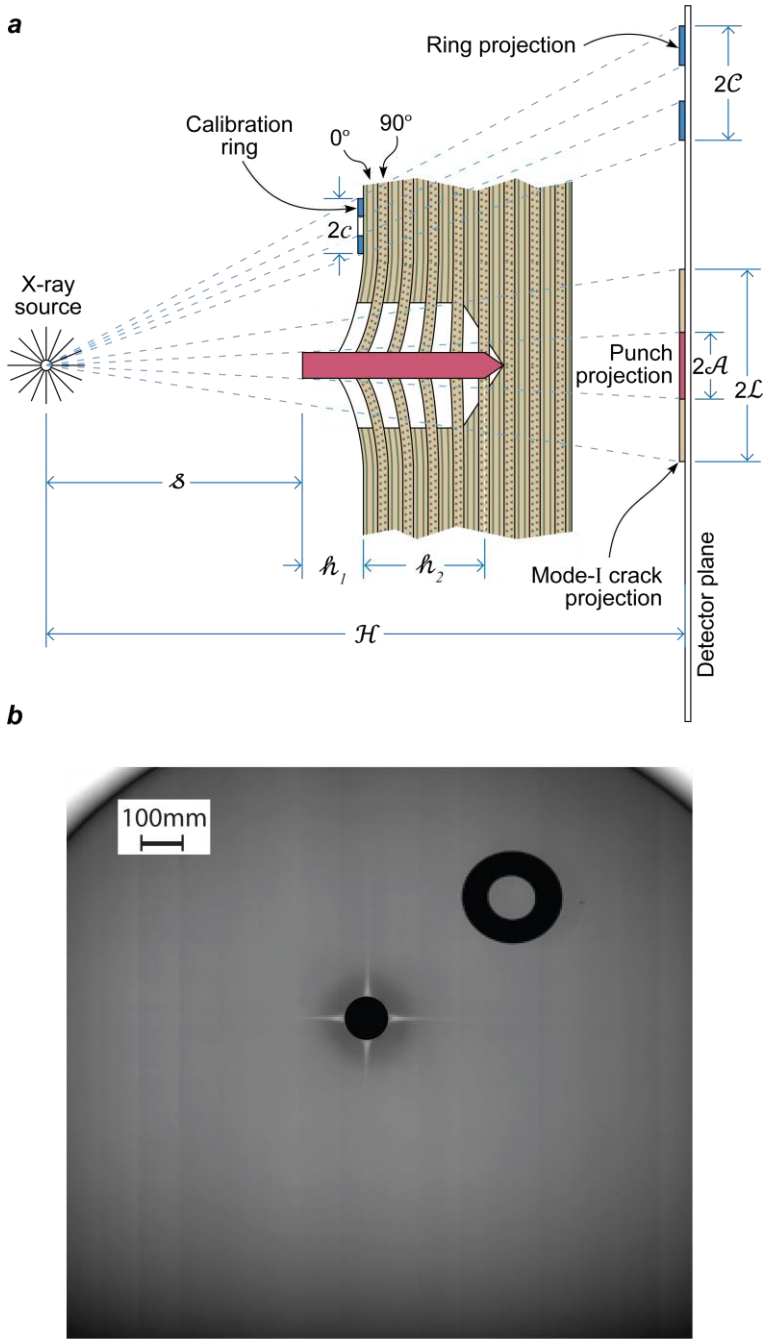

Figure 3.16: (a) Sketch of the setup for a plain radiograph of the penetrated cross-ply composite with the symbols of key dimensions marked. (b) A plane radiograph of a $t = 60$ μm cross-ply composite penetrated by a $2a = 3$ mm punch. The radiograph shows the entire image on the detector plane including the image of the calibration ring. The scale bar shows the size of the image on the detector plane.

Consider the imaging of a cross-ply composite along with the penetrator. The plain radiograph is taken by shining an X-ray source in the X_3 −direction with the rear of the punch nearest to the source as sketched in Fig. 3.16. For the sake of simplicity, we neglect the finite size of the

focal spot of the X-ray source and hence ignore the resulting unsharpness in the image on the detector plane. The radiographic magnification is clearly seen in Fig. 3.16a where the cylindrical punch of diameter $2a$ appears as a shadow of diameter $2\mathcal{A}$ on the detector plane. We wish to determine the mode-I crack size $2\ell_{ss}$ from its image of length $2\mathcal{L}$ on the detector plane. With $\mathcal{H}$ denoting the source-detector distance, geometric constructions based on similar triangles give

$$\frac{\ell_{ss}}{\mathcal{L}} = \frac{\mathcal{s} + \mathcal{h}_1 + \mathcal{h}_2}{\mathcal{H}} \quad \text{and} \quad \frac{a}{\mathcal{A}} = \frac{\mathcal{s}}{\mathcal{H}}, \tag{A1}$$

where $\mathcal{s}$ is the distance from the source to the rear of the punch while $\mathcal{h}_1$ and $\mathcal{h}_2$ are the punch lengths outside and within the specimen such that $\mathcal{h}_1 + \mathcal{h}_2$ is the total length of the punch (here we assume that the mode-I crack attains its steady-state length at $\xi \approx a\tan\alpha$). Combining the equations in (A1) we can eliminate $\mathcal{H}$ to obtain

$$\frac{\ell_{ss}}{a} = \left(\frac{\mathcal{s} + \mathcal{h}_1 + \mathcal{h}_2}{a}\right)\left(\frac{\mathcal{L}}{\mathcal{A}}\right). \tag{A2}$$

A direct measure of $\mathcal{s}$ is not available from the X-ray setup and hence an indirect method was used to estimate $\mathcal{s}$. An X-ray opaque circular calibration ring of external diameter $2c$ was placed on the flat surface of the specimen. This ring casts a shadow of diameter $2\mathcal{C}$ (Fig. 3.16b) on the detector plane and again using similar triangles we have

$$\frac{c}{\mathcal{C}} = \frac{\mathcal{s} + \mathcal{h}_1}{\mathcal{H}}, \tag{A3}$$

which upon combining with (A1) gives

$$\mathcal{s} = \left(\frac{a/\mathcal{A}}{c/\mathcal{C} - a/\mathcal{A}}\right)\mathcal{h}_1 . \tag{A4}$$

Equations (A2) and (A4) then directly provides an estimate of ℓ_{ss}: measurements of $\mathcal{L}$, $\mathcal{A}$ and $\mathcal{C}$ are directly available from measurements from the radiograph while a and c are known sizes of the punch and the ring. The length $\mathcal{h}_1$ is measured from the penetrated specimen while $\mathcal{h}_2$ is the residual length of the punch.

Appendix B: FE predictions of the non-dimensional deformation energies $\mathcal{F}$ and $\mathcal{G}$

FE predictions of the non-dimensional deformation energy $\mathcal{F}$ for the UD composite is included in Fig. 3.17a for non-dimensional mode-I crack lengths in the range $2 \le \ell/a \le 5$ while the

equivalent energy $\mathcal{G}$ for the cross-ply is plotted in Fig. 3.17b as a function of ℓ/a for selected values of the non-dimensional delamination zone size b/a. Given the toughnesses, J_{IC} and J_{dC}, the derivatives of these functions directly provide the steady-state crack sizes and the penetration pressures as detailed in Section 3.4.

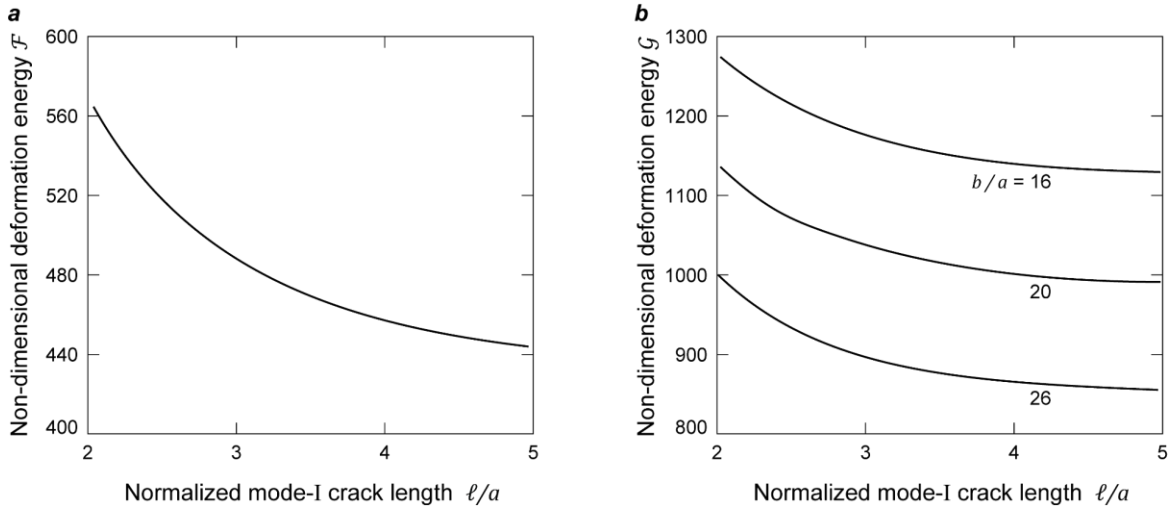

Figure 3.17: FE predictions of the non-dimensional deformation energies (a) $\mathcal{F}$ for the UD composite and (b) $\mathcal{G}$ for the cross-ply composite as a function of the normalized mode-I crack length ℓ/a. In (b) $\mathcal{G}$ is shown for selected values of the normalized delamination zone radius b/a.

References

Asaro, R.J., 1983. Micromechanics of Crystals and Polycrystals. Adv. Appl. Mech. 23, 1–115. https://doi.org/10.1016/S0065-2156(08)70242-4

Asaro, R.J., Needleman, A., 1985. Overview no. 42 Texture development and strain hardening in rate dependent polycrystals. Acta Metall. 33, 923–953. https://doi.org/10.1016/0001-6160(85)90188-9

Attwood, J.P., Khaderi, S.N., Karthikeyan, K., Fleck, N.A., O′Masta, M.R., Wadley, H.N.G., Deshpande, V.S., 2014. The out-of-plane compressive response of Dyneema composites. J. Mech. Phys. Solids 70, 200–226. https://doi.org/10.1016/j.jmps.2014.05.017

Attwood, J.P., Russell, B.P., Wadley, H.N.G., Deshpande, V.S., 2016. Mechanisms of the penetration of ultra-high molecular weight polyethylene composite beams. Int. J. Impact Eng. 93, 153–165. https://doi.org/10.1016/j.ijimpeng.2016.02.010

Bao, L., Sato, S., Morikawa, H., Soma, S., 2016. Improving stab-resistant textile materials with a non-woven fabric structure. J. Text. Eng. 62, 37–42. https://doi.org/10.4188/jte.62.37

Bilisik, K., 2017. Two-dimensional (2D) fabrics and three-dimensional (3D) preforms for ballistic and stabbing protection: A review. Text. Res. J. 87, 2275–2304. https://doi.org/10.1177/0040517516669075

Cheeseman, B.A., Bogetti, T.A., 2003. Ballistic impact into fabric and compliant composite laminates. Compos. Struct. 61, 161–173. https://doi.org/10.1016/S0263-8223(03)00029-1

Chocron, S., Nicholls, A.E., Brill, A., Malka, A., Namir, T., Havazelet, D., Werff, H. van der, Heisserer, U., Walker, J.D., 2014. Modeling unidirectional composites by bundling fibers into strips with experimental determination of shear and compression properties at high pressures. Compos. Sci. Technol. 101, 32–40. https://doi.org/10.1016/j.compscitech.2014.06.016

Cunniff, P.M., 1999. Dimensionless Parameters for Optimization of Textile-Based Body Armor Systems. 18th Int. Symp. Ballist. 1303–1310.

Decker, M.J., Halbach, C.J., Nam, C.H., Wagner, N.J., Wetzel, E.D., 2007. Stab resistance of shear thickening fluid (STF)-treated fabrics. Compos. Sci. Technol. 67, 565–578. https://doi.org/10.1016/j.compscitech.2006.08.007

Grujicic, M., Arakere, G., He, T., Bell, W.C., Cheeseman, B.A., Yen, C.F., Scott, B., 2008. A ballistic material model for cross-plied unidirectional ultra-high molecular-weight polyethylene fiber-reinforced armor-grade composites. Mater. Sci. Eng. A 498, 231–241. https://doi.org/10.1016/j.msea.2008.07.056

Heisserer, U., Werff, H. Van Der, Hendrix, J., 2013. Ballistic depth of penetration studies in Dyneema® composites, in: Proceedings of the 27th International Symposium on Ballistics, Vol. 2. Freiburg, Germany. pp. 1936–1943.

Hill, R., Rice, J.R., 1972. Constitutive analysis of elastic-plastic crystals at arbitrary strain. J. Mech. Phys. Solids 20, 401–413. https://doi.org/10.1016/0022-5096(72)90017-8

Iannucci, L., Pope, D., 2011. High velocity impact and armour design. Express Polym. Lett. 5, 262–272. https://doi.org/10.3144/expresspolymlett.2011.26

Karthikeyan, K., Russell, B.P., 2014. Polyethylene ballistic laminates: Failure mechanics and interface effect. Mater. Des. 63, 115–125. https://doi.org/10.1016/j.matdes.2014.05.069

Kim, S.J., Goo, N.S., 1997. Dynamic contact responses of laminated composite plates according to the impactor's shapes. Comput. Struct. 65, 83–90. https://doi.org/10.1016/S0045-7949(95)00408-4

Lässig, T.R., Nolte, F., Riedel, W., May, M., 2016. An assessment of experimental techniques for measuring the mode I fracture toughness of uhmw-pe composites. Proc. 17th Eur. Conf. Compos. Mater. ECCM17 26–30.

Li, W., Xiong, D., Zhao, X., Sun, L., Liu, J., 2016. Dynamic stab resistance of ultra-high molecular weight polyethylene fabric impregnated with shear thickening fluid. Mater. Des. 102, 162–167. https://doi.org/10.1016/j.matdes.2016.04.006

Liu, G., Thouless, M.D., Deshpande, V.S., Fleck, N.A., 2014. Collapse of a composite beam made from ultra high molecular-weight polyethylene fibres. J. Mech. Phys. Solids 63, 320–335. https://doi.org/10.1016/j.jmps.2013.08.021

Mayo, J.B., Wetzel, E.D., Hosur, M. V., Jeelani, S., 2009. Stab and puncture characterization of thermoplastic-impregnated aramid fabrics. Int. J. Impact Eng. 36, 1095–1105. https://doi.org/10.1016/j.ijimpeng.2009.03.006

Mines, R.A.W., Roach, A.M., Jones, N., 1999. High velocity perforation behaviour of polymer composite laminates. Int. J. Impact Eng. 22, 561–588. https://doi.org/10.1016/S0734-743X(99)00019-6

Mitrevski, T., Marshall, I.H., Thomson, R., Jones, R., Whittingham, B., 2005. The effect of impactor shape on the impact response of composite laminates. Compos. Struct. 67, 139–148. https://doi.org/10.1016/j.compstruct.2004.09.007

Nazarian, O., Zok, F.W., 2014. Constitutive model for the shear response of Dyneema® fiber composites. Compos. Part A Appl. Sci. Manuf. 66, 73–81. https://doi.org/10.1016/j.compositesa.2014.06.012

O'Masta, M.R., Crayton, D.H., Deshpande, V.S., Wadley, H.N.G., 2016. Indentation of polyethylene laminates by a flat-bottomed cylindrical punch. Compos. Part A Appl. Sci. Manuf. 80, 138–147. https://doi.org/10.1016/j.compositesa.2015.10.015

O'Masta, M.R., Crayton, D.H., Deshpande, V.S., Wadley, H.N.G., 2015. Mechanisms of penetration in polyethylene reinforced cross-ply laminates. Int. J. Impact Eng. 86, 249–264. https://doi.org/10.1016/j.ijimpeng.2015.08.012

Onyechi, P.C., Edelugo, S.O., Chukwumuanya, E.O., Obuka, S.P.N., 2014. Ballistic Penetration Response Of Glass Fibre Reinforced Polyester (Gfrp) Composites : Body Amour 3, 226–237.

Phoenix, S.L., Porwal, P.K., 2003. A new membrane model for the ballistic impact response and V50 performance of multi-ply fibrous systems. Int. J. Solids Struct. 40, 6723–6765. https://doi.org/10.1016/S0020-7683(03)00329-9

Russell, B.P., Karthikeyan, K., Deshpande, V.S., Fleck, N.A., 2013. The high strain rate response of Ultra High Molecular-weight Polyethylene: From fibre to laminate. Int. J. Impact Eng. 60, 1–9. https://doi.org/10.1016/j.ijimpeng.2013.03.010

Shergold, O. a., Fleck, N. a., 2004. Mechanisms of deep penetration of soft solids, with application to the injection and wounding of skin. Proc. R. Soc. A Math. Phys. Eng. Sci. 460, 3037–3058. https://doi.org/10.1098/rspa.2004.1315

Smith, P., Lemstra, P.J., 1980. Ultra-high strength polyethylene filaments by solution spinning/drawing. J Mater Sci 15, 505–514. https://doi.org/10.1016/0032-3861(80)90205-0

Smith, P., Lemstra, P.J., Kalb, B., Pennings, A.J., 1979. Ultrahigh-strength polyethylene filaments by solution spinning and hot drawing. Polym. Bull. 1, 733–736. https://doi.org/10.1007/BF00256272

van Dingenen, J., 1989. High performance dyneema fibres in composites. Mater. Des. 10, 101–104. https://doi.org/10.1016/S0261-3069(89)80021-4

Wen, H.M., 2000. Predicting the penetration and perforation of FRP laminates struck normally by projectiles with different nose shapes. Compos. Struct. 49, 321–329. https://doi.org/10.1016/S0263-8223(00)00064-7

Chapter four

4. Failure mechanism maps for ultra-high molecular weight polyethylene fibre composite beams impacted by blunt projectiles

Synopsis

The mechanisms via which failure is initiated in $[0^o/90^o]_n$ ultra-high molecular weight polyethylene fibre reinforced composite beams during impact by cylindrical projectiles is investigated using detailed finite element (FE) calculations. Each ply of the beam is discretely modelled using a pressure-dependent crystal plasticity framework that accurately accounts for both the large shear strains and fibre rotations that occur within each ply. These FE calculations were used to construct failure mechanism maps for a range of impact velocities, beam shear strengths and ply tensile strengths. Two dominant failure mechanisms emerged from the study: (i) Failure of plies immediately under the projectile via an indirect tension mechanism in which compressive stress imposed normal to the plies by the projectile induces tensile in-plane ply strains due to the anisotropic expansion of the alternating $0^o/90^o$ plies. This is referred to as mode I failure. (ii) Failure due to tensile fibre straining at the rear of the impacted beam resulting from beam bending and accompanying ply stretching. This is referred to as mode II failure. The mode I indirect tension failure mode is dominant at low shear strengths while mode II failure dominates at high shear strengths. The simulations show that low beam shear strengths help relax tensile stresses within the beams, and this typically results in the need for a higher impact velocity to initiate failure. The calculations thus give a mechanistic understanding of experimental observations that have shown low shear strength composites possess a superior ballistic performance. The failure mechanism maps also reveal the existence of an optimal shear strength at which the velocity required to initiate failure is maximised: this optimal shear strength increases with increasing tensile fibre (or ply) strength thereby suggesting a route to developing composites that might serve as “structural armours”.

4.1. Introduction

Fibre composites with high tensile strengths but low shear strengths are known to have excellent ballistic protection properties. The most common examples of such ballistic fibre composites include aramid (e.g., Kevlar) fibre composites (Grujicic et al., 2012) and fibre composites comprising ultra-high molecular weight polyethylene (UHMWPE) fibres (Van Der Werff and Heisserer, 2016). In the majority of these applications, the fibre composites are used in a $[0^o/90^o]_n$ layup. For example, the HB26 Dyneema® composite manufactured by DSM (DSM, Het Overloon 1, 6411 TE Heerlen, The Netherlands) comprises approximately 80 % by volume SK76 UHMWPE fibres in a polyurethane matrix with a ply thickness of about 60 μm. UHMWPE fibre composites are typically constructed from plies of aligned polyethylene fibres (with fibre Young's moduli and tensile strengths approaching 130 GPa and 2.5 GPa respectively) in a polymer matrix with a low elastic modulus. In the fibre direction, the ply modulus/strength is very high and approaches the Voigt bound. However, the Young's modulus and tensile strengths in the directions orthogonal to the fibres as well as the shear moduli and strengths are very low (on the order of a few MPa). This extreme anisotropy in both moduli and strengths has dramatic effects on the mechanism of penetration by blunt projectiles. In ceramic materials, such an impact induces cone and radial cracking with severe comminution directly beneath the projectile (Gooch, 2011) and similar modes are also observed in carbon fibre reinforced polymer (CFRP) composites (Cantwell and Morton, 1991). On the other hand, in ductile metals such an impact results in either adiabatic shear facilitated plug formation or failure by petalling (Corbett et al., 1996). However, none of these failure modes have been observed in UHMWPE composites, and this is thought to be related to their highly anisotropic nature. This study seeks to develop a mechanistic understanding of failure modes in UHMWPE composites and to relate them to the underlying material properties.

As discussed in Chapter 2, while the Cunniff (1999) theory for ranking the ballistic performance of fibres has proven invaluable, using Eq. (2.2) to gauge the ballistic performance of fibre composite structures has proved less successful. The primary limitation of the Cunniff (1999) analysis is that it suggests that the V_{50} is independent of the composite shear strength. This is however contrary to a range of experimental findings; see for example Karthikeyan et al. (2013) for UHMWPE composites and carbon fibre reinforced polymer (CFRP) composites, De Ruijter et al. (2010) for aramid composites and Yu et al. (2017) for CFRPs. For example Karthikeyan et al. (2013) showed that the V_{50} of a clamped circular CFRP plate impacted by a

8.3 g spherical steel projectile reduces from $300\ \mathrm{ms}^{-1}$ to $100\ \mathrm{ms}^{-1}$ as the composite shear strength τ_Y is increased from 0.1 MPa to 100 MPa even though the fibre type, composite layup and fibre volume fraction all remained unchanged. The reason that the Cunniff (1999) model fails to predict this large sensitivity of the ballistic performance to shear strength can be traced back to the fact that it implicitly assumes failure in the stretching mode, as analysed by Phoenix and Porwal (2003). This means that the composite structures either survive impact with no failure or for impact at a velocity $\geq V_{50}$ allow the projectile to pass through with failure of all plies. Again, this is contrary to observations. For example, Karthikeyan et al. (2013) reported a progressive failure of clamped circular HB26 Dyneema® plates impacted by spherical steel projectiles. X-ray micrographs after impact shown in Fig. 4.1 clearly illustrate: (i) plies that make initial contact with the projectile fail first and (ii) an increasing number of plies fail with increasing impact velocity V. At $V \approx 450\ \mathrm{ms}^{-1}$ the projectile fully penetrates through the plate due to the failure of all plies. This failure mode is not consistent with that assumed in the Phoenix and Porwal (2003) analysis used to rationalise the Cunniff (1999) scaling.

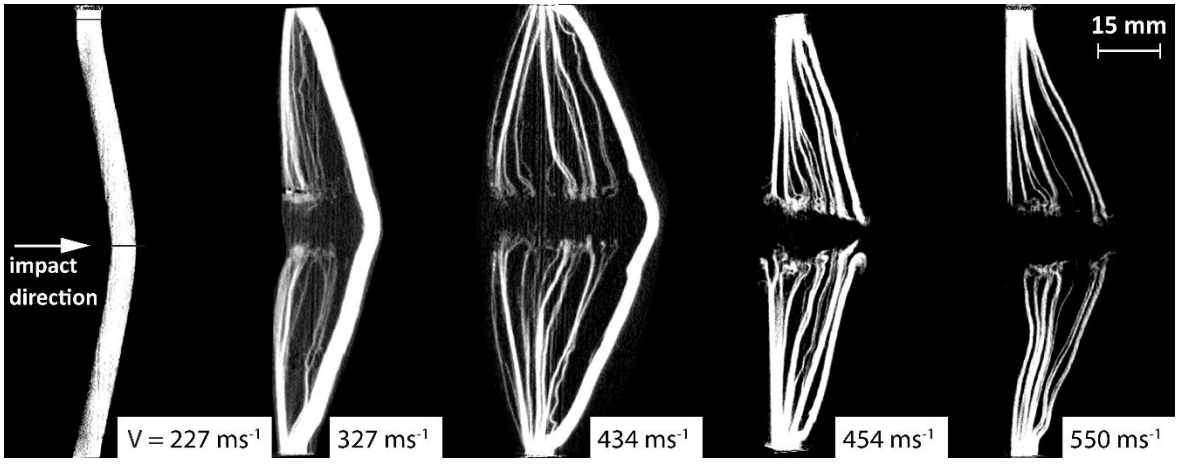

Figure 4. 1: Summary of the penetration mode of HB26 Dyneema® composite plates impacted normally and centrally by an 8.3 g spherical steel projectile at a velocity V. The figure adapted from Karthikeyan et al. (2013) shows X-ray cross-sectional images of the composite plates that reveal an increasing number of failed plies with increasing impact velocity (the direction of impact is marked).

The above observations have been confirmed via a number of independent studies. Greenhalgh et al. (2013) have reported a detailed fractography study and qualitatively argued that the matrix shear strength influences energy absorption and failure mechanisms in UHMWPE composites while O'Masta et al. (2015) also confirmed that failure in UHMWPE composites occurs in a progressive manner immediately under the projectile. A consequence of this dependence of the

ballistic performance on shear strength is that the Cunniff (1999) analysis significantly overpredicts the ballistic resistance of UHMWPE composites as shown by Karthikeyan and Russell (2014). Shear plugging has been proposed as a possible mode that intervenes and sets the ballistic resistance of CFRP composite plates (Cantwell and Morton, 1991, 1989; Lee et al., 2001). However, a recent experimental study by Attwood et al. (2016) demonstrated that failure, at-least in UHMWPE composites, is not set by shear plugging but via an indirect tension mechanism proposed in Attwood et al. (2014) and Woodward et al. (1994). Such a failure mechanism was also suggested in the experimental study of O'Masta et al. (2016). A number of continuum models (Grujicic et al., 2008; Hazzard et al., 2018; Iannucci and Pope, 2011) within a finite element setting have been employed in attempts to capture these observations. However, while these models have had some success in making quantitative predictions (Nguyen, 2015), they have been unable to reproduce the progressive failure processes and do not give a mechanistic understanding of the failure processes and more importantly, they are not capable of explaining the dependency of the ballistic performance on the shear strength.

In the current study, we investigate the interplay between ply shear strength, tensile ply (or fibre) strength, beam thickness and impact velocity on the mechanisms by which failure is initiated in $[0^o/90^o]_n$ composite beams impacted by blunt projectiles. While the focus of the study is on UHMWPE composites, the numerical model and the results are general and can be readily interpreted for most other fibre composites such as those made from aramid and even carbon fibres. The outline of the paper is as follows. We begin by describing the problem under consideration and then detail the crystal plasticity based constitutive model used to model each individual ply in the composite beam. Numerical results for the impact of beams are then presented and used to develop failure mechanism maps that illustrate the failure mechanisms as a function of shear strength, impact velocity and fibre/ply tensile strength.

4.2. Analysis of the dynamic impact of an UHMWPE composite beam

The aim of this study is to develop a mechanistic understanding of the *initiation* of failure in a UHMWPE structure impacted by a blunt projectile. In keeping with this overall aim, we design a significantly simplified model problem where these mechanisms are most readily revealed. The failure mechanisms we are primarily interested in are those immediately under the projectile and its vicinity; see for example Fig. 4.1. This is because the impacted structures are

typically very large compared to the projectiles. Thus, to eliminate issues associated with the precise boundary conditions we consider an infinite free-standing UHMWPE structure impacted by a blunt projectile as shown in Fig. 4.2. Moreover, in order to reduce computational cost, we shall consider a plane strain two-dimensional (2D) situation of an infinite free-standing beam in the $X_1 - X_2$ plane as shown in Fig. 4.2 impacted by a cylindrical projectile whose axis is parallel to the X_3-direction. This 2D simplified model will be shown to display deformation and failure mechanisms that are qualitatively similar to observations such as those discussed in Karthikeyan et al. (2013) for a circular plate impacted centrally by a spherical projectile.

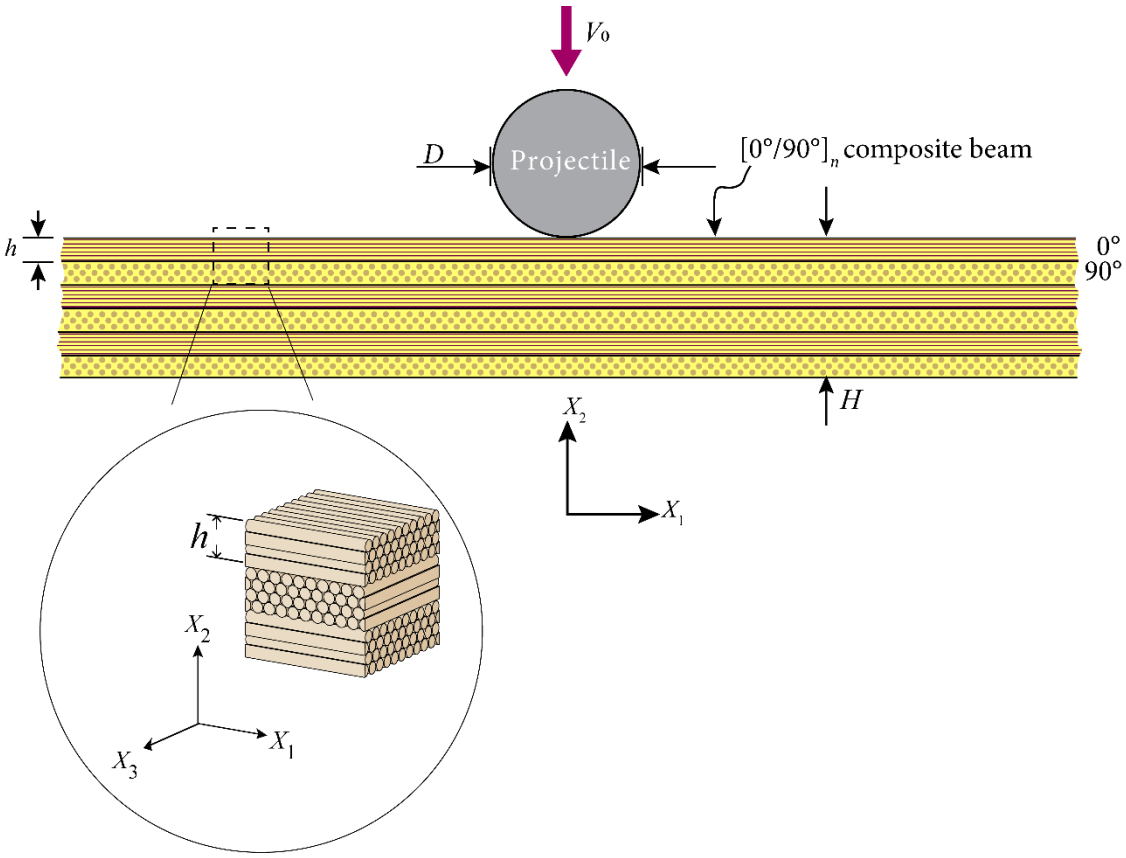

Figure 4.2: Sketch of the problem under consideration in this study. An infinitely long $[0^o/90^o]_n$ composite beam with ply thickness h is impacted normally and centrally by a cylindrical projectile of diameter D at time $t = 0$ with a constant velocity V_0. The global co-ordinate system $X_1 - X_2$ is indicated with the sketch showing an $n = 3$ beam. The inset shows a zoom-in of the $0^o/90^o$ ply architecture.

4.2.1 Description of the boundary value problem of the impact of a beam

Consider an infinitely long free-standing beam comprising an alternating [0°/90°] stacking sequence of $2n$ unidirectional (UD) layers of the UHMWPE composite, i.e., alternating layers (plies) with fibres aligned along the X_1 longitudinal beam direction (labelled as 0° fibres) and

layers with fibres in the X_3-direction (labelled as 90° fibres); see inset in Fig. 4.2. Each UD layer is of thickness h so that the $[0^o/90^o]_n$ composite beam has an overall thickness $H = 2nh$. Deformation of the beam of density ρ is constrained to occur in the $X_1 - X_2$ plane with plane strain conditions assumed. This initially straight beam is assumed to be normally impacted by a rigid cylindrical projectile of diameter D at time $t = 0$, and we set the location of the origin of the co-ordinate system such that impact occurs at $X_1 = 0$. The initiation of failure (if it occurs) typically takes place very early in the impact process when there has been a negligible deceleration of the projectile. Thus, in order to reduce the number of variables under consideration, we restrict our analysis to the case of a projectile constrained to move with a constant velocity V_0 in the negative X_2-direction. This approximation only is valid throughout the history of the beam deformation when $m_p/(\rho H^2) \to \infty$ where m_p is the mass of the projectile per unit depth in the X_3-direction, i.e., an infinitely heavy projectile that is not decelerated by the beam.

4.2.2 Constitutive model

In order to solve this impact problem, we need to specify an appropriate constitutive model for the UHMWPE composite. Existing models broadly fall into one of two categories: type (i) homogenised models (Grujicic et al., 2008; Hazzard et al., 2018; Iannucci and Pope, 2011) at the composite scale using effective properties of the $[0^o/90^o]$ composite and thus not accounting for the heterogeneity of the beam in terms of the $[0^o/90^o]$ layup; and type (ii) homogenised models for individual UD composite layers; see for example Attwood et al. (2014) and Liu et al., (2018). The choice of the model depends on the deformation and failure mechanisms we consider to be important for this impact problem and the relative abilities of the models to capture these mechanisms. We thus briefly review some key observations to motivate our choice of constitutive model.

Impact of UHMWPE composite structures results in numerous deformation and failure processes including ply delamination. With failure defined as an event that permits the projectile to pass through the structure, delamination is not a failure mode because each individual ply remains intact. Thus, failure is only associated with tensile fibre fracture. With this definition in mind, failure of UHMWPE composite plates under impact loading is primarily associated with two failure modes (Fig. 4.3):

(i) Failure of plies via fibre fracture immediately under the projectile (Fig. 4.3a). This tensile failure of the plies initiates very early in the impact process (Attwood et al., 2015) when the loading is primarily the transverse compressive loading imposed by the impacting projectile. It is thus conjectured that the mechanism of failure, in this case, is the so-called indirect tension mechanism (Attwood et al., 2014) as illustrated in the inset of Fig. 4.3a. Here the anisotropic in-plane deformation of the alternating $[0^o/90^o]$ plies results in the build-up of fibre tension from the imposition of an out-of-plane (transverse) compressive stress.

(ii) Tensile failure of the plies due to bending/stretching of the plate or beam. The precise mechanism of this mode is unclear as no direct experimental observations of this mode have been reported to-date. Such direct tensile failure can occur in two ways: (a) uniform tensile stretching of the beam in a string-like model as assumed by Phoenix and Porwal (2003) and shown in Fig. 4.3b and (b) bending of the beam resulting in tensile straining on the rear face (Fig. 4.3c).

Constitutive models of type (i) are computationally more efficient as we do not need to discretely model each ply in the structure. However, as these models do not account for the anisotropy between alternating plies, they cannot capture the indirect tension mechanism. Hence, here we consider models of type (ii) with the plies modelled discretely. A number of such models have been proposed for UHMWPE composites including (a) the rebar approach proposed by Nazarian and Zok (2014) where fibres are included as so-called rebars within an isotropic matrix and (b) the continuum anisotropic elastic-plastic model of Attwood et al. (2014). While the rebar model of Nazarian and Zok (2014) accounts for the rotation of the fibres in the finite deformation setting, it is difficult to include the pressure sensitivity of yield that is known to be significant for UHMWPE composites (Chocron et al., 2014; Attwood et al., 2014). On the other hand, the anisotropic plasticity model of Attwood et al. (2014) includes the pressure sensitivity but does not accurately account for the evolution of fibre orientations in a finite deformation. A crystal plasticity approach recently proposed by Liu et al. (2018) and detailed in Chapter 3 addresses these deficiencies by including both the effects of fibre rotation and the pressure sensitivity of the UHMWPE composite and here we adopt this constitutive model.

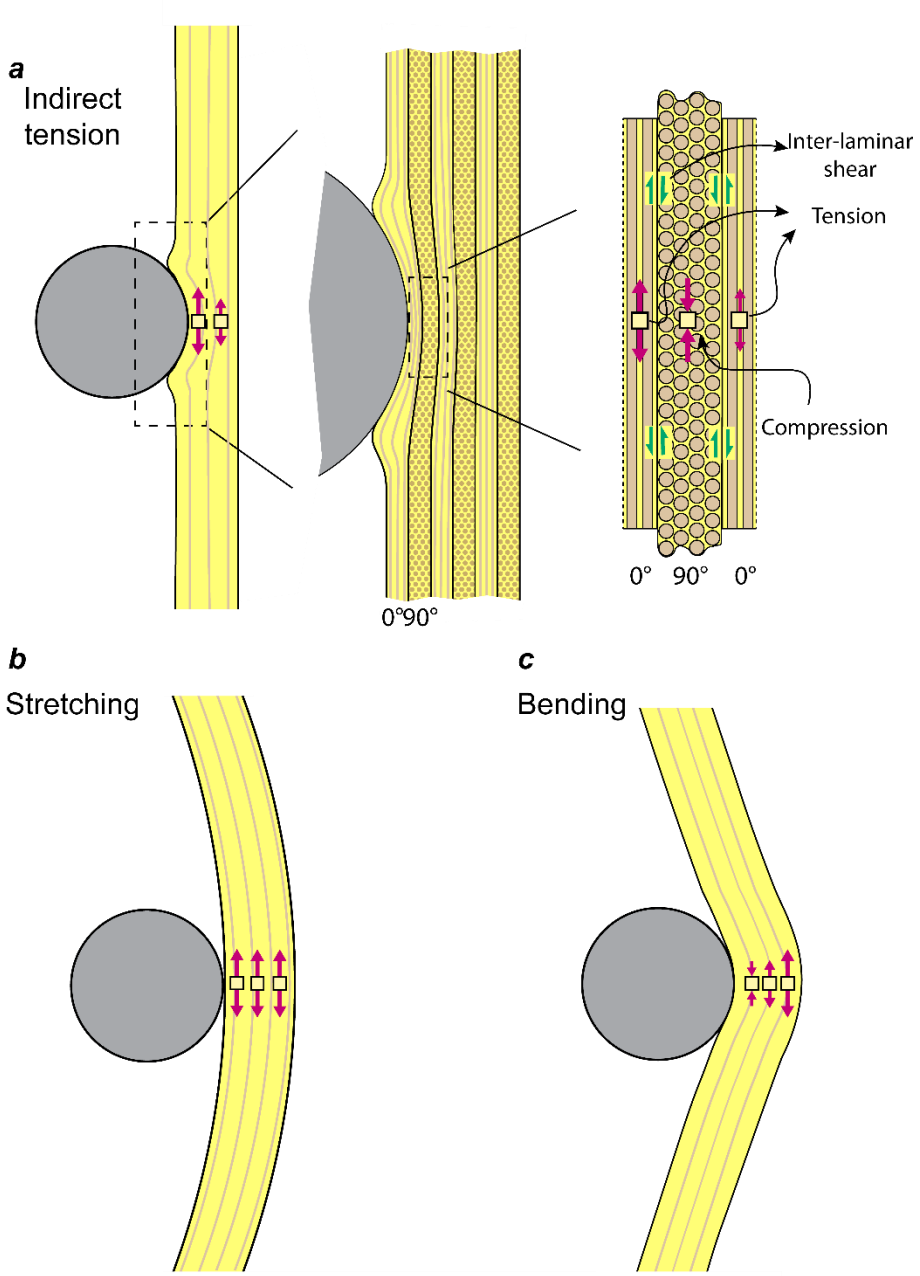

Figure 4.3: Sketches of tensile fibre failure modes in UHMWPE composites under impact loading. (a) Indirect tension failure in the ply immediately under the projectile. The insets show the development of the indirect tension under compressive loading due to the anisotropic expansion of the alternating 0^o and 90^o plies. (b) Tensile fracture by uniform stretching of the beam in a string-like mode. (c) Tensile fracture at the rear of the beam due to bending deformation of the beam.

4.2.2.1 Crystal plasticity model for a single UD ply

The crystal plasticity model developed in Chapter 3 is used to model each single UD ply. Unless otherwise specified, the parameters used in the current study are based on the experimental measurements reported in Russell et al. (2013) and Attwood et al. (2014) for UHMWPE composites comprising SK76 fibres in a polyurethane matrix manufactured by DSM under the

tradename Dyneema® (commercial designation from the manufacturer is HB26). The elastic moduli in the fibre and transverse directions are $E_f = 80$ GPa and $E_m = 10$ GPa, respectively while the corresponding Poisson's ratios are $\upsilon_{12} = 0$ and $\upsilon_{23} = 0.5$ with $G_{12} = 3$ GPa. The shear yield strength of the HB26 composite is $\tau_Y = 2$ MPa and rate independent plastic behaviour is approximated by taking $\dot{\gamma}_0 = 0.1\ \mathrm{s}^{-1}$ and $m = 0.1$. The measurements of Attwood et al. (2014) and Chocron et al. (2014) suggest that the friction coefficient $\mu = 0.05$ and the density of the UD plies is taken to be $\rho = 970\ \mathrm{kg\ m}^{-3}$ in the dynamic calculations reported subsequently.

4.2.3 Numerical solution of the impact problem

All simulations were performed for a $[0^o/90^o]_n$ HB26 UHMWPE composite beam with ply thickness $h = 60$ μm. A scoping study indicated that the initial failure mode is insensitive to the order to the plies, i.e., results are independent of whether the impacted surface of the beam is a 0^o or 90^o ply. Thus, all results presented here are for a beam where the impacted surface is a 0^o ply. In the majority of the simulations, the beam comprised $n = 10$ cross-plies (i.e., 20 UD plies in total) with some selected results also presented for the $n = 20$ case. The projectile was assumed to be rigid with diameter $D = 4$ mm so that $D/h \approx 67$ in all simulations. The simulations focussed on tensile fracture of the plies in which delamination was neglected, i.e., perfect bonding was assumed between the alternating 0^o and 90^o plies.

All simulations were performed in a dynamic setting using the explicit version of commercial Finite Element (FE) Package ABAQUS (Dassault Systems Simulia Corp, 2013). Finite strain calculations were performed with the beams discretised using 3D eight-noded linear elements with reduced integration (C3D8R in the ABAQUS notation). Plane strain conditions were imposed by using one element in the X_3-direction with the displacement u_3 of all nodes in the X_3- direction set to zero. Elements of size $e \approx h/10$ were employed so as to accurately capture both wave propagation as well as bending of individual plies so that the $n = 20$ beams comprised ~500k elements. The explicit FE calculations required a time step of 0.01 ns and typically calculations were run over a timespan of 100 μs. Loading was imposed by the rigid projectile of diameter D normally impacting the beam with a velocity V_0 as shown in Fig. 4.2. Impact occurred at $X_1 = 0$ at time $t = 0$ with the velocity V_0 remaining constant throughout the loading history. Contact between the rigid projectile and the beam was modelled as a hard-frictionless contact within ABAQUS.

The constitutive model developed in Chapter 3 was implemented using the VUMAT functionality provided in ABAQUS. In addition to the deformation mechanisms, a key output of the analysis is the prediction of the initiation of failure. As discussed above, we define material failure as an event which permits the projectile to begin to penetrate through the beam, and this requires fibre fracture. Fibre fracture in the context of the constitutive model is set by the Cauchy stress in a UD ply in the fibre direction. Here the co-rotational stress tensor $\hat{\sigma}_{ij}$ defined in Chapter 3 (3.28) is used, and $\hat{\sigma}_{11}$ is the ply stress in the local fibre direction for a 0^o ply (and similarly $\hat{\sigma}_{33}$ is the stress in the local fibre direction in a 90^o ply), Fracture is expected to be initiated when these stresses attain a critical value Σ_f. Experiments (Russell et al., 2013) on HB26 composites suggest that $\Sigma_f = 2.5$ GPa and this will be used as a reference value in the numerical results presented below. The sensitivity of beam failure to this ply strength will also be investigated.

4.3. Impact response of UHMWPE composite beams

We now proceed to discuss numerical predictions of the deformation and failure initiation mechanisms in these UHMWPE composite beams and illustrate the role of the shear strength τ_Y. We do this by keeping all material properties, other than τ_Y, fixed (at their reference value given in Section 4.2.2.1) and present results for the case of low and high shear strength beams with $\tau_Y = 2$ MPa and 20 MPa, respectively. Unless otherwise stated, we also focus in this section on the case of an impact velocity $V_0 = 200$ ms^{-1}. Predictions of the deformation of the UHMWPE composite beams at selected times t and yield strength $\tau_Y = 2$ MPa and 20 MPa are shown in Figs. 4.4 and 4.5, respectively with $t = 0$ corresponding to the instant of impact of the projectile. Contours of the ply stress $\hat{\sigma}_{11}$ are included in the figures along with lines marked perpendicular to the longitudinal axis of the beam (in the undeformed configuration) to aid visualisation of the deformation modes.

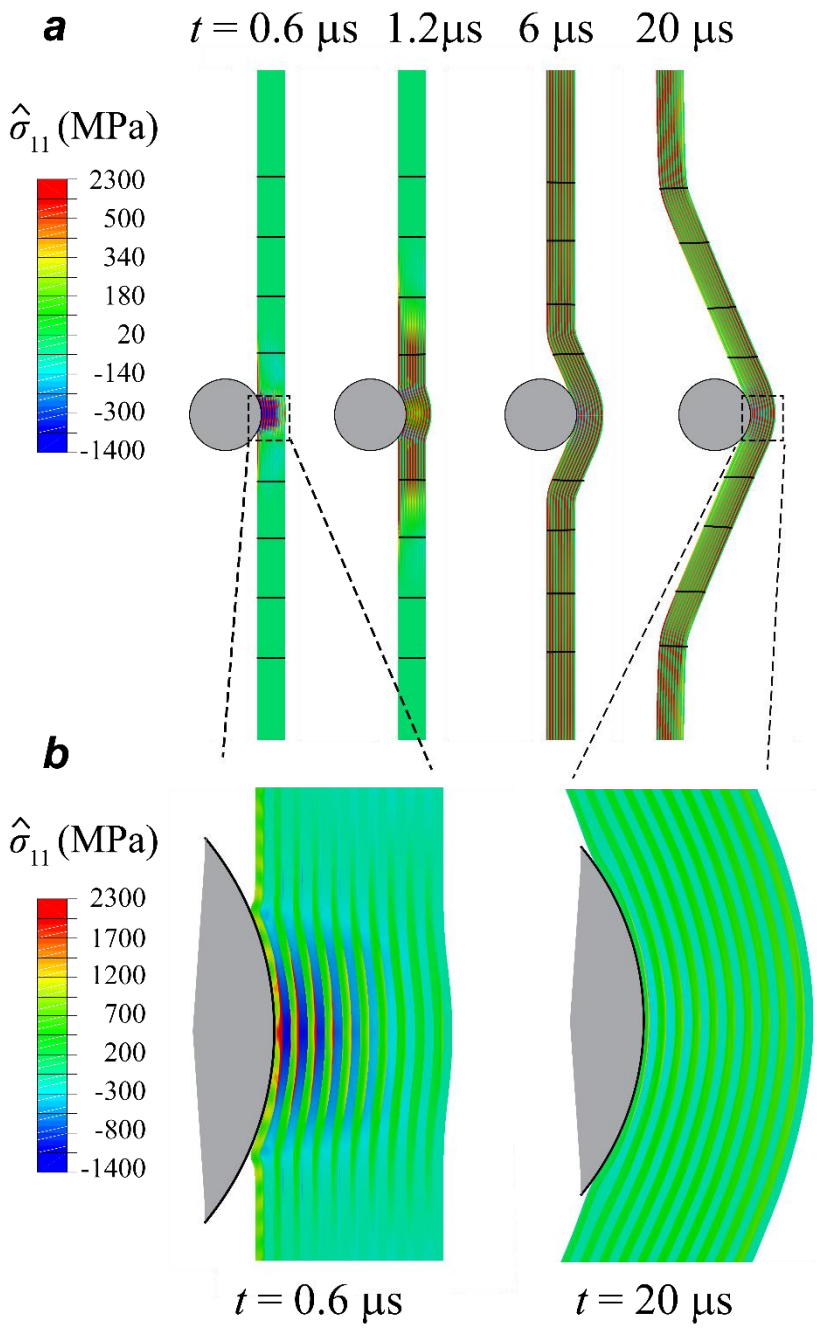

Figure 4.4: FE predictions of the deformation of a $n = 10$ beam with shear strength $\tau_Y = 2$ MPa impacted at $V_0 = 200$ ms^{-1}. (a) The overall deformation mode at four selected times t after impact with $t = 0$ corresponding to the instant of impact. (b) A zoom-in of the region immediately under the projectile at two selected times. Contours of the co-rotational stress $\hat{\sigma}_{11}$ are included to illustrate the ply stresses in the fibre direction in the 0^o plies. In (a) we include lines marked on the material perpendicular to the longitudinal axis (in the undeformed configuration) of the beam to aid visualisation of the overall deformation mode.

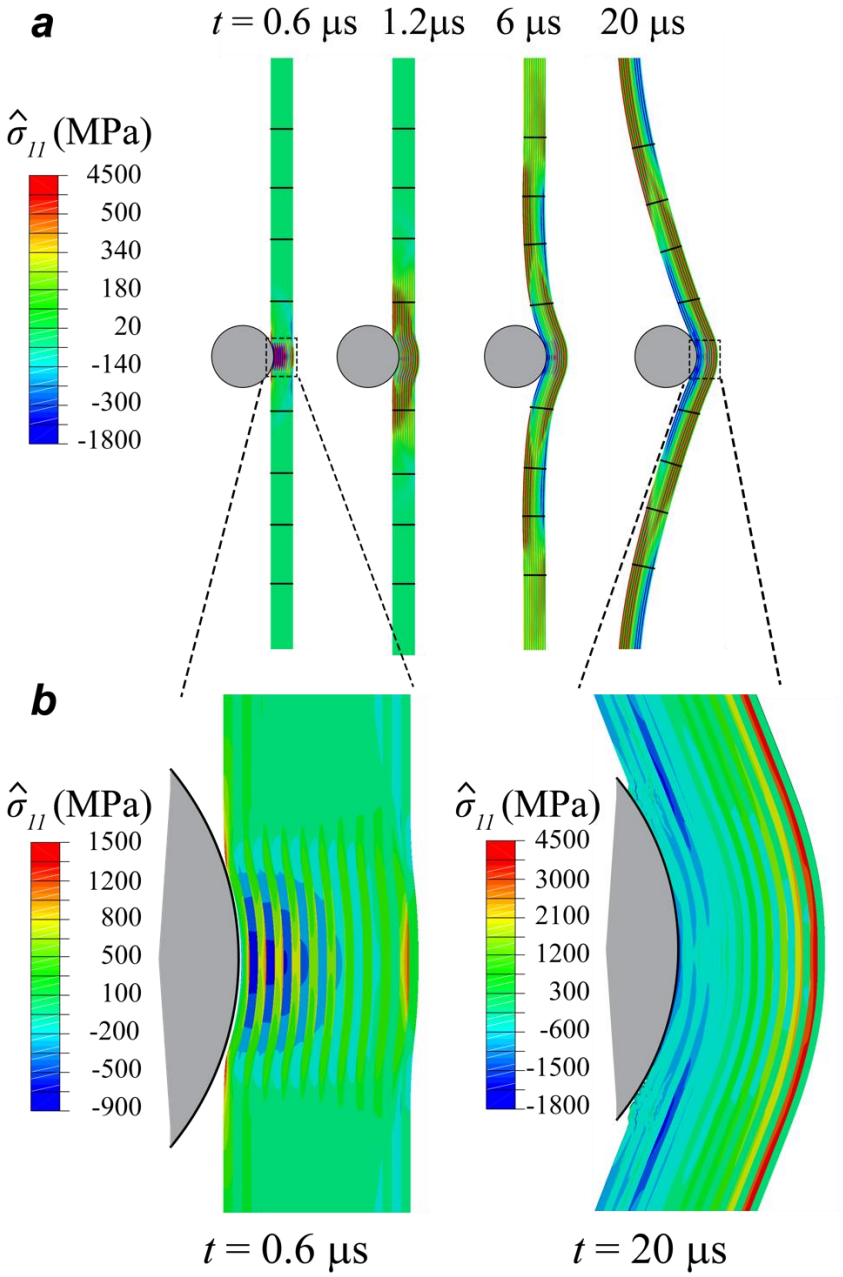

Figure 4.5: FE predictions of the deformation of a $n = 10$ beam with shear strength $\tau_Y = 20$ MPa impacted at $V_0 = 200$ ms^{-1}. (a) The overall deformation mode at four selected times t after impact with $t = 0$ corresponding to the instant of impact. (b) A zoom-in of the region immediately under the projectile at two selected times. Contours of the co-rotational stress $\hat{\sigma}_{11}$ are included to illustrate the ply stresses in the fibre direction in the 0^o plies. In (a) we include lines marked on the material perpendicular to the longitudinal axis (in the undeformed configuration) of the beam to aid visualisation of the overall deformation mode.

4.3.1 Deformation mechanisms for low shear strength beams

We first consider the overall deformation modes as seen in Fig. 4.4a and then focus on the more detailed local deformation modes immediately under the projectile (Fig. 4.4b). The overall deformation mode as seen in Fig. 4.4a comprises an approximately triangular shaped deflected profile with the distance to the apex of the triangle increasing at the imposed velocity V_0 and the base width increasing at a rate $2\dot{\xi}$ as shown schematically in Fig. 4.6. Lines perpendicular to the longitudinal axis of the beam (in the undeformed configuration) are included in Fig. 4.4a to better illustrate the transverse deflection mode. These lines were fixed to material points in order to track the movement of the beam cross-section thus reveal the transverse deflection mode. Visual inspection of Fig. 4.4a clearly shows that with continued transverse deflection, the lines do not rotate (and thus no longer remain perpendicular to the longitudinal axis), indicating that transverse deflection is primarily associated with longitudinal shearing of the beam with a negligible bending component. We thus refer to the kink that separates the deflected and non-deflected regions of the beam as a "shear hinge" and $\dot{\xi}$ as the shear hinge velocity. We also note that the lines marked on the beam cross-section translate in the X_1-direction (moving towards the location of impact). This indicates that the beam undergoes longitudinal tensile straining in addition to longitudinal shear.

To quantify these observations, deformed profiles of the beams at selected times, for two impact velocities V_0, are included in Fig. 4.7. They show that beams deform in a self-similar manner in the sense that the deflected triangular profiles grow in time such that the triangles remain self-similar isosceles triangles with a temporally constant base angle γ defined in Fig. 4.6 although Fig. 4.7 indicates that γ is dependent on the impact velocity. Note that geometrical considerations dictate that a temporally constant γ implies that the velocity $\dot{\xi}$ is also temporally invariant (since the mid-span deflection rate is constant at V_0). To quantify these observations, we first define an average Green-Lagrange strain $\bar{E}_{11}$ in the global co-ordinate system X_i as

$$\bar{E}_{11}(X_1, t) = \frac{1}{H}\int_{-H/2}^{H/2} E_{11}(X_1, X_2, t)\, dX_2, \qquad (4.1)$$

and include in Fig. 4.8a predictions of the spatial variation of $\bar{E}_{11}$ at $t = 20$ μs for $V_0 = 150\ \mathrm{ms}^{-1}$ and $350\ \mathrm{ms}^{-1}$. In general, the strains are larger for the higher impact velocity with the spatial distributions having a complex variation in the regime immediately under the impactor (i.e., $|X_1| \leq D/2$). However, the strains are approximately spatially piecewise

constant for $|X_1| > D/2$. In Fig. 4.8b we focus on this regime away from that impact site and show predictions for $V_0 = 150\ \mathrm{ms}^{-1}$ and $350\ \mathrm{ms}^{-1}$ at selected times t. These indicate that for $|X_1| > D/2$ the axial strains are well approximated by the Heaviside step function

$$\bar{E}_{11}(X_1, t) = \Xi(V_0)\mathcal{H}[C_L t - X_1]. \qquad (4.2)$$

Here $\Xi(V_0)$ is the velocity dependent strain amplitude and $\mathcal{H}[\mathrm{x}]$ is the Heaviside step function such that $\mathcal{H}[\mathrm{x}] = 0$ for $\mathrm{x} < 0$ and unity otherwise while $C_L \equiv \sqrt{E_b/\rho}$ is the longitudinal elastic wave speed in the beam with $E_b = (E_f + E_m)/2$ denoting the Voigt bound for the longitudinal elastic modulus of the $[0^o/90^o]$ composite comprising equal thickness plies. Thus, the numerical results suggest that the extra beam length required for the transverse deflection of the beam is obtained by uniform axial straining of the beam behind a longitudinal elastic wave that emanates from the impact location and travels along the longitudinal axis of the beam at a speed $C_L \gg \dot{\xi}$. FE predictions of the dependence of the strain amplitude Ξ and the base γ on V_0 are included in Figs. 4.9a and 4.9b, respectively. Both γ and V_0 increase with increasing impact velocity and we shall now use these findings to motivate a simple analytical model.

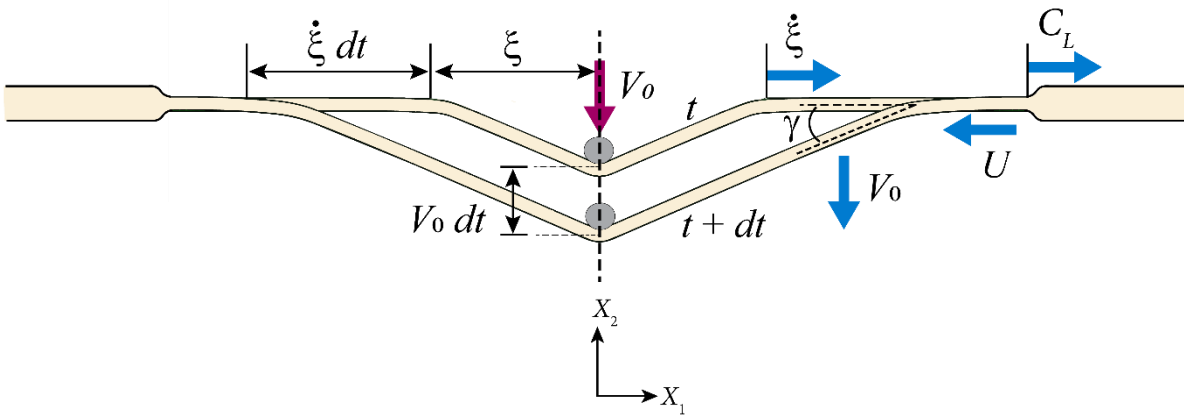

Figure 4.6: Schematic illustrations showing the deformation mode of a low shear strength beam with a constant imposed deflection rate V_0 at mid-span. Sketches are shown at times t and $t + dt$ to illustrate the self-similar deformation mode and the movement of the shear hinge at a rate $\dot{\xi}$. The longitudinal elastic wave travelling at a rate $C_L \gg \dot{\xi}$ is also illustrated.

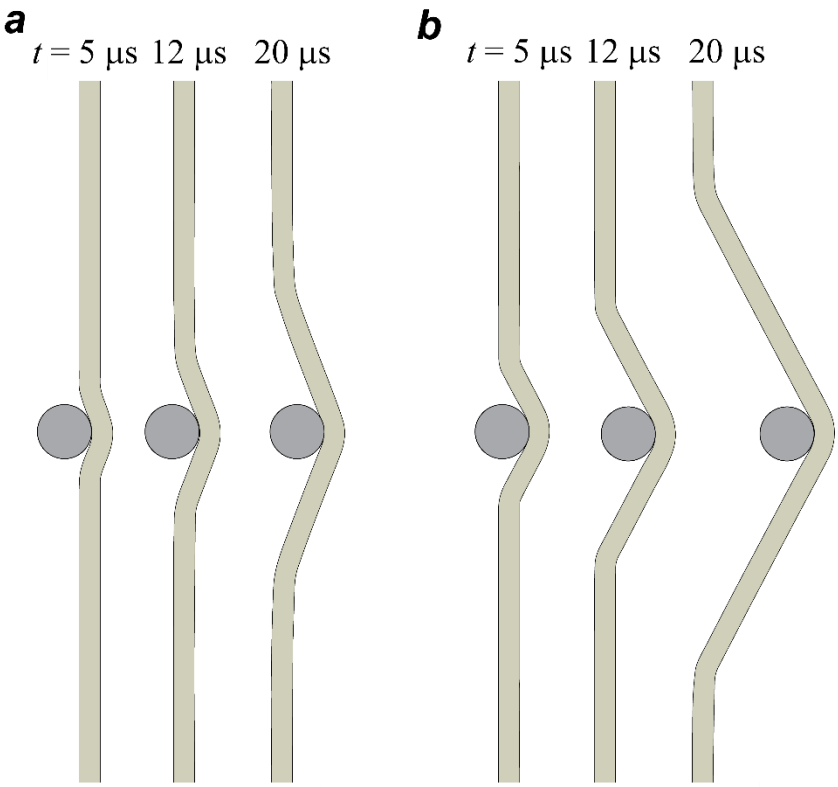

Figure 4.7: FE predictions of the deformed profiles of the $n = 10$ low shear strength ($\tau_Y = 2$ MPa) beam at selected times t impacted at velocities (a) $V_0 = 150\ \mathrm{ms}^{-1}$ and (b) $V_0 = 350\ \mathrm{ms}^{-1}$.

4.3.1.1 Analytical model for the shear-dominated dynamic beam deflection

We develop an analytical model for the overall deflection mode of the beam by modifying the analysis of Wang (2007) for the dynamic deflection of single fibres. This model will not only provide simple analytical expressions for the key variables such as the base angle and shear hinge velocity but also help improve the understanding of the overall deformation mechanism.

Consider an elastic beam with zero longitudinal shear strength and stiffness, and a longitudinal Young's modulus E_b. This implies that transverse deflection is achieved via a combination of longitudinal stretching and transverse shearing with no bending. Upon projectile impact, a longitudinal elastic wave emanates from the impact location travelling at a speed C_L in the $\pm X_1$ directions inducing a longitudinal particle velocity U in the beam. The longitudinal stress σ_L is then given by $\sigma_L = \rho C_L U$ and the corresponding longitudinal strain is $\varepsilon_L = U/C_L$ in the portion $|X_1| \leq C_L t$ of the beam that has been traversed by this elastic wave. The remainder of the beam located at $|X_1| > C_L t$ remains unstrained with $\sigma_L = 0$ and $\varepsilon_L = 0$.

At time t after impact, the deflected profile of the beam is as sketched in Fig. 4.6 with the shear hinges located at $X_1 = \pm\xi$. The particle velocities in the deflected region are $-V_0$ in the negative X_2-direction and zero velocity in the X_1-direction, i.e., across the shear hinge the particle velocities switch from U in the X_1-direction to $-V_0$ in the negative X_2-direction. Momentum conservation in the X_2-direction implies that $\sigma_L \sin\gamma = \rho C_S V_0$, where C_S is the Lagrangian speed of the shear hinge. Recalling that the deflected region of the beam is stretched by a strain ε_L, and that the particle velocity prior to the arrival of the shear hinge was U in the X_1-direction, this Lagrangian speed is related to $\dot{\xi}$ by,

$$\dot{\xi} = C_S(1 + \varepsilon_L) - U. \tag{4.3}$$

Examination of the deflected profiles at times t and $t + dt$ as sketched in Fig. 4.6, indicates

$$V_0 = C_S(1 + \varepsilon_L)\sin\gamma = \left(\dot{\xi} + U\right)\sin\gamma, \tag{4.4}$$

and $\dot{\xi} = V_0/\tan\gamma$. These equations can be simplified and combined to give an implicit equation for $\dot{\xi}$ as

$$V_0 = \frac{\dot{\xi}}{C_L - 2\dot{\xi}}\sqrt{\dot{\xi}(2C_L - 3\dot{\xi})}. \tag{4.5}$$

In the limit of $\dot{\xi} \ll C_L$, the binomial approximation gives

$$\dot{\xi} = \left(\frac{C_L}{2}\right)^{1/3} V_0^{2/3}, \tag{4.6}$$

and the base angle of the deflected triangular profile follows as

$$\gamma = \tan^{-1}\left(\frac{2V_0}{C_L}\right)^{1/3}. \tag{4.7}$$

while strain ε_L is given by (4.4) by employing the relation $U = \varepsilon_L C_L$.

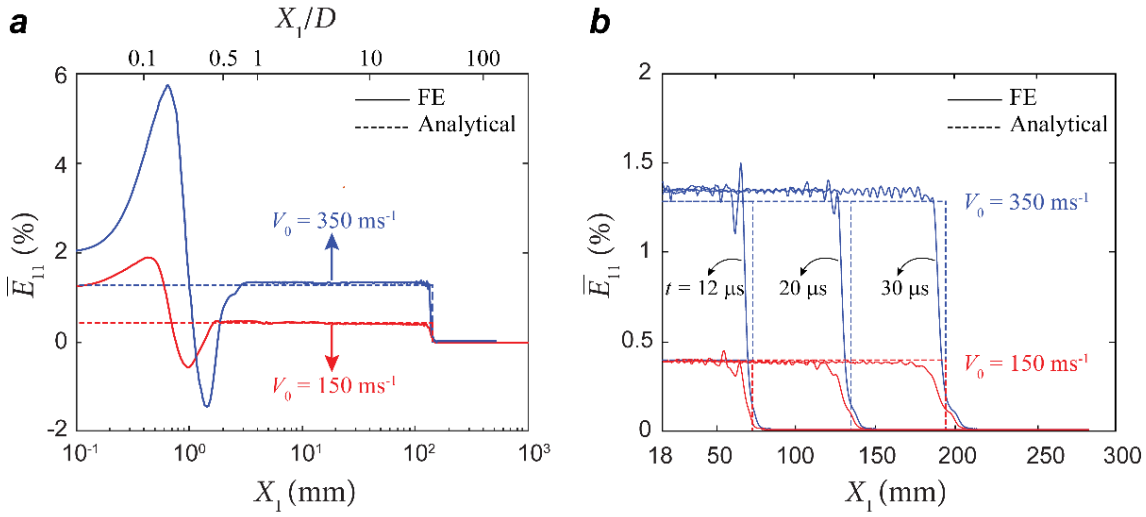

Figure 4. 8: Analytical and FE predictions of the dependence of the spatial distributions of the axial strain $\bar{E}_{11}$ in a beam impacted at velocities $V_0 = 150$ ms^{-1} and 350 ms^{-1} at (a) $t = 20$ μs and (b) at three selected times. In (a) the distributions are shown over a large portion of the beam including immediately under the projectile with the upper abscissa X_1/D showing the region of the beam compared to the diameter of the projectile, while in (b) the focus is in the region away from that impacted zone with results shown for a region $X_1 \geq 18$ mm. All results pertain to the $n = 10$ low shear strength ($\tau_Y = 2$ MPa) beam with time $t = 0$ corresponding to the instant of impact.

We identify ε_L with the average strain $\bar{E}_{11}$ and the analytical as well as FE predictions of $\bar{E}_{11}$ are included in Fig. 4.8. Excellent agreement is observed away from the immediate vicinity of the impacted region, i.e., $|X_1| \geq D/2$. To give a more complete comparison between analytical and FE predictions we compare the strain amplitude Ξ and base angle γ predictions as a function of impact velocity V_0; see Figs 4.9a and 4.9b, respectively. Again, excellent agreement is observed confirming the fidelity of this simple analytical model for predicting the overall dynamic deformation of the beams in the regime where the response is dominated by longitudinal shear.

While this simple picture for the dynamic deformation mechanism of the beam provides insight into the overall deflection mechanism, it is unable to predict the onset of failure in the beam. To understand this, recall that the model predicts a temporally constant axial stretch ε_L such that either the beam completely fails at the impact location immediately upon impact or continues to deflect with no fibre fracture. This is contrary to the experimental observations discussed in Section 4.1 (also see Fig. 4.1) where failure occurs in a progressive manner with plies immediately in contact with the projectile failing first and the fraction of failed plies increasing with impact velocity. This discrepancy arises because the analytical model neglects

the details of the deformation mechanisms immediately under the projectile, resulting in its inability to accurately predict the strains immediately under the projectile; see Fig. 4.8a. Therefore, we proceed to use the FE calculations to examine the stress/strain states in this region in detail.

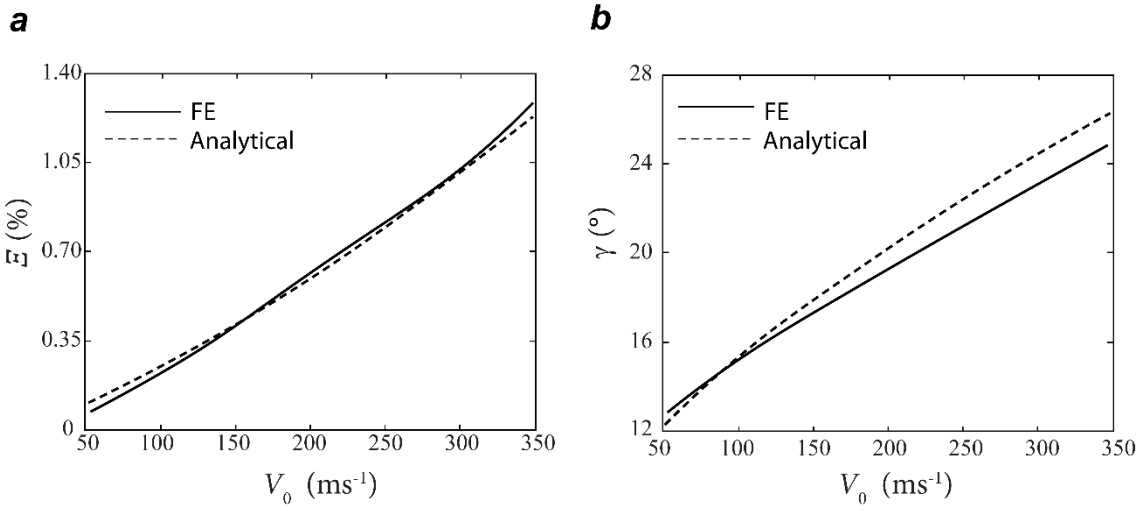

Figure 4.9: Analytical and FE predictions of the dependence of the (a) strain amplitude Ξ and (b) base angle γ and on impact velocity V_0. All results pertain to the $n = 10$ low shear strength ($\tau_Y =$ 2 MPa) beam.

4.3.1.2 Deformation modes immediately under the projectile

Expanded views of the deformation and stress-state immediately under the projectile are shown in Fig. 4.4b at two times after impact: (i) very early in the deformation history at $t = 0.6$ μs when the rear face deflection of the beam is negligible; and (ii) later at $t = 20$ μs when the beam has undergone significant deflection. Clearly, very early in the deformation history, the deformation and therefore stress state is non-uniform across the beam cross-section contrary to the assumption of the simplified analysis described above. In fact, development of the indirect tension mechanism is clearly seen at $t = 0.6$ μs. We understand this as follows:

(i) A compressive stress wave in the transverse direction is initiated by the impacting projectile. This wave travels at a speed $C_T \approx \sqrt{E_m/\rho}$ towards the rear surface of the beam.

(ii) This compressive stress wave induces the development of alternating layers of compressive and tensile stresses $\hat{\sigma}_{11}$ in the plies with the 0^o plies under tension and compression in the 90^o plies. These stresses diminish in the X_2 −direction away

from the impact site with the plies in the immediate vicinity of the impactor most highly stressed.

(iii) While the average value of $\hat{\sigma}_{11}$ across the thickness of the 0^o and 90^o plies is tensile and compressive, respectively the plies also undergo local bending. As a consequence, the tensile stresses $\hat{\sigma}_{11}$ in the individual 0^o plies are higher on their rear faces; see Fig. 4.4b.

(iv) Local indentation effects cause pile-up at the edge of the contact zone; see Fig. 4.4b

This stress-state at $t = 0.6$ μs can be contrasted with the stress-state later in the deformation at $t = 20$ μs. At this stage, the overall deflection of the beam has become significant but the stresses $\hat{\sigma}_{11}$ in the plies have significantly reduced. In fact, both the 0^o and 90^o plies are under tensile stresses $\hat{\sigma}_{11}$ due to the deflection of the beams much like that assumed in the analytical model. This suggests that later in the deformation history, the transverse forces imposed by the projectile are small and this relaxes the indirect tension deformation mode. Also, as a consequence, material no longer piles-up at the edge of the contact between the projectile and the beam. These results give the first indication that: (i) failure, if it occurs, is expected to initiate early in the deformation history; (ii) failure is by the indirect tension mechanism and therefore only affects plies immediately in contact with the projectile; and (iii) shear-dominated deflection relaxes stresses within the beam with failure not expected to occur due to the overall longitudinal stretching of the beam.

4.3.2 Deformation mechanisms for high shear strength beams

The deformation mechanisms discussed above are relevant for commercial UHMWPE composite structures with low shear strengths. Our aim here however is to understand the effect of material parameters, and we thus now present numerical results for the case of a beam with a high shear strength of $\tau_Y = 20$ MPa. This shear strength is sufficiently high that deflection of the beam is dominated by bending, and this will aid in highlighting the role of the beam shear strength. The overall deflection mode of the high shear strength beam at selected times t is illustrated in Fig. 4.5a. The lines marked perpendicular to the longitudinal axis of the beam in the undeformed configuration now rotate with increasing beam deflection, confirming that deflection occurs in a bending-dominated mode. In fact, the deflected profile is no longer triangular and a distinct hinge separating the deflected and the un-deflected regions of the beam cannot be identified. Rather dynamic deflection occurs in a more classical sense by the

propagation of an elastic/plastic flexural wave that emanates from the impact site (Yu et al., 1996). Therefore a simple analytical model for the overall deflection mode can no longer be developed and readers are referred to Stronge (2000) for a detailed exposition of the elastic-plastic dynamic deflection of Euler-Bernoulli beams.

This change in the mode to a bending-dominated deflection has a dramatic effect on the stress-state immediately under the projectile as seen in Fig. 4.5b where we show zoom-ins at times $t = 0.6\ \mu s$ and $20\ \mu s$. Indirect tension is again seen to develop immediately under the projectile at $t = 0.6\ \mu s$, but now the highest stresses develop in plies at the rear of the beam. Continued deflection is achieved via beam bending, and unlike in the low shear strength case (Fig. 4.4), stresses no longer relax with increasing deflection. Rather, large tensile and compressive stresses develop on the rear and impacted faces, respectively at $t = 20\ \mu s$. The magnitudes of these stresses are generally higher than those early in the deformation history ($t = 0.6\ \mu s$). In fact, the longitudinal compressive stresses at the edge of the impacted region are so high that they initiate wrinkling/kinking of the plies (Fig. 4.5b). Thus, now unlike in the low shear strength case we expect failure to initiate later in the deformation history and to occur by tensile stretching of the plies on the rear face.

4.4. Failure mechanism maps

The discussion in Section 4.3 indicates that the dynamic failure of the composites is governed by the local stress field in the immediate vicinity of the impacted surface rather than the overall deflection/stress fields. With tensile fibre fracture being the only operative failure mechanism, failure is initiated when the stress $\hat{\sigma}_{11}$ in a 0^o ply attains a critical value Σ_f. We now proceed to first investigate the temporal and spatial evolution of $\hat{\sigma}_{11}$ and then use that understanding to develop failure mechanism maps for the initiation of failure in $[0^o/90^o]$ composite beams.

The maximum value of $\hat{\sigma}_{11}$ occurs either in the ply immediately in contact with the projectile or in the rearmost 0^o ply at $X_1 \approx 0$ (Section 4.3). It is thus insightful to monitor the values of $\hat{\sigma}_{11}$ in the region $X_1 \approx 0$ as a function of time t. We denote $\hat{\sigma}^f_{\max}(t)$ as the spatially maximum value of $\hat{\sigma}_{11}$ in the ply in contact with the projectile and $\hat{\sigma}^r_{\max}(t)$ as the corresponding maximum value of $\hat{\sigma}_{11}$ in the rearmost 0^o ply at time t. The temporal evolutions of these maximum stresses for beams with $\tau_Y = 2$ MPa and 20 MPa are plotted in Figs. 4.10a and

4.10b, respectively for the case of impact at $V_0 = 200\ \mathrm{ms}^{-1}$. So as to enable visualization of the details of the temporal stress evolution over a relatively long time-span, yet still reveal details of the early temporal evolution, we use a logarithmic time-scale in Fig. 4.10.

Consider first the case of the low shear strength beam. Over the time period shown in Fig. 4.10, $\hat{\sigma}^f_{\max} > \hat{\sigma}^r_{\max}$, i.e., failure, if it occurs, initiates in the ply in contact with the projectile. Now consider the early time history of $\hat{\sigma}^f_{\max}$. We define a time period $T \equiv H/C_T$ as the time required by a transverse elastic wave travelling at $C_T = \sqrt{E_m/\rho}$ to traverse through the thickness of the beam as illustrated in Fig. 4.11. Thus, for $t < T$, the stress in the rear ply remains zero while the stress in the ply in contact with the projectile continues to rise due to the continued motion of the projectile into the beam. The elastic wave travelling through the beam thickness reflects from the rear free surface as a tensile wave (Fig. 4.11b), and arrives back at the impact site at $t = 2T$. Therefore, until $t \approx 2T$ the stress $\hat{\sigma}^f_{\max}$ continues to rise but upon arrival of this tensile unloading wave $\hat{\sigma}^f_{\max}$ begins to drop. Subsequently, $\hat{\sigma}^f_{\max}$ remains relatively constant, and thus failure is expected to be initiated immediately under the projectile only if $\hat{\sigma}^f_{\max} \geq \Sigma_f$ at time $t \approx 2T$.

Next consider the high shear strength beam ($\tau_Y = 20$ MPa). There is now a marked difference in the temporal evolution of the stresses compared to the $\tau_Y = 2$ MPa case. Early in the time history, the responses are relatively similar with $\hat{\sigma}^r_{\max} = 0$ for $t < T$. However, the high shear strength of the beam induces bending deflections with the consequence that $\hat{\sigma}^f_{\max}$ rises at a comparatively lower rate while $\hat{\sigma}^r_{\max}$ increases sharply at times $t > T$. In fact, around $t \approx 2T$, the temporal histories of $\hat{\sigma}^f_{\max}$ and $\hat{\sigma}^r_{\max}$ crossover with $\hat{\sigma}^r_{\max}$ continuing to increase up to $t \approx 10\ \mu\mathrm{s}$ while $\hat{\sigma}^f_{\max}$ reduces to relatively small values (and is mainly compressive). The consequence is that while the peak value of $\hat{\sigma}^f_{\max}$ was approximately 2.5 GPa in the low shear strength beam and was attained at time $t \approx 2T$, $\hat{\sigma}^f_{\max}$ remains below 2 GPa in the high shear strength beam. By contrast, $\hat{\sigma}^r_{\max}$ for the high strength beam rises to values well in excess of 2.5 GPa albeit at a much later stage in the deformation. Thus, failure in the high shear strength beams is likely to be initiated at the rear of the beam.

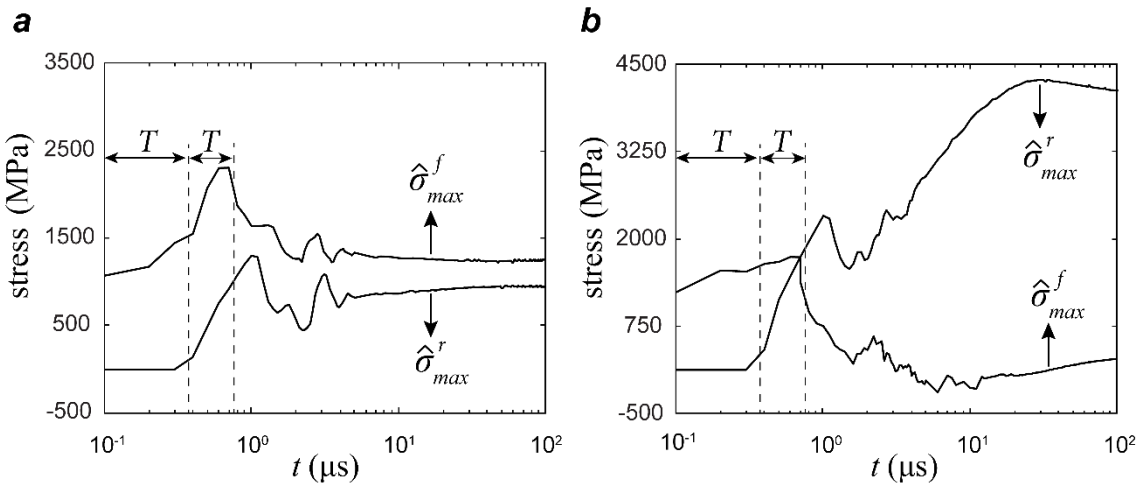

Figure 4.10: FE predictions of the temporal evolution of the maximum ply stresses $\hat{\sigma}^f_{\max}$ and $\hat{\sigma}^r_{\max}$ in the 0^o ply in contact with the projectile and at the rear of the beam, respectively. The predictions are for the $n = 10$ beams with shear strengths (a) $\tau_Y = 2$ MPa and (b) $\tau_Y = 20$ MPa impacted at a velocity $V_0 = 200\ \text{ms}^{-1}$. In order to enable visualization of the details of the temporal stress evolutions over relatively long time-spans, we use a logarithmic abscissa. We have marked times $t = T$ and $t = 2T$ to indicate the instants at which the transverse elastic wave reaches the rear surface and the reflected wave reaches the impact site.

The above discussion on the temporal evolution of the stresses that govern failure initiation is restricted to an impact velocity $V_0 = 200\ \text{ms}^{-1}$. These findings can be generalized for the full range of impact velocities by first defining $\hat{\sigma}_{\max} \equiv \max(\hat{\sigma}^f_{\max}, \hat{\sigma}^r_{\max})$ so that we are able to specify whether the initiation of failure is immediately under the projectile or at the rear surface of the beam. Predictions of $\hat{\sigma}_{\max}$ as a function of time t are included in Figs. 4.12a and 4.12b for beams with $\tau_Y = 2$ MPa and 20 MPa, respectively. The predictions are shown for a range of impact velocities and the dashed line is the boundary where $\hat{\sigma}^f_{\max} = \hat{\sigma}^r_{\max}$, i.e., on the side of the line marked "front ply" $\hat{\sigma}_{\max} = \hat{\sigma}^f_{\max}$ while in the region marked "rear ply" $\hat{\sigma}_{\max} = \hat{\sigma}^r_{\max}$.

For the low shear strength beam, the results in Fig. 4.12a can be summarised as follows:

(i) At low impact velocities, $\hat{\sigma}_{\max}$ transitions from being located immediately under the projectile early in the impact, to the rear of the beam later in the deformation history. By contrast, $\hat{\sigma}_{\max}$ is always located immediately under the projectile at higher impact velocities.

(ii) However, even at low impact velocities, $\max[\hat{\sigma}_{\max}(t)\ ]$ over all t is always attained early in the deformation history. Consequently, failure, if it occurs, is expected to initiate immediately under the projectile early in the deformation history.

By contrast, in the high shear strength beams, $\hat{\sigma}_{\max} = \hat{\sigma}^{f}_{\max}$ for $t \approx< 2T$ with $\hat{\sigma}_{\max} = \hat{\sigma}^{r}_{\max}$ later in the deformation history for all impact velocities. Moreover, for any given impact velocity, the maximum value of $\hat{\sigma}_{\max}$ over the entire deformation history is always attained late in the deformation history when $\hat{\sigma}_{\max} = \hat{\sigma}^{r}_{\max}$ and thus failure, if it occurs, initiates on the rear face of the beam.

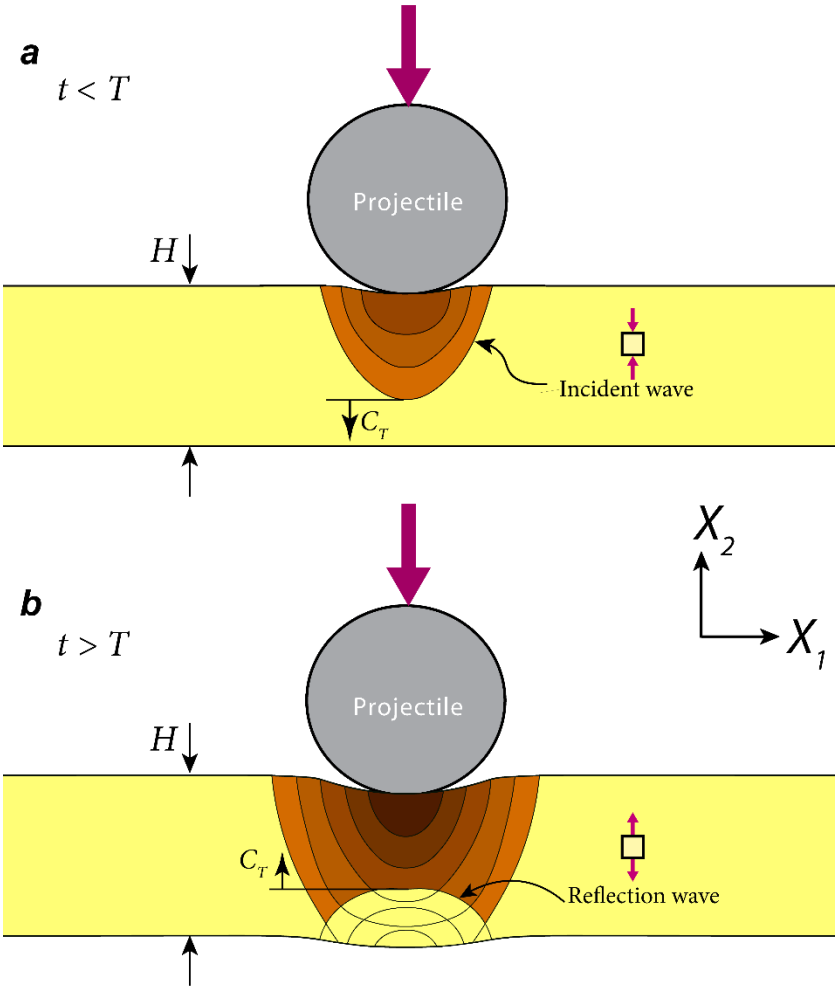

Figure 4.11: Sketch of the propagation of the transverse elastic wave initiated by the impact of the projectile. (a) The compressive wave prior to it reaching the rear surface and (b) the wave after it reflects as a tensile wave from the free rear surface.

4.4.1 Failure modes and construction of failure mechanism maps

The above discussion of the temporal and spatial distributions of ply stresses in the fibre direction suggests that failure initiates in the impacted beams via one of the two modes:

Mode I: Failure by indirect tension as sketched in Fig. 4.3a where the compressive loading imposed by the projectile generates tensile loading in the fibre direction in the plies

immediately under the impact site. Fibre fracture occurs when these tensile stresses exceed a critical value Σ_f.

Mode II: Failure of the rear ply by tensile fibre straining due to bending as sketched in Fig. 4.3c. Again, fibre fracture occurs when this tensile stress exceeds a critical value Σ_f.

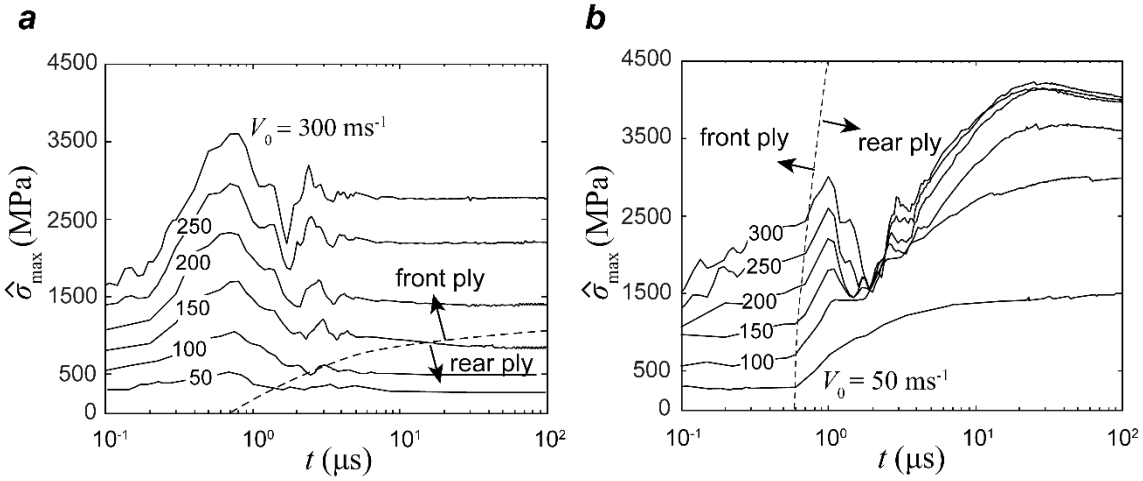

Figure 4.12: FE predictions of the temporal evolution of the maximum ply stresses $\hat{\sigma}_{\max} \equiv \max(\hat{\sigma}^f_{\max}, \hat{\sigma}^r_{\max})$ in the 0^o plies. The predictions are for the $n = 10$ beams with shear strengths (a) $\tau_Y = 2$ MPa and (b) $\tau_Y = 20$ MPa at selected impact velocities V_0. In order to enable visualization of the details of the temporal stress evolutions over relatively long time-spans we use a logarithmic abscissa. A line marking the boundary where $\hat{\sigma}^f_{\max} = \hat{\sigma}^r_{\max}$ is marked in each case with $\hat{\sigma}_{\max} = \hat{\sigma}^f_{\max}$ in the region marked "front ply" and $\hat{\sigma}_{\max} = \hat{\sigma}^r_{\max}$ in the region marked "rear ply".

Failure mechanism maps for the initiation of failure in the impacted UHMWPE composite beams can be constructed to illustrate the competition between these two failure modes and the region where the beam continues to deform with no fibre fracture. We choose to construct maps with axes of impact velocity V_0 and shear strength τ_Y to best illustrate the interplay between impact velocity and shear strength (as is alluded to in the discussion above). The failure mechanism maps are constructed as follows. We first choose the material dependent tensile failure strength Σ_f and then examine the temporal variations of $\hat{\sigma}_{\max}$ as shown in Fig. 4.12. For a given choice of (τ_Y, V_0) we locate the time at which $\hat{\sigma}_{\max}$ first attains the value Σ_f and this presents three possibilities:

(i) *No failure*: $\hat{\sigma}_{\max}$ always remains below Σ_f and this implies continued deformation of the beam with no fibre fracture/failure.

(ii) *Mode I failure*: $\hat{\sigma}_{\max}$ first attains the critical value Σ_f in the front ply so failure initiation is by the indirect tension mechanism.

(iii) *Mode II failure*: $\hat{\sigma}_{\max}$ first attains the critical value Σ_f in the rear ply so failure initiation is by tensile straining of the rear ply of the beam due to the bending deformation of the beam.

A failure mechanism map showing these three regimes with axis ranges $0 \leq V_0 \leq 400\ \mathrm{ms}^{-1}$ and $1\ \mathrm{MPa} \leq \tau_Y \leq 20\ \mathrm{MPa}$ is shown in Fig. 4.13 for the choice $\Sigma_f = 2.5\ \mathrm{GPa}$. Based on this map we subdivide mode I failure into "dominated" and "non-dominated" regimes. The non-dominated regime is defined as the regime where reducing the impact velocity for a given shear strength results in a transition, at a velocity $V_c(\tau_Y)$, into a regime where no failure occurs. This transition $V_c(\tau_Y)$ is marked by a solid line in Fig. 4.13. We observe from Fig. 4.13 that mode II failure is always non-dominated. However, mode I failure is non-dominated at low shear strengths but dominated at high shear strengths in the sense that reducing the impact velocity for a given shear strength results in a transition into mode II failure at a velocity $V_I(\tau_Y)$. This boundary marking $V_I(\tau_Y)$ is shown as a dashed line in Fig. 4.13.

Of immediate practical interest is the dependency of the critical impact velocity V_c, below which fibre fracture is not expected, on the beam shear strength τ_Y. This critical velocity first increases with τ_Y but then dramatically reduces as the non-dominated failure regime switches from mode I to mode II. We label the shear strength at which this transition occurs as an optimum shear strength τ_{OPT} as the critical impact velocity V_c is maximised at this value of τ_Y for a given tensile ply strength Σ_f.

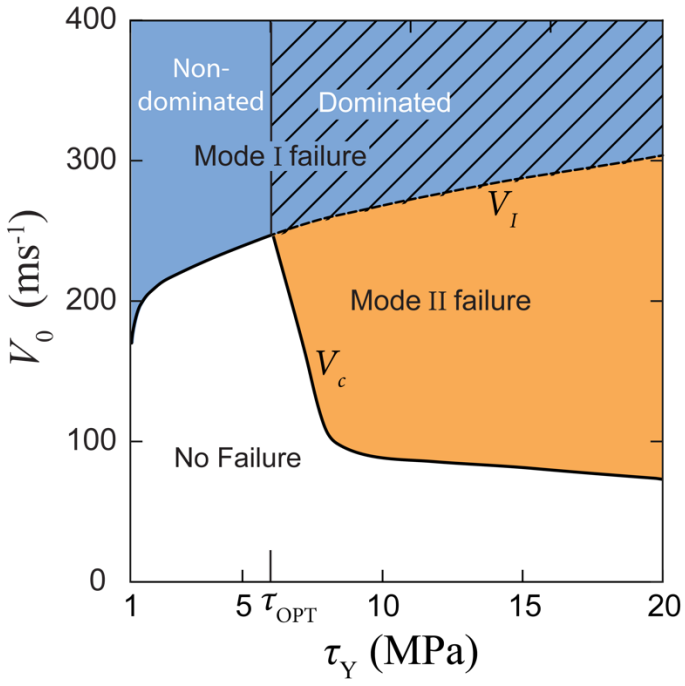

Figure 4.13: Failure mechanism map with axes of shear strength τ_Y and impact velocity V_0 for a $n = 10$ beam with ply tensile strength $\Sigma_f = 2.5$ GPa. The "dominated" mode I failure zone is shown hatched. The boundary of the critical velocity V_c between a regime of failure and no failure is marked by a solid line while the boundary V_I between failure regimes I and II shown via a dashed line. The optimum shear strength is indicated as τ_{OPT}.

The failure map in Fig. 4.13 enables a number of predictions to be made that are consistent with experimental observations, but that to-date, had eluded a mechanistic understanding:

(i) For a given strength Σ_f, the critical velocity to induce failure in the impacted beam is higher in lower shear strength beams. Such observations have been extensively reported (De Ruijter et al., 2010; Yu et al., 2017) including a detailed study by Karthikeyan et al. (2013) on the effect of shear strength on the ballistic performance. The numerical simulations reported here show that the switch in the failure mechanism from the mode I indirect tension failure to mode II tensile straining (due to increased bending deformations with increasing shear strength) results in a decrease in ballistic performance with increasing shear strength.

(ii) Failure in low shear strength UHMWPE composite structures is mostly restricted to the plies immediately under the impact site (Attwood et al., 2016). The map in Fig. 4.13 clearly shows failure initiation at low shear strength is dominated by the indirect tension failure mode that occurs in plies immediately in contact with the projectile.

4.4.2 Parametric studies: effect of ply strength and beam thickness

A failure mechanism map is included in Fig. 4.14a for ply strength values in the range $1.5\ \text{GPa} \leq \Sigma_f \leq 3.0\ \text{GPa}$. Unsurprisingly, the no failure regime expands with increasing Σ_f with the velocities required to initiate both mode I and mode II failures increasing with increasing Σ_f for any given τ_Y. More interestingly, τ_{OPT} also increases with increasing Σ_f. This predicted dependency of τ_{OPT} on Σ_f is shown in Fig. 4.14b with τ_{OPT} increasing to nearly 20 MPa for a ply tensile strength of $\Sigma_f = 4$ GPa. The importance of this finding lies in helping overcome the conundrum faced in designing "structural armours" as we shall now proceed to discuss.

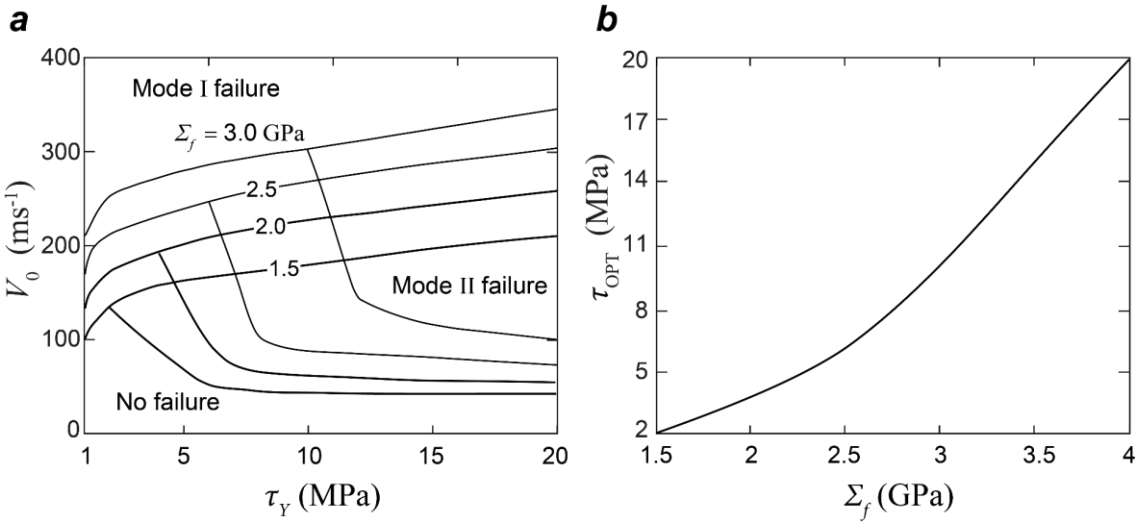

Figure 4.14: (a) Failure mechanism map with axes of shear strength τ_Y and impact velocity V_0 for $n = 10$ beams with the ply strengths in the range $1.5\ \text{GPa} \leq \Sigma_f \leq 3.0\ \text{GPa}$. (b) The dependence of the optimal shear strength τ_{OPT} on the ply strength Σ_f for the $n = 10$ beams.

Experimental observations (De Ruijter et al., 2010; Yu et al., 2017; Karthikeyan et al., 2013), now also supported by numerical results presented here, indicate that lowering the shear strength enhances ballistic resistance. However, such low strength materials (e.g., the HB26 or HB50 ballistic-grade Dyneema® composites have shear strengths of 2 MPa and 0.5 MPa, respectively) possess little structural load carrying capacity. Thus, such composites are used "parasitically" for just their ballistic protection capability. By contrast, high shear strength composites that have excellent structural properties (e.g., CFRPs) have a low ballistic protection capability as discussed in Section 4.1. Composites that serve a dual ballistic and structural load carrying role, i.e., "structural armours" would inevitably help in reducing the

overall system weight but inventing such composites has proven elusive. The results in Fig. 4.14b suggest that increasing the tensile ply strength will not only enhance the impact velocities to initiate failure (i.e., enhance their ballistic protection capability) but also allow these excellent ballistic protection properties to be attained at high shear strength. In fact, the predictions of Fig. 4.14b suggest that an optimal ballistic performance will be attained at a shear strength of 20 MPa if the ply tensile strength is increased to $\Sigma_f = 4$ GPa. This shear strength is comparable to most CFRPs and would endow the UHMWPE composite with acceptable structural load carrying capability. Of course, a ply strength of $\Sigma_f = 4$ GPa is higher than most current commercial grades of Dyneema® but continued advances in enhancing tensile strength of UHMPE fibres (for example the experimental, non-commercial grade X131 and X-DARPA fibres developed by DSM and characterised in Cain et al. (2018)) makes this a very achievable goal.

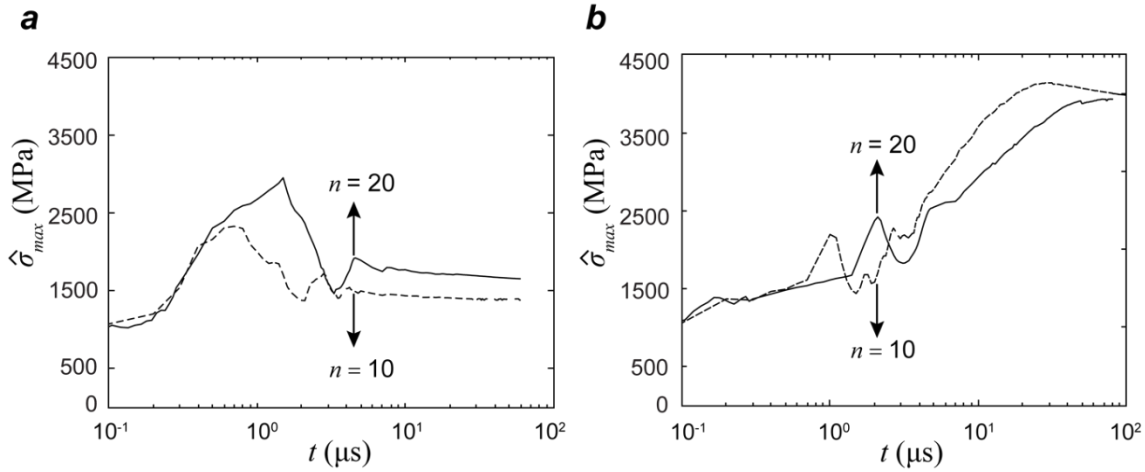

Figure 4.15: FE predictions of the temporal evolution of the maximum ply stresses $\hat{\sigma}_{\max} \equiv \max(\hat{\sigma}^f_{\max}, \hat{\sigma}^r_{\max})$ in the 0^o plies in the $n = 10$ and $n = 20$ beams impacted at $V_0 = 200$ ms^{-1}. Predictions are shown for the beams with shear strengths (a) $\tau_Y = 2$ MPa and (b) $\tau_Y = 20$ MPa. In order to enable visualization of the details of the temporal stress evolutions over relatively long time-spans we use a logarithmic abscissa.

All results presented so far are for a composite with 20 plies (i.e., $n = 10$). The effect of the overall beam thickness on the failure mechanism map is now examined by increasing the beam to comprise 40 plies (i.e., $n = 20$) but keeping the projectile diameter and ply thickness fixed at the reference values. A comparison between the temporal evolutions of $\hat{\sigma}_{\max}$ for the $n = 10$ and 20 beams impacted at $V_0 = 200$ ms^{-1} is shown in Figs. 4.15a and 4.15b for shear strengths $\tau_Y = 2$ MPa and 20 MPa, respectively. For both the $n = 10$ and 20 cases, $\hat{\sigma}_{\max}$ is set by the tensile stresses immediately under the projectile generated by the indirect tension mechanism

in the low shear strength ($\tau_Y = 2$ MPa) beams while in the high shear strength ($\tau_Y = 20$ MPa) beams, tensile straining on the rear face due to beam bending governs $\hat{\sigma}_{\max}$. The differences in $\hat{\sigma}_{\max}$ between the $n = 10$ and 20 beams are negligible in the high shear strength beams but in the low shear strength case, the peak value of $\hat{\sigma}_{\max}$ is significantly higher in the $n = 20$ beam. To understand this difference recall that the tensile stresses due to indirect tension continue to build-up under the projectile until the elastic wave reflected from the rear face arrives at the impact site at time $t \approx 2T = 2H/C_T$; see Section 4.4. Increasing the beam thickness H increases T hence $\hat{\sigma}_{\max}$ can continue to build-up via indirect tension to higher values as seen in Fig. 4.15a. The effect of these changes in the stress evolutions within the beams on the failure mechanism map is summarised in Fig. 4.16 where we show the boundaries between the three regimes for both the $n = 10$ and 20 beams for a ply strength $\Sigma_f = 2.5$ GPa. The beam thickness has only a small effect on the boundary between mode II failure and no failure. However, as discussed above, beam thickness has a more significant effect on mode I failure and lowers the velocity (for any given value of τ_Y) at which we transition from either no failure to mode I failure or from mode II to mode I failure.

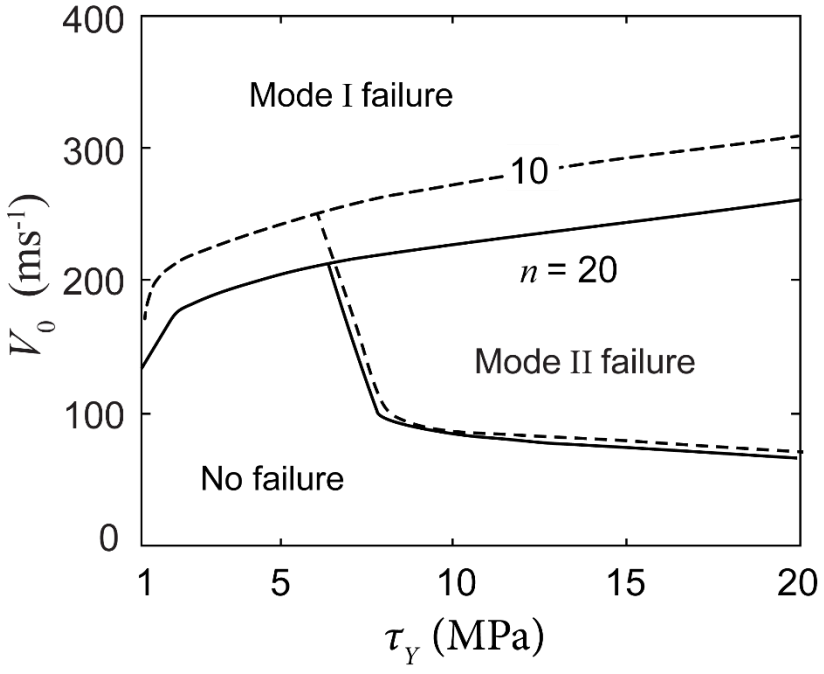

Figure 4.16: Failure mechanism maps with axes of shear strength τ_Y and impact velocity V_0 for the $n = 10$ and $n = 20$ beams with ply strengths $\Sigma_f = 2.5$ GPa. The three regimes are indicated on the map.

4.5. Concluding remarks

Failure mechanism maps have been developed to illustrate the mechanisms by which failure can initiate in $[0^o/90^o]_n$ ultra-high polyethylene (UHMWPE) fibre composite beams impacted by a rigid, cylindrical projectile. All the $0^o/90^o$ plies in the beams are explicitly modelled using a pressure-dependent crystal plasticity framework that accurately accounts for large shear deformations as well as fibre rotations.

Two distinct failure modes have been uncovered: (i) mode I failure immediately under the projectile where compressive loading imposed by the projectile induces tensile fibre strains due to the anisotropic expansion of the alternating $0^o/90^o$ plies (i.e., the indirect tension mechanism) and (ii) mode II failure due to tensile fibre straining at the rear of the beam resulting from beam bending. Mode I failure dominates at low shear strengths while mode II is the dominant mechanism at higher shear strengths. Most commercial UHMWPE fibre composites have relatively low shear strengths, and consistent with the experimental observations, these calculations suggest that failure in these beams will occur in a progressive manner, i.e., the number of failed plies will progressively increase with impact velocity. Moreover, the calculations also show that the maximum tensile fibre stresses are lower in the low shear strength beams and thus consistent with experimental observations higher impact velocities are required to initiate failure in low shear strength beams. In fact, the calculations predict the existence of an optimal shear strength that maximises the impact velocity for failure initiation at a given tensile strength of the fibres.

The conundrum that increasing the ballistic resistance requires a low shear strength, and therefore a reduction in the structural strength of composites, is well-known amongst composite material designers. The calculations presented here provide a mechanistic rationalisation for this dilemma. However, the calculations also show that the shear strength required to attain optimal impact performance increases with increasing tensile strength of the plies/fibres. In fact, we show that a shear strength of about 20 MPa will be optimal for a composite with ply tensile strength of about 4 GPa −such a composite is expected to have acceptable levels of structural performance and excellent ballistic properties. The calculations presented here thus suggest that enhancing tensile fibre strengths, and thereby the tensile strengths of the composite, would be a significant step toward the design of “structural armours”. We emphasize that this investigation was restricted to the initiation of failure in the

UHMWPE fibre composite beams- further work on extending this methodology to include the evolution of damage is essential to predict the penetration velocity and modes and thereby confirm the generality of the conclusions drawn here.

References

Attwood, J.P., Fleck, N.A., Wadley, H.N.G., Deshpande, V.S., 2015. The compressive response of ultra-high molecular weight polyethylene fibres and composites. Int. J. Solids Struct. 71, 141–155. https://doi.org/10.1016/j.ijsolstr.2015.06.015

Attwood, J.P., Khaderi, S.N., Karthikeyan, K., Fleck, N.A., O′Masta, M.R., Wadley, H.N.G., Deshpande, V.S., 2014. The out-of-plane compressive response of Dyneema composites. J. Mech. Phys. Solids 70, 200–226. https://doi.org/10.1016/j.jmps.2014.05.017

Attwood, J.P., Russell, B.P., Wadley, H.N.G., Deshpande, V.S., 2016. Mechanisms of the penetration of ultra-high molecular weight polyethylene composite beams. Int. J. Impact Eng. 93, 153–165. https://doi.org/10.1016/j.ijimpeng.2016.02.010

Cantwell, W.J., Morton, J., 1991. The impact resistance of composite materials — a review. Composites 22, 347–362. https://doi.org/10.1016/0010-4361(91)90549-V

Cantwell, W.J., Morton, J., 1989. Comparison of the low and high velocity impact response of CFRP. Composites 20, 545–551. https://doi.org/10.1016/0010-4361(89)90913-0

Chocron, S., Nicholls, A.E., Brill, A., Malka, A., Namir, T., Havazelet, D., Werff, H. van der, Heisserer, U., Walker, J.D., 2014. Modeling unidirectional composites by bundling fibers into strips with experimental determination of shear and compression properties at high pressures. Compos. Sci. Technol. 101, 32–40. https://doi.org/10.1016/j.compscitech.2014.06.016

Cunniff, P.M., 1999. Dimensionless Parameters for Optimization of Textile-Based Body Armor Systems. 18th Int. Symp. Ballist. 1303–1310.

Dassault Systems Simulia Corp, 2013. ABAQUS V6.13.

De Ruijter, C., Van Der Zwaag, S., Stolze, R., Dingemans, T.J., 2010. Liquid crystalline matrix polymers for aramid ballistic composites. Polym. Compos. 31, 612–619. https://doi.org/10.1002/pc.20835

Greenhalgh, E.S., Bloodworth, V.M., Iannucci, L., Pope, D., 2013. Fractographic observations on Dyneema?? composites under ballistic impact. Compos. Part A Appl. Sci. Manuf. 44, 51–62. https://doi.org/10.1016/j.compositesa.2012.08.012

Grujicic, M., Arakere, G., He, T., Bell, W.C., Cheeseman, B.A., Yen, C.F., Scott, B., 2008. A ballistic material model for cross-plied unidirectional ultra-high molecular-weight

polyethylene fiber-reinforced armor-grade composites. Mater. Sci. Eng. A 498, 231–241. https://doi.org/10.1016/j.msea.2008.07.056

Grujicic, M., Hariharan, A., Pandurangan, B., Yen, C.F., Cheeseman, B.A., Wang, Y., Miao, Y., Zheng, J.Q., 2012. Fiber-level modeling of dynamic strength of kevlar® KM2 ballistic fabric. J. Mater. Eng. Perform. 21, 1107–1119. https://doi.org/10.1007/s11665-011-0006-1

Hazzard, M.K., Trask, R.S., Heisserer, U., Van Der Kamp, M., Hallett, S.R., 2018. Finite element modelling of Dyneema® composites: From quasi-static rates to ballistic impact. Compos. Part A Appl. Sci. Manuf. 115, 31–45. https://doi.org/10.1016/j.compositesa.2018.09.005

Iannucci, L., Pope, D., 2011. High velocity impact and armour design. Express Polym. Lett. 5, 262–272. https://doi.org/10.3144/expresspolymlett.2011.26

Karthikeyan, K., Russell, B.P., 2014. Polyethylene ballistic laminates: Failure mechanics and interface effect. Mater. Des. 63, 115–125. https://doi.org/10.1016/j.matdes.2014.05.069

Karthikeyan, K., Russell, B.P., Fleck, N.A., Wadley, H.N.G., Deshpande, V.S., 2013. The effect of shear strength on the ballistic response of laminated composite plates. Eur. J. Mech. - A/Solids 42, 35–53. https://doi.org/10.1016/j.euromechsol.2013.04.002

Lee, B.L., Walsh, T.F., Won, S.T., Patts, H.M., Song, J.W., Mayer, A.H., 2001. Penetration Failure Mechanisms of Armor-Grade Fiber Composites under Impact. J. Compos. Mater. 35, 1605–1633. https://doi.org/10.1177/002199801772661551

Leigh Phoenix, S., Porwal, P.K., 2003. A new membrane model for the ballistic impact response and V50 performance of multi-ply fibrous systems. Int. J. Solids Struct. 40, 6723–6765. https://doi.org/10.1016/S0020-7683(03)00329-9

Liu, B.G., Kandan, K., Wadley, H.N.G., Deshpande, V.S., 2018. Deep penetration of ultra-high molecular weight polyethylene composites by a sharp-tipped punch. J. Mech. Phys. Solids 0, 1–23. https://doi.org/10.1016/j.jmps.2018.06.001

Nazarian, O., Zok, F.W., 2014. Constitutive model for the shear response of Dyneema® fiber composites. Compos. Part A Appl. Sci. Manuf. 66, 73–81. https://doi.org/10.1016/j.compositesa.2014.06.012

Nguyen, L., 2015. The ballistic performance of thick ultra high molecular weight polyethylene composite, RMIT university.

O'Masta, M.R., Crayton, D.H., Deshpande, V.S., Wadley, H.N.G., 2016. Indentation of polyethylene laminates by a flat-bottomed cylindrical punch. Compos. Part A Appl. Sci. Manuf. 80, 138–147. https://doi.org/10.1016/j.compositesa.2015.10.015

O'Masta, M.R., Crayton, D.H., Deshpande, V.S., Wadley, H.N.G., 2015. Mechanisms of penetration in polyethylene reinforced cross-ply laminates. Int. J. Impact Eng. 86, 249–264. https://doi.org/10.1016/j.ijimpeng.2015.08.012

Russell, B.P., Karthikeyan, K., Deshpande, V.S., Fleck, N.A., 2013. The high strain rate response of Ultra High Molecular-weight Polyethylene: From fibre to laminate. Int. J. Impact Eng. 60, 1–9. https://doi.org/10.1016/j.ijimpeng.2013.03.010

Stronge, W.J., 2000. Impact Mechanics. https://doi.org/10.1017/CBO9780511626432

Van Der Werff, H., Heisserer, U., 2016. High-performance ballistic fibers: Ultra-high molecular weight polyethylene (UHMWPE), in: Advanced Fibrous Composite Materials for Ballistic Protection. https://doi.org/10.1016/B978-1-78242-461-1.00003-0

Wang, L., 2007. Foundations of Stress Waves, Elsevier. https://doi.org/10.1017/CBO9781107415324.004

Woodward, R.L., Egglestone, G.T., Baxter, B.J., Challis, K., 1994. Resistance to penetration and compression of fibre-reinforced composite materials. Compos. Eng. 4, 329–341. https://doi.org/10.1016/0961-9526(94)90083-3

Yu, B., Karthikeyan, K., Deshpande, V.S., Fleck, N.A., 2017. Perforation resistance of CFRP beams to quasi-static and ballistic loading: The role of matrix strength. Int. J. Impact Eng. 108, 389–401. https://doi.org/10.1016/j.ijimpeng.2017.04.002

Yu, T.X., Yang, J.L., Reid, S.R., Austin, C.D., 1996. Dynamic behaviour of elastic-plastic free-free beams subjected to impulsive loading. Int. J. Solids Struct. 33, 2659–2680. https://doi.org/10.1016/0020-7683(95)00169-7

Chapter 5

5. High strain rate compressive response of ultra-high molecular weight polyethylene fibre composites

Synopsis

The dynamic in-plane compressive response of $[0^o/90^o]_n$ ultra-high molecular weight polyethylene (UHMWPE) fibre composites has been investigated for strain rates in the range $0.01\ s^{-1}$ to $4000\ s^{-1}$. The measured strain rate sensitivity is mild for strain rates less than about $100\ s^{-1}$ but increases sharply at higher rates. X-ray tomography and optical micrographs reveal that over the whole range of strain rates investigated here, the deformation mechanism is kinking (micro-buckling) of the plies with a kink width of about 1 mm. Ply delamination is also observed although this is mainly prevalent after the peak strength is attained and occurs during the subsequent softening phase of the response. In order to gain a mechanistic understanding of the measured strain rate sensitivity, we performed finite element (FE) calculations of the compression experiments. In these calculations, each ply of the specimen is explicitly modelled using a pressure-dependent crystal plasticity framework that accurately accounts for the large shear strains and fibre rotations that occur within the kink band in each ply. Two limits are considered with perfectly-bonded plies and completely un-bonded plies. Good agreement between measurements and predictions is obtained when plies are assumed to be perfectly bonded confirming that ply delamination plays a small role in setting the strength at least at moderate strain levels. However, the calculations illustrate that misalignment of the specimen between the compression platens has a strong influence on response and especially the initial stiffness. Importantly, the FE calculations demonstrate that over the range of strain rates investigated here, inertial stabilisation plays a minor role with the strong rate sensitivity observed for strain rates above $100\ s^{-1}$ mainly associated with the rate sensitivity of the matrix.

5.1. Introduction

In Chapter 4, we have shown that the ballistic impact loading of $[0^o/90^o]_n$ ultra-high molecular weight polyethylene (UHMWPE) fibre composite structures involves complex multi-axial states of stress including large in-plane compressive stress along the fibre direction. However as detailed in Chapter 2, few studies have investigated the in-plane compressive response of the UHMWPE composites. One exception is Attwood et al. (2015) who explored the quasi-static in-plane compressive response of UHMWPE composites (the HB26 grade of Dyneema®) using notched specimens as sketched in Fig. 5.1a. Their results suggest that compressive deformation occurs by the formation of a ply level kink band involving first rotation of plies followed by band broadening that is induced by the lock-up of the ply rotation; see Fig. 5.1b. This deformation mode is analogous to the compressive deformation of unidirectional (UD) carbon fibre reinforced polymer (CFRP) composites, albeit the kinking in CFRP composites occurs at the fibre level while in the $[0^o/90^o]_n$ HB26 Dyneema® composite the kinks form at the ply level.

With ballistic and blast protection being the primary applications of UHMWPE composites, their dynamic properties are of significant interest. However, remarkably few studies have reported direct measurements of dynamic material properties. Early works (Govaert and Lemstra, 1992; Kromm et al., 2003; Peijs et al., 1994) investigated the tensile fibre responses for strain rates ranging from the creep regime of 10^{-7} s^{-1} to quasi-static rates of 10^{-1} s^{-1}. More recently, Russell et al. (2013) reported that the tensile fibre strengths display minimal rate sensitivity for strain rates from 10^{-1} s^{-1} up to 10^{3} s^{-1} and this has been confirmed by subsequent investigations (Sanborn et al., 2015). Data on the dynamic material properties of the composites are even more sparse. Drop weight (Walley et al., 2009) and split Hopkinson pressure bar (SHPB) tests (Shaker et al., 2017; Zhu et al., 2017) have been performed to examine the out-of-plane compressive response of $[0^o/90^o]_n$ UHMWPE fibre composites for strain rates up to 3000 s^{-1}. Mild rate sensitivity is observed and this is in-line with dynamic data reported by Rodríguez et al. (1996) and Benloulo et al. (1997) for the tensile response of the composites in the fibre direction.

By contrast, the static and dynamic material properties of CFRP composites have been extensively investigated via theoretical models that are supported by experimental measurements. Specifically, plastic micro-buckling of CFRP composites has received

significant attention and readers are referred to Fleck (1997) for a comprehensive review. In CFRP composites, plastic micro-buckling is associated with a load drop and early investigations revealed that the peak strength is set by the initial fibre waviness and the matrix shear strength (Budiansky and Fleck, 1993). Typically, compressive deformation occurs by rotation of fibres within a kink band and Vogler and Kyriakides (1997) demonstrated that the composite can maintain significant post-buckling strength after fibre rotation with the kink band is inhibited and deformation progresses by broadening of the band. Fibre-matrix splitting also plays a role in this process as reported in the experiments of Gutkin et al. (2010) and supported by analytical (Skovsgaard and Jensen, 2018) and numerical (Prabhakar and Waas, 2013) models.

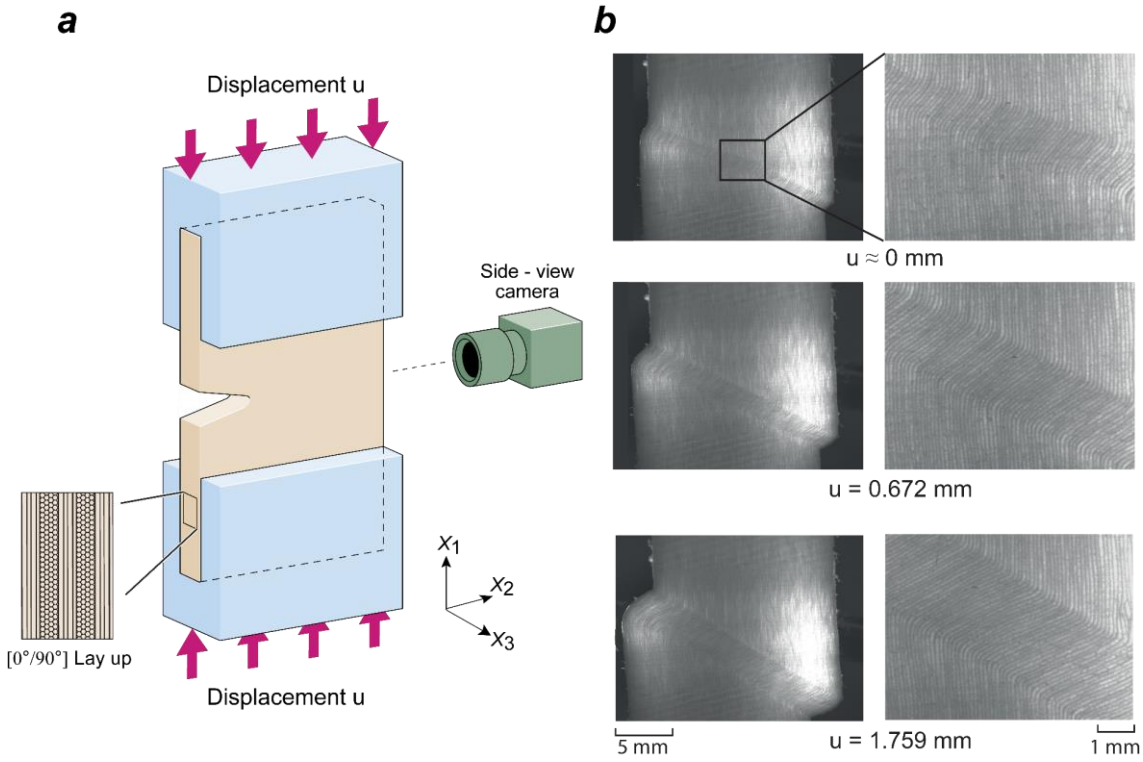

Figure 5.1: Summary of the findings of Attwood et al. (2015) for the quasi-static compression of the HB26 Dyneema® fibre composite. (a) Sketch of the notched compression specimen and (b) photographs, with the camera view indicated in (a), showing fibre rotation within a kink band and the subsequent broadening of the band with increasing remote compressive displacement u.

There also exists an extensive literature on the out-of-plane (Collings, 1974; Henriksson, 1990) compressive response of CFRP composites including studies on the effect of loading rate. Typically, the strain rate sensitivity for out-of-plane compressive loading is relatively low with the response governed by the tensile fibre properties as dictated by the indirect tension

mechanism; see Yu et al. (2018). However, the dynamic in-plane response is again set by plastic micro-buckling and hence displays a strong strain rate sensitivity (Hsiao et al., 1998) due to a combination of the rate sensitivity of the matrix and inertial stabilisation of micro-buckling. Slaughter et al. (1996) as well as Fan and Slaughter (1997) extended the couple stress micro-buckling model of Fleck et al. (1995) to the dynamic setting and predicted the overall strain rate sensitivity of the in-plane response of UD composites. While these studies did not report direct comparisons with experimental measurements, Tsai and Sun (2004), employing a viscoplastic model for the matrix made direct comparisons with measurements. Such studies have aided an understanding of the effect of inertia and matrix rate sensitivity in setting the overall strain rate sensitivity of CFRP composites. However, no equivalent understanding exists for UHMWPE fibre composites.

In the current study, we report a combined experimental and numerical study of the static and dynamic in-plane compressive response of UHMWPE fibre composites. The aim is to understand the strain rate sensitivity of these materials and the relative influence of inertia and matrix rate effects.

5.2. Experimental protocol

The aim of the experimental study is to contrast the in-plane quasi-static and dynamic compressive response of cross-ply UHMWPE composites by (i) measuring the rate sensitivity of the response and (ii) uncovering the deformation modes as a function of the imposed strain rate. We first give a description of the UHMWPE composite investigated in the study, followed by a description of the measurement protocol.

5.2.1 Materials

The HB26 grade of the Dyneema® UHMWPE fibre composite supplied by DSM was used in this study. The cross-ply $[0^o/90^o]_n$ composite comprised approximately 83% by volume SK76 UHMWPE fibres in a polyurethane matrix with a ply thickness $h = 60$ μm; see the sketch in Fig. 5.2a along with the global co-ordinate system X_i such that the X_1 and X_2 directions lie along the $0^o/90^o$ fibre directions, respectively while X_3 is perpendicular to the plane of the plies. Details of the manufacturing method and microstructure are given in Attwood et al. (2014). An optical micrograph of a cross-section of the HB26 composite is

shown in Fig. 5.2b. Russell et al. (2013) have reported that bright field microscopy (and SEM observations) of the as-polished surface of Dyneema® composites is misleading due to the presence of a very thin (of thickness on the order of a few microns) layer of smeared matrix and fibres. To obviate this problem, the image in Fig. 5.2b is taken using dark field microscopy.

5.2.2 Compression measurements

The compressive response of the Dyneema® composites was measured using cuboidal specimens of size $W \times H \times B = 6\ \text{mm} \times 4\ \text{mm} \times 9\ \text{mm}$ as shown in Fig. 5.3a with compression conducted in the X_1-direction. The specimens were cut from the as-manufactured HB26 composite plates using a medium-fine blade band-saw and comprised $n = 100$ plies along the side of length W. The compressive response is reported in terms of the applied nominal stress $\sigma_n \equiv F/(BW)$, where F is the applied compressive force in the X_1-direction, as a function of the nominal strain $\varepsilon_n \equiv \delta/H$, where δ is the work-conjugate compressive displacement to the force F. The details of the measurement of F and δ are explained in the context of the low and high strain rate measurements discussed subsequently.

5.2.2.1Low and intermediate strain rate tests

Low strain rate tests with strain rates in the range $0.01\ \text{s}^{-1} \leq \dot{\varepsilon}_n \leq 0.1\ \text{s}^{-1}$ were conducted in a screw-driven test machine while intermediate rate tests with strain rates in the range $0.1\ \text{s}^{-1} \leq \dot{\varepsilon}_n \leq 10\ \text{s}^{-1}$ required platen speeds up to $0.05\ \text{ms}^{-1}$. These intermediate rate tests were thus conducted in a hydraulic test machine. In both cases, the load cell of the test machine was used to measure the applied compressive force F while the displacement δ was inferred using a laser extensometer to measure the relative displacement of the compression platens of the test machine (Fig. 5.3a).

5.2.2.2High strain rate split Hopkinson bar tests

A split Hopkinson pressure bar (SHPB) setup was used to measure the compressive response for strain rates in the range $500\ \text{s}^{-1} \leq \dot{\varepsilon}_n \leq 4000\ \text{s}^{-1}$. A sketch of the setup is shown in Fig. 5.3b and was operated as follows. A striker bar was accelerated along a gun barrel by pressured nitrogen gas (0.05 - 0.1MPa). The striker bar velocity ($4\ \text{ms}^{-1} - 16\ \text{ms}^{-1}$) was measured using two light sensors at a spacing of 50 mm. Impact of the striker bar against the end of the input bar caused an elastic compression wave (incident wave) to propagate along the input bar. The resulting displacement of the input bar compressed the composite specimen sandwiched

between the input bar and an output bar. A fraction of the compression wave was transmitted through the specimen and into the output bar, whilst the remainder was reflected back along the input bar as a tensile wave. Strain gauges mounted mid-way along the input and output bars measured the bar strain as the incident, reflected and transmitted waves pass. These strain gauge readings were used to determine the stress versus strain response of the specimen.

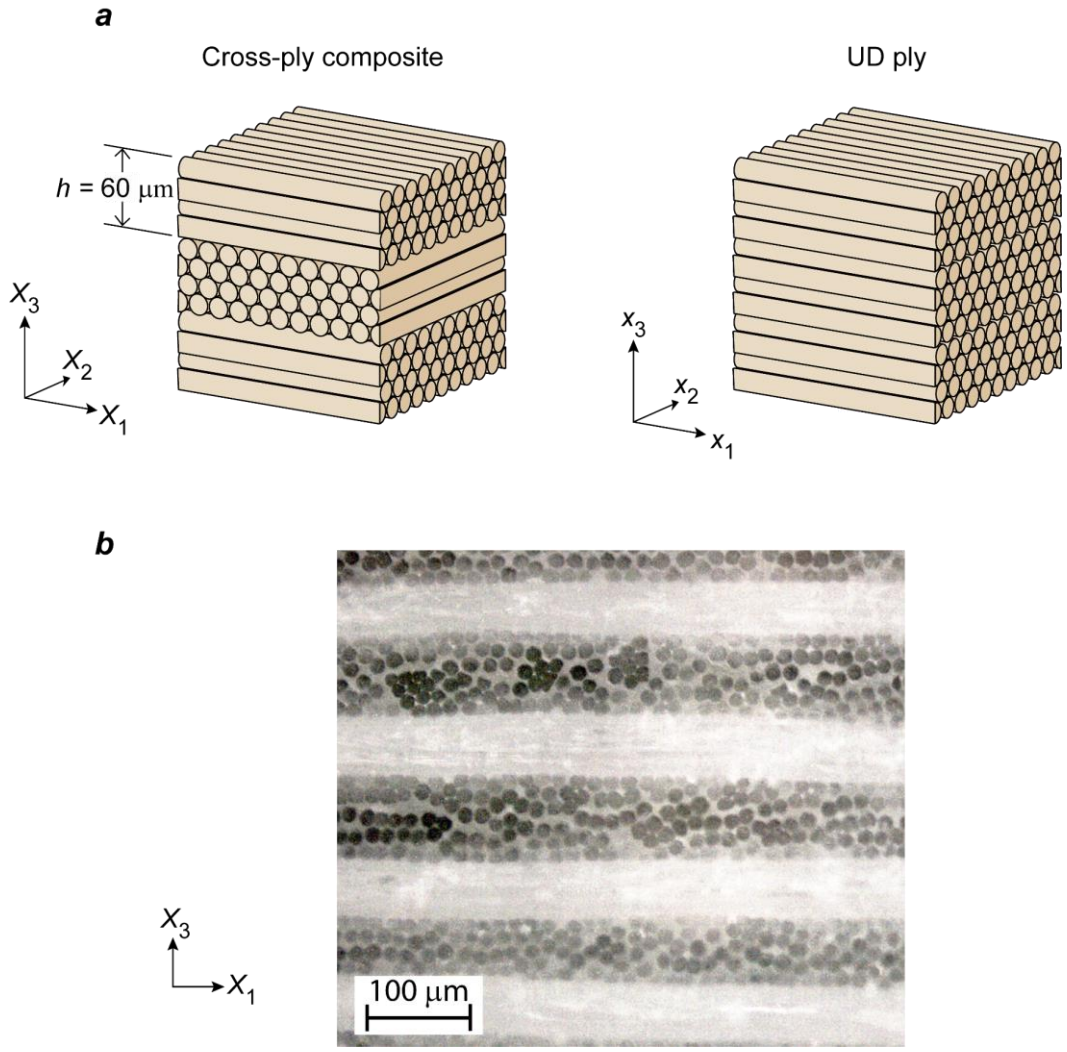

Figure 5.2: (a) Sketch of the $[0^o/90^o]_n$ composite comprising alternating plies of thickness h with 0^o and 90^o fibres. The global co-ordinate system X_i with the X_1 and X_2 directions aligned with the fibres in the alternating plies is shown along with a sketch of a single UD ply with the local co-ordinate system x_i. Here x_1 is along the fibre direction while x_3 is perpendicular to the plane of the ply. (b) Dark-field optical micrograph showing a section of the $X_1 - X_3$ plane through the HB26 Dyneema® composite.

The striker bar (of length 0.4 m), input bar (of length 1 m) and output bar (of length 1 m) were each made from $d = 12.7$ mm diameter AZM magnesium alloy rods. Magnesium alloy was

chosen to maximise the axial strain in the bars, as magnesium alloys have one of the lowest Young's modulus (44 GPa) of all metallic alloys readily available in rod form. Metallic pressure bars are preferable to polymeric pressure bars as they avoid the complications of dispersion and attenuation of the stress wave as it propagates along the bar (Bacon, 1999). The velocity of the striker was limited to ensure that the magnesium alloy did not yield during the impact between the striker and the input bar. Although the yield strength of the magnesium alloy (80 MPa) theoretically limits the striker impact velocity to $20\ \mathrm{ms}^{-1}$, in practice a safety margin is allowed for, and the striker was not fired at velocities in excess of $16\ \mathrm{ms}^{-1}$. Striker velocities of below $4\ \mathrm{ms}^{-1}$ could not be reliably produced due to barrel friction and this placed a lower limit on the strain rates that can be investigated in these tests.

The axial strains in the input bar and output bars were measured by two semi-conductor strain gauges (AFP-500-090 supplied by Kulite Sensors, Basingstoke, UK) bonded diametrically opposite to each other, and mid-way along the length of each bar. Semi-conductor strain gauges were preferred to conventional foil gauges as they are more sensitive: the AFP-500-090 gauges have gauge factors of 140, whereas foil gauges have gauges factors of about 2. The gauges were bonded onto the bars using a two-part room temperature cure adhesive AE10 (Micro-measurements, Basingstoke). The two AFP-500-090 gauges were connected in series with a $2200\ \Omega$ resistor. The axial strain was detected by measuring the change in the voltage across the series resistor. A Tektronix TDS420A oscilloscope measured and recorded the voltage versus time response during a compression test.

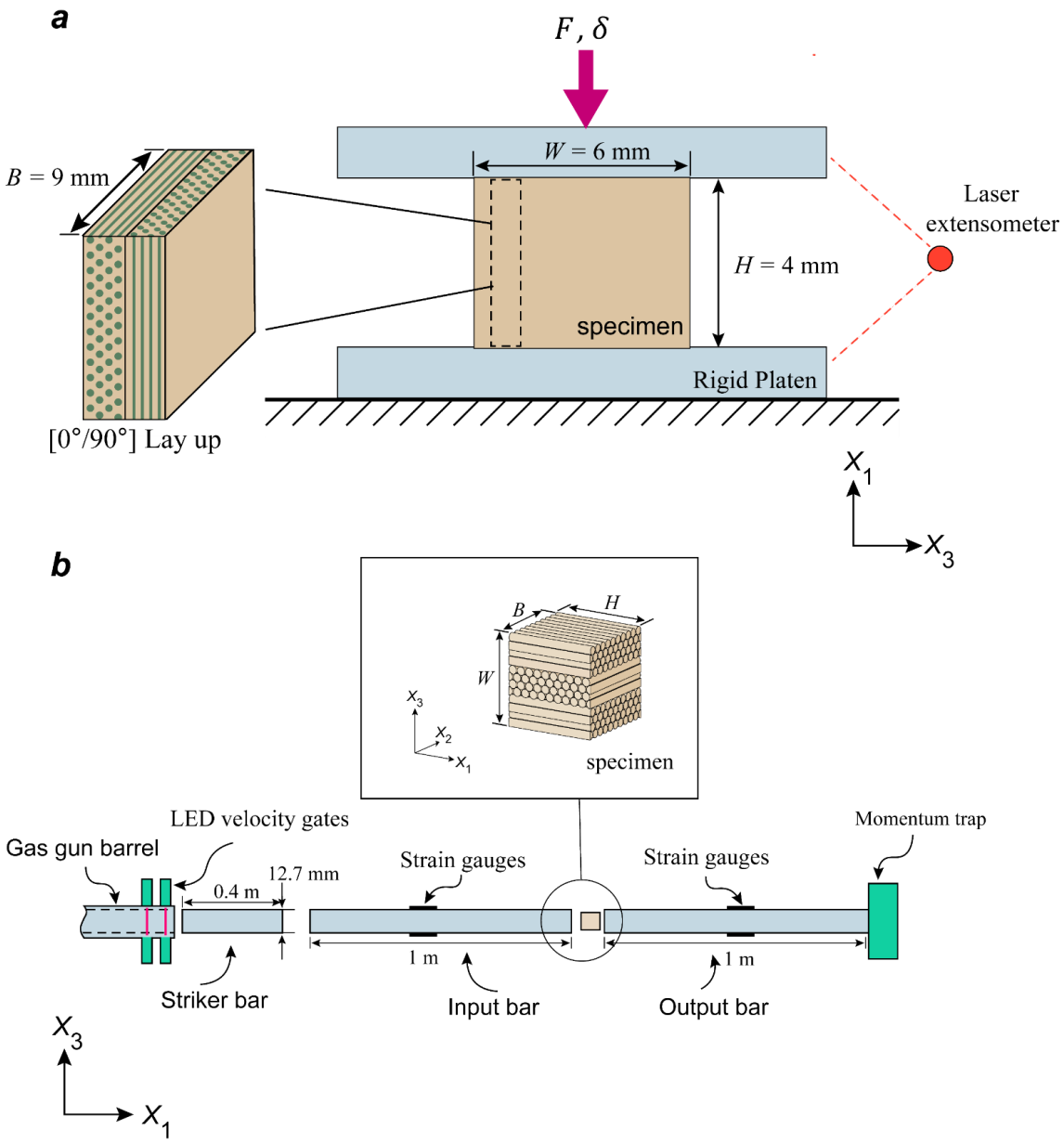

Figure 5.3: (a) Sketch of the specimen along with the co-ordinate system X_i. The compressive response is measured for compression in the X_1 direction. The specimen comprised $n = 100$ plies. (b) A schematic drawing of the split Hopkinson pressure bar experimental setup.

The nominal strain $\varepsilon_n(t)$ in the specimen at time t is given by

$$\varepsilon_n(t) = \frac{c_m}{H}\int_0^t [\varepsilon_i(t') - \varepsilon_r(t') - \varepsilon_t(t')]\, dt', \qquad (5.1)$$

where $c_m = 4944\ \text{ms}^{-1}$ is the measured elastic wave speed in the Mg bar, $\varepsilon_i(t)$ and $\varepsilon_r(t)$ are the axial strains in the input bar associated with the incident wave and reflected wave while $\varepsilon_t(t)$ is the engineering axial strain in the output bar associated with the transmitted wave. Here time $t = 0$ corresponds to the instant that that incident wave impinges upon the specimen and

the signals ε_i, ε_r and ε_t are shifted in Eq. (5.1) to this reference. The forces $F_i(t)$ on the impacted (i.e. specimen face in contact with the incident bar) and the force $F_t(t)$ on the specimen rear face are given by

$$F_i(t) = \frac{\pi d^2}{4} E_m[\varepsilon_i(t) + \varepsilon_r(t)], \tag{5.2}$$

and

$$F_t(t) = \frac{\pi d^2}{4} E_m \varepsilon_t(t), \tag{5.3}$$

respectively. The measurements revealed that the specimens attained axial equilibrium with $F_i \approx F_t$ for times $t > 2$ μs corresponding to approximately 5 elastic wave reflections over the specimen height H. The maximum strain rate investigated here is $\dot{\varepsilon}_n = 4000\ \mathrm{s}^{-1}$ and thus the specimen was in equilibrium at nominal strains in excess of 0.8 %. Thus, for all practical purposes it is reasonable to assume axial equilibrium throughout the test and we report the measured nominal stress as

$$\sigma_n(t) \equiv \frac{F_i(t) + F_t(t)}{2(BW)}. \tag{5.4}$$

Moreover, $F_i \approx F_t$ implies that $\varepsilon_t \approx \varepsilon_i + \varepsilon_r$ and (5.1) simplifies to

$$\varepsilon_n(t) = -\frac{2c_m}{H} \int_0^t \varepsilon_r(t')\, dt', \tag{5.5}$$

with the nominal applied strain rate given by

$$\dot{\varepsilon}_n = -\frac{2c_m}{H} \varepsilon_r. \tag{5.6}$$

Since $\varepsilon_t \ll \varepsilon_i$ (i.e., the transmitted pressure pulse is small compared to the incident wave due to the low strength of the Dyneema® composite), we have $\varepsilon_r \approx -\varepsilon_i$. However, recall that the incident pulse due to the impact of the striker is approximately is square wave and thus the applied strain rate is approximately constant over the test duration. Nevertheless, while reporting the results we report the time-averaged strain rate over the duration of the measurements.

5.3. Experimental results

We proceed to discuss the measurements of the compressive σ_n versus ε_n response and observations of the deformation modes for strain rates in the range $0.01\ \mathrm{s}^{-1} \leq \dot{\varepsilon}_n \leq 4000\ \mathrm{s}^{-1}$.

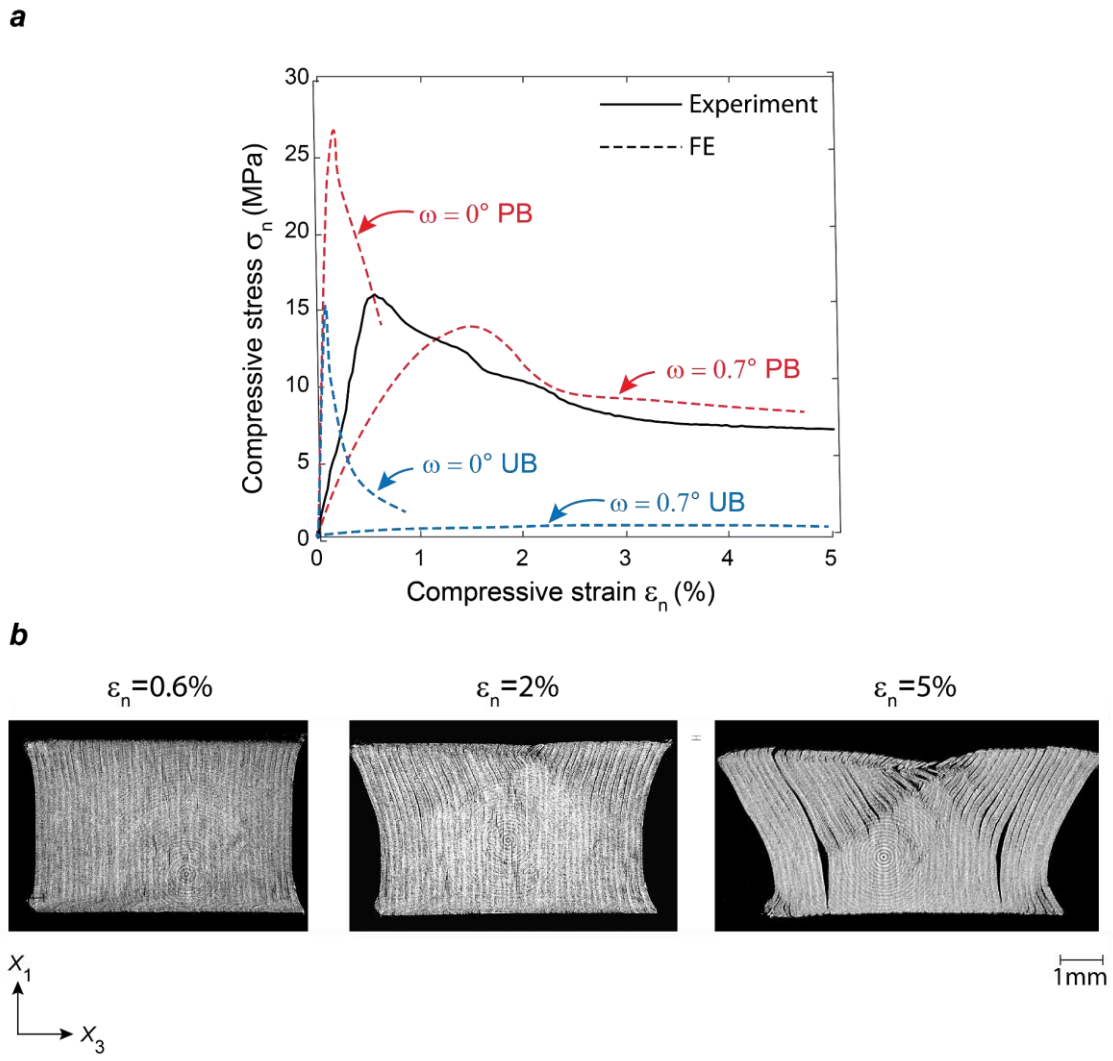

Figure 5.4: (a) The measured compressive stress σ_n versus strain ε_n response at an imposed quasi-static strain rate $\dot{\varepsilon}_n = 0.01\ \mathrm{s}^{-1}$. The corresponding perfectly bonded (PB) and un-bonded (UB) FE predictions for specimen misalignments $\omega = 0^o$ and $\omega = 0.7^o$ are also included. (b) X-ray computed tomography images of the quasi-statically tested specimen at three levels of compression ε_n. The images show the $X_1 - X_3$ midplane of the specimen.

5.3.1 Quasi-static compression

The measured σ_n versus ε_n response at an imposed nominal strain rate $\dot{\varepsilon}_n = 0.01\ \mathrm{s}^{-1}$ is included in Fig. 5.4a. After an initially linear response a peak compressive strength is attained at $\sigma_c \approx 16$ MPa followed by softening. To better understand the deformation mode, we include

in Fig. 5.4b X-ray computed tomography (XCT) micrographs of the specimen at three levels of applied strain ε_n. These images showing the $X_1 - X_3$ midplane of the specimen were taken by interrupting the compression tests at these selected strain levels. The peak compressive strength is attained at $\varepsilon_n \approx 0.6$ %: at this strain level there are no clear signs of localised ply level deformation within the specimen although overall deformation of the specimen is observed resulting in it assuming an hourglass shape. Beyond the peak strength at $\varepsilon_n = 2$ % the hourglass shape of the specimen is accentuated but now the formation of a ply-level kink band near the top edge of the specimen is observed. This kind band is seen to propagate and broaden for an imposed strain $\varepsilon_n = 5$ % and this is accompanied by extensive ply delamination.

The peak strength and deformation mode comprising ply level kink band formation and propagation are largely consistent with detailed quasi-static observations reported by Attwood et al. (2015). However, there is one crucial discrepancy. Attwood et al. (2015) as well as the quasi-static tension study by Russell et al. (2013) both have reported a Young's modulus of the HB26 Dyneema® composite that is largely consistent with a simple rule of mixtures estimate. This is calculated as follows. The Young's moduli of the SK76 fibres and matrix are $\mathcal{E}_f = 100$ GPa and $\mathcal{E}_m = 10$ GPa, respectively while the fibre volume fraction $V_f = 0.83$. Then the Young's modulus of the 0^o plies in the fibre direction is given by a Voigt bound as $E_0 = V_f\mathcal{E}_f + (1 - V_f)\mathcal{E}_m = 80$ GPa and assuming the transverse fibre modulus is equal to that of the matrix, the Young's modulus of the 90^o plies in the same direction is $E_{90} = E_m$. The Young's modulus (in the X_1 direction) of the composite comprising equal thickness 0^o and 90^o plies then follows as $E_c = (E_{90} + E_0)/2 = 45$ GPa. This estimate is significantly higher than the modulus we infer from the initial linear regime of the σ_n versus ε_n response in Fig. 5.4a. We shall subsequently argue that this is due to misalignment of the specimen with the compression platens.

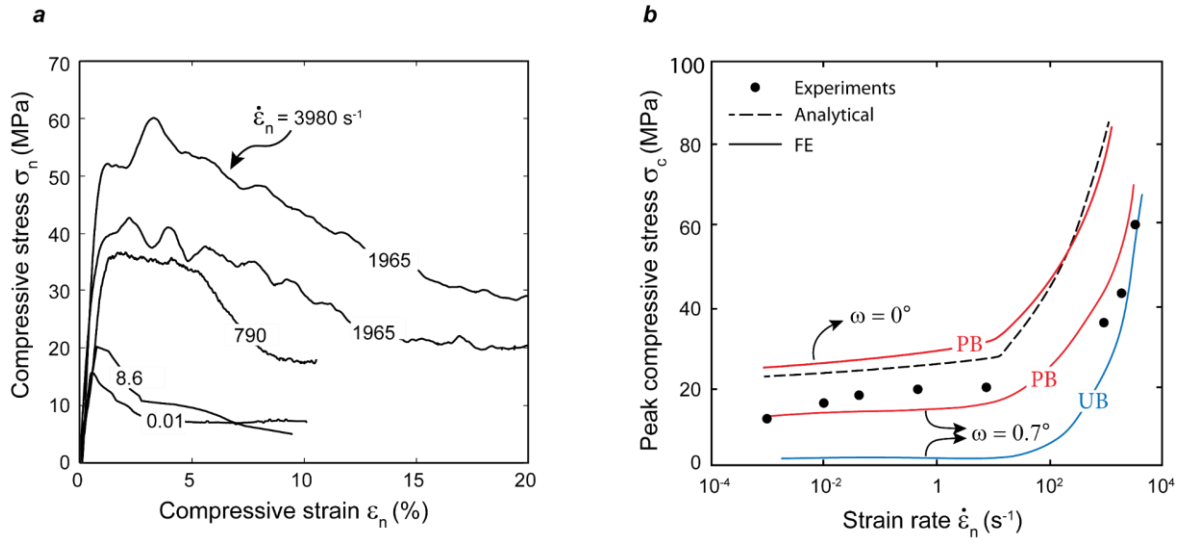

Figure 5.5: (a) The measured compressive stress σ_n versus compressive strain ε_n responses for imposed strain rates in the range $8\ \mathrm{s}^{-1} < \dot{\varepsilon}_n < 4000\ \mathrm{s}^{-1}$. The quasi-static measurement from Fig. 5.4a is also included for comparison purposes. (b) A summary of the measured peak compressive strength σ_c as a function of the imposed strain rate $\dot{\varepsilon}_n$. The corresponding FE predictions for a specimen misalignment $\omega = 0.7^{\mathrm{o}}$ for the perfectly bonded (PB) and un-bonded (UB) cases are included along with the PB analytical and FE predictions of the aligned specimen with $\omega = 0^{\mathrm{o}}$.

5.3.2 Intermediate and high strain rate compression

The measured compressive responses for strain rates in the range $8\ \mathrm{s}^{-1} < \dot{\varepsilon}_n < 4000\ \mathrm{s}^{-1}$ are plotted in Fig. 5.5a with the quasi-static measurement from Fig. 5.4a also included for comparison purposes. The initial linear regime is largely unaffected by the imposed strain rate but clearly the peak strength σ_c and the strain at which this strength is attained both increase with increasing $\dot{\varepsilon}_n$. Moreover, this increase in σ_c is relatively mild for the strain rates in the range $0.01\ \mathrm{s}^{-1} < \dot{\varepsilon}_n < 10\ \mathrm{s}^{-1}$ but clearly there is a strong strain rate dependency at the higher strain rates $\dot{\varepsilon}_n > 700\ \mathrm{s}^{-1}$. To better quantify this effect, we include in Fig. 5.5b the measurements of the peak compressive strength σ_c as a function of $\dot{\varepsilon}_n$ over the whole range of strain rates investigated here with the abscissa of Fig. 5.5b using a logarithmic scale. Here the inference drawn from Fig. 5.5a is confirmed with σ_c showing a mild strain rate dependency at low and intermediate strain rates but with the peak compressive strength increasing sharply with increasing strain rate for $\dot{\varepsilon}_n > 100\ \mathrm{s}^{-1}$.

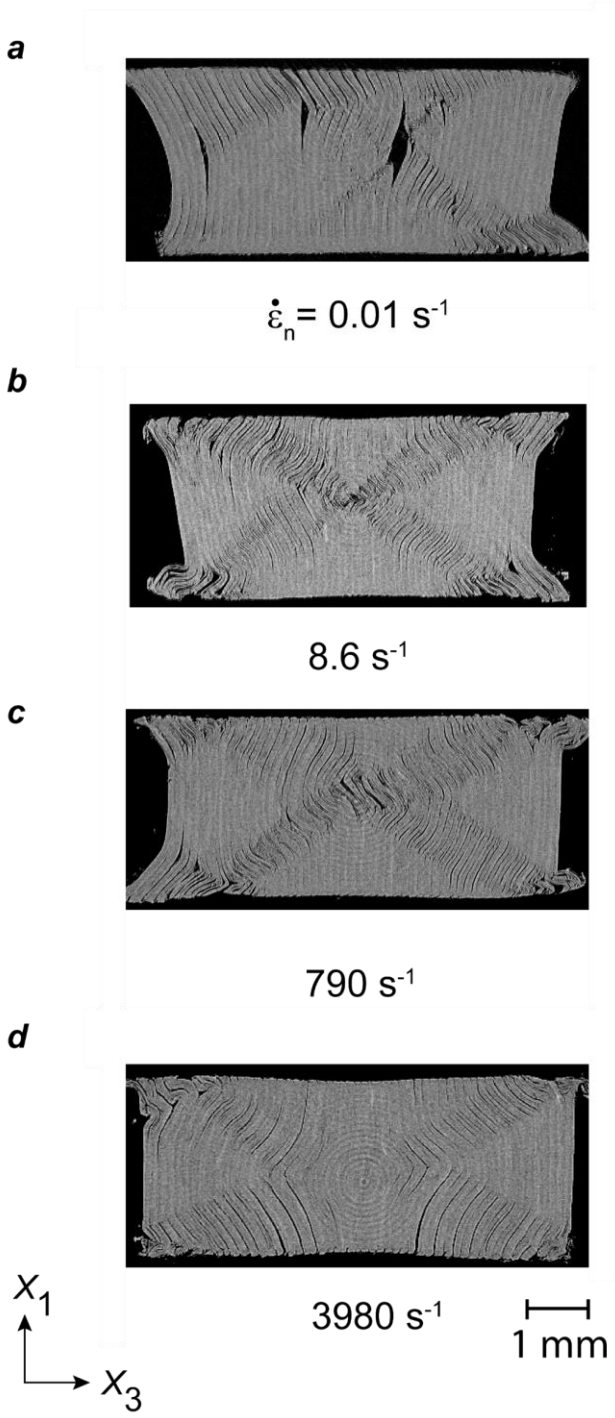

Figure 5.6: X-ray computed tomography images of the specimen after compression to $\varepsilon_n \approx 25$ % at strain rates (a) $\dot{\varepsilon}_n = 0.01\ \mathrm{s}^{-1}$, (b) $\dot{\varepsilon}_n = 8.6\ \mathrm{s}^{-1}$, (c) $\dot{\varepsilon}_n = 790\ \mathrm{s}^{-1}$ and (d) $\dot{\varepsilon}_n = 3980\ \mathrm{s}^{-1}$. The images show the $X_1 - X_3$ midplane of the specimen.

To better understand the deformation modes over the range of strain rates investigated here we again attempted to visualise the specimen deformations using XCT micrographs similar to those for the quasi-static case in Fig. 5.4b. Interrupting specimen compression in an SHPB test

requires encasing the specimen in a steel jacket that arrests the displacement imposed by the input bar and prevents continued deformation of the specimen after the jacket has contacted the bar. However, this generates large stresses within the Magnesium (Mg) bars and results in either the fracture or yield of the bars. Thus, we did not arrest compression early in the SHPB tests but rather only visualised deformation after full compression at strains $\varepsilon_n \approx 25\ \%$. XCT micrographs of the $X_1 - X_3$ midplane of the specimens deformed to $\varepsilon_n \approx 25\ \%$ at four selected strain rates in the range $0.01\ \mathrm{s}^{-1} < \dot{\varepsilon}_n < 4000\ \mathrm{s}^{-1}$ are included in Fig. 5.6. While kink bands are observed in all cases, some crucial differences emerge with increasing strain rate. In particular, the level of delamination decreases with increasing strain rate and this seems to be associated with specimens deforming in a more symmetric manner that is associated with the formation of symmetric kind bands and a consequent reduction in the hourglass shape of the deformed specimen. In fact, at high strain rates the kink bands seem to be co-incident with the specimen diagonals suggesting that they are initiated by stress concentrations at the specimen corners.

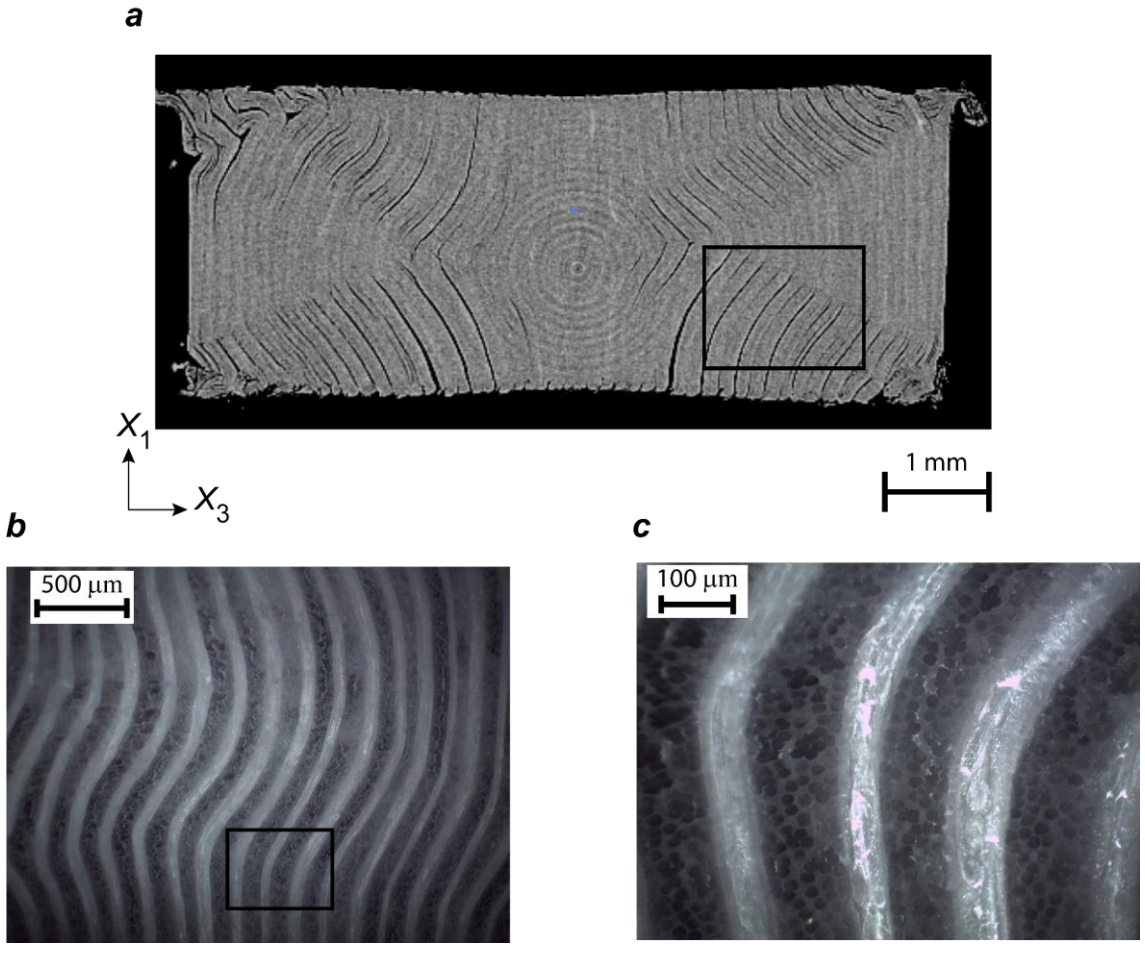

Figure 5.7: Magnified views of the kink-band within the specimen compressed at a strain rate $\dot{\varepsilon}_n = 3980\ \mathrm{s}^{-1}$ to a strain $\varepsilon_n \approx 25\ \%$. (a) X-ray computed tomography image of the $X_1 - X_3$ midplane of the specimen. (b) Dark-field optical micrograph of the area highlighted in Fig. 5.7a and (c) a higher magnification optical micrograph of the area highlighted in Fig. 5.7b.

The structure of the kink band under quasi-static compression has been reported by Attwood et al. (2015); see Fig. 5.1b. To better visualise the details of the kink bands that develop under high rate compression we consider the $\dot{\varepsilon}_n = 3980\ \mathrm{s}^{-1}$ test. The $\dot{\varepsilon}_n = 3980\ \mathrm{s}^{-1}$ specimen was sectioned and polished to reveal the midplane shown in the XCT micrograph in Fig. 5.6d. Dark field optical micrographs of the area marked in Fig. 5.7a are shown at two levels of magnification in Figs. 5.7b and 5.7c. The kinks bands under high rate compression are similar to those observed by Attwood et al. (2015) under quasi-static compression with the micro-buckling occurring at the ply level. The main difference is that the kink band under high rate compression is less distinct with smaller ply curvatures delineating the kinked and unkinked regions of the specimen.

5.4. Numerical simulations of the compressive response

5.4.1 Constitutive model

In order to gain an understanding of the mechanisms governing the compressive response under quasi-static and high rates of compression we now develop a numerical approach to model the experiments via detailed finite element (FE) calculations. In these calculations, each ply within the composite specimen is explicitly modelled using the pressure-dependent crystal plasticity framework developed in Chapter 3. This approach not only appropriately models the fibre and ply rotations that are critical to accurately capture the large rotations within the kink bands, but also the pressure-dependent yield of the HB26 Dyneema® composite. In chapter 3, we employed a viscoplastic relation for effective resolved shear stress $\hat{\tau}^{(\kappa)}$ and the shear rate $\dot{\gamma}^{(\kappa)}$ that approximated a rate independent response, see (3.16). However, the measurements reported in this study indicate a strongly rate dependent response which has motivated us to propose a relation in terms of a reference strain rate $\dot{\gamma}_0$ of the form

$$\frac{\dot{\gamma}^{(\kappa)}}{\dot{\gamma}_0} = \begin{cases} 0 & 2\hat{\tau}^{(\kappa)} \le \tau_Y \\ \left[\dfrac{2\hat{\tau}^{(\kappa)}}{\tau_Y} - 1\right]^q & \tau_Y < 2\hat{\tau}^{(\kappa)} \le \tau_Y \left[\left(\dfrac{\dot{\gamma}_t}{\dot{\gamma}_0}\right)^{1/q} + 1\right] \\ \left[\dfrac{\dot{\gamma}_0}{\dot{\gamma}_t}\right]^{(e-q)/q} \left[\dfrac{2\hat{\tau}^{(\kappa)}}{\tau_0} - 1\right]^e & 2\hat{\tau}^{(\kappa)} > \tau_Y \left[\left(\dfrac{\dot{\gamma}_t}{\dot{\gamma}_0}\right)^{1/q} + 1\right], \end{cases} \tag{5.7}$$

such that the slip system remains elastic below a yield strength τ_Y with the plastic strain rate vanishing for $2\hat{\tau}^{(\kappa)} \le \tau_Y$. With increasing strain rate, we propose two regimes with power law exponents q and e on either side of a transition strain rate $\dot{\gamma}_t$.

Most of the material properties employed here are taken from previous investigations for the Dyneema® HB26 composite; see Chapter 3. The exceptions are the rate dependent plastic properties in Eq. (5.7) that are calibrated using the measurements reported in this study. For the sake of completeness here we specify all the properties required for the constitutive model. Based on the experimental measurements reported in Russell et al. (2013) and Attwood et al. (2014), the elastic moduli are $E_f = 80$ GPa, $E_m = 10$ GPa and $G_{12} = 3$ GPa while the Poisson's ratios are $\upsilon_{12} = 0$ and $\upsilon_{23} = 0.5$. The shear strength of the composites is $\tau_Y = 2$ MPa at reference strain rate $\dot{\gamma}_0 = 0.1\ \mathrm{s}^{-1}$ while the pressure sensitivity co-efficient is $\mu = 0.05$ (Attwood et al., 2014; Chocron et al., 2014). The strain rate sensitivity parameters are chosen to be $\dot{\gamma}_t = 533\ \mathrm{s}^{-1}$ with $q = 26$ used to set a mild strain rate sensitivity in the low strain rate regime while the strong strain rate sensitivity in the high strain rate regime is captured using $e = 3$. The FE calculations were performed in a dynamic setting to allow for inertial effects with the material density set to $\rho = 970\ \mathrm{kg\ m}^{-3}$ consistent with the measured density of Dyneema® composites.

5.4.2 Finite element simulations

We simulated the compression of the specimen of dimension $W \times H$ in a plane strain setting with deformation constrained to the $X_1 - X_3$ plane as shown in Fig. 5.8a. Consistent with the experiments, the specimens were modelled comprising alternating $0^o/90^o$ plies of thickness $h = 60$ μm with overall specimen dimensions $W = 6$ mm and $H = 4$ mm (unit thickness in the X_2-direction). Each of the $n = 100$ plies were modelled using the constitutive model detailed in Section 5.4.1 with x_1 along the X_1-direction for the 0^o plies and x_1 along the X_2-direction for the 90^o plies. The FE calculations were conducted using the explicit dynamic version of the commercial finite element package ABAQUS with the crystal plasticity

constitutive model implemented using the user-defined material model functionality VUMAT. The plies were discretised via eight-noded linear elements with reduced integration (C3D8R in the ABAQUS notation) of size $h/10$. This implies that there were approximately 10 elements across each ply and this enabled the calculations to accurately capture the bending deformation of each ply. The experiments were simulated by modelling compression of the specimen between rigid platens (Fig. 5.8a) using the frictionless contact capability in ABAQUS and imposing a velocity $\dot{\delta}$ on the top platen with the bottom platen held fixed. The nominal strain rate is then given as in the experiments by $\dot{\varepsilon}_n \equiv \dot{\delta}/H$ with the nominal stress defined as $\sigma_n \equiv F/W$, where F is the force work-conjugate to the imposed displacement δ and the corresponding nominal strain is given by $\varepsilon_n \equiv \delta/H$.

Two types of imperfections were included in the specimens in order to trigger the appropriate kinking modes and obtain agreement with the measurements reported in Section 5.3. Misalignment between the specimen and the loading platens was considered by modelling a trapezoidal shaped specimen such that the specimen's top surface made was inclined at an angle ω with respect to the platen as shown in Fig. 5.8a. Simulations are presented for $0^{\mathrm{o}} \leq \omega \leq 1^{\mathrm{o}}$. In addition, to appropriately capture the micro-buckling deformation we also included fibre misalignment/waviness within the specimen as employed in numerous previous investigations (Budiansky and Fleck, 1993; Slaughter et al., 1996; Vogler and Kyriakides, 1997) of the micro-buckling of fibre composites. Here we include two bands of misaligned fibres that are inclined at angle $\pm\beta$ and along the specimen diagonals as shown in Fig. 5.8a. In these bands of width w, the x_1 fibre direction in the 0^{o} plies was assumed to be misaligned by an angle $\bar{\phi}$ with respect to the global X_1 −direction as shown in the inset of Fig. 5.8b. This directly simulates the initial fibre waviness/misalignment within the 0^{o} plies. Attwood et al. (2015) reported detailed measurements of kink band formation in the HB26 composite under quasi-static loading conditions and based on those measurements we set $\beta = 30^{\mathrm{o}}$, $\bar{\phi} = 5^{\mathrm{o}}$ and $w = 1$ mm in the simulations reported here.

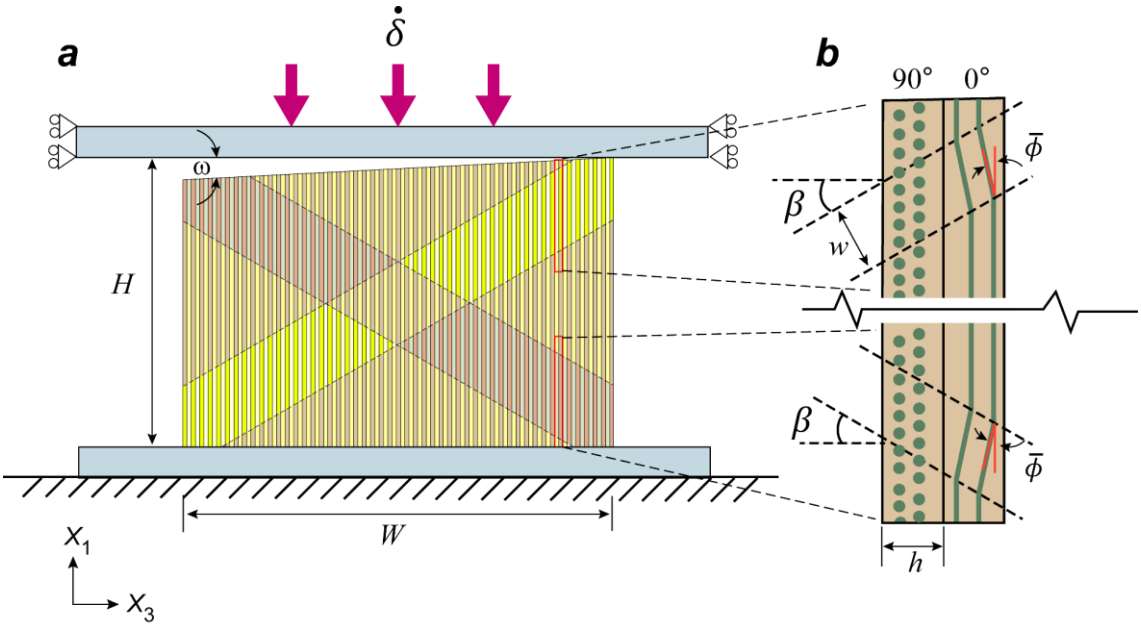

Figure 5.8: (a) Sketch of the plane strain boundary value problem of the compression of a specimen comprising $n = 100$ alternating $0^o/90^o$ plies between rigid-frictionless platens. The specimen is shown with the two bands in which the fibres are initially misaligned with the 0^o plies. The misalignment angle ω between the specimen and the platens is also indicated. (b) A detailed view of the structure of the initial fibre misalignments $\bar{\phi}$ within the bands of width w oriented at angles $\pm\beta$.

It now remains to specify the bonding between the alternating $0^o/90^o$ plies in the specimens. The experiments discussed in Section 5.3 show that while there is no significant delamination between the plies prior to the peak strength being attained, significant delamination is observed later in the deformation. Here we do not model the details of this delamination process as it requires detailed knowledge of the mixed-mode delamination strengths and toughnesses. Rather we take a simplified view and model two extremes:

(i) The perfectly-bonded limit (PB) where the plies are assumed to be perfectly bonded throughout the deformation history such that adjacent material points on the $0^o/90^o$ plies in contact with each other share a common displacement.

(ii) The un-bonded limit (UB) where we assume no bonding between the plies throughout the deformation history. In these calculations each ply is modelled individually along with frictionless hard contact defined between the plies.

5.5. Numerical results and discussion

5.5.1 Quasi-static compression and the effect of specimen misalignment

We first establish the effect of specimen misalignment in the quasi-static setting for an imposed strain rate $\dot{\varepsilon}_n = 0.01\ \mathrm{s}^{-1}$ and consider the perfectly-bonded (PB) limit. Predictions of the σ_n versus ε_n response are included in Fig. 5.9 for misalignment angles in the range $0^{\mathrm{o}} \leq \omega \leq 1^{\mathrm{o}}$. With increasing ω we observe that not only does the initial stiffness $d\sigma_n/d\varepsilon_n$ decrease, but also the peak compressive strength σ_c reduces. Moreover, the post peak strength softening rate is also reduced with increasing misalignment ω. In order to visualise the predicted deformation mode, we include in Figs. 5.10a and 5.10b FE predictions of the spatial distributions of the total Green-Lagrange strain E_{13} at two levels of applied strains ε_n for the $\omega = 0^{\mathrm{o}}$ and $\omega = 0.7^{\mathrm{o}}$ cases, respectively. Employing the global co-ordinate system X_i, E_{ij} is defined as

$$E_{ij} = \frac{1}{2}\left(F_{ki}F_{kj} - \delta_{ij}\right), \tag{5.8}$$

and measures the total strain that includes the elastic and plastic contributions to the deformation. In both Figs. 5.10a and 5.10b the two strain levels shown are selected so that they correspond to the strain at which the peak stress occurs and another higher strain level during the softening phase. For the specimen with no misalignment (i.e., $\omega = 0^{\mathrm{o}}$), deformation is symmetric and occurs by the formation of kink bands that mirror the fibre misalignments included a priori in the calculations. By contrast, misalignment breaks this initial symmetry with now one dominant kink band forming as seen in Fig. 5.10b.

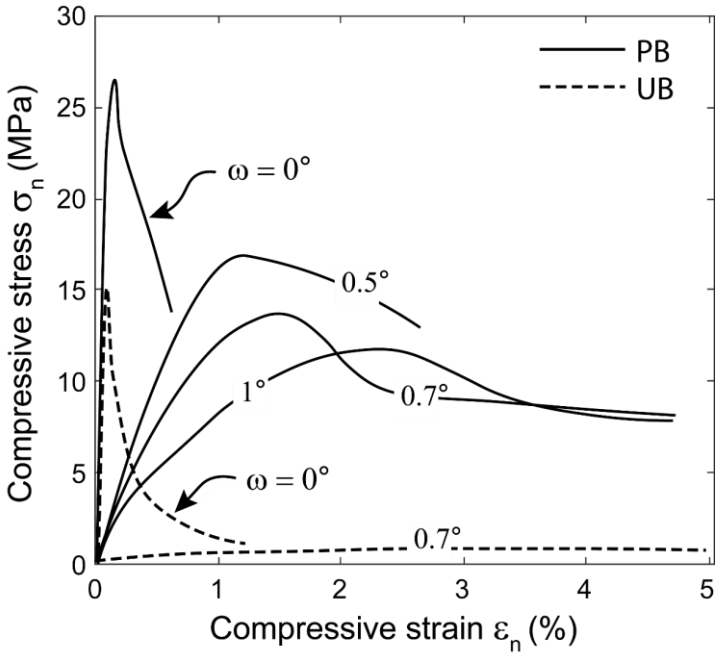

Figure 5.9: FE predictions of the compressive stress σ_n versus strain ε_n response for quasi-static compression at a strain rate $\dot{\varepsilon}_n = 0.01\ \mathrm{s}^{-1}$. Predictions are shown for calculations with perfectly-bonded (PB) and un-bonded (UB) plies for a selection of specimen misalignments ω.

Next consider the un-bonded (UB) limit. Predictions of the σ_n versus ε_n response are included as dashed lines in Fig. 5.9 for misalignment angles $\omega = 0^{\mathrm{o}}$ and $\omega = 0.7^{\mathrm{o}}$ respectively. In the absence of misalignment, the initial stiffness $d\sigma_n/d\varepsilon_n$ is similar to the PB case but the peak strength is significantly reduced. However, with increasing specimen misalignment, both $d\sigma_n/d\varepsilon_n$ and the peak strength σ_c are lower in the UB case compared to the PB limit. In order to understand the deformation modes that give rise to differences between the UB and PB limits we include in Figs. 5.11a and 5.11b the UB predictions of the spatial distributions of E_{13} for the $\omega = 0^{\mathrm{o}}$ and $\omega = 0.7^{\mathrm{o}}$ cases, respectively at two strain levels ε_n equal to those chosen in Fig. 5.10. For the perfectly aligned specimen (Fig. 5.11a), at $\varepsilon_n = 0.1$ % there is negligible separation between the plies which results in the initial stiffness of the PB and UB cases being very similar. However, the absence of shear coupling or bonding between the plies implies that each ply deforms independently resulting in the lower peak strength. In fact, even at $\varepsilon_n = 0.1$ % we observe that although a kind band is seen to initiate, the deformation mode is not perfectly symmetric. Continued ply rotation within the kink band results in the plies separating as clearly seen for an imposed deformation of $\varepsilon_n = 1$ %. For the misaligned specimen with $\omega = 0.7^{\mathrm{o}}$, complete ply separation occurs very early in the deformation history with no distinct kink band formation. Rather the mode now just involves independent deformation of each ply.

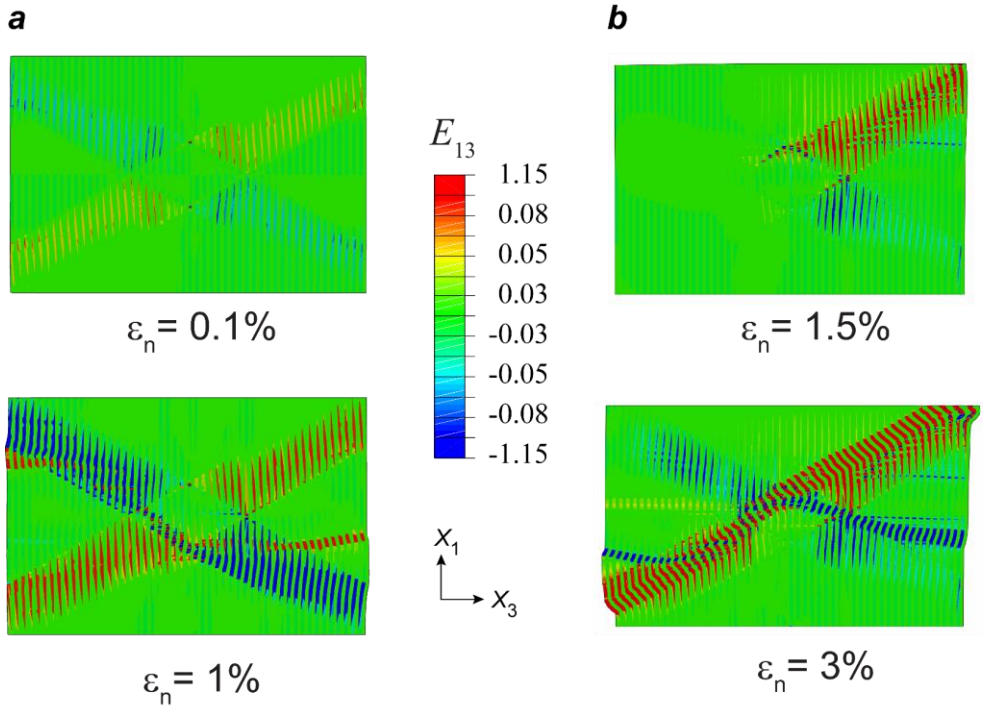

Figure 5. 10: FE predictions of the deformation modes for quasi-static compression at a strain rate $\dot{\varepsilon}_n = 0.01\ s^{-1}$ in the perfectly-bonded (PB) case with specimen misalignments (a) $\omega = 0^o$ and (b) $\omega = 0.7^o$. In both cases the deformed states are shown with spatial distributions of the Green-Lagrange strain E_{13} at two levels of applied strain ε_n.

A comparison between selected predictions ($\omega = 0^o$ and 0.7^o for both the PB and UB cases) and measurements is included in Fig. 5.4a. While the perfectly aligned specimen with $\omega = 0^o$ overpredicts the modulus significantly, the PB case with a misalignment $\omega = 0.7^o$ is in reasonable overall agreement with the measured response. On the other hand, UB case gives poor agreement with the perfectly aligned specimen overpredicting the modulus and the softening rate while the $\omega = 0.7^o$ significantly underestimating both the modulus and strength. We emphasize that the agreement between the simulations and measurements for the PB is not perfect but the results clearly demonstrate that a small specimen misalignment (of a level that is unavoidable in UHMWPE composite specimen preparation) has a significant influence and that the perfectly-bonded limit gives results closer to the measurements. Given these results we shall focus the remainder of the simulations on specimens with a misalignment $\omega = 0.7^o$ and discuss results for both the UB and PB cases.

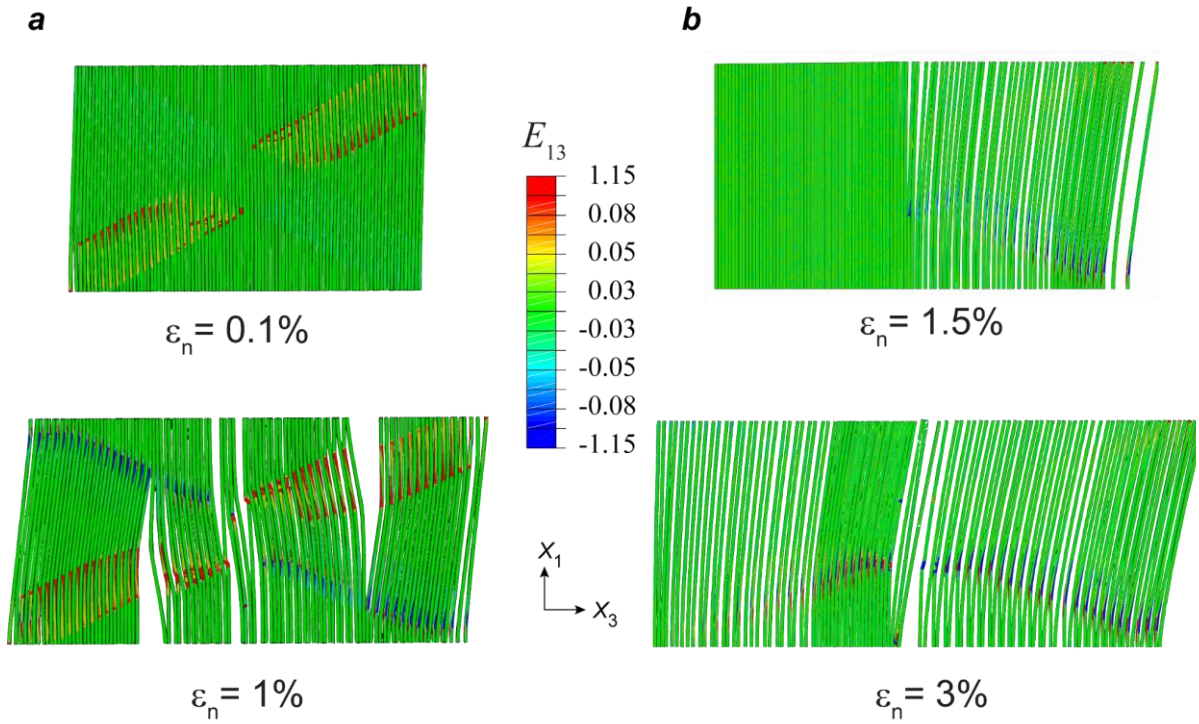

Figure 5.11: FE predictions of the deformation modes for quasi-static compression at a strain rate $\dot{\varepsilon}_n = 0.01\ s^{-1}$ in the un-bonded (UB) case with specimen misalignments (a) $\omega = 0^o$ and (b) $\omega = 0.7^o$. In both cases the deformed states are shown with spatial distributions of the Green-Lagrange strain E_{13} at two levels of applied strain ε_n.

5.5.2 Comparison between measurements and predictions for high strain rate compression

A comparison between the measured and predicted σ_n versus ε_n responses for applied strain rates $\dot{\varepsilon}_n = 790\ s^{-1}$ and $3980\ s^{-1}$ is shown in Figs. 5.12a and 5.12b, respectively. Both the UB and PB case simulations are included for a specimen misalignment $\omega = 0.7^o$. At the lower strain rate of $\dot{\varepsilon}_n = 790\ s^{-1}$, the PB case is in good agreement with the measurements capturing both the peak strength and the subsequent softening. By contrast, the UB case under-predicts the strength as well as overpredicting the subsequent softening rate. These results are generally in line with the corresponding comparisons in the quasi-static case (Fig. 5.4a) where again the PB case was in better agreement with the measurements. On the other hand, at the high strain rate of $\dot{\varepsilon}_n = 3980\ s^{-1}$, the PB simulations are in good agreement with measurements of the peak strength as well as the strength at large strains ($\varepsilon_n > 0.15$). However, the simulations predict a softening rate immediately after the peak strength is attained that is higher than that in the measurements. The reason for this discrepancy is not immediately clear but could be related to the imperfections (both microstructural as well as specimen level misalignments) not

being appropriately modelled. The UB simulations capture the peak strength with reasonable accuracy but significantly overpredict the subsequent softening rate. In fact, the UB simulations predict complete ply separation with negligible strength for strains $\varepsilon_n > 0.04$ and hence the predictions are terminated prematurely in Fig. 5.12b.

Predictions of the high strain rate ($\dot{\varepsilon}_n = 790\ \mathrm{s}^{-1}$) deformation modes for the UB and PB cases are included in Figs. 5.13a and 5.13b, respectively. In these figures we show spatial distributions of E_{13} at applied strains $\varepsilon_n = 2$ % and 6 % on the deformed configurations. The PB simulations (Fig. 5.13b) are very much in line with the XCT micrograph in Fig. 5.6c with symmetric kink bands forming along the specimen diagonals. Thus, unlike in the quasi-static case (Fig. 5.10b), the specimen misalignment does not break the symmetry of the initially imposed ply level imperfections with inertia ensuring a symmetric deformation mode. Similarly, differences also emerge in the UB case with the quasi-static simulations. Now, unlike the results in Fig. 5.11, ply separation occurs relatively late in the simulations with no clear signs of separation seen at $\varepsilon_n = 2$ % (Fig. 5.13a). This is because transverse inertia retards the separation of the plies at these high rates of deformation. As a consequence, UB simulations even with misaligned specimens capture the peak strength with good accuracy at the higher strain rates; see Fig. 5.12b. However, ply separation sets in by $\varepsilon_n = 6$ % and this is the reason behind the high softening rates in the UB simulations (Fig. 5.12).

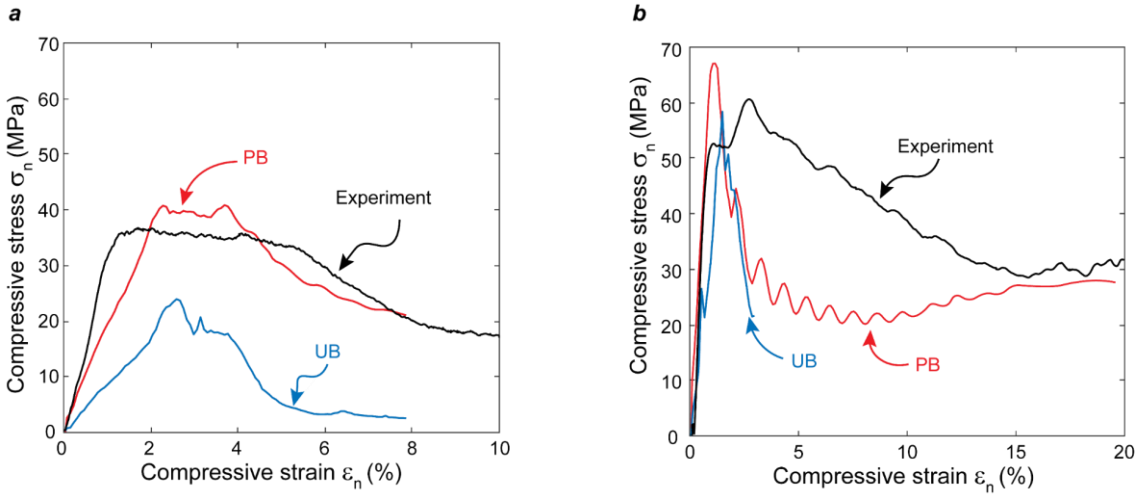

Figure 5.12: A comparison between measurements and FE predictions of the high strain rate compressive response for applied strain rates (a) $\dot{\varepsilon}_n = 790\ \mathrm{s}^{-1}$ and (b) $\dot{\varepsilon}_n = 3980\ \mathrm{s}^{-1}$. Both the perfectly-bonded (PB) and un-bonded (UB) FE predictions are included for a specimen misalignment $\omega = 0.7^{\mathrm{o}}$.

A comparison between measurements and predictions of the peak compressive strength σ_c is included in Fig. 5.5b over the entire range of strain rates investigated here. With a specimen misalignment $\omega = 0.7^o$, the PB simulations are in excellent agreement while the UB simulations significantly under-predict the strength especially at the lower strain rates. This underprediction by the UB simulations is a result of premature ply separation and this separation is retarded by transverse inertia results at the higher strain rates. As a consequence, the UB simulations predict the peak strength at the higher strain rates as discussed in the context of Fig. 5.12b. Predictions of the PB simulations for the perfectly aligned specimen ($\omega = 0^o$) are also included in Fig. 5.5b and those overpredict the peak strength. In summary, the PB simulations including specimen misalignment represent a reasonable method to simulate the compressive response over the wide range of strain rates, $0.01\ \mathrm{s}^{-1} \leq \dot{\varepsilon}_n < 4000\ \mathrm{s}^{-1}$, investigated here.

5.5.3 Matrix strain rate sensitivity versus inertia effects

The strong strain rate sensitivity of the compressive strength σ_c in both the measurements and simulations could have two possible origins:

(i) Matrix strain rate sensitivity such that the shear strength of the composite (which is mainly governed by the shear strength of the matrix) increases with increasing strain rate.

(ii) Micro-inertial effects where the kinking/micro-buckling is retarded due to the transverse inertia of the plies. Such an effect was proposed by Slaughter et al. (1996) in the context of micro-buckling of UD fibre composites and by Calladine and English (1984) for understanding rate sensitivity of the collapse load of columnar structures. This latter situation of the inertial stabilisation of the buckling modes has been extended to various structural settings by numerous subsequent researchers; see for example Radford et al. (2007) and Vaughn and Hutchinson (2006).

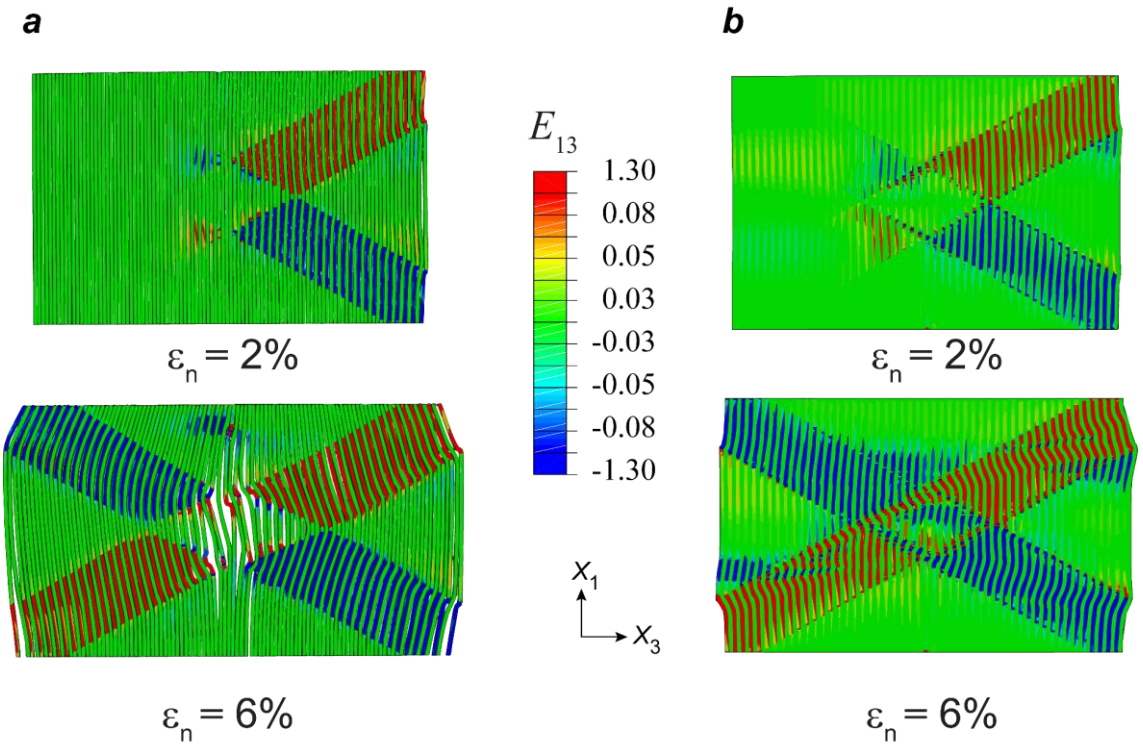

Figure 5.13: FE predictions of the deformation modes for high strain rate compression at $\dot{\varepsilon}_n = 790\ \mathrm{s}^{-1}$ with a specimen misalignment $\omega = 0.7^{\mathrm{o}}$. The spatial distributions of the Green-Lagrange strain E_{13} are shown on the deformed states at applied strain levels $\varepsilon_n = 2$ % and 6 % for the (a) un-bonded (UB) and (b) perfectly-bonded (PB) simulations.

To try and delineate these two effects that can both give rise to an increase in strength with increasing strain rate, we performed FE simulations wherein we reduced the density ρ of the UD plies of the composite while keeping all other properties fixed at their reference value. Reducing the material density reduces the effect of inertia and thereby permits uncovering the relative effect of inertia versus material strain rate sensitivity in the simulations. The predicted compressive response at $\dot{\varepsilon}_n = 3980\ \mathrm{s}^{-1}$ in the PB case with $\omega = 0.7^{\mathrm{o}}$ is shown in Fig. 5.14a for densities ranging from the actual material value of $\rho = 970\ \mathrm{kg\,m}^{-3}$ to an artificially low value of $\rho = 9.7\ \mathrm{kg\,m}^{-3}$. Reducing the density (and thereby the inertial contribution) by two orders of magnitude has a negligible effect on the high strain rate σ_n versus ε_n response. This strongly suggests that over the strain rates investigated here, the observed rate sensitivity is mainly associated with material rate effects rather than linked to inertial effects. These findings are summarised in Fig. 5.14b where we show FE predictions of the peak compressive strength σ_c over the range of strain rates investigated here for both the PB and UB cases with $\rho = 970\ \mathrm{kg\,m}^{-3}$ and $97\ \mathrm{kg\,m}^{-3}$. In the PB case the effect of material density is minor with a reduction in density only reducing the strength slightly at the highest strain rates. However,

there is a larger effect in the UB case. In particular, reducing the density in the UB case increases the strain rate at which the strong sensitivity of σ_c to strain rate commences. This is rationalised as follows. Recall that transverse inertia retards the separation of the plies in the UB case and this allows σ_c to be set by microbuckling of the plies in the UB case (similar to the mode in the PB case). Reducing the material density diminishes the effect of transverse inertia and thus a higher rate of loading is required to prevent ply separation at lower material densities. Nevertheless, given that the PB case represents a better approximation to the behaviour of these composites and we conclude that the observed rate effects over the range of strain rates investigated here are primarily due to the strain rate sensitivity of the material (or rather the matrix).

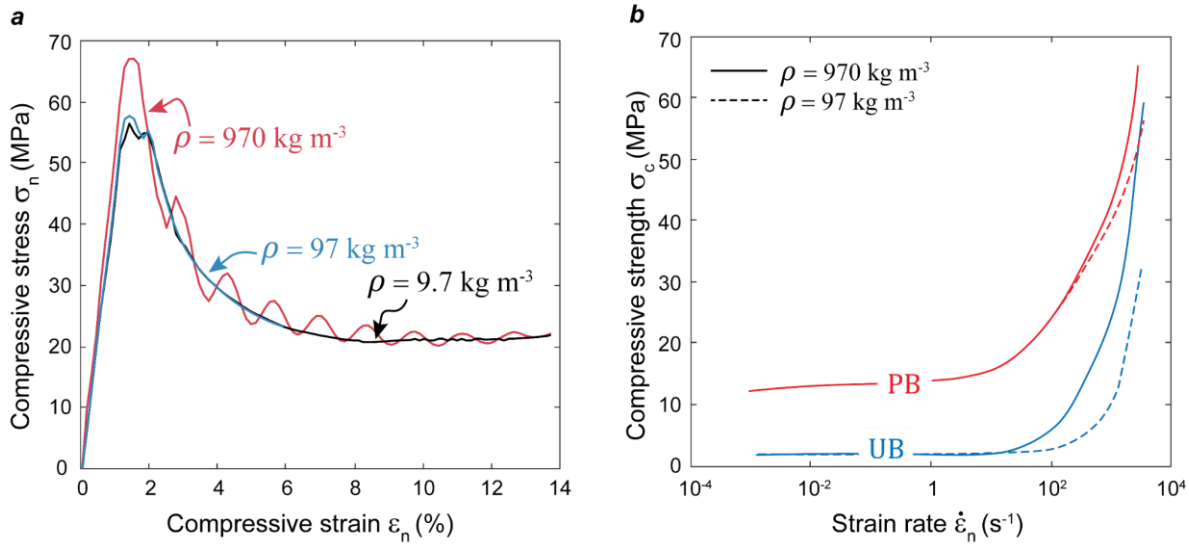

Figure 5.14: (a) FE predictions of the high strain rate ($\dot{\varepsilon}_n = 3980\ \mathrm{s}^{-1}$) compressive stress σ_n versus strain ε_n response for the perfectly-bonded (PB) case with three choices of the material density ρ. (b) FE predictions of the variation of the peak compressive strength σ_c with applied strain rate $\dot{\varepsilon}_n$ for the perfectly-bonded (PB) and un-bonded (UB) cases with a specimen misalignment $\omega = 0.7^{\mathrm{o}}$. Results in (b) are shown for two material densities ρ.

5.5.4 An analytical model for the rate dependence of the compressive response

The finding that the observed rate sensitivity is mainly set by material strain rate effects implies that we can develop a relatively simple analytical estimate relating the dependence of σ_c on the $\dot{\varepsilon}_n$. We do this by employing the kinematics of microbuckling as first developed by Budiansky and Fleck (1993) in the context of UD fibre composites.

Consider a UHMWPE composite with an initial fibre misalignment $\bar{\phi}$ in the 0^o plies in a band of width w that is inclined at an angle β as shown in Fig. 5.15. The imposed overall compressive strain rate $\dot{\varepsilon}_n$ is assumed to be accommodated by deformation that is restricted to this (kink) band such that shear and transverse straining vanishes outside the band. Then the initial deformation proceeds with $\dot{\beta} = 0$ such that the imposed deformation results in a material rotation ϕ as shown in Fig. 5.15 and no broadening of the kink band. This mode proceeds until lock-up at a rotation $\phi = 2(\beta - \bar{\phi})$ (Fleck et al., 1995) whereupon broadening commences. Since our aim is to provide an estimate of the peak strength σ_c we restrict our analysis to the initial regime where the kink width w remains fixed and deformation proceeds by material rotation within the band but no band broadening. Then a simple geometrical construction gives the relation between specimen shortening ΔH (Fig. 5.15) and the total misalignment $\bar{\phi} + \phi$ as

$$\Delta H = w[\cos\bar{\phi} - \cos(\bar{\phi} + \phi)], \tag{5.9}$$

with $\varepsilon_n \equiv \Delta H/H$ and H denoting the overall height of the specimen in its undeformed state. In the absence of transverse straining or shear strains outside the kink band, the shear strain γ_{13} within the kink band reduces to $\gamma_{13} = \gamma_b = \phi$ (Budiansky and Fleck, 1993) and it then follows that the shear strain rate within the kink band is related to the macroscopic imposed $\dot{\varepsilon}_n$ via

$$\frac{\dot{\gamma}_b}{\dot{\varepsilon}_n} = \frac{H}{w\sin(\bar{\phi} + \phi)}. \tag{5.10}$$

In the limit of the shear yield strain $\tau_Y/G_{12} \ll \bar{\phi}$, the compressive strength is given by the Argon (1972) analysis as

$$\sigma_c = \frac{\tau_f(\dot{\gamma}_b)}{\bar{\phi}}, \tag{5.11}$$

where τ_f is the shear flow strength of the matrix at shear strain rate $\dot{\gamma}_b$. Setting $\tau_f = \hat{\tau}^{(\kappa)}$ and $\dot{\gamma}_b = \dot{\gamma}$ in Eq. (5.7) and using Eq. (5.10) to relate $\dot{\gamma}_b$ to the imposed strain rate $\dot{\varepsilon}_n$ gives the required relation for the compressive strength $\sigma_c(\dot{\varepsilon}_n)$.

The above analysis is applicable to the perfectly aligned specimen ($\omega = 0^o$) with perfectly-bonded plies. A comparison between analytical and FE predictions of the $\sigma_c(\dot{\varepsilon}_n)$ is included in Fig. 5.5b for the PB case with $\omega = 0^o$. Excellent agreement is observed demonstrating the validity of this simple analysis. The key insight obtained from this analysis is that the imposed strain rates are magnified within the kink band as specified by Eq. (5.10). As a consequence, the strain rate sensitivity of the composite is enhanced compared to that of the underlying matrix properties. This is clearly evidenced in Fig. 5.5b where σ_c shows a high sensitivity to

strain rate for $\dot{\varepsilon}_n > 100\ \mathrm{s}^{-1}$ even though the transition strain rate for enhanced rate sensitivity of the underlying material properties is $\dot{\gamma}_t = 533\ \mathrm{s}^{-1}$.

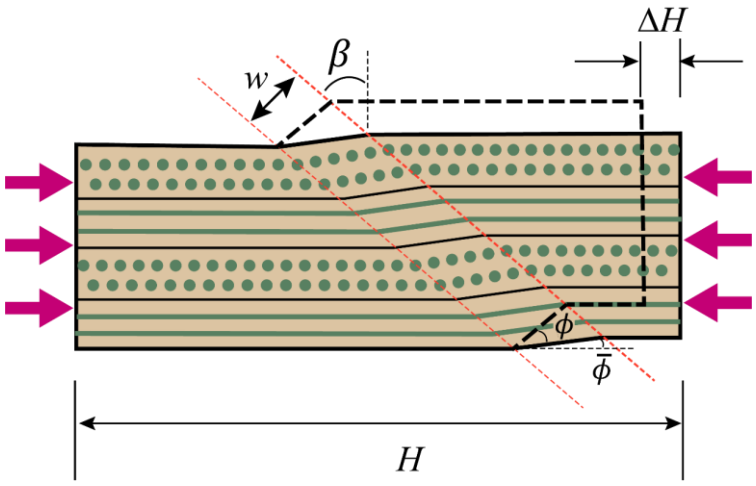

Figure 5.15: Sketch of kinematics of the deformation of the $[0^o/90^o]_n$ composite comprising in-extensional plies under compressive loading. The overall specimen shortens by ΔH (shown by the dashed lines) due to material rotating through an angle ϕ from its initial misalignment $\bar{\phi}$ in the band of width w. This band is oriented at an angle β with respect to the X_3-direction.

5.6. Concluding remarks

The in-plane compressive response of $[0^o/90^o]_n$ ultra-high molecular weight polyethylene (UHMWPE) fibre composites was investigated for strain rates in the ranging from $0.01\ \mathrm{s}^{-1}$ to $4000\ \mathrm{s}^{-1}$. The measurements, supported by optical microscopy and X-ray tomography, reveal that compressive deformation occurs by ply level kink band formation. This kinking is accompanied by ply delamination although delamination typically sets in after the peak strength is attained. The measurements show that the peak strength of the composite has a mild rate sensitivity for strain rates less than about $100\ \mathrm{s}^{-1}$ but is strongly rate dependent at higher strain rates.

Finite element (FE) calculations were also reported to understand the role of matrix rate sensitivity and inertia in setting the overall strain rate sensitivity of the composite. In these calculations, each ply within the specimen was discretely modelled using a pressure-dependent crystal plasticity framework that accurately accounts for the large shear strains and fibre rotations that occurs within each ply in the kink band. The calculations with plies assumed to be perfectly-bonded are in good agreement with measurements confirming that ply

delamination plays a secondary role in governing the compressive response, at least at moderate levels of applied strain. Importantly, the calculations show that for the range of strain rates investigated here, material inertia plays a negligible role with the observed strong rate sensitivity almost exclusively associated with the strain rate sensitivity of the matrix.

References

Argon, A.S., 1972. Fracture of composites. Treatise Mater. Sci. Technol. 1, 79–114.

Argon, A.S., 1972. Fracture of composites. Treatise Mater. Sci. Technol. vol.1 1, 79–114. https://doi.org/10.1016/B978-0-12-341801-2.50007-2

Attwood, J.P., Fleck, N.A., Wadley, H.N.G., Deshpande, V.S., 2015. The compressive response of ultra-high molecular weight polyethylene fibres and composites. Int. J. Solids Struct. 71, 141–155. https://doi.org/10.1016/j.ijsolstr.2015.06.015

Attwood, J.P., Khaderi, S.N., Karthikeyan, K., Fleck, N.A., O′Masta, M.R., Wadley, H.N.G., Deshpande, V.S., 2014. The out-of-plane compressive response of Dyneema composites. J. Mech. Phys. Solids 70, 200–226. https://doi.org/10.1016/j.jmps.2014.05.017

Bacon, C., 1999. Separation of waves propagating in an elastic or viscoelastic Hopkinson pressure bar with three-dimensional effects. Int. J. Impact Eng. 22, 55–69. https://doi.org/10.1016/S0734-743X(98)00048-7

Budiansky, B., Fleck, N.A., 1993. Compressive failure of fibre composites. J. Mech. Phys. Solids 41, 183–211. https://doi.org/10.1016/0022-5096(93)90068-Q

Calladine, C.R., English, R.W., 1984. Strain-rate and inertia effects in the collapse of two types of energy-absorbing structure. Int. J. Mech. Sci. 26, 689–701. https://doi.org/10.1016/0020-7403(84)90021-3

Chocron Benloulo, I.S., Rodríguez, J., Martínez, M.A., Sánchez Gálvez, V., 1997. Dynamic tensile testing of aramid and polyethylene fiber composites. Int. J. Impact Eng. 19, 135–146. https://doi.org/10.1016/S0734-743X(96)00017-6

Chocron, S., Nicholls, A.E., Brill, A., Malka, A., Namir, T., Havazelet, D., Werff, H. van der, Heisserer, U., Walker, J.D., 2014. Modeling unidirectional composites by bundling fibers into strips with experimental determination of shear and compression properties at high pressures. Compos. Sci. Technol. 101, 32–40. https://doi.org/10.1016/j.compscitech.2014.06.016

Collings, T.A., 1974. Transverse compressive behaviour of unidirectional carbon fibre reinforced plastics. Composites 5, 108–116. https://doi.org/10.1016/0010-4361(74)90548-5

Fan, J., Slaughter, W.S., 1997. High strain rate compression of fiber composites. J. Mech. Phys. Solids 45, 731–751. https://doi.org/10.1016/S0022-5096(96)00101-9

Fleck, N.A., 1997. Compressive Failure of Fiber Composites. Adv. Appl. Mech. https://doi.org/10.1016/S0065-2156(08)70385-5

Fleck, N.A., Deng, L., Budiansky, B., 1995. Prediction of Kink Width in Compressed Fiber Composites. J. Appl. Mech. 62, 329. https://doi.org/10.1115/1.2895935

Govaert, L.E., Lemstra, P.J., 1992. Deformation behavior of oriented UHMW-PE fibers. Colloid Polym. Sci. 270, 455–464. https://doi.org/10.1007/BF00665989

Gutkin, R., Pinho, S.T., Robinson, P., Curtis, P.T., 2010. On the transition from shear-driven fibre compressive failure to fibre kinking in notched CFRP laminates under longitudinal compression. Compos. Sci. Technol. 70, 1223–1231. https://doi.org/10.1016/j.compscitech.2010.03.010

Henriksson, A., 1990. Transverse compressive behavior of carbon-epoxy laminates and its influence on contact laws (Master's thesis). The Aeronautical Research Institute of Sweden, Stockholm, Sweden.

Hsiao, H.M., Daniel, I.M., Cordes, R.D., 1998. Dynamic compressive behavior of thick composite materials. Exp. Mech. 38, 172–180. https://doi.org/10.1007/BF02325740

Kromm, F.X., Lorriot, T., Coutand, B., Harry, R., Quenisset, J.M., 2003. Tensile and creep properties of ultra high molecular weight PE fibres. Polym. Test. 22, 463–470. https://doi.org/10.1016/S0142-9418(02)00127-7

Peijs, T., Smets, E.A.M., Govaert, L.E., 1994. Strain rate and temperature effects on energy absorption of polyethylene fibres and composites. Appl. Compos. Mater. 1, 35–54. https://doi.org/10.1007/BF00567210

Prabhakar, P., Waas, A.M., 2013. Interaction between kinking and splitting in the compressive failure of unidirectional fiber reinforced laminated composites. Compos. Struct. 98, 85–92. https://doi.org/10.1016/j.compstruct.2012.11.005

Radford, D.D., McShane, G.J., Deshpande, V.S., Fleck, N.A., 2007. Dynamic Compressive Response of Stainless-Steel Square Honeycombs. J. Appl. Mech. 74, 658–667. https://doi.org/10.1016/j.compositesa.2011.11.022

Rodríguez, J., Chocron, I.S., Martínez, M.A., Sánchez-Gálvez, V., 1996. High strain rate properties of aramid and polyethylene woven fabric composites. Compos. Part B Eng. https://doi.org/10.1016/1359-8368(95)00036-4

Russell, B.P., Karthikeyan, K., Deshpande, V.S., Fleck, N.A., 2013. The high strain rate response of Ultra High Molecular-weight Polyethylene: From fibre to laminate. Int. J. Impact Eng. 60, 1–9. https://doi.org/10.1016/j.ijimpeng.2013.03.010

Sanborn, B., DiLeonardi, A.M., Weerasooriya, T., 2015. Tensile Properties of Dyneema SK76 Single Fibers at Multiple Loading Rates Using a Direct Gripping Method. J. Dyn. Behav. Mater. 1, 4–14. https://doi.org/10.1007/s40870-014-0001-3

Shaker, K., Jabbar, A., Karahan, M., Karahan, N., Nawab, Y., 2017. Study of dynamic compressive behaviour of aramid and ultrahigh molecular weight polyethylene composites using Split Hopkinson Pressure Bar. J. Compos. Mater. 51, 81–94. https://doi.org/10.1177/0021998316635241

Skovsgaard, S.P.H., Jensen, H.M., 2018. Constitutive model for imperfectly bonded fibre-reinforced composites. Compos. Struct. 192, 82–92. https://doi.org/10.1016/j.compstruct.2018.02.053

Slaughter, W.S., Fan, J., Fleck, N.A., 1996. Dynamic compressive failure of fiber composites. J. Mech. Phys. Solids 44, 1867–1890. https://doi.org/10.1016/0022-5096(96)00050-6

Tsai, J., Sun, C.T., 2004. Dynamic compressive strengths of polymeric composites. Int. J. Solids Struct. 41, 3211–3224. https://doi.org/10.1016/j.ijsolstr.2003.12.010

Vaughn, D.G., Hutchinson, J.W., 2006. Bucklewaves. Eur. J. Mech. A/Solids 25, 1–12. https://doi.org/10.1016/j.euromechsol.2005.09.003

Vogler, T.J., Kyriakides, S., 1997. Initiation and axial propagation of kink bands in fiber composites. Acta Mater. 45, 2443–2454. https://doi.org/10.1016/S1359-6454(96)00350-3

Walley, S.M., Chapman, D.J., Williamson, D.M., Morley, M.J., Fairhead, T.W., Proud, W.G., 2009. High rate mechanical properties of Dyneema in compression. DYMAT 2009 - 9th Int. Conf. Mech. Phys. Behav. Mater. under Dyn. Load. 2, 1133–1138. https://doi.org/10.1051/dymat/2009158

Yu, B., Khaderi, S.N., Deshpande, V.S., Fleck, N.A., 2018. The effect of matrix shear strength on the out-of-plane compressive strength of CFRP cross-ply laminates. Int. J. Solids Struct. 139–140, 79–95. https://doi.org/10.1016/j.ijsolstr.2018.01.023

Zhu, L., Li, Y., Zhu, X., Zhu, Z., 2017. Compressive Mechanics and Failure Mechanism for Uhmwpe Fiber Reinforced Composite Laminates Under Hygrothermal Environment 20–25.

CHAPTER 6

6 Conclusions and Future work

The aim of this thesis was to investigate the micromechanics of ultra-high molecular weight polyethylene (UHMWPE) fibre composites. We began with a combined experimental and theoretical study on the deep penetration mechanisms of UHMWPE composites by a sharp-tipped punch and revealed the associated failure mechanisms. Micromechanical models were developed to predict the steady state pressure and the observed size effect upon punch diameter and ply thickness. We then explored the impact mechanisms of UHMWPE composite beams by blunt projectiles using a detailed finite element (FE) study. Failure mechanism maps were developed which provide a mechanistic understanding of the effect of shear strength on the ballistic performance of the composites. Finally, we investigated the dynamic in-plane compressive response of UHMWPE composites via experiments and finite element modelling. We demonstrated that the observed strong strain rate sensitivity was dependent on the matrix rate sensitivity rather than the inertial stabilization effect. Here we present our conclusions from this work and provide recommendations on future work.

6.1 Penetration of ultra-high molecular weight polyethylene composites

The quasi-static penetration response of both unidirectional (UD) and cross-ply UHMWPE composites was investigated. In both cases, the penetration pressure increased with increasing punch diameter and the penetration occurred without any fibre fracture. The size dependency of the penetration pressure was found on punches with diameters on the order of millimeters. For cross-ply composites, the penetration pressure also increased with decreasing ply thickness. The sharp-tipped punch penetrates the UD and cross-ply composites by the formation of mode-I cracks along the fibre directions, followed by the wedge open of the crack to accommodate the punch. For cross-ply composites, the incompatible deformation between the adjacent plies resulted in delamination around the punch. Micromechanical models were developed to model the steady state pressure and the associated crack lengths. A pressure-dependent crystal plasticity framework was developed to account for the finite fibre rotation and large shear strains within the individual plies. The models suggest that the observed size dependency of

the penetration pressure was caused by the competition between deformation of the composites by wedging open of the cracks and the extension of the mode-I and delamination cracks.

Based on the experimental measurements and micromechanical models, we estimate the mode-I inter-fibre splitting toughness $J_{IC} = 10\ \mathrm{kJ\ m^{-2}}$ with a combined mode-II/III delamination toughness $J_{IC} = 25\ \mathrm{J\ m^{-2}}$. In addition, the study indicates that the high penetration resistance of the UHMWPE composites by sharp-tipped punches results from their high toughness.

6.2 Impact failure mechanism maps for UHMWPE composites

The idealized problem of an infinite long, cross-ply UHMWPE composite beam impacted by a cylindrical projectile were investigated using detailed finite element (FE) calculations. All the individual plies in the beams were explicitly modelled using the crystal plasticity framework developed in Chapter 3.

We reported two distinct failure modes which can happen in the beams. The first is the mode I failure immediately under the projectile caused by the indirect tension mechanism. The second is the mode II failure at the rear of the beam resulting from beam bending. It is revealed that the mode I failure is dominant for beams with low shear strength while the mode II failure is the major failure mechanism for beams with high shear strength. The calculation predicts that the maximum tensile fibre stresses are lower in the low shear strength beams and thus higher impact velocities are required to initiate failure.

The failure mechanism maps provide a mechanistic understanding of the experimental observations that high ballistic performance composites require lower shear strength. Furthermore, the numerical calculations predict that there exists an optimal shear strength at which the velocity needed to initiate failure is maximized at a given fibre tensile strength. This optimal shear strength is shown to increase with increasing fibre strength and hence composite designs with ultra-high strength fibres might be a significant step towards “structural armours” which provide excellent ballistic performance as well as static load carrying capacity simultaneously.

6.3 Dynamic compressive response of UHMWPE composites

The in-plane compressive response of cross-ply UHMWPE composites was investigated for the strain rate in the range $0.01\ s^{-1}$ to $4000\ s^{-1}$. The stress response comprised a linear elastic phase followed by a softening phase with increasing strain. Optical microscopy and X-ray tomography demonstrated that the composites deformed by ply level kink band formation accompanied with ply delamination after the peak compressive stress was attained. A strong strain rate sensitivity of the peak compressive strength was observed for strain rates larger than $100\ s^{-1}$, but a mild strain rate dependence was observed at lower strain rates.

In order to understand the effect of matrix rate sensitivity and inertia on the overall strain rate sensitivity of the composite, we employed FE calculations to simulate the measured compressive response. The pressure-dependent crystal plasticity framework developed in Chapter 3 was used to explicitly model each individual ply. The calculations suggest that at moderate applied strain levels, the delamination between the plies play a secondary role in setting the overall compressive response. More importantly, the observed compressive strain rate sensitivity was shown to mainly result from the matrix strain rate sensitivity rather than the inertia stabilisation effect.

6.4 Future work

6.4.1 Dynamic penetration of UHMWPE composites

We have analysed in Chapter 3 the quasi-static penetration response of UHMWPE composites by a sharp-tipped punch and developed micromechanical models which successfully predicted the steady-state pressure and the associated crack lengths. A significant future step would be to investigate the dynamic penetration response and develop the associated modelling framework. Three-dimensional numerical models might be needed to be developed in order to incorporate the stress wave effects as well as the complex fracture modes underneath the projectile.

6.4.2 Constitutive models with damage initiation and propagation

We have developed a pressure dependent crystal plasticity framework in Chapter 3 and employed it to model the UHMWPE composites throughout the thesis. This model is capable of accounting for the finite shear strains and large fibre rotations within each individual ply. However, as the composites are mainly used in ballistic protection applications, constitutive

models which incorporate axial damage initiation and propagation under single and multi-axle load need to be developed. This is of course a significant challenge as the damage of UHMWPE composites is highly energetic and often accompanied with spring back of the fibres upon fracture. Recent development on advanced numerical modelling techniques such as the phase-field method might serve as an appropriate tool to incorporate damage into the constitutive modelling scheme.

6.4.3 Failure mechanism maps for the ballistic limit velocity

In Chapter 4 we have developed failure mechanism maps for the critical velocities required to initiate failure in cross-ply UHMWPE composite beams. This might serve as a first step towards a full understanding of the ballistic performance of the composites. A critical parameter which governs the ballistic performance is the ballistic limit velocity, and it requires the projectile to completely penetrate the composite. Therefore, failure mechanism maps based on ballistic limit velocity will be the ideal choice to gauge the ballistic performance of composites and study the interplay of that with different material properties such as shear strength and tensile strength. In order to achieve this, a robust numerical model is needed to quantitatively model the damage and fracture within the composites although this has proved elusive for a long period of time.

6.4.4 The dynamic kink band propagation of UHMWPE composites

In Chapter 5 we have investigated the peak compressive stress as a function of applied strain rate. However, the peak compressive strength is achieved at relatively small strains with negligible fibre rotations. It is well known that under quasi-static loading, the compression of composite materials at finite strains is associated with kink band broadening at which the kink band rotation angle is locked to a constant value of approximately two times of the kink inclination angle. Therefore, it would be of great use to investigate the dynamic compressive response at finite strain and study the kink band propagation. The challenge is to correctly record the deformation of the composite experimentally within the small time scales during the dynamic impact process. The numerical modelling framework developed in this thesis might serve as a starting point to analyse the rotation and broadening of the kink band for such problems.